ENVIRONMENTAL EFFECTS ON A SUSPENSION BRIDGE'S PERFORMANCE

Robert James Westgate

July 2012

Department of Civil and Structural Engineering

The University of Sheffield

A thesis submitted for the Degree of Doctor of Philosophy in Engineering

DECLARATION

This thesis is submitted for the degree of Doctor of Philosophy in the Department of Civil and Structural Engineering at the University of Sheffield. The thesis is based on independent work performed by the Author between October 2008 and July 2012 under the supervision of Professor James M. W. Brownjohn.

All the ideas and work are original except where referenced in the text and detailed in the "Division of work" sections of several chapters. The work contained in the thesis has not previously been submitted for any other qualification.

Robert James Westgate

July 2012

ABSTRACT

Current Structural Health Monitoring (SHM) research uses changes in a bridge's behaviour to locate and quantify the damage in a structure. However the structural responses are also linked to environmental effects, such as its temperature and the traffic load.

In order to understand a typical suspension bridge's behaviour to environmental conditions, studies on the Tamar Suspension Bridge's response to temperature and traffic are contained in this thesis. This was achieved by observing data collected from long-term monitoring systems installed on the structure, and simulated responses derived from a three-dimensional finite element model of the bridge.

The data of the bridge have shown that the profile of the suspension bridge reconfigures when the temperature of its structure increases, causing the deck to sag and expand. The natural frequencies of the bridge were noted to drop during the day. Transient thermal responses were also indentified; the differing rates of warming up between the deck, towers and cables manifested in the structural responses of the bridge. Phenomena caused by the temperature differential across the bridge's surface were also studied.

Investigations on the effect of traffic demonstrated its additional mass causes the natural frequencies to decrease for certain modes. This was identifiable in the time series data, where the largest reduction in frequencies is during rush hours. The investigations have shown that the changes the modal frequencies and modal mass are dependent on the eccentricity of the traffic flow on the bridge, which may increase or decrease depending on the mode shape. The loading of an abnormally heavy trailer on the bridge has also demonstrated the deformation to the bridge's quasi-static shape as the vehicle travelled across. The location of the vehicle on the bridge was also able to affect the modal properties of the suspension bridge, according to simulated results.

ACKNOWLEDGEMENTS

ACKNOWLEDGEMENT OF WORK FROM OTHER AUTHORS

Some of the work within this thesis was not produced by Robert Westgate, but from people whom he collaborated with to produce the research. The following section is for the reader to acknowledge which work was provided by other sources.

The installation and maintenance of the VES monitoring system on the bridge is credited to Ki-Young Koo, as well as the processing of Robotic Total Station signals to acquire the monitored quasi-static properties of the structure, and the processing of accelerometer signals to acquire the monitored dynamic properties of the structure. Ki-Young Koo also managed the monitoring equipment on the bridge during a site investigation which monitored the transit of a heavy vehicle (in Chapter 8).

In Chapter 2, Figure 2.9 and Figure 2.10 are taken from a 4th year undergraduate coursework by A. Spencer and M. Roberts.

In Chapter 4, Figure 4.1 and Figure 4.2 were created by Ki-Young Koo.

CONTENTS

LIST OF FIGURES

LIST OF TABLES

NOMENCLATURE FOR CHAPTERS 2 TO 5, 7 AND 8

A	area
C	coefficient
$\vec{D}$	vector of nodal degrees of freedom
d	mid-span sag
E	Young's modulus
F	applied force
f	frequency
G	function
$\overline{G}$	shear modulus
g	gravity
H, h	horizontal tension, additional horizontal tension
$\tilde{h}$	modal amplitude of additional horizontal tension
I	second moment of area
J	torsional moment of inertia
$\mathbf{K}$	stiffness matrix
L	span
$\mathbf{M}$	mass matrix
M	bending moment
MAC	Modal assurance criterion value
m	mass per unit length
P	structural parameter
p	spectral power

q	uniformly distributed load
R	structural response
$\mathbf{S}$	sensitivity matrix
S	length of cable; error sum of squares (for regression analysis)
s	coordinate; arc length
SYM	symmetry of the elements within a matrix
T, τ	axial tension, additional axial tension
$t, \hat{t}$	Time, time offset
u, v, w, θ	displacement; longitudinal, vertical, transverse, rotational
$\bar{u}, \bar{v}, \bar{w}$	modal displacement; longitudinal, vertical, transverse
V	vertical force at the support
$\mathbf{W}$	Weighting matrix (for updating parameters)
x, y, z	coordinates; longitudinal, vertical, transverse; non-descript variables
$\alpha, \beta, \gamma, \delta, \varepsilon, \zeta, \phi$	sub-functions used within 3D beam stiffness matrix
μ, σ	statistical properties; mean, standard deviation
ξ	error, error function (for sensitivity analyses)
ρ	total load per unit length; density
ω	circular natural frequency ($\omega = 2\pi f$)
τ	temperature
φ	mode shape vector

<div align="center">Mode shapes</div>

V, L, T, SS	shape; vertical, lateral, torsional, side-span.
S, A	symmetric, anti-symmetric
1, 2, 3, ...	number of sine waves

Subscripts/Superscripts

0	baseline
an	analytical
c	cable
d	deck
eq	equivalent
ex	experimental
fe, m	derived from data; monitored, finite element model
geo	geometric
h	hanger
$impo$	imposed load
S	Shear (to denote "Shear area")
s	sampling (for data sampling rates)
st	structural
t, v	environmental effect; temperature, vehicles
tr	truss
x, y, z	direction; horizontal, vertical, transverse

NOMENCLATURE FOR CHAPTER 6 AND APPENDIX A

c	specific heat capacity
D	day length
d	day of the year
F	solar radiation fixed factor
f	factor (value depends on subscript)
k	thermal conductivity coefficient
h	convection coefficient
J	radiation
n	direction vector that is normal to surface
p	fraction of radiation in full spectrum sunlight
q	heat flow
S	sunshine duration
T	temperature
t	time
w	deck thickness
v	elevation from sea level
x, y, z	coordinates; longitudinal, vertical, transverse
α	absorption coefficient
β	slope inclination from horizontal
γ	aspect of face
ε	emissivity coefficient

θ	solar zenith angle
λ,μ	coordinate of location; latitude, longitude
ξ	equation for time
ζ	net time correction factor
ρ	density
σ	Stefan–Boltzmann constant
$\mathbb{T}$	temperature difference
τ	atmospheric transmissivity
$\varnothing$	solar elevation
ψ	solar azimuth
φ	hour angle

Subscripts/Superscripts

0	at noon
a,b	solar radiation; unaffected by, affected by
air,sur	air, surface
blue,cloudy	sky conditions; blue (clear) sky, cloudy sky
c,j,r	heat; convection, solar irradiation, surface radiation
cc	cloud cover
GMT	Greenwich mean time
i	inclined
min, max	values; Minimum, maximum
s	time interval
t	time
x,y,z	direction; horizontal, vertical, transverse

CHAPTER ONE

INTRODUCTION TO THE RESEARCH

1.1 STRUCTURAL HEALTH MONITORING

Structural Health Monitoring (SHM) is the term that describes the range of systems implemented on various civil infrastructure, which inform operators whether it is fit for its purpose. The demand for SHM systems to be fitted to structures has grown over the last few decades, whether it is to observe the construction of the structure, a portion of its lifetime, or to monitor its demolition. Accompanying the monitoring systems are giant databases of records detailing the structure's behaviour, which may be picked apart and rearranged, from which an analyst may derive some conclusions. Deterioration or sudden deviations in responses may indicate a structural failure, which the analyst may wish to react upon.

For long span bridges, SHM is driven by range of reasons, typically from extreme or freak loading due to their size, such as earthquakes or wind. SHM may also be applied to validate bridge design assumptions and guidelines, deterioration of the bridge, and provide real-time information of the structure. Additionally, long term monitoring may capture interesting behaviour in real life operational conditions. These phenomena may surprise the most experienced of bridge engineers, and catch them out unexpectedly. The possibility of characterising and describing a complete set of these occurrences increases when the bridge is constantly monitored.

The scope of this project will be considering suspension bridges, which are typically high profile, critical infrastructure objects that are relatively flexible compared to other bridge forms. There are numerous examples of suspension bridges fitted with long-term monitoring systems, mainly in Japan, Hong Kong, mainland China, Korea, North America and Europe.

1.2 MOTIVATION FOR THE STUDY

Data collected from long-term monitoring have shown that the quasi-static and dynamic response of a bridge may change, depending on the environmental and operating conditions. Contributors are found to be ambient temperature, wind speed and direction, humidity, solar radiation and vehicular loading. All of these loadings lead not only to a direct response from the structure, but can also affect physical parameters (such as the material properties) and mechanisms in a bridge (such as boundary conditions and cable relaxation).

SHM research often focuses on changes in dynamic properties and the quasi-static global performance. Warning systems use performance thresholds to determine whether the fitted structure is performing tolerably, or warn if it may be unfit for use. A threshold can be indicated by static or modal responses, either globally (observing the response of the whole

structure) or locally (the change in response of an individual member). Responses that are affected by environmental conditions may trigger the warning system, when in fact the structure might be considered healthy. Worse, a faulty structure may go unnoticed. Solutions are developed from understanding the environmental behaviour, and adjusting the thresholds.

Hence a prerequisite is to model responses to environmental loading effects with reasonable accuracy. The behaviour of the bridge to such loads may be replicated by using either 'data driven' models (such as regression analyses, principal component analyses and meta-models) or 'physics-based' models (such as Finite Element (FE) models). Both types of model may be calibrated from a back catalogue of data on the structure's performance and environmental condition database, which can be provided by installed long-term monitoring systems.

There are also design considerations that account for the environment that would benefit from long-term recordings of the structure performance and loading. Expansion joint design in bridges are adopted from analysis of similar structures, as opposed to recorded evidence and analytical information. Cables may slacken due to thermal expansion or by deck uplift from the wind. This behaviour can be explored easily if there is well populated database available.

A problem with identifying structural responses caused by environmental conditions is that they may correlate with other contributors. Thermal radiation on the deck would be at the hours of daylight when traffic would run across the span, both of which affect the modal results. However, since they occur at similar times it presents a difficulty of distinguishing each of their contributions. It is the task of the analyst to differentiate the responses to the condition of the bridge, either by looking at monitored data which has a limited variance from other environmental effects, or simulate their performance to such loads by using models.

The aim of the investigations in this thesis is to quantify changes in suspension bridge behaviour from thermal and vehicle loading, and identify their mechanisms. This will be achieved by collecting results for the Tamar Suspension Bridge, which connects Plymouth and Cornwall in the United Kingdom. Data have been collected from the long-term monitoring systems installed upon the structure, and an FE model of the structure was developed to simulate its behaviour from thermal and vehicle loading.

Other environmental conditions, such as wind and humidity, have not been investigated, to avoid dilution of the studies by considering too many parameters. Of particular note is wind loading, which is known to have a considerable effect on the performance of suspension bridges, such as buffeting and flutter. Due to the considerable body of literature on the complex phenomena of wind loading on suspension bridges, changes in behaviour due to wind

would require independent investigation outside the scope of this thesis.

While the performance between two structures will never be alike, due to unique structural systems and surroundings, this thesis contains methodology and behaviour that can be applied or observed elsewhere.

1.3 ORGANIZATION

The study begins with a literature review in Chapter 2 on the history of suspension bridge analyses to date. This review is used to appreciate developments in physics based modelling of this type of structure, and provide an overview of the development and application of FE models in current suspension bridge research. The literature review also contains a review of research upon changes in bridge performance due to thermal and traffic loads.

Chapter 3 uses the acquired knowledge from the literature review to assist the development of an FE model of the Tamar Suspension Bridge, including a method for determining the internal force equilibrium between the tensions in the cables and the deflection of the deck structure and tower tops.

Chapter 4 considers how the temperature of the structure affects the quasi-static behaviour of the structure, using results from the developed FE model and data from the monitoring systems installed on the bridge.

Chapter 5 looks at how the dynamic response of the structure may be linked with the thermal response of the structure, both for changes in its structural properties and adjustments to its configuration that relate to its temperature.

In Chapter 6 the time-dependent thermal responses through the structure are observed, using monitored data and 60 days of simulated results from transient heat analyses upon the suspension bridge model.

Chapter 7 considers the effect of traffic mass on the performance of the bridge, by looking at monitored responses in the structure which suggest the presence of traffic, and replicating that behaviour in the FE model.

To accompany the traffic studies, Chapter 8 is a report on the behaviour of the Tamar Suspension Bridge during transit of an abnormal load, providing an extreme example of bridge static response due to passage of a single vehicle.

Chapter 9 completes the thesis with conclusions from the investigations, as well as suggestions to take the research further.

CHAPTER TWO

A HISTORY OF NUMERICAL ANALYSES USED FOR SUSPENSION BRIDGES: A LITERATURE REVIEW

2.1 INTRODUCTION

The behaviour of suspension bridges is a complex problem that is still being extensively explored, since these type of structure exhibits some unique behaviour in comparison to others. An objective for some researchers is to identify the possible causes to the responses identified on the structure via monitoring or observations, and investigate possible controllable measures if they impede the bridge's operation. An example of this is the "fluttering" behaviour exhibited by the Tacoma Narrows Bridge, before it failed catastrophically (Larsen 2000).

History has produced several methods to analyse a typical standard suspension bridge structure; which originally began as an investigation by the Bernoulli brothers on the catenary equation. Navier's report and findings on European bridges paved the way for elastic and deflection theory (Buonopane & Billington 1993), which has developed more efficient and longer bridges. The advent of computer technology has produced more advanced analytical methods, which models to consider more variables and conditions, and produce results even more rapidly.

Common practise at the time of writing is the use of finite element (FE) to demonstrate a structure's performance, where its continuous form is discretised to a finite mesh of degrees of freedom. The partial differential equations determining its performance may then be solved for each mesh node, provided that the boundary conditions and loading are given.

The literature review is presented to introduce the reader to the mathematical methods used to analyse suspension bridges, up to the present practise of finite element models.

2.2 HISTORY

2.2.1 CATENARY DERIVATION

In the 15th Century Leonardo da Vinci was the first to draw and propose a theoretical model of a catenary; the shape adopted by a hanging cable. Later, in 1638, Galileo wrote in "Discorsi" that the cable's internal forces may resemble the flight of a projectile, and would "assume the form of a parabola". The hanging cable was later identified to be a hyperbolic profile by the Bernoulli brothers, Leibnitz and Huygens, in 1691. It is observed that the profile of the catenary is the adopted shape of bending moments from a uniform distributed load acting upon a simply-supported beam (Valiente 2005).

The equations presented here have been reproduced from material derived predominantly by Irvine (1981), as well as Brownjohn (1994).

It is assumed that

- Cables are uniform and elastic,

- The cable supports are rigid, and

- Cables only support tension loads, and the mean tension in the cable is much greater than the fluctuating component of tension during vibration, an assumption relevant to dynamic analyses.

For static equilibrium of a cable, as shown in Figure 2.1, under a uniform distributed load ρ per unit length, the increment of tension T of a cable with elemental length ds resolved vertically is given by:

$$\frac{d}{dx}\left(T\frac{dy}{ds}\right) = mg = \rho\Delta s = \rho ds \qquad (2.1)$$

where m is the mass per unit length and g the gravitational acceleration.
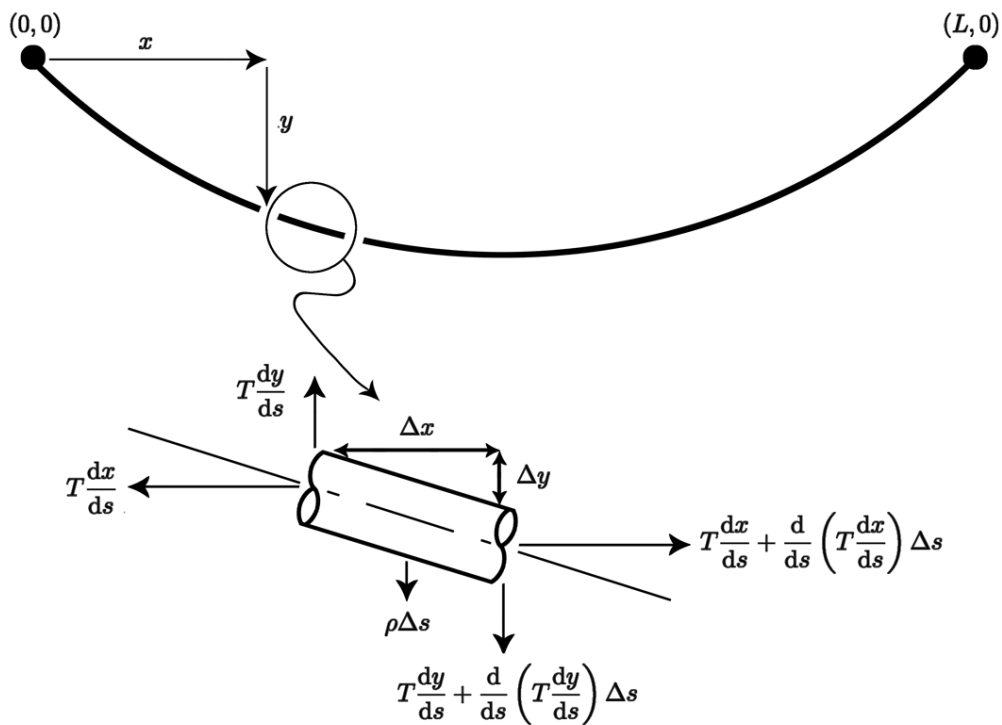
Figure 2.1: Geometry of catenary

where x and y are the horizontal and vertical coordinates, s is the length of cable, L is the span of the catenary, and T is the axial tension in the cable.

Since there are no longitudinal loads acting on the cable ($dH / dx = 0$) and $T = Hds / dx$,

32

where *H* is the horizontal component of the tension, horizontal equilibrium provides

$$H\frac{d^2y}{dx^2} = \rho ds \tag{2.2}$$

For the geometry of the catenary, we know from Pythagoras' theorem that

$$ds = \sqrt{1 + \left(\frac{dy}{dx}\right)^2} \, dx \tag{2.3}$$

Temporarily replacing dy/dx with κ and substituting Equation 2.3 into Equation 2.2, integration of both sides leads to

$$\int \frac{d\kappa}{\sqrt{1+\kappa^2}} = \int \frac{\rho}{H} dx$$
$$\sinh^{-1}\kappa = \frac{\rho}{H} x$$
$$\sinh^{-1}\frac{dy}{dx} = \frac{\rho}{H} x \tag{2.4}$$
$$\frac{dy}{dx} = \sinh\left(\frac{\rho}{H} x\right)$$

which is integrated to produce

$$y = \frac{H}{\rho}\left(\cosh\left(\frac{\rho}{H} x\right) - 1\right) \tag{2.5}$$

Equation 2.5 is used to find the length of the cable S, and its sag d:

$$S = \frac{2H}{\rho}\sinh\left(\frac{\rho L}{2H}\right) \tag{2.6}$$

$$d = \frac{H}{\rho}\cosh\left(\frac{\rho L}{2H} - 1\right) \tag{2.7}$$

Equations 2.6 and 2.7 can then combined to produce an equation for the horizontal force in the cable H, with contains parameters that are fairly simple to calculate.

$$H = \frac{\rho}{8d}\left(S^2 - 4d^2\right) \tag{2.8}$$

The length of the cable L can also be found by rearranging Equation 2.6

$$L = \frac{2H}{\rho} \sinh^{-1}\left(\frac{\rho S}{2H}\right) \qquad (2.9)$$

The vertical force at the cable's support is $V = \rho S / 2$, which can be used to calculate the tension at the support.

$$T^2_{x=\pm L/2} = H^2 + \left(\frac{\rho S}{2}\right)^2 \qquad (2.10)$$

When Equation 2.5 is expanded into powers of x, the lowest term will yield

$$y = \frac{\rho x^2}{2H} \qquad (2.11)$$

Alternatively, a straight-forward solution may be derived if the distributed load ρ is simplified to per unit horizontal length, as opposed to per unit length of the cable. The right hand side of Equation 2.1 would then equal ρdx and Equation 2.2 would be $H d^2 y / dx^2 = \rho dx$ Integration of this equation and applying boundary conditions would also yield Equation 2.11. Substituting $x = L / 2$ would provide an approximate solution to the sag of the cable:

$$d = \frac{\rho L^2}{8H} \qquad (2.12)$$

2.2.2 NAVIER'S THEORY

In 1823, the mathematical theory of the catenary equation was extended by Claude Navier to include live-load effects (Buonopane & Billington 1993). Navier's findings were recorded in his book, "Mémoire sur les ponts suspendus", which documented his research into the theory and history of early English suspension bridges (Navier 1823).

Navier recognised that the vertical deflections of the cable decrease as the increased dead load supported by the catenary, demonstrating the tension stiffening of the cable. He also noticed that bridges with shallower sags were also more capable of supporting heavier loads, and proposed a small 1:17 sag-to-span ratio of a suspension bridge over the Reine, as opposed to 1:12, which was typical for early English suspension bridges.

Charles Ellet's Wheeling Bridge was designed by applying Navier's theories, which provided vertical stiffness with a shallow (1:14) catenary cable and large dead load. The design contained an un-stiffened deck, since he believed a truss would provide an unnecessary rigidity. Unfortunately, due to the lack of provision for wind loads, the suspension bridge failed

in a storm in 1854, with vibration amplitudes of 9m!

In 1855, Roebling adopted a different approach when designing the Niagara Bridge by providing a combination of stiffening systems. This approach was used throughout Roebling's designs, especially the Brooklyn Bridge, which was completed in 1883 with a span of 486m long: a huge progression in bridge spans at the time.

2.2.3 RANKINE THEORY

William Rankine developed the first theoretical treatment of suspension bridges in 1858, following an experiment by Peter Barlow demonstrating that a significant reduction in material is possible by suspending the bridge structure from a chain (Barlow 1858). The Rankine theory assumes that any concentrated live load applied to the stiffening structure will be transferred to the cable as a uniformly distributed load (UDL).

For example, as shown in Figure 2.2, a centred imposed load which takes up half the span is supported by an equivalent uniform load on the cable, $0.5L\rho_{impo} + L\rho_{eq,c} = 0$, where L is the span of the girder, ρ_{impo} is the imposed load, and $\rho_{eq,c}$ is the equivalent load in the cable.
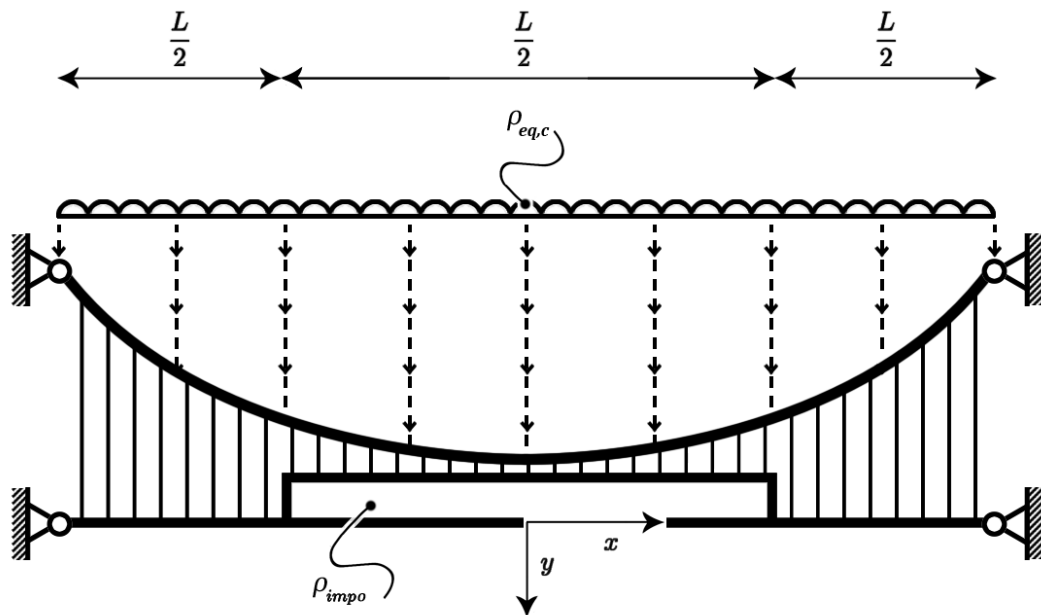
Figure 2.2: Demonstration of Rankine's suspended girder theory

The equivalent bending moments in the stiffening structure M_{st} and cables M_c are found to be:

$$M_{st} = \frac{3\rho_{impo}L^2}{32} - \frac{\rho_{impo}x^2}{2}$$
$$M_c = \frac{\rho_{eq,c}L^2}{4} - \rho_{eq,c}x^2$$

(2.13)

The moments at the centre of the span, $x = 0$, are found to be:

$$M_{st} = \frac{3\rho_{impo}L^2}{32}$$
$$M_c = \frac{\rho_{eq,c}L^2}{4} = -\frac{\rho_{impo}L^2}{8}$$

(2.14)

The addition of these two moments gives the total applied moment at the centreline of the stiffening structure, $M = -\rho_{impo}L^2/32$. The mid-span moment of an unsuspended beam under an equivalent UDL of the imposed load would be $\rho_{impo}L^2/8$; demonstrating that the suspended girder only supports a quarter of the moment.

2.2.4 ELASTIC THEORY

Elastic theory was developed after the Rankine Theory by several authors, most notably Ritter, Levy, Melan and Steinman. Consider the beam suspended by a cable, as shown in Figure 2.3, where ρ_{dead} and ρ_{impo} are respectively dead and imposed loads upon the beam.
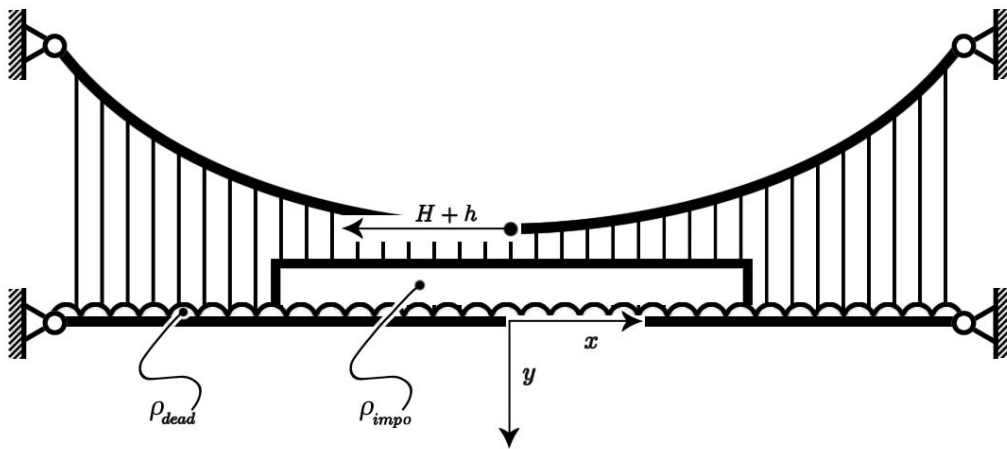
Figure 2.3: Demonstration of elastic theory.

where H the horizontal cable tension due to the dead load, and h the additional horizontal cable tension due to the imposed load.

Total moments on the beam, M, are thus found to be:

$$M = M_{dead} + M_{impo} - (H + h)y \qquad (2.15)$$

where M_{dead} and M_{impo} are the moments caused by the dead and imposed loads, respectively. Since $Hy = M_{dead}$, Equation 2.15 is reduced to

$$M = M_{impo} - hy \qquad (2.16)$$

Thus the live load moment in the girder is reduced by the vertical location, and the horizontal force in the cable.

2.2.5 DEFLECTION THEORY

In 1888, deflection theory was developed by Melan in "Theorie der eiseren Bogenbrücken und der Hängenbrücken" as a development of the elastic theory, which was the first to allow for non-linear behavior and second order effects in the cables (Melan 1888). It assumes that the deck prevents the cable from having an optimum profile as an unstiffened cable, and by making the truss more flexible the bridge would be able to support more load.

Assuming that the ordinary theory for bending applies, the flexure of the suspension bridge may be considered as a beam. Assuming that the dead load of the deck is already supported via the cable, bending will be caused by the imposed loading on the deck, ρ_{impo}, and a relieving load from the hangers, q_h.

$$E_d I_d \frac{d^4 v}{dx^4} = \rho_{impo} - q_h \qquad (2.17)$$

where $E_d I_d$ is the bending stiffness of the bridge deck.

On similar lines the suspension cable has to support the additional load from the hangers. Equation 2.2 is adapted to incorporate this additional load, which creates additional horizontal tension of the cable, h, and a change in its vertical deflection, v.

$$(H + h) \frac{d^2}{dx^2}(y + v) = \rho_c + q_h \qquad (2.18)$$

Remove the dead load condition $Hd^2y / dx^2 = \rho_c$ and combine with Equation 2.17 to get

$$E_d I_d \frac{d^4v}{dx^4} + (H+h)\frac{d^2v}{dx^2} + h\frac{d^2y}{dx^2} = \rho_{impo} \tag{2.19}$$

This equation in the fundamental differential equation for a suspension bridge in its classical form. Using this equation, the bending moments from the suspension bridge may be observed (Buonopane & Billington 1993)

$$M = M_{imp} - hy - (H+h)v \tag{2.20}$$

Equation 2.20 is similar to the bending moment equation developed from elastic theory (2.16), except it has an additional term $(H+h)v$. This shows that the elastic theory fails to account for the additional relieving moment from the horizontal component of the total cable tension, dead and live load together, when the bridge deflects a distance of v under the live load.

Cobo del Arco and Aparicio (2001) analysed 19 already-built suspension bridges using the equations developed from deflection theory, to help understand the static behaviour of suspension bridges.

2.2.6 RELAXATION THEORY

Equation 2.19 may be treated as a trigonometrical series, and was first proposed by Timoshenko (1930), which incorporated terms which are normally neglected, such as the horizontal cable movement. Atkinson and Southwell (1939) developed a relaxation procedure along similar lines. The subsection presented here is a shortened version taken from Pugsley (1957).

Consider that Equation 2.19 may be written as an equivalent Fourier series:

$$E_d I_d \frac{d^4v}{dx^4} + (H+h)\frac{d^2v}{dx^2} = \sum_{i=1}^{\infty} b_i \sin\frac{i\pi x}{L} \tag{2.21}$$

where b_i is a typical Fourier coefficient dependent on the sag of the cable, the additional horizontal tension, and the location and amount of imposed load. Thus the additional deflection v and bending moments M_{impo} on the bridge deck may also be defined as a Fourier series:

$$v = \sum_{j=1} a_j \sin \frac{j\pi x}{L} \qquad (2.22)$$

$$M_{impo} = \sum_{k=1} c_k \sin \frac{k\pi x}{L} \qquad (2.23)$$

These two Fourier series may be truncated to a convenient finite number; Atkinson and Southwell adopted the sum of 9 series for his first example. The coefficients c_k may be determined for any given external loading on the bridge. Therefore a_j needs to be redefined in terms of c_k. This can be achieved by reintroducing Equation 2.19, as well as using an equation which relates the changes in geometry of the cable to changes in its tension when the cable is displaced from its equilibrium, as shown in Figure 2.4.
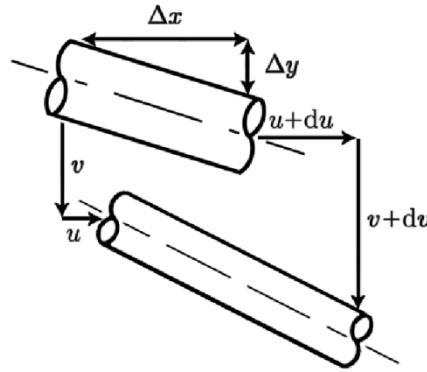
Figure 2.4: Displacements of a cable element.

If $\mathrm{d}s$ is the original length of the segment, and $\overline{\mathrm{d}s}$ its new length, then

$$\mathrm{d}s^2 = \mathrm{d}x^2 + \mathrm{d}y^2$$

$$\overline{\mathrm{d}s}^2 = (\mathrm{d}x + \mathrm{d}u)^2 + (\mathrm{d}y + \mathrm{d}v)^2 \qquad (2.24)$$

where u is the additional horizontal deflection. For cables with limited sag, the fractional change in length, correct to second order of small quantities, is

$$\frac{\overline{\mathrm{d}s} - \mathrm{d}s}{\mathrm{d}s} \approx \frac{\mathrm{d}u}{\mathrm{d}s}\frac{\mathrm{d}x}{\mathrm{d}s} + \frac{\mathrm{d}y}{\mathrm{d}s}\frac{\mathrm{d}v}{\mathrm{d}s} + \frac{1}{2}\left(\frac{\mathrm{d}v}{\mathrm{d}s}\right)^2 \qquad (2.25)$$

while according to Hooke's law:

$$\frac{\tau}{E_c A_c} = \frac{\overline{\mathrm{d}s} - \mathrm{d}s}{\mathrm{d}s} \tag{2.26}$$

where τ is the additional tension on the element, E_c is the Young's modulus of the cable, and A_c its area. At second order $\tau = h \cdot \mathrm{d}s / \mathrm{d}x$, so Equation 2.26 now becomes

$$\frac{h}{E_c A_c} \left(\frac{\mathrm{d}s}{\mathrm{d}x} \right)^3 \approx \frac{\mathrm{d}u}{\mathrm{d}x} + \frac{\mathrm{d}y}{\mathrm{d}x} \frac{\mathrm{d}v}{\mathrm{d}x} + \frac{1}{2} \left(\frac{\mathrm{d}v}{\mathrm{d}x} \right)^2 \tag{2.27}$$

Integrating between 0 and L leads to

$$\frac{hL_{eq}}{E_c A_c} \left(\frac{\mathrm{d}s}{\mathrm{d}x} \right)^3 = u(L) - u(0) + \int_0^L \frac{\mathrm{d}y}{\mathrm{d}x} \frac{\mathrm{d}v}{\mathrm{d}x} + \frac{1}{2} \int_0^L \left(\frac{\mathrm{d}v}{\mathrm{d}x} \right)^2 \tag{2.28}$$

where $L_{eq} \approx L(1 + 8(d/L)^2)$, and $u(0)$ and $u(L)$ are the longitudinal movement of the cable supports. Since it is assumed the supports are unable to move longitudinally, and that Equation 2.2 ($H \cdot \mathrm{d}^2 y / \mathrm{d}x^2 = \rho \mathrm{d}s$) demonstrates that $\mathrm{d}y / \mathrm{d}x$ remains continuous along the span of the cable, then Equation 2.28 is modified to become

$$\frac{hL_{eq}}{E_c A_c} = \frac{\rho}{H} \int_0^L u \mathrm{d}x + \frac{1}{2} \int_0^L \left(\frac{\mathrm{d}v}{\mathrm{d}x} \right)^2 \mathrm{d}x \tag{2.29}$$

By ignoring second order terms, and rewriting Equations 2.19 and 2.29 in terms of Equations 2.22 and 2.23, the following two equations are derived

$$c_j - h \sum_{j=1} \left(A_{j,k} + B_{j,k} \right) a_j = H \sum_{j=1} F_{j,k} a_j \tag{2.30}$$

$$h = \sum_j D_j a_j \tag{2.31}$$

where $A_{j,k}$, $B_{j,k}$, D_j and $F_{j,k}$ are coefficients that are dependent on the design of the bridge. These values may be tabulated for a variety of given j and k values; several examples are provided by Atkinson and Southwell.

2.2.7 RESPONSE TO POINT LOADS

It is understood that the response of the cable acting under a load is non-linear. As the load is incrementally increased under successive loads the subsequent deflections reduce (Irvine &

Sinclair 1976). Consider a point load F acting at a point x_1 on a suspended cable, as shown in Figure 2.5.
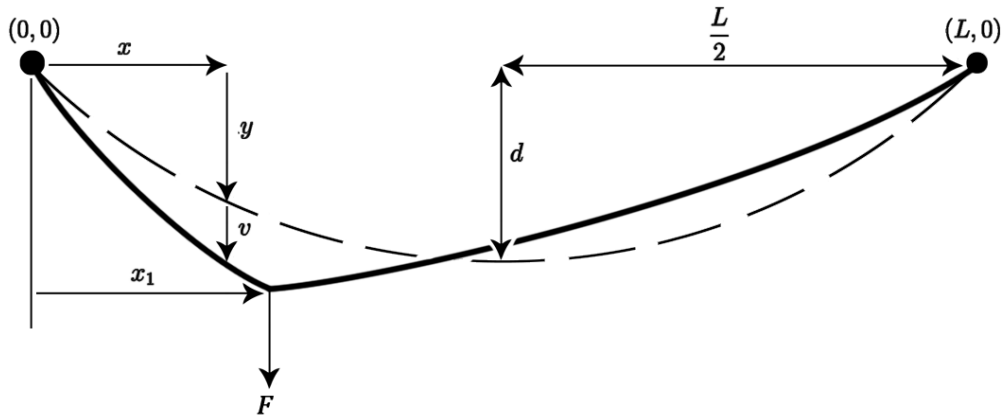
Figure 2.5: Deflection of catenary under a single point load.

For the vertical equilibrium of the cable, it is found that

$$(H+h)\frac{d}{dx}(y+v) = \frac{\rho L}{2}\left(\frac{2x}{L}-1\right)+F\left(1-\frac{x_1}{L}\right) \qquad 0 \le x \le x_1$$

$$(H+h)\frac{d}{dx}(y+v) = \frac{\rho L}{2}\left(1-\frac{2x}{L}\right)-F\frac{x_1}{L} \qquad x_1 \le x \le L$$

(2.32)

Removing terms associated with the self-weight of the cable, the equations simplify to

$$(H+h)\frac{dv}{dx} = F\left(1-\frac{x_1}{L}\right)-h\frac{dy}{dx} \qquad 0 \le x \le x_1$$

$$(H+h)\frac{dv}{dx} = -F\frac{x_1}{L}-h\frac{dy}{dx} \qquad x_1 \le x \le L$$

(2.33)

of which both equations may be integrated directly to provide dimensionless equations for the additional vertical displacements:

$$\mathbf{v} = \frac{1}{1+\mathbf{h}}\left\{(1-\mathbf{x}_1)\mathbf{x}-\frac{\mathbf{h}}{2\mathbf{F}}\mathbf{x}(1-\mathbf{x})\right\} \qquad 0 \le \mathbf{x} \le \mathbf{x}_1$$

$$\mathbf{v} = \frac{1}{1+\mathbf{h}}\left\{\mathbf{x}_1(\mathbf{x}-1)-\frac{\mathbf{h}}{2\mathbf{F}}\mathbf{x}(1-\mathbf{x})\right\} \qquad \mathbf{x}_1 \le \mathbf{x} \le 1$$

(2.34)

where $\mathbf{v} = (v/L)/(H/F)$, $\mathbf{h} = h/H$, $\mathbf{x} = x/L$ and $\mathbf{F} = F/mgL$. Thus, the only unknown

variable is $\mathbf{h}$, which can be determined from Equation 2.29. However at the location where point loading is applied dv/dx becomes discontinuous, and the last integral in Equation 2.29, when integrated in parts, becomes

$$\frac{1}{2}\int_0^L\left(\frac{dv}{dx}\right)^2 dx = -\frac{1}{2}\left\{\frac{dv}{dx}v\Big|_{x_1^-}^{x_1^+} + \frac{d^2v}{dx^2}\int_0^{x_1} v\,dx + \frac{d^2v}{dx^2}\int_{x_1}^L v\,dx\right\}$$

(2.35)

Combining Equations 2.29 and 2.35 together, then performing the integration with Equation 2.34 yields the dimensionless cubic equation for the additional horizontal component, $\mathbf{h}$:

$$\mathbf{h}^3 + \left(2+\frac{\lambda^2}{24}\right)\mathbf{h}^2 + \left(1+\frac{\lambda^2}{12}\right)\mathbf{h} - \frac{\lambda^2 \mathbf{x}_1}{2}(1-\mathbf{x}_1)\mathbf{F}(1+\mathbf{F}) = 0$$

(2.36)

where λ^2 is the Irvine-Caughey non-dimensional cable parameter (Irvine, 1981). Using Equation 2.12, this parameter is equal to

$$\lambda^2 = \frac{\left(\dfrac{\rho L}{H}\right)^2 L}{\dfrac{HL_{eq}}{E_c A_c}}$$

$$= \frac{64}{L_{eq}}\frac{E_c A_c}{H}\left(\frac{d}{L}\right)^2$$

(2.37)

The Irvine-Caughey parameter relates the geometric stiffness of the cable's profile (the numerator) with its axial stiffness (the denominator). On suspension bridges it is generally the profile which governs the value of this parameter, and should be large as $\rho L/H$ approaches 1.

2.2.8 LINEAR DYNAMIC RESPONSE OF CABLE

Daniel Bernoulli published an infinite series solution for the natural frequencies of a cable in 1738. In 1764 Euler found the equation of motion of a vibrating taut membrane, the equation of which was partially solved by Poisson in 1829, and completed by Clebsch in 1862 with the inclusion of anti-symmetric modes.

According to Bleich et al. (1950), the vertical equation of motion for the equilibrium of a cable element shown in Figure 2.6 under a periodic force can be described as

$$-\left(\rho + m\frac{\partial^2 y}{\partial t^2}\right) = \frac{(H+h)}{\partial x}\left\{\partial\left(y_2 + v_2\right) - \partial\left(y_1 + v_1\right)\right\}$$

$$= (H+h)\left(\frac{d^2 y}{dx^2} + \frac{\partial^2 v}{\partial x^2}\right) \qquad (2.38)$$

$$= H\frac{d^2 y}{dx^2} + h\frac{d^2 y}{dx^2} + H\frac{\partial^2 v}{\partial x^2} + h\frac{\partial^2 v}{\partial x^2}$$

where t is an increment of time.
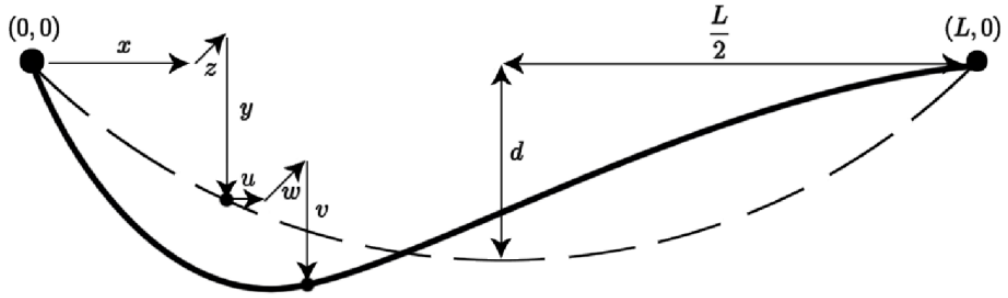
Figure 2.6: Dynamic displacement of a cable

The term $h\ \partial v^2 / \partial x^2$ is a minute quantity multiplied by a second-order term, and is considered negligible. $H\ dy^2 / dx^2 = \rho dx$, a simplification of Equation 2.2, is substituted into Equation 2.38, which produces

$$H\frac{\partial^2 v}{\partial x^2} + h\frac{mg}{H} = m\frac{\partial^2 v}{\partial t^2} \qquad (2.39)$$

The longitudinal and transverse equations are found in a similar way.

$$H\frac{\partial^2 u}{\partial x^2} + \frac{\partial h}{\partial x} = m\frac{\partial^2 u}{\partial t^2}$$
$$\qquad (2.40)$$
$$H\frac{\partial^2 w}{\partial x^2} = m\frac{\partial^2 w}{\partial t^2}$$

Substitution of $v(x,t) = \tilde{v}(x)e^{i\omega t}$ and $h(t) = \tilde{h}e^{i\omega t}$ into the vertical equation of motion (2.39) provides

$$H\frac{\partial^2 \tilde{v}}{\partial x^2} + m\omega^2 = \frac{mg}{H}\tilde{h} \qquad (2.41)$$

which is broken down into a dimensionless form

$$\frac{d^2 \tilde{\mathbf{v}}}{d\mathbf{x}^2} + \boldsymbol{\omega}^2 \tilde{\mathbf{v}} = \mathbf{h} \tag{2.42}$$

where $\tilde{\mathbf{v}} = \tilde{v}/(mgL^2/H)$, $\mathbf{x} = x/L$, $\tilde{\mathbf{h}} = \tilde{h}/H$ and $\boldsymbol{\omega} = \omega/(H/mL^2)^{1/2}$.

The cable Equation 2.29 is all-important for solving frequency equations, since on anti-symmetric modes the right-hand side equals 0 (if the negligible second order terms are ignored), which means there is no overall additional tension, so the term can be removed from Equation 2.42, which is easier to solve. Thus for anti-symmetric modes, solving the differential equation and inputting boundary conditions neatly provides solutions for the mode shapes and natural frequencies:

$$\boldsymbol{\omega}_n = 2n\pi$$
$$\tilde{\mathbf{v}}_n = A_n \sin(2n\pi\mathbf{x}) \tag{2.43}$$

where $n = 1, 2, 3, \ldots$ signify the relative natural frequencies and anti-symmetric mode shapes, and A_n is the amplitude of the respective mode shape.

For symmetric modes the additional horizontal component is included. Solving the differential equation and using relevant boundary condition, the mode shapes take the form:

$$\tilde{\mathbf{v}} = \tilde{\mathbf{h}}\left(1 - \tan\left(\boldsymbol{\omega}/2\right) \cdot \sin(\boldsymbol{\omega}\mathbf{x}) - \cos(\boldsymbol{\omega}\mathbf{x})\right) \tag{2.44}$$

which corresponds to natural frequencies given by

$$\tan\left(\frac{\boldsymbol{\omega}}{2}\right) = \frac{\boldsymbol{\omega}}{2} - \frac{4}{\lambda^2}\left(\frac{\boldsymbol{\omega}}{2}\right)^3 \tag{2.45}$$

where λ^2 is the Irvine-Caughey non-dimensional cable parameter. This factor is fundamentally important for the dynamic performance of cable elements, since it determines the ordering of the mode shapes of the cable, depending on whether it behaves as a taut string or a sagging cable.

Figure 2.7 demonstrates the reordering of the first four modes, as the Irvine-Caughey parameters becomes larger, and behaves as a sagging cable. The two lines $\omega/\pi = 2$ and $\omega/\pi = 4$ represent the first and second anti-symmetric mode shapes, respectively, which frequencies remain unchanged. The lines which are initially at $\omega/\pi = 1$ and $\omega/\pi = 3$ are the first two symmetric mode shapes, which grow larger than the anti-symmetric modes at the roots of Equation 2.45.
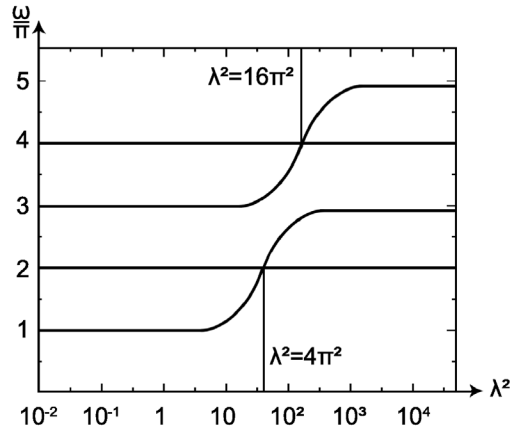
Figure 2.7: Variance of first four circular frequencies, ω, to the squared Irvine-Caughey parameter λ.

Concerning movement at the supports, finite element models are the most applicable method to measure dynamic behaviour, since the effects of boundary conditions are straight-forward to control, and simple to understand. However, Rega and Luongo (1980) produced a finite difference algorithm that includes support flexibility. Gattulli et al. (1997) uses continuum equations to demonstrate active control of a suspended cable by adjusting the support conditions.

2.2.9 DYNAMIC RESPONSE WITH STIFFENING FRAME

The combined dynamic response of the cable and deck structure may be identified by merging the deflection equation of a continuous beam, with the equation for the motion of the cable, found in the previous section (Bleich et al. 1950).

$$E_d I_d \frac{\partial^4 v}{\partial x^4} - H \frac{\partial^2 v}{\partial x^2} + h \frac{mg}{H} = -\left(m_d + m_c\right)\frac{\partial^2 v}{\partial t^2} = -m \frac{\partial^2 v}{\partial t^2} \tag{2.46}$$

Alternatively, the equations may be treated separately, but are coupled by the hangers, which are treated as springs but having no strength when under compression. As the hangers are in tension, this will cause a downwards deflection on the suspension cable, and an upwards deflection in the stiffening frame. Below is a version of Lazer and McKenna (1990) equation:

$$m_c \frac{\partial^2 v_c}{\partial t^2} - H \frac{\partial^2 v_c}{\partial x^2} + h \frac{m_c g}{H} - k_h \left(v_d - v_c\right) = F_c\left(t\right)$$

$$m_d \frac{\partial^2 v_d}{\partial t^2} - E_d I_d \frac{\partial^4 v_d}{\partial x^4} + k_h \left(v_d - v_c\right) = F_d(t) \tag{2.47}$$

where k_h represents an equivalent spring stiffness of the hangers, F is the resultant force from the hanger, and subscripts d and c each relate to the suspension bridge's deck structure

and main suspension cable. Both of these combined responses may be solved via the finite difference method.

2.3 APPLICATION OF FINITE ELEMENT MODELS

As the years pass, the designed spans of new suspension bridges have grown larger and larger. Lengthening spans have encouraged heavier cables for their designs, so most of the stress in the cable stress comes from supporting its own weight. Other factors need to be considered, such as the stiffening and non-linear effects of cables, deterioration of structural members, and the structure's response to its environment and external loads. The analysis of suspension bridge is multifaceted, with a unique response for each structure. Expanding the variables and contributors in continuum equations may help develop our understanding, but the preference of many researchers is to create a finite element (FE) model, which is a powerful analytical tool. Once constructed, a model is always available to demonstrate a subject's behaviour, and is simple to adjust for corrections or to solve problems different to its original intended use. By The same model may be subjected to various types of analysis, such as modal, fluid or thermal analyses, depending on the analytical program used and whether the element types require swapping for the different analyses.

2.3.1 CONSTRUCTION OF MODELS

Since modern computers have become capable of processing detailed analyses a finite element model's complexity is dependent on the designer's expertise, and how much time is available to construct the model and post-process the results. Suspension bridge FE models are either two dimensional or three dimensional (Yeung & Smith 2005; He et al. 2009). For thermal analyses each element has a single degree of freedom at each node, which would be the node's temperature. The type of element establishes heat transfer between the two points, which may be due to convection, conduction or radiation.

For structural analyses the number of degrees of freedom depends on the number of dimensions in the model. If two dimensional, each node will have 3 degrees of freedom; allowing vertical and horizontal displacements, and rotations about the transverse axis. If the model is three dimensional, however, each node will have 6 degrees of freedom; allowing vertical, horizontal and transverse displacements, and rotations about all three axis.

Trusses and girders are modelled with beam elements, whilst deck plates and box girders may be modelled as a series of shell elements, or equivalent beam elements. Cable elements may be modelled in a variety of ways; as spar elements with no rotational rigidity at either node, as

a series of beam elements (Forars et al. 2000), and as isoparametric elements where the curvature of the cable is incorporated (Ren et al. 2008). Additionally the elements should have little or no stiffness under compression, since they operate under axial tensile forces.

Geometric stiffening is the additional stiffness that elements gain when under tension. The elemental stiffness matrix of a single beam takes the form:

$$\mathbf{K} = \mathbf{K}_{st} + \mathbf{K}_{geo} \tag{2.48}$$

where $\mathbf{K}_{st}$ is the typical FE stiffness sub-matrix, and $\mathbf{K}_{geo}$ is the geometric stiffening sub-matrix. For a 2D beam element (where the corresponding degrees of freedom are $\vec{D} = \begin{bmatrix} u_1 & v_1 & \theta_{z,1} & u_2 & v_2 & \theta_{z,2} \end{bmatrix}^T$; $\theta_{z,1}$ being the rotation about the element's local z axis at node 1, $\mathbf{K}_{st}$ and $\mathbf{K}_{geo}$ equal (Przemieniecki 1968):

$$\mathbf{K}_{st} = \begin{bmatrix} AE/L & 0 & 0 & -AE/L & 0 & 0 \\ & 12EI/L^3 & 6EI/L^2 & 0 & -12EI/L^3 & 6EI/L^2 \\ & & 4EI/L & 0 & -6EI/L^2 & 2EI/L \\ & & & AE/L & 0 & 0 \\ & \text{SYM} & & & 12EI/L^3 & -6EI/L^2 \\ & & & & & 4EI/L \end{bmatrix} \tag{2.49}$$

$$\mathbf{K}_{geo} = \frac{T}{L} \begin{bmatrix} 0 & 0 & 0 & 0 & 0 & 0 \\ & 6/5 & L/10 & 0 & -6/5 & L/10 \\ & & 2L^2/5 & 0 & -L/10 & -L^2/30 \\ & & & 0 & 0 & 0 \\ & \text{SYM} & & & 6/5 & -L/10 \\ & & & & & 2L^2/15 \end{bmatrix} \tag{2.50}$$

where E and I is the Young's modulus and second moment of area for the member, respectively, L is the length of the attached element and T the axial tensile force within the element. Also, SYM denotes diagonal symmetry of the elements in the opposite side of the matrix. For a 3D beam, where the corresponding degrees of freedom are $\vec{D} = \begin{bmatrix} u_1 & v_1 & w_1 & \theta_{x,1} & \theta_{y,1} & \theta_{z,1} & u_2 & v_2 & w_2 & \theta_{x,2} & \theta_{y,2} & \theta_{z,2} \end{bmatrix}^T$, they are equal to

$$\mathbf{K}_{st} = \begin{bmatrix}
\alpha & 0 & 0 & 0 & 0 & 0 & -\alpha & 0 & 0 & 0 & 0 & 0 \\
 & \gamma_z & 0 & 0 & 0 & \delta_z & 0 & -\gamma_z & 0 & 0 & 0 & \delta_z \\
 & & \gamma_y & 0 & -\delta_y & 0 & 0 & 0 & -\gamma_y & 0 & -\delta_y & 0 \\
 & & & \beta & 0 & 0 & 0 & 0 & 0 & -\beta & 0 & 0 \\
 & & & & \varepsilon_y & 0 & 0 & 0 & \delta_y & 0 & \zeta_y & 0 \\
 & & & & & \varepsilon_z & 0 & -\delta_z & 0 & 0 & 0 & \zeta_z \\
 & & & & & & \alpha & 0 & 0 & 0 & 0 & 0 \\
 & & & & & & & \gamma_z & 0 & 0 & 0 & -\delta_z \\
 & & & & & & & & \gamma_y & 0 & \delta_y & 0 \\
 & & \text{SYM} & & & & & & & \beta & 0 & 0 \\
 & & & & & & & & & & \varepsilon_y & 0 \\
 & & & & & & & & & & & \varepsilon_z
\end{bmatrix}$$

$$\gamma_z = \gamma\left(I_z, \phi_y\right)$$

$$\gamma_y = \gamma\left(I_y, \phi_z\right)$$

$$\delta_z = \delta\left(I_z, \phi_y\right)$$

$$\vdots$$

$$\zeta_z = \zeta\left(I_z, \phi_y\right)$$ (2.51)

$$\zeta_y = \zeta\left(I_y, \phi_z\right)$$

$$\alpha = \frac{AE}{L}$$

$$\beta = \frac{\overline{GJ}}{L}$$

$$\gamma(I, \phi) = \frac{12EI}{L^3(1+\phi)}$$

$$\delta(I, \phi) = \frac{6EI}{L^2(1+\phi)}$$

$$\varepsilon(I, \phi) = \frac{(4+\phi)EI}{L^2(1+\phi)}$$

$$\zeta(I, \phi) = \frac{(2-\phi)EI}{L(1+\phi)}$$

$$\phi_y = \frac{12EI_z}{GA_z^s L^2}$$

$$\phi_z = \frac{12EI_y}{GA_y^s L^2}$$

$$\mathbf{K}_{geo} = \frac{T}{L}\begin{bmatrix} 0 & 0 & 0 & 0 & 0 & 0 & 0 & 0 & 0 & 0 & 0 & 0 \\ & \frac{6}{5} & 0 & 0 & 0 & \frac{L}{10} & 0 & -\frac{6}{5} & 0 & 0 & 0 & \frac{L}{10} \\ & & \frac{6}{5} & 0 & -\frac{L}{10} & 0 & 0 & 0 & -\frac{6}{5} & 0 & -\frac{L}{10} & 0 \\ & & & 0 & 0 & 0 & 0 & 0 & 0 & 0 & 0 & 0 \\ & & & & \frac{2L^2}{15} & 0 & 0 & 0 & \frac{L}{10} & 0 & \frac{L^2}{30} & 0 \\ & & & & & \frac{2L^2}{15} & 0 & -\frac{L}{10} & 0 & 0 & 0 & -\frac{L^2}{30} \\ & & & & & & 0 & 0 & 0 & 0 & 0 & 0 \\ & & & & & & & \frac{6}{5} & 0 & 0 & 0 & -\frac{L}{10} \\ & & & & & & & & \frac{6}{5} & 0 & \frac{L}{10} & 0 \\ & \text{SYM} & & & & & & & & 0 & 0 & 0 \\ & & & & & & & & & & \frac{2L^2}{15} & 0 \\ & & & & & & & & & & & \frac{2L^2}{15} \end{bmatrix} \tag{2.52}$$

where I_y and I_z is the second moment of area in the direction normal to y and z, respectively, J is the section's torsional moment of inertia, $\overline{G}$ is the material's shear modulus, and A_y^S and A_z^S is the shear area in the direction normal to y and z, respectively. The combination of the structural and geometric stiffness is used to ensure that the dead load is fully supported by the structure.

An initial estimate for the forces supporting the dead load of the structure may be calculated from Equation 2.12, if the cable profile is known. In certain FE programs, this value can be used as the applied load, e.g. SAP2000, or an initial strain applied to the cable elements, such as in ANSYS and ABAQUS.

Back stay cables are incorporated to ensure the horizontal force in the cases of the main span is supported, so that no bending is induced in the towers. If they are straight, the forces should be easy to calculate through fundamental geometry. If allowed to sag, or supporting side spans, the profile of the cable can be calculated from the required horizontal forces at the tower, or vice versa.

The two initial estimates for the forces in the suspension and back stay cables may require some iteration to determine values for a dead load configuration, where deflections and hence moments in the stiffening structure are limited. It is similar to the Newton-Raphson method, except the derivations in the Jacobian are represented in finite difference form. This is very useful for complicated mathematical models where derivatives of optimisation functions are difficult to obtain, such as determining the cable tensions and minimising bridge deflections. The iteration is represented by:

$$
\begin{pmatrix} x_{1,i+1} \\ \vdots \\ x_{N,i+1} \end{pmatrix} = \begin{pmatrix} x_{1,i} \\ \vdots \\ x_{N,i} \end{pmatrix} - \mathbf{D}^{-1} \begin{pmatrix} G_1\left(x_{1,i},\ldots x_{N,i}\right) \\ \vdots \\ G_N\left(x_{1,i},\ldots x_{N,i}\right) \end{pmatrix}
\tag{2.53}
$$

$$
\mathbf{D} = \frac{\partial(G_1,\ldots,G_N)}{\partial(x_1,\ldots,x_N)} = \begin{bmatrix} \dfrac{\partial G_1}{\partial x_1} & \cdots & \dfrac{\partial G_1}{\partial x_N} \\ \vdots & \ddots & \vdots \\ \dfrac{\partial G_N}{\partial x_1} & \cdots & \dfrac{\partial G_N}{\partial x_N} \end{bmatrix}
\tag{2.54}
$$

$$
\frac{\partial G_m}{\partial x_n} \approx \frac{G_m\left(x_{1,i},\ldots x_{N,i}\right) - G_m(x_{1,i},\ldots x_{N,i-1})}{x_{n,i} - x_{n,i-1}}
\tag{2.55}
$$

where $x_{n,i}$ is the nth variable out of N variables at the i th iteration step, and G_m is the m th function of N functions, with variables . The matrix $\mathbf{D}$ is the Jacobian.

Figure 2.8 demonstrates an exaggerated iteration of a suspension bridge, as the forces are iterated to reach equilibrium of the deck.
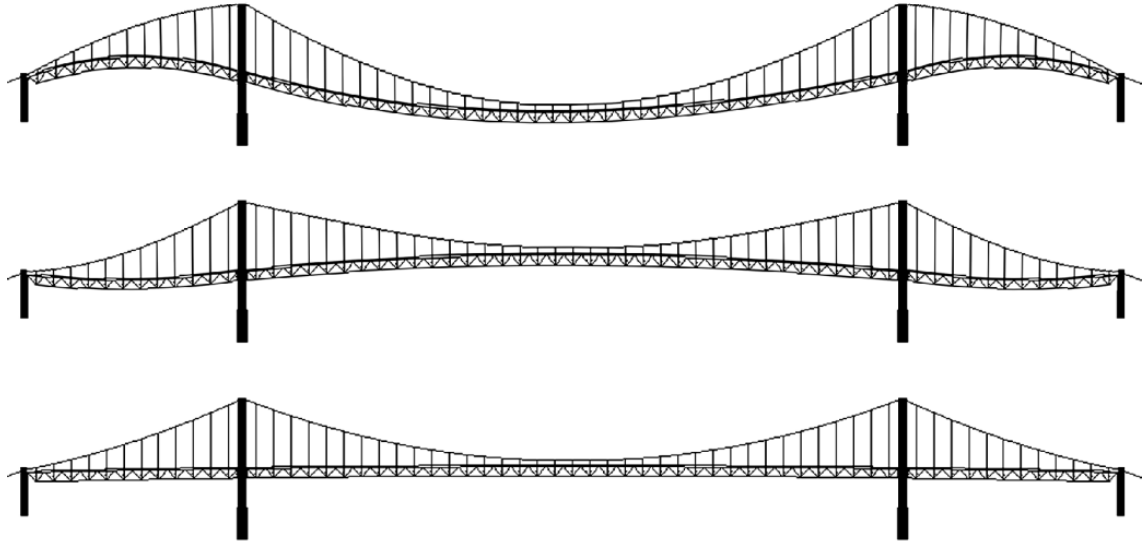
Figure 2.8: The progressive iteration of the cable forces in a suspension bridge, to reach a shape in equilibrium.

The model also has to consider tensile effects in the hangers. The tension in a hanger is equal to the dead load of the stiffening structure it supports. A reasonable approximation for this value is provided by:

$$T_h = \frac{\rho L}{n_h n_d}$$
(2.56)

where T_h is the tension in a single hanger, n_h is the number of the divisions on the span and n_d is the number of hangers found in a single division. If the hangers are tested for ambient vibration, the hanger tension may instead be found from their measured natural frequencies:

$$\left(\frac{f_n}{n}\right)^2 = \frac{T_h g}{4 m_h L_h^2} + \frac{n^2 \pi^2 E_h I_h g}{4 m_h L_h^4}$$
(2.57)

where f_n represents the nth order natural frequency, g the gravitational acceleration, and subscript h denotes that the property relates to the hanger.

2.3.2 CASE STUDIES OF FE MODELS APPLIED TO SUSPENSION BRIDGES

The following subsection highlights a few suspension bridge finite element models used for research and published as a paper. This list is certainly not exhaustive, since FE models are also used for bridge design and analysis which are not accessible in the public domain.

The Hong Kong Polytechnic University's long term monitoring and vibration study of the Tsing-Ma Bridge is supported by a finite element model designed by Xu et al. (1997b). The bridge deck was modelled as an equivalent beam, rather than using a fully detailed model. This was due to sectional properties having a greater effect on the natural frequencies and mode shapes of the deck than the structural detailing, which is an approach shared by Dumanoglu et al. (1992). A detailed finite element model of a box girder section was developed, and analysed to define equivalent section properties for the model. Determination of the response of the towers and cables was also conducted (Xu et al. 1997a), which were similarly modelled as equivalent beams. The movement joints in the bridge were modelled as rigid links which had the ability to rotate, in order to restrain movement in all but the span-wise direction. The finite element model was also used to predict the dynamic properties of the bridge in the construction phase as the deck sections were being erected (Ko et al. 1998).

A second detailed FE model of the Tsing-Ma Bridge was made by Chan et al. (2003), with 20000 structural members. The model accommodates details of the weld-connections and spatial configuration of the structure with the application of some additional elements to analyse fatigue from traffic and trains. This model was used to identify stress hot-spots in the structure, which were analysed separately. There are other such examples where finite element models are used to demonstrate vehicle transit on suspension bridges (Xia et al. 2000; Xu et al. 2003).

Bridges which are hybrids of suspension and cabled stayed bridges are problematic to model without knowing the size of the forces in the stay cables. They are a combination of two nonlinear structural systems; their tension stiffening contributions coupled by the deflection of the deck. Ren et al. (2004) produced a detailed finite element model to accompany ambient testing of the Roebling Suspension Bridge (Ren, Harik, et al. 2004); an example of a hybrid suspension/stay-cabled bridge. The forces in the suspension cable were first iterated until the bridge exhibited a small deflection in the deck structure. This was followed by an adjustment of the forces in the stay cables to further reduce the deformation. Ambient vibration tests on hybrid suspension bridges have also been performed, e.g. by Paultre et al. (2000), but no published FE models is available for this example.

2.4 SENSITIVITY TO STRUCTURAL PARAMETERS

Despite the production of highly detailed FE models, there may be variances between performance determined from their theoretical results, and the performance recorded from a live structure. This may be due to human error from the processes, uncertainties or approximations from the modelling, or from the discretisation of the model's mesh. There are several references concerning finite element model updating, which may be of interest to the reader (Mottershead 1993; Hemez & Doebling 2001; Stein et al. 2004).

Finite element model updating aims to adjust the FE model so that it produces similar results to the monitored structure. This is identified by ensuring that the differences between the two sets of results are as minimal as possible. Typically it is the natural frequencies and modal displacements of the mode shapes which are compared, but the dynamic flexibility (Jaishi & Ren 2006; Jung et al. 2008) and strain energy (Jaishi & Ren 2007) of the modes may also be examined.

A correlation analysis of the results may be conducted by observing the modal assurance criterion (MAC) value, which compares the ordinates of the mode shapes; mode shapes being a measure of the dynamic performance, producing a value of unity for perfectly correlated modes.

$$MAC\left(\varphi_{ex},\varphi_{an}\right) = \frac{\left|\varphi_{an}^{T}\varphi_{ex}\right|^{2}}{\left(\varphi_{an}^{T}\varphi_{an}\right)\left(\varphi_{ex}^{T}\varphi_{ex}\right)} \tag{2.58}$$

where φ_{an} and φ_{ex} are the analytical and experimental mode shape vectors, respectively.

2.4.1 SITE INVESTIGATIONS

On-site vibration testing provides information of the modal properties of the subjected structure. The results may used to identify base-lines for future health monitoring, or for correlating theoretical models, such as FE model updating.

For the excitation of suspension bridges, most researchers will rely on ambient measurements, where the modal properties may be measured when the structure is excited by environmental conditions, such as by wind and traffic. Ambient vibration testing (AVT) is commonly used to evaluate the operating condition of the structure. Artificial excitation for forced vibration loading requires an arranged absence of traffic, which is unlikely to be allowed since lane closures cause a significant inconvenience to the public. Also the shakers needed to excite these large structures would be huge, and therefore expensive. Managed external excitation

may be in the form of controlled traffic loads, e.g. using heavily loaded lorries (Conte et al. 2008). It is worth noting that during a marathon most vehicular traffic is removed from the bridge (Erdoğan et al. 2007), and provides perfect opportunities for a day's testing of environmental effects, with or without pedestrian loading en-masse.

2.4.2 UPDATING PARAMETERS

There are generally two approaches to updating an FE model of a structure; either by single-step adjustment of system matrices or by adjusting structural parameters (Zhang et al. 2000). System matrix updating changes the stiffness and mass matrices by solving a system of matrix equations. However, this method fails to handle occasions when the stiffness and mass matrices may be coupled, which is characteristic of tension-stiffening structures. In addition, direct adjustment of the system matrices does not provide occasions for direct physical interpretation of the model's behaviour.

The parameter adjustment method ascertains the change in the performance when certain parameters are modified. This method has the advantage of preserving symmetry, positive-definiteness, and the sparseness of the stiffness and mass matrices. It also provides a physical interpretation of the results, which may be easier to comprehend for the analyst. The parameter updating method is typically used for suspension bridge FE models for these reasons.

The choice of parameters is a crucial step in model updating, and requires some judgement to determine their influences on the physical and mathematical behaviour predicted by the model. Physical properties of the structure may be indeterminable and approximated from previous models, or they may have limited effect on the structure's behaviour. Mathematically, choosing too many parameters demonstrates that the initial problem may be poorly conditioned, or that parameters are applied with little logic. Therefore, the number of updating parameters should be kept minimal, whilst those chosen must have a strong influence on particular targeted responses.

One method to assess the parameters' influence on the model's performance, e.g. a modal frequency, is to perform a sensitivity analysis. The sensitivity analysis determines the rate of change of particular response value, with respect to an alteration of a structural parameter. An element of a sensitivity matrix, $\mathbf{S}$, is obtained as follows:

$$\mathbf{S}_{i,j} = \frac{\partial R_i}{\partial P_j} \qquad (2.59)$$

where R_i and P_j are a structural response and parameter respectively. The subscripts are $i = 1, \ldots, N$ for N responses, and $j = 1, \ldots, M$ for M parameters. The sensitivity analysis may be performed on most of the structural parameters to identify those with high sensitivity, which may be effective candidates for model tuning.

Modification of the stiffness properties of simple suspension bridge models has demonstrated that the frequency of the first global vertical mode, where both suspension cable and stiffening structure displace, is reliant on the stiffness of the suspension cable. Higher global modes are more dependent upon the stiffness of the supported deck. Therefore adjusting the stiffness of the cable has a pronounced effect on the first mode. This may be achieved either by adjusting the forces in the cables, or varying the cables' area. The forces in the cables may have been approximated, which may make it an ideal candidate for an updating parameter. For long span suspension bridges, where the cables have significant width and weight, it seems reasonable to adjust their density as well.

Figure 2.9 and Figure 2.10 show the changes in the natural frequencies with regard to the deck's stiffness, and cable tension. The results come from a 2D FE model of the Golden Gate Bridge. These graphs demonstrate that the order of the mode shapes may change, depending on the stiffness of the structure. Mode 1 and 2 shows a switching of the first vertical symmetrical and asymmetrical modes identified in Figure 2.9, as the support of the structure becomes governed by tension. Figure 2.10 also demonstrates that the first vertical mode is less reliant on the deck's stiffness than higher modes. A similar study was conducted on a 3D FE model of the Taizhou Yangtze River Bridge by Wang et al. (2010) which showed that adjusting the stiffness of the steel box girder made little influence on the first vertical and lateral modes.
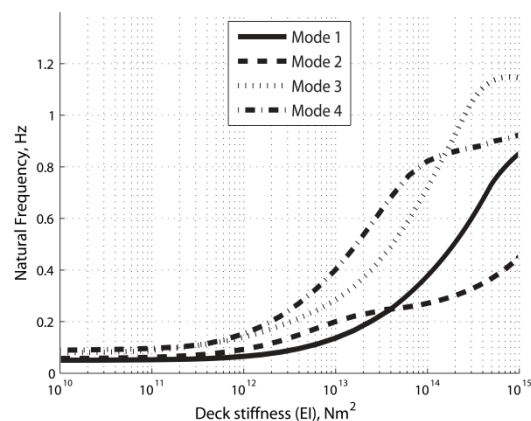
Figure 2.9: Variance of natural frequencies of Golden Gate Suspension Bridge with the stiffening structure's stiffness.
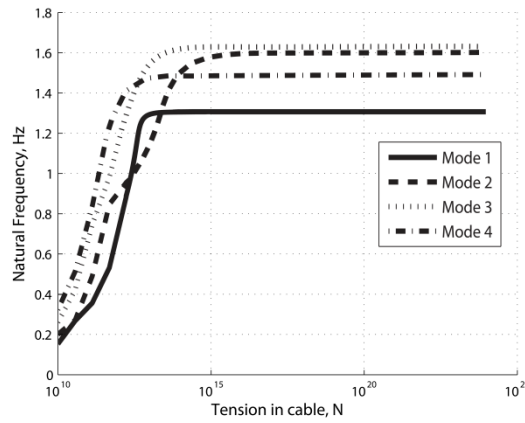
Figure 2.10: Variance of natural frequencies of Golden Gate Suspension Bridge with the cable tensions.

Other choices for parameters would relate to the stiffening structure. Identification of other unknown values have been highlighted on reports from other types of bridges (Brownjohn & Xia 2000; Jaishi & Ren 2005), such as the Young's modulus and densities of the materials, the second moment of area of stringers and girders, the thickness of deck elements, and parameters describing the rigidity of the boundary conditions.

An example of finite element model updating for suspension bridges is demonstrated by Gentile and Gallino (2008), who modified a model of the Morca Suspension footbridge to correlate with their ambient vibration test results. The parameters used for updating were the Young's modulus, shear modulus of the timber deck elements, and the vertical moment of inertia of the stringers.

2.4.3 ADJUSTMENT OF PARAMETERS

For most studies, it is assumed that the parameters in the finite element model are the primary contributor to the inaccuracies in the model, and require some modification. Their functional relationship may be approximated by a first order Taylor series expansion, with respect to the adjustment of the structural parameters:

$$\vec{R}_{ex} - \vec{R}_{an} = \mathbf{S}\left(\vec{P}_{ex} - \vec{P}_0\right)$$
$$\Delta \vec{R} = \mathbf{S}\Delta \vec{P}$$

(2.60)

where vectors $\vec{R}_{ex}$ and $\vec{R}_{an}$ are vectors of the response values from the experimental and analytical results, respectively, where $\vec{R} = \left[R_1 \cdots R_n\right]^T$, n being the amount of target responses. Also, vectors $\vec{P}_{ex}$ and $\vec{P}_0$ are vectors of the parameter values from the experimental and current analytical results, respectively, where $\vec{P} = \left[P_1 \cdots P_m\right]^T$; m the number of selected parameters. Higher order terms in the Taylor series expansions are

neglected, since it is assumed that the modifications to the parameters are small. It should be noted that when there are huge discrepancies between analytical and experimental results, the validity of the Taylor series truncation would be weakened, and the results are prone to diverge.

The modification of the structural parameters can be found by solving Equation 2.60. If there are more measured modal properties than structural parameters, an optimal solution can be derived that minimizes an error function, ξ_1 :

$$\xi_1 = \left(\mathbf{S}\Delta\bar{P} - \Delta\bar{\mathrm{R}} \right)^T \mathbf{W}_1 \left(\mathbf{S}\Delta\bar{P} - \Delta\bar{\mathrm{R}} \right) \tag{2.61}$$

where $\mathbf{W}_1$ is a positive-definite weighting matrix, reflecting a relative confidence in accuracy between particular measured modes. However, the solution of Equation 2.61 is not sufficient, especially when structural parameters have similar or little effect on certain frequencies.

When there are more structural parameters than measured properties, the problem may become a constrained optimization problem, found by:

$$\text{minimise:} \qquad \xi_2 = \Delta\bar{P}^{\mathrm{T}} \mathbf{W}_2 \Delta\bar{P} \tag{2.62}$$

$$\text{subject:} \qquad \mathbf{S}\Delta\bar{P} = \Delta\bar{R} \tag{2.63}$$

where $\mathbf{W}_2$ is a different positive-definite weighting matrix. By adjusting this weighting matrix, it is possible to limit the alteration of the structural parameters separately, to reflect properties which may be known more precisely.

The combination of the two objective functions from Equations 2.61 and 2.62 provides an objective function that has the advantages of ξ_1 and ξ_2 (Zhang et al. 2000); ξ_2 regulates possible ill-conditioned problems associated with ξ_1, and also constraining the updated parameters:

$$\xi_3 = \Delta\bar{P}^{\mathrm{T}} \mathbf{W}_2 \Delta\bar{P} + \left(\mathbf{S}\Delta\bar{P} - \Delta\bar{\mathrm{R}} \right)^T \mathbf{W}_1 \left(\mathbf{S}\Delta\bar{P} - \Delta\bar{\mathrm{R}} \right) \tag{2.64}$$

2.5 STRUCTURAL HEALTH MONITORING

The application of finite element models typically accompanies dynamic testing and/or long term monitoring of loading and responses, which are described as Structural Health Monitoring (SHM). The objective of SHM is to ascertain whether faults, such as damaged

members, weakened connections and other forms of degradation, are present in the structure. These may affect the stiffness, mass or energy dissipation of the structure, which in turn may be reflected in either the static or dynamic response of the system. Initially data is collected from the structure under typical operational conditions, and features are extracted of its supposedly undamaged response. Subsequent data collected from the structure are compared to this training data, and if the features deviate significantly then it may be a sign some part of the structure may be below operational standards. Several reviews on SHM are available (Doebling et al. 1998; Farrar et al. 2001; Ko & Ni 2005; Brownjohn 2007).

For long span bridges, SHM is driven by range of reasons, typically from extreme or freak loading due to their size such as earthquakes, wind, and sheets of ice (Cheung et al. 1997; Wong 2004). Structural health monitoring is important for bridges to validate design assumptions and guidelines, detect loading anomalies and deterioration of the structure, and provide real-time information of the structure (Ni et al. 2005).

Constant monitoring of the bridges may provide abundant information of the structure, as long as it is well managed. Long term monitoring may capture interesting behaviour in real life operational conditions, despite new advances in areas such as earthquake engineering and aero-elasticity. These phenomena may surprise the most experienced of bridge engineers, and catch them out unexpectedly; infamous examples are the Tacoma Narrows Bridge (Larsen 2000) and London's Millennium Footbridge (Fitzpatrick et al. 2001). Recent years have also demonstrated unusual responses, such as vortex shedding (Larsen et al. 2000) and excessive stay cable vibrations (Macdonald et al. 2002). The possibility of characterising and describing a complete set of for these occurrences would increase when the bridge is constantly monitored.

2.6   ENVIRONMENTAL EFFECTS UPON SUSPENSION BRIDGES

Other than damage and faults, variations in the structural response may also be a result of changing environmental and operational conditions. Environmental conditions include the air temperature, solar radiation, wind speed and direction and humidity. Operational conditions may be ambient loads, transient loads or internal machinery. Some environmental conditions may also affect how the bridge operates, e.g. seizing up of moving joints may cause changes in the stiffness or the boundary conditions (Peeters & De Roeck 2000; Moser & Moaveni 2011). In SHM systems these contributions need to be determined, otherwise the systems' ability to identify changes caused by structural damage will be compromised.

Researchers typically aim to use modal parameter changes to detect damage, although changes due to normal variation of environmental loads are likely to be much greater. Hence a prerequisite for such techniques is an ability to model environmental loading effects either using 'physics-based' models, such as those described in this chapter, or 'data driven' models based purely on numerical representations of historic data. Some of these data-driven techniques have been reviewed by Sohn (2007). Many structures have been fitted with long-term monitoring systems, which provide a back-catalogue of data of their performance and local environmental conditions that allow for development of data driven models, as well as calibration of physics-based models. One of the problems with data driven models is separating the effects of different loading forms, since time series of loads may correlate (e.g. traffic and wind speeds are both increased in daylight hours, as are structural temperatures).

Methods to disentangle effects includes examining periods of response where only one parameter varies, such as during the month of December (for the UK), where daylight hours are low and temperatures barely change, or during the early hours of the morning when traffic levels are low. Principal component analysis (PCA) may be used to discriminate these variables, and identify their performance, by performing a multi-variate analysis transforming the original coordinate system into a new orthogonal one with maximised variance (Yan et al. 2005; Giraldo 2006).

Several site investigations have studied the influences of environmental conditions (Nayeri et al. 2008), some concerning long-span bridges (Farrar 1997; Cornwell et al. 1999; Sohn et al. 1999; Alampalli 2000; Peeters & De Roeck 2000; Bolton et al. 2001; Ko & Ni 2005; Ni et al. 2005; Hua et al. 2007; Liu & DeWolf 2007). In the majority of these studies, it was found that temperature dominated the bridge's quasi-static response.

One aim of SHM is to identify environmental effects and feed them back into the design process. The following sections consider the influences of bridge temperature, traffic mass and wind loading, which are some of the every-day environmental loads experienced by suspension bridges.

2.6.1 THERMAL CONDITIONS

Temperature variation causes either shrinkage or elongation of structural elements, which at the scale of a suspension bridge can lead to significant movements that are accommodated by the structure's design. When a bounded element is heated, it expands and is subjected to compressive thermal stresses, which might reduce the stiffness of the structure. Simulations using simple FE models showing a reduction in the natural frequencies, caused by thermal

variation of the Young's modulus (Vangipuram & Ganesan 2007). Thermal expansion may also have implications for the boundary conditions of large structures, which may adapt, depending on the temperature and expansion limits.

Several studies have observed the local displacement of a bridge at the expansion gaps and correlated the response to the temperature of the overall structure, such as on the Ting Kau stay cabled bridge (Ni et al. 2007) and the Runyang Suspension Bridge (Ding & Li 2011a). Other researchers have installed positioning systems on bridges that allow the displacements of several points in the structure to be monitored. Such systems have been implemented on suspension bridges, such as Rosenbrücke suspension bridge in Austria (Wieser & Brunner 2002), Clifton Bridge in Nottingham, UK (Roberts et al. 2004) and the Tsing-Ma Bridge in Hong Kong (Xu et al. 2010), as well as being applied to stay cabled bridges like the Batman Bridge in Tasmania (Watson et al. 2007).

Significant changes in dynamic response may result from changes in the structure's temperature (Xia et al. 2012). Instances of this behaviour have been shown on the concrete bridges analysed by Cornwell et al. (1999), Peeters and de Roeck (2000) and Liu et al. (2009) where the modal properties exhibit daily variations. Data where wind speeds were below 2m/s collected from the Ting-Kau stay cabled bridge have shown that there is an inverse relationship between temperature and frequency for the first few examined vibration modes (Ko et al. 2003; Hua et al. 2007; Zhou et al. 2010). It is known that the changes in the Young's modulus of the structure with the temperature may cause these variations, but in steel structures these effects are quite small, so it is suspected that on cable-supported structures the consequent changes in static configuration of a bridge may also have a significant effect, since the tensions and the shape of the structure will also change as the elements expand and contract.

There have been a few studies that have considered how the environment affects the dynamic properties of suspension bridges. Kernel Principal Component Analysis (KPCA), a nonlinear PCA, was conducted by Oh et al. (2009) on the hanger tensions of the Yeongjong Grand Bridge. They found that there was a linear inverse relationship between the temperature and the first principal component, meaning that as temperature rose the frequencies dropped.

Ding and Li (2011) observed the variations in the modal properties of the vertical modes on the Runyang Bridge, using only data with wind speeds less than 2m/s and traffic conditions that only caused vertical accelerations less than 2.5cm/s². Since Ding & Li adopted a value taken as an average of the temperature sensors on the bridge, they found the data were too dispersed to provide a good correlation. Instead the data were further regressed to a single daily average

temperature to identify seasonal variations in the modal response. Their results demonstrated an inverse relationship with temperature, with larger variations for higher modes; their fifth vertical modes varying by 0.56% over a 40°C range.

Miao et al. (2011) also identified changes in dynamic response of the Runyang Bridge using a finite element model. The beam stiffnesses were iterated to find an equivalent stiffness, depending on the change of the internal forces. They found that the larger variations in frequency also occurred for the higher modes, although the variations were not as large as the values calculated by Ding and Li. They also found that the shorter stay-cabled bridge across Rungyang River is affected more by temperature than the suspension bridge; the largest variation in stay cable bridge model is 0.25%/°C on the first mode, while on the suspension bridge there was no more than 0.034%/°C.

2.6.2 TRAFFIC AND VEHICLE MASS

Numerous studies have observed the interaction between a bridge and a vehicle traversing across it, some of which leads to changes in the observed dynamic properties (Yang et al. 1995; Cheung et al. 1999; Li et al. 2003; Yang 2004; Kwon et al. 2005; Chen & Wu 2010). However these lead to variations in high order modes, since they are excited by high-frequency forces caused by rough road surfaces and bobbing of the suspension units. For SHM of long span bridges, we are more interested in lower frequency modes (<1Hz) that are not activated by this level of excitation.

However, the dynamic properties of the bridge may change due to the added mass of the traffic upon the structure. For bridges where the deck structure is relatively large compared to the mass of traffic, the changes are fairly insignificant compared to variations caused by temperature and structural damage. However for cable supported bridges the changes in the dynamic properties caused by traffic mass is more pronounced, since not only do their deck structures have a lower weight due to the slenderness of their design, but the elevated tensions in the cables caused by the increased load raises the bridge's stiffness, which in turn affect the bridge's deformed shape and its first few global modes of vibration. While the mass of the traffic is unlikely to hinder the serviceability of the bridge (unless it's poorly designed!), SHM is interested in the sensitivity of the bridge to these everyday parameters.

Several papers have already studied variations in the modal properties of bridges caused by vehicular loading, through experimental study and simulation. During a series of ambient vibration tests on a highway bridge Farrar (1997) observed higher frequencies and lower modal damping during tests when no traffic was present. De Roeck et al. (2002) simulated

vehicles of differing mass travelling across a box girder bridge, the natural frequency of the structure decreased in each subsequent analysis when a heavier vehicle model is used. Zhang et al. (2002) tested a cable-stay bridge over a 24 hour period during conditions of calm wind minimal ambient temperature variation. They found variations of approximately 1% for the natural frequencies and 10% for the modal displacements, and also noted a nonlinear relationship between structural damping and RMS vertical acceleration response due to traffic excitation. Kim et al. (2003) reported lower natural frequencies for several highway bridges when excited by heavy vehicles rather than cars, although there was less variation when the tested structure was a suspension bridge, due to the higher bridge-vehicle mass ratio.

2.6.3 WIND CONDITIONS

Wind conditions are also acknowledged affect the performance of cable supported bridges, since the deck structure is comparatively more flexible compared to other bridge structural systems. It is now well known that depending on the wind speed, bridge decks and towers may respond to wind through vortex shedding, buffeting galloping or flutter. In flutter and galloping the wind-induced deformation feeds back into loads and interpreted as aerodynamic damping and stiffness. This effect is termed 'aero-elasticity'.

The effect of wind loading on the performance of suspension bridges is not explored in this thesis, since there is an abundance of research papers on the topic in comparison to the temperature and traffic response. There are several documented examples of applications, developments and frameworks of wind loading to suspension bridge finite element models which may be of interest to the reader, for buffeting analyses (Zhu & Xu 2005; Salvatori & Spinelli 2006; He et al. 2008) and studies on flutter (Zhang, Xiang, et al. 2002; Frandsen 2004; Cheng et al. 2005; Boonyapinyo et al. 2006).

2.7 SUMMARY

Continuum equations are useful for conceptual understanding of suspension bridge performance but it is standard practice to develop adequately but not overly detailed finite element models of suspension bridges. A correct "dead load" state is not so simple to obtain, since the suspension bridge configuration will respond to external loads and environmental conditions. Furthermore, correct modelling of detail of expansion joints and bearings, which appear to have significant influence on full-scale performance, is vital.

Finite element model updating has allowed models to closely represent the monitored structure without necessarily precisely modelling elements such as stiffeners, connection

details, or non-structural members. However, the absence of detail in the FE model may lead to responses that cannot be determined since their cause does not exist in the model. In addition, the updating process may not make the whole modelling procedure more time economic than exact detailing. This is subjected to the analyst's ability to apply updating procedures, and their understanding of suspension bridges' behaviour. Further investigation to bridges' properties and elements that govern particular static and dynamic responses would profit model updating.

The number of data sources for long-term monitoring of global engineering structures is growing, with examples in most countries. Loading simulations would benefit substantially from access to this data, since comparisons can be drawn across different operational structures. This would boost our understanding of their behaviour in ambient conditions, benefiting future developments in the structural construction and its maintenance, and feeding back into design of effective SHM systems.

There remain challenges in FE modelling of suspension bridges in respect of how to apply loads to the model. At the time of writing there is no published research on modelling theoretical thermal effects on long-span suspension bridges, and there is little work which explores how the structure's performance is affected by the levels of traffic. This thesis aims to expand the available knowledge by using a FE model of a suspension bridge to simulate changes in its static and dynamic performance that are caused by thermal and traffic loads.

REFERENCES

Alampalli, S., 2000. Effects of testing, analysis, damage, and environment on modal parameters. *Mechanical Systems and Signal Processing*, 14(1), pp.63–74.

Atkinson, R.J. & Southwell, R.V., 1939. On the problem of stiffened suspension-bridges, and its treatment by relaxation methods. *Journal of the Institution of Civil Engineers*, 11(5), pp.289–312.

Barlow, P.W., 1858. On the mechanical effect of combining girders and suspension chains; and a comparison of the weight of metal in ordinary and suspension girders to produce equal deflections from a given load. *Journal of the Franklin Institute*, 65(5), pp.301–309.

Bleich, F., McCullough, C.B., Rosecrans, R. & Vincent, G.S., 1950. *The mathematical theory of vibration in suspension bridges*, United States Government printing office.

Bolton, R., Stubbs, N., Park, S., Choi, S. & Sikorsky, C., 2001. Documentation of changes in modal properties of a concrete box-girder bridge due to environmental and internal conditions. *Computer-Aided Civil and Infrastructure Engineering*, 16(1), pp.42–57.

Boonyapinyo, V., Lauhatanon, Y. & Lukkunaprasit, P., 2006. Nonlinear aerostatic stability analysis of suspension bridges. *Engineering Structures*, 28(5), pp.793–803.

Brownjohn, J.M.W., 1994. Observations on nonlinear dynamic characteristics of suspension bridges. *Earthquake Engineering and Structural Dynamics*, 23, pp.1351–1367.

Brownjohn, J.M.W., 2007. Structural health monitoring of civil infrastructure. *Philosophical Transactions of the Royal Society of London, Series A, Mathematical and Physical Sciences*, 365(1851), pp.589–622.

Brownjohn, J.M.W. & Xia, P.-Q., 2000. Dynamic assesment of curved cable-stayed bridge by model updating. *Journal of Structural Engineering*, 126(2), pp.252–260.

Buonopane, S.G. & Billington, D.P., 1993. Theory and History of Suspension Bridge design from 1823 to 1940. *Journal of Structural Engineering*, 119(3), pp.954–977.

Chan, T.H., Guo, L. & Li, Z.X., 2003. Finite element modelling for fatigue stress analysis of large suspension bridges. *Journal of Sound Vibration*, 261(3), pp.443–464.

Chen, S.R. & Wu, J., 2010. Dynamic Performance Simulation of Long-Span Bridge under Combined Loads of Stochastic Traffic and Wind. *Journal of Bridge Engineering*, 15(3), pp.219–230.

Cheng, J., Cai, C.S., Xiao, R. & Chen, S.R., 2005. Flutter reliability analysis of suspension bridges. *Journal of Wind Engineering and Industrial Aerodynamics*, 93(10), pp.757–775.

Cheung, M.S., Tadros, G.S., Brown, T., Dilger, W.H., Ghali, A. & Lau, D.T., 1997. Field monitoring and research on performance of the Confederation Bridge. *Canadian Journal of Civil Engineering*, 24(6), pp.951–962.

Cheung, Y.K., Au, F.T.K., Zheng, D.Y. & Cheng, Y.S., 1999. Vibration of multi-span non-uniform bridges under moving vehicles and trains by using modified beam vibration functions. *Journal of Sound and Vibration*, 228(3), pp.611–628.

Cobo del Arco, D. & Aparicio, Á.C., 2001. Preliminary static analysis of suspension bridges. *Engineering Structures*, 23(9), pp.1096–1103.

Conte, J.P., He, X., Moaveni, B., Masri, S.F., Caffrey, J.P., Wahbeh, M., Tasbihgoo, F., Whang, D.H. & Elgamal, A., 2008. Dynamic testing of Alfred Zampa Memorial Bridge. *ASCE Journal of Structural Engineering*, 134(6), pp.1006–1015.

Cornwell, P., Farrar, C.R., Doebling, S.W. & Sohn, H., 1999. Environmental variability of modal properties. *Experimental Techniques*, 23(6), pp.45–48.

Ding, Y.-L. & Li, A., 2011a. Assessment of bridge expansion joints using long-term displacement measurement under changing environmental conditions. *Frontiers of Architecture and Civil Engineering in China*, 5(3), pp.374–380.

Ding, Y.-L. & Li, A., 2011b. Temperature-induced variations of measured modal frequencies of steel box girder for a long-span suspension bridge. *International Journal of Steel Structures*, 11(2), pp.145–155.

Doebling, S.W., Farrar, C.R. & Prime, M.B., 1998. A summary review of vibration-based damage identification methods. *Shock and Vibration Digest*, 30(2), pp.91–105.

Dumanoglu, A.A., Brownjohn, J.M.W. & Severn, R.T., 1992. Seismic analysis of the Fatih Sultan Mehmet (Second Bosporus) Suspension Bridge. *Earthquake Engineering and Structural Dynamics*, 21, pp.881–906.

Erdoğan, H., Akpinar, B., Gülal, E. & Ata, E., 2007. Monitoring the dynamic behaviors of the Bosporus Bridge by GPS during Eurasia Marathon. *Nonlinear Processes in Geophysics*, 14(4), pp.513–523.

Farrar, C.R., 1997. System identification from ambient vibration measurements on a bridge. *Journal of Sound and Vibration*, 1(205), pp.1–18.

Farrar, C.R., Doebling, S.W. & Nix, D.A., 2001. Vibration-based structural damage identification. *Philosophical Transactions of the Royal Society A: Mathematical, Physical and Engineering Sciences*, 359(1778), pp.131–149.

Fitzpatrick, A., Dallard, P., le Bourva, S., Low, A., Ridsill Smith, R. & Willford, M., 2001. Linking London: The Millennium Bridge. , pp.1–31.

Forars, K., Brownjohn, J.M.W. & Warnitchai, P., 2000. Effects of cable dynamics on the seismic performance of cable stayed bridges. *Advances in structural dynamics*, 1, pp.497–504.

Frandsen, J.B., 2004. Numerical bridge deck studies using finite elements. Part I: flutter. *Journal of Fluids and Structures*, 19(2), pp.171–191.

Gattulli, V., Pasca, M. & Vestroni, F., 1997. Nonlinear oscillations of a nonresonant cable under in-plane excitation with a longitudinal control. *Nonlinear dynamics*, 14(2), pp.139–156.

Gentile, C. & Gallino, N., 2008. Ambient vibration testing and structural evaluation of an historic suspension footbridge. *Advances in Engineering Software*, 39(4), pp.356–366.

Giraldo, D.F., 2006. Damage detection accommodating varying environmental conditions. *Structural Health Monitoring*, 5(2), pp.155–172.

He, X., Moaveni, B., Conte, J.P., Elgamal, A. & Masri, S.F., 2008. Modal identification study of Vincent Thomas Bridge using simulated wind-induced ambient vibration data. *Computer-Aided Civil and Infrastructure Engineering*, 23(5), pp.373–388.

He, X., Moaveni, B., Conte, J.P., Elgamal, A. & Masri. S. F., 2009. System identification of Alfred Zampa Memorial Bridge using dynamic field data. *Journal of Structural Engineering*, 135, pp.1–31.

Hemez, F.M. & Doebling, S.W., 2001. Review and assessment of model updating for non-linear, transient dynamics. *Mechanical Systems and Signal Processing*, 15(1), pp.45–74.

Hua, X.G., Ni, Y.Q., Ko, J.M. & Wong, K.-Y., 2007. Modeling of temperature–frequency correlation using combined Principal Component Analysis and Support Vector Regression technique. *Journal of Computing in Civil Engineering*, 21(2), p.122.

Irvine, H.M., 1981. *Cable Structures*, Library of Congress Cataloging in Publication Data.

Irvine, H.M. & Sinclair, G.B., 1976. The suspended elastic cable under the action of concentrated vertical loads. *International Journal of Solids and Structures*, 12(4), pp.309–317.

Jaishi, B. & Ren, W.-X., 2006. Damage detection by finite element model updating using modal flexibility residual. *Journal of Sound and Vibration*, 290(1-2), pp.369–387.

Jaishi, B. & Ren, W.-X., 2007. Finite element model updating based on eigenvalue and strain energy residuals using multiobjective optimisation technique. *Mechanical Systems and Signal Processing*, 21(5), pp.2295–2317.

Jaishi, B. & Ren, W.-X., 2005. Structural Finite Element Model Updating Using Ambient Vibration Test Results. *Journal of Structural Engineering*, 131(4), pp.617–628.

Jung, H.Y., Kim, D., Koo, K.Y. & Cui, J., 2008. Modal flexibility-based FEM model updating for bridges. In H.-M. Koh & D. M. Frangopol, eds. *Bridge Maintenance, Safety Management, Health Monitoring and Informatics*. Seoul, Korea: Taylor & Francis.

Kim, C.-Y., Jung, D.-S., Kim, N.-S., Kwon, S.-D. & Feng, M.Q., 2003. Effect of vehicle weight on natural frequencies of bridges measured from traffic-induced vibration. *Earthquake Engineering and Engineering Vibration*, 2(1), pp.109–115.

Ko, J.M. & Ni, Y.Q., 2005. Technology developments in structural health monitoring of large-scale bridges. *Engineering Structures*, 27(12), pp.1715–1725.

Ko, J.M., Wang, J.Y., Ni, Y.Q. & Chak, K.K., 2003. Observation on Environmental Variability of Modal Properties of a Cable-Stayed Bridge from One-Year Monitoring Data. *Structural Health Monitoring*, p.1552.

Ko, J.M., Xue, S.D. & Xu, Y.L., 1998. Modal analysis of suspension bridge deck units in erection stage. *Engineering Structures*, 20(12), pp.1102–1112.

Kwon, S.-D., Kim, C.-Y. & Chang, S.-P., 2005. Change of Modal Parameters of Bridge Due to Vehicle Pass. In *IMAC-XXIII: Conference & Exposition on Structural Dynamics - Structural Health Monitoring*. pp.283–290.

Larsen, A., 2000. Aerodynamics of the Tacoma Narrows Bridge - 60 years later. *Structural Engineering International*, 10(4), pp.243–248.

Larsen, A., Esdahl, S., Andersen, J.E. & Vejrum, T., 2000. Storebaelt suspension bridge - vortex shedding excitation and mitigation by guide vanes. *Journal of Wind Engineering and Industrial Aerodynamics*, 88(2-3), pp.283–296.

Lazer, A.C. & Mckenna, P.J., 1990. Large-amplitude periodic oscillations in suspension bridges: Some new connections with nonlinear analysis. *SIAM Review*, 32(4), pp.537–578.

Li, J., Su, M. & Fan, L.C., 2003. Natural Frequency of Railway Girder Bridges under Vehicle Loads. *Journal of Bridge Engineering*, 8(4), pp.199–203.

Liu, C. & DeWolf, J.T., 2007. Effect of temperature on modal variability of a curved concrete bridge under ambient loads. *Journal of structural engineering*, 133(12), pp.1742–1751.

Liu, C., DeWolf, J.T. & Kim, J.-H., 2009. Development of a baseline for structural health monitoring for a curved post-tensioned concrete box–girder bridge. *Engineering Structures*, 31(12), pp.3107–3115.

Macdonald, J.H.G., Irwin, P.A. & Fletcher, M.S., 2002. Vortex-induced vibrations of the Second Severn Crossing cable-stayed bridge: Full-scale and wind tunnel measurements. *Proceedings of the Institution of Civil Engineers. Structures and buildings*, 152(2), pp.123–134.

Melan, J., 1888. Theorie der eisernen Bogenbrücken und der Hängebrücken. In W. Engelmann, ed. *Handbuch der Ingenieurwissenschaften*. Leipzig, Germany.

Miao, C.-Q., Chen, L. & Feng, Z.-X., 2011. Research on correlation of modal frequency of long-span bridge structures and environmental temperature. In *2011 International Conference on Multimedia Technology*. IEEE, pp.1175–1179.

Moser, P. & Moaveni, B., 2011. Environmental effects on the identified natural frequencies of the Dowling Hall Footbridge. *Mechanical Systems and Signal Processing*, 25(7), pp.2336–2357.

Mottershead, J.E., 1993. Model updating in structural dynamics: A survey. *Journal of Sound and Vibration*, 167(2), pp.347–375.

Navier, C.L.M.H., 1823. *Rapport a Monsieur Becquey, conseiller d'Otat, directeur général des ponts et chausdes et des mines; et mémoire sur les ponts suspendus*, Paris, France: Imprimérie Royal.

Nayeri, R.D., Masri, S.F., Ghanem, R.G. & Nigbor, R.L., 2008. A novel approach for the structural identification and monitoring of a full-scale 17-story building based on ambient vibration measurements. *Smart Materials and Structures*, 17(2), p.025006.

Ni, Y.Q., Hua, X.G., Fan, K.Q. & Ko, J.M., 2005. Correlating modal properties with temperature using long-term monitoring data and support vector machine technique. *Engineering Structures*, 27(12), pp.1762–1773.

Ni, Y.Q., Hua, X.G., Wong, K.-Y. & Ko, J.M., 2007. Assessment of Bridge Expansion Joints Using Long-Term Displacement and Temperature Measurement. *Journal of Performance of Constructed Facilities*, 21(2), pp.143–151.

Oh, C.K., Sohn, H. & Bae, I.-H., 2009. Statistical novelty detection within the Yeongjong suspension bridge under environmental and operational variations. *Smart Materials and Structures*, 18(12), p.125022.

Paultre, P., Proulx, J. & Bégin, T., 2000. Dynamic investigation of a hybrid suspension and cable-stayed bridge. *Earthquake Engineering & Structural Dynamics*, 29(5), pp.731–739.

Peeters, B. & De Roeck, G., 2000. One year monitoring of the Z24-bridge: Environmental influences versus damage events. In *Modal Analysis*. SEM, United States, pp.1570–1576.

Przemieniecki, J.S., 1968. *Theory of Matrix Structural Analysis*, New York: McGraw-Hill.

Pugsley, A., 1957. *The theory of suspension bridges*, London, England: Arnold.

Rega, G. & Luongo, A., 1980. Natural vibrations of suspended cables with flexible supports. *Computers & Structures*, 12(1), pp.65–75.

Ren, W.-X., Blandford, G.E. & Harik, I.E., 2004. Roebling Suspension Bridge. I: Finite-element Model and free vibration response. *Journal of Bridge Engineering*, 9(2), p.110.

Ren, W.-X., Harik, I.E., Blandford, G.E., Lenett, M. & Baseheart, T.M., 2004. Roebling Suspension Bridge. II: Ambient testing and live-load response. *Journal of Bridge Engineering*, 9(2), pp.119–126.

Ren, W.-X., Huang, M.-G. & Hu, W.-H., 2008. A parabolic cable element for static analysis of cable structures. *Engineering Computations*, 25(4), pp.366–384.

Roberts, G.W., Meng, X. & Dodson, A.H., 2004. Integrating a Global Positioning System and Accelerometers to Monitor the Deflection of Bridges. *Journal of Surveying Engineering*, 130(2), pp.65–72.

De Roeck, G., Maeck, J., Michielsen, T. & Seynaeve, E., 2002. Traffic-induced shifts in modal properties of bridges. In *IMAC-XX: Conference & Exposition on Structural Dynamics*. pp.630–636.

Salvatori, L. & Spinelli, P., 2006. Effects of structural nonlinearity and along-span wind coherence on suspension bridge aerodynamics: Some numerical simulation results. *Journal of Wind Engineering and Industrial Aerodynamics*, 94(5), pp.415–430.

Sohn, H., 2007. Effects of environmental and operational variability on structural health monitoring. *Philosophical transactions. Series A, Mathematical, physical, and engineering sciences*, 365(1851), pp.539–60.

Sohn, H., Dzwonczyk, M., Straser, E.G., Kiremidjian, A.S., Law, K.H. & Meng, T., 1999. An experimental study of temperature effect on modal parameters of the Alamosa Canyon Bridge. *Earthquake Engineering and Structural Dynamics*, 28, pp.879–897.

Stein, E., Rüter, M. & Ohnimus, S., 2004. Adaptive finite element analysis and modelling of solids and structures. Findings, problems and trends. *International Journal for Numerical Methods in Engineering*, 60(1), pp.103–138.

Timoshenko, S., 1930. The stiffness of suspension bridges. *Transactions of the American Society of Civil Engineers*, 94(1), pp.377–405.

Valiente, A., 2005. Symmetric catenary of a uniform elastic cable of neo-Hookean material. *Journal of Engineering Mechanics*, 132(7), pp.747–753.

Vangipuram, P. & Ganesan, N., 2007. Buckling and vibration of rectangular composite viscoelastic sandwich plates under thermal loads. *Composite Structures*, 77(4), pp.419–429.

Wang, H., Zou, K., Li, A. & Jiao, C., 2010. Parameter effects on the dynamic characteristics of a super-long-span triple-tower suspension bridge. *Journal of Zhejiang University - Science A (Applied Physics and Engineering)*, 11(5), pp.305–316.

Watson, C., Watson, T. & Coleman, R., 2007. Structural Monitoring of Cable-Stayed Bridge: Analysis of GPS versus Modeled Deflections. *Journal of Surveying Engineering*, 133(1), pp.23–28.

Wieser, A. & Brunner, F.K., 2002. Analysis of Bridge Deformations using Continuous GPS Measurements. In A. Kopáčik & P. Kyrinovič, eds. *INGEO2002: 2nd Conference of Engineering Surveying*. Bratislava, pp.45–52.

Wong, K.-Y., 2004. Instrumentation and health monitoring of cable-supported bridges. *Structural Control and Health Monitoring*, 11(2), pp.91–124.

Xia, H., Xu, Y.L. & Chan, T.H.T., 2000. Dynamic interaction of long suspension bridges with running trains. *Journal of Sound and Vibration*, 237(2), pp.263–280.

Xia, Y., Chen, B., Weng, S., Ni, Y.-Q. & Xu, Y.-L., 2012. Temperature effect on vibration properties of civil structures: a literature review and case studies. *Journal of Civil Structural Health Monitoring*, 2(1), pp.29–46.

Xu, Y.L., Chen, B., Ng, C.L., Wong, K.-Y. & Chan, W.Y., 2010. Monitoring temperature effect on a long suspension bridge. *Structural Control and Health Monitoring*, 17, pp.632–652.

Xu, Y.L., Ko, J.M. & Yu, Z., 1997. Modal analysis of tower-cable system of Tsing Ma long suspension bridge. *Engineering Structures*, 19(10), pp.857–867.

Xu, Y.L., Ko, J.M. & Zhang, W.S., 1997. Vibration studies of Tsing Ma Suspension Bridge. *Journal of Bridge Engineering*, 2(4), pp.149–156.

Xu, Y.L., Xia, H. & Yan, Q.S., 2003. Dynamic response of suspension bridge to high wind and running train. *Journal of Bridge Engineering*, 8(1), p.46.

Yan, A.-M., Kerschen, G., De Boe, P. & Golinval, J.-C., 2005. Structural damage diagnosis under varying environmental conditions—part II: local PCA for non-linear cases. *Mechanical Systems and Signal Processing*, 19(4), pp.865–880.

Yang, Y.-B., 2004. Extracting bridge frequencies from the dynamic response of a passing vehicle. *Journal of Sound and Vibration*, 272(3-5), pp.471–493.

Yang, Y.-B., Liao, S.-S. & Lin, B.-H., 1995. Impact Formulas for Vehicles Moving over Simple and Continuous Beams. *Journal of Structural Engineering*, 121(11), pp.1644–1650.

Yeung, W.T. & Smith, J.W., 2005. Damage detection in bridges using neural networks for pattern recognition of vibration signatures. *Engineering Structures*, 27(5), pp.685–698.

Zhang, Q.W., Chang, C.C. & Chang, T.Y., 2000. Finite element model updating for structures with parametric constraints. *Earthquake Engineering and Structural Dynamics*, 29(7), pp.927–944.

Zhang, Q.W., Fan, L.C. & Yuan, W.C., 2002. Traffic-induced variability in dynamic properties of cable-stayed bridge. *Earthquake Engineering & Structural Dynamics*, 31(11), pp.2015–2021.

Zhang, X., Xiang, H. & Sun, B., 2002. Nonlinear aerostatic and aerodynamic analysis of long-span suspension bridges considering wind-structure interactions. *Journal of Wind Engineering and Industrial Aerodynamics*, 90(9), pp.1065–1080.

Zhou, H.F., Ni, Y.Q. & Ko, J.M., 2010. Constructing input to neural networks for modeling temperature-caused modal variability: Mean temperatures, effective temperatures, and principal components of temperatures. *Engineering Structures*, 32(6), pp.1747–1759.

Zhu, L.D. & Xu, Y.L., 2005. Buffeting response of long-span cable-supported bridges under skew winds. Part 1: theory. *Journal of Sound and Vibration*, 281(3-5), pp.647–673.

CHAPTER THREE

DEVELOPMENT OF A TAMAR SUSPENSION BRIDGE FINITE ELEMENT MODEL

3.1 INTRODUCTION

Ever since Abdel-Ghaffar applied the finite element method to suspension bridges (Abdel-Ghaffar 1976), the enhanced capability of computers and the development of new analysis techniques, finite element (FE) analyses have become regarded as the analytic method of choice for suspension bridges compared to its predecessor the deflection theory (Buonopane & Billington 1993).

The structural systems of suspension bridges are more complex compared to other bridges, since they rely on the equilibrium of the deck and the tensions in the suspension cables. Generally the (almost) parabolic profile of a taut cable counteracts the parabolic bending moments caused by the dead load, providing negligible displacements in the deflected shape, as well as minimising the axial loads in the deck. Horizontal forces from the main suspension cable are balanced by similar forces from adjoined spans or back-stay cables, ensuring only vertical loads are transmitted down the towers.

Since the configuration of the bridge deck is intrinsically linked with the tension of the cable elements, designers cannot arbitrarily determine the initial shape of the structure: it is determined as a force equilibrium between the external dead loads and the internal member forces. It is only when the deflections are minimal may further static and dynamic analyses be carried out. This process may be referred to as "shape finding" as defined by Murakami (2001), or "form finding". The target shape of the suspension bridge when it is in an equilibrium state under dead loads may be expressed as its "initial configuration".

Several studies have been performed using non-linear FE analyses to date. Karoumi (1999) determined an initial shape for the cables on a suspension bridge via trial and error, Kim and Hae (2001) performed a shape-finding analysis using the Newton-Raphson method, and Kim et. al (2002) determined the shape of a self-anchored suspension bridge by identifying the shape of a cable only system first, before optimising the configuration with the whole bridge deck

For the purposes of this chapter, a "hybrid" suspension bridge is defined as a cable supported bridge that has both a pair of suspension cables and one or more stay cables. These structural systems may be designed from its conception or as a remedial measure to support increased load levels. The number of papers concerning hybrid suspension bridges is limited and only touch upon the theory. The Roebling Suspension Bridge is a hybrid cabled bridge, which has also been modelled with finite elements (Ren et al. 2004), and was designed with a suspension cable and 72 stay cables. Their approach to identify the tension in the suspension cables was

by trial and error, with no optimisation required when the stay cables were added to the model since they were not jacked on the bridge.

A difficulty when applying shape-finding techniques to hybrid suspension bridges is that if the stay cables are post-tensioned several point loads develop across the structure, in addition to the uniformly distributed load from the bridge deck itself. The addition of point loads creates an additional triangular bending moment profile, which is not ideal for the suspension cabled systems that would have a better performance with absolutely parabolic profiles.

This chapter presents a methodology for creating a FE model for this type of suspension bridge, and optimising the tensions by shape-finding. This chapter follows a different method compared to other published works and considers that the cable forces are all contributing simultaneously. A simple parametric sensitivity study has also been presented, to demonstrate how the components of the hybrid suspension bridge contribute to its natural frequencies and its static response.

3.2 BRIDGE DESCRIPTION AND HISTORY

The Tamar Suspension Bridge shown in Figure 3.1 carries the A38 trunk road across the River Tamar from Saltash in Cornwall to Plymouth in Devon, and is financed by toll income from traffic usage. It was first opened in 1961, with a design by Mott Hay and Anderson, as a bridge supported by suspension cables and a truss girder, with a reinforced concrete deck.

The bridge has a main span of 335m and symmetrical side spans of 114m. Accompanied by anchorage and support spans, it has a total length of 642m. The main towers are constructed from reinforced concrete, are seated on caisson foundations and are 73m tall, with the deck suspended halfway up. The truss is 15.2m wide and 4.9m deep. Vertical locked coil hangers are at 9.2m, meeting at the truss' cross girders. Further information about the original design of the bridge may be found in a paper by Anderson (Anderson 1965).

Figure 3.1: Photograph of the Tamar Suspension Bridge, Plymouth, UK.

During the bridge's service it has supported vehicles loads in excess of its design capacity, so it subsequently underwent a strengthening and widening (upgrading) scheme that was completed in December 2001. This involved adding a lane each side of the truss via cantilevers, and replacing the original concrete deck with an orthotropic steel deck and shear boxes. Additionally, eighteen stay cables were installed as shown in Figure 3.2. Sixteen of which span from points close to the saddles on the main towers to either the truss or the base of the side towers. The tensions in the stay cables were jacked once they were attached to the bridge, unlike the Roebling Bridge. The remaining pair were attached to the underside of the truss, and were also jacked.
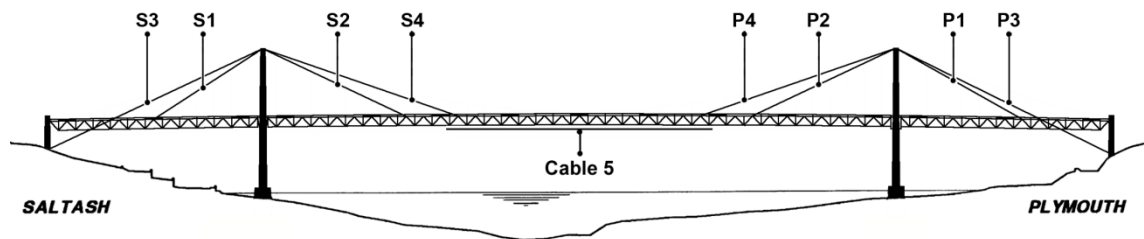
Figure 3.2: Additional stay cables in the strengthening and widening scheme.

3.3 FINITE ELEMENT MODELLING OF THE BRIDGE MODEL

A high resolution 3D FE model was developed as part of a long term structural health monitoring (SHM) project, intended as a numerical representation of the suspension bridge, and a research tool for investigating its performance under varying environmental conditions, such as ambient temperature and wind. The program of choice was ANSYS 12.1.

For the FE model shown in Figure 3.3, the truss was modelled as a repeating series of beam elements, with six degrees of freedom at each node. The deck was treated as a series of shell elements with 6 degrees of freedom at each node, as well. Cable elements (suspension, additional stay and hangers) were modelled as elements with only three degrees of freedom at each node – no rotational stiffness. Furthermore, cable elements have zero stiffness when they come under a compressive load. Altogether, the model contains almost 5900 nodes, and 10500 elements.
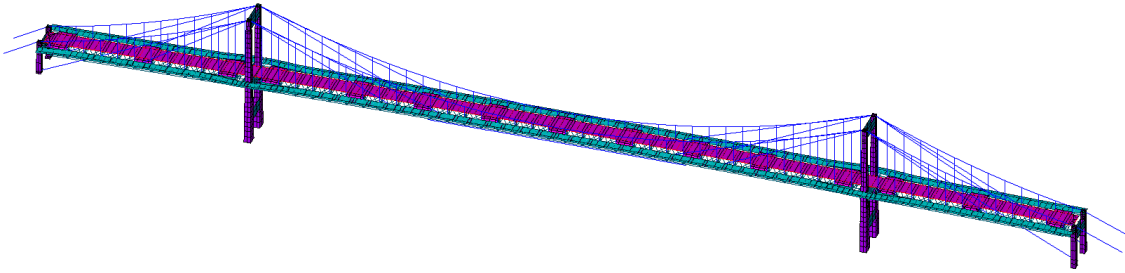
Figure 3.3: Finite Element model of the Tamar Suspension Bridge developed for the project.

3.3.1 BOUNDARY CONDITIONS USED IN FE MODEL

Boundary conditions in finite element modelling are designed to imitate the behaviour of the actual structure correctly, while simple enough to control. The boundary conditions were either fixed, coupled with the displacements of other parts of the structure or controlled via a single spring or beam element.

The boreholes collected by Mott Hay and Anderson (Anderson 1965) assumed that the strata was adequate to seat the suspension bridge's towers on concrete towers; the bearing pressure the caissons are seated on can take a bearing pressure of 10 tons per square foot. In order to reach the solid rock the loose soil was excavated away, so that the caissons are seated 10.2m or more below the river bed. Since the towers are on solid footing and seated deep within the ground, the spring stiffness of the soil was unlikely to cause significant discrepencies between the monitored and simulated results. Therefore the base of the towers could be safely assumed as fully fixed to the strata.

The bridge behaves in a manner similar to Figure 3.4, where the expansion gap is located at the main tower at Saltash, and the deck structure is continuous at the Plymouth main tower for both the 1961 and 2001 versions of the Tamar Suspension Bridge. While the bridge is allowed to move longitudinally at the expansion gap, the deck is supported vertically by both the suspension cable and the bearings. The bridge structure is assumed to be simply supported at the side towers, with some rotational stiffness. There is also some longitudinal stiffness at the expansion gap caused by friction at the bearings, which may affect longitudinal movements of the deck.
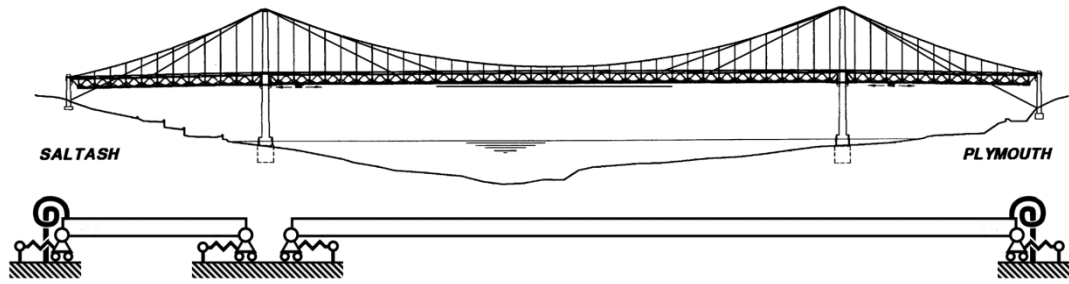
Figure 3.4: Simple diagram of the bridge's boundary conditions.

The lateral thrust girders shown in Figure 3.5 are housed within the towers to prevent the ends of the truss from swaying, while allowing longitudinal motion for a variety of imposed loads. In the FE model, the lateral and vertical response of the lateral thrust girder was coupled with the motion of the towers, as demonstrated by the magenta lines in Figure 3.6. Nonlinear displacements and rotations for the lateral motion of the thrust girder were not considered, since it is assumed these motions were small; only a few centimetres spaces is allowed on either side of the thrust girder.

The longitudinal displacement of the truss, while requiring some freedom to allow the bridge to expand, may in reality be hindered by friction at the boundary conditions, or even seizure (Moser & Moaveni 2011). In the FE model four linear springs (COMBIN14 in ANSYS) stiffen the longitudinal motion of the truss: one on either side of the expansion gap at Saltash connected to the truss elements, and the other two at the ends of the side span. The spring stiffnesses at the side towers are larger than the spring stiffness at the expansion gap to encourage thermal expansion in the FE model towards the gap, as observed in the monitored behaviour of the structure.
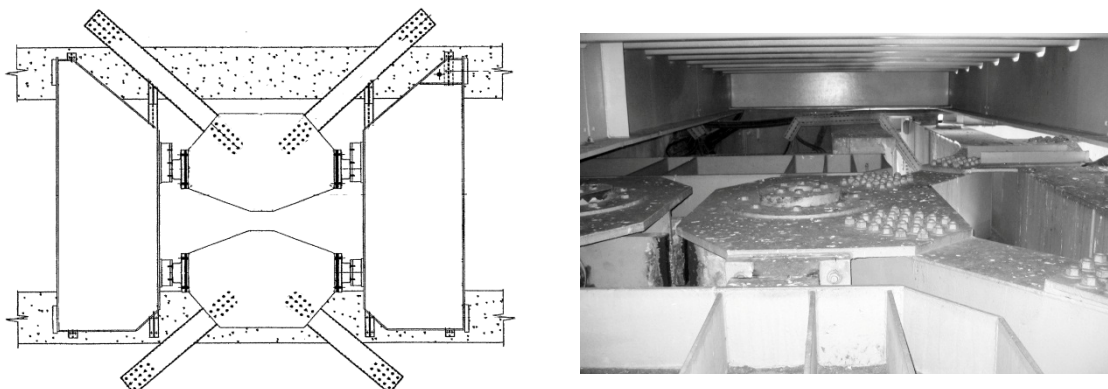
Figure 3.5: Lateral thrust girder at Saltash and Plymouth tower.
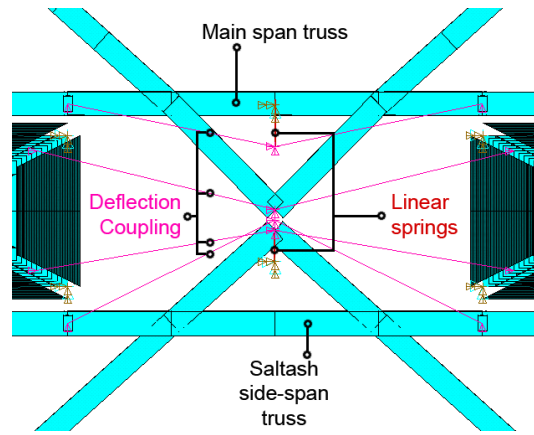
Figure 3.6: FE simulated lateral thrust girder.

Vertical hinges connecting the truss to a seat on each tower shown in Figure 3.7 allow the ends of the truss to rest on the towers, while allowing longitudinal motion. These rockers were modelled as BEAM44; beam elements with rotational resistance released in the span-wise direction, as shown in Figure 3.8. Although it is possible that there may be rotational friction on the rockers caused by the supported mass, it is assumed that any additional longitudinal stiffness would be accounted for by the spring modelled at the lateral thrust girder.
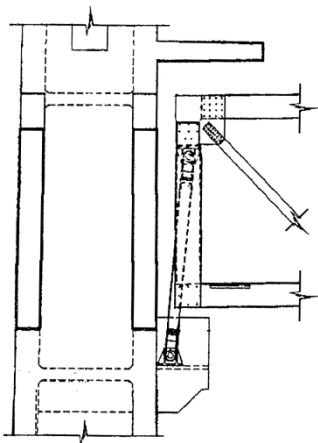
Figure 3.7: Rocker elements on towers.   **Figure 3.8: FE simulated rockers.**
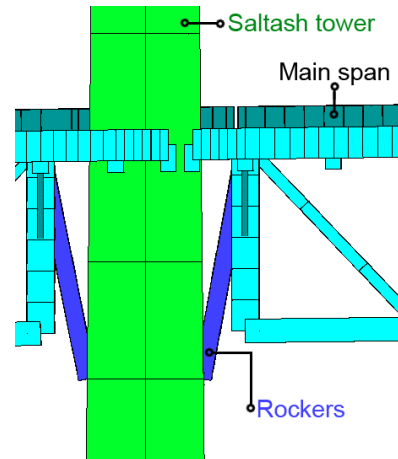
3.3.2 STRUCTURAL PROPERTIES

The structural properties in Table 3.1 were either taken from both technical drawings provided by the Tamar office, the paper by Anderson (1965) or assumed from typical values (Cobb 2008).

Table 3.1: Summary of main structural properties.

	Parameter		Value	Comment
Young's modulus	Main suspension cable; Stay cables; Hangers.		155×10^6 kN/m^2	Consists of 31 steel locked coil rope; ropes shift when pulled.
	Truss; Orthotropic deck; Cantilevers; Shear boxes.		205×10^6 kN/m^2	Steel
	Towers.		30×10^6 kN/m^2	Concrete.
Density	Main suspension cable; Stay cables; Hangers.		8 300 kg/m^3	Calculated from weight of cable divided by area.
	Truss; Orthotropic deck; Cantilevers; Shear boxes.		7800 kg/m^3	Steel
	Towers.		2400 kg/m^3	Concrete
Area	Main cable.		882 cm^2	
	Hangers.		23 cm^2	
	Stay cables.	S1; S3; S4; P4; P3; P1	70.7 cm^2	
		S2; P2; Cable 5	87.0 cm^2	Larger area than other stay cables.

Due to the regular spacing of the hangers, it is expected that each pair is tensioned to support approximately 9.2m of bridge deck. The majority of the hangers support the same mass, including the deck around the towers where the cantilevered deck is projected further, so it was reasonable to treat them all with the same properties. Thus the supporting force of the hanger is half the dead load of a single 9.2m deck section.

The stay cable elements were modelled as single elements, since the scope of the SHM project was mostly concerned with the mode shapes associated with the deck, and not local modes associated with the suspension and stay cables. However, some consideration was required for the elastic stretch and lengthening of the cable from geometry change. Thus Ernst's formula is implemented to reduce the Young's modulus of the cable E_c to an equivalent Young's modulus E_{eq} by a factor that is a function of both the sag and tensile forces of the cable (Ernst 1965):

$$E_{eq} = \frac{E_c}{1 + \dfrac{E_c A_c (L A_c \rho)^2}{12 T^3}} \tag{3.1}$$

where A_c is the area of the cable, L the horizontal span of the cable, ρ the density of the cable and T the cable tension.

Unlike the main cable tensions, the forces in the additional stay cables were monitored by the SHM system, which were used to determine the forces in the FE model. Stay cable tensions

could also be derived from the frequency of the first mode, assuming that it behaves as a taut string. The frequencies are obtained from cable accelerations from a previous site investigation.

3.4 INTERNAL FORCE EQUILIBRIUM BETWEEN SUSPENSION CABLE TENSIONS AND DECK STRUCTURE DEFLECTIONS

3.4.1 PROCEDURE

The process of shape-finding was to ensure that the forces provided by the cable elements would remove deflections caused by the dead load as much as possible. For the Tamar Suspension Bridge, this involved adjusting the main-span and side-span suspension cables, and the stay cables, at every iteration step to minimise the deflections in the spans and towers. The secant iteration method was used to find the cable tension at dead load to reach a suitable profile, which is detailed in Chapter 2, subsection 2.3.1. For shape-finding the variables would be the tensions in the suspension and stay cables, and the functions could be the displacement of either one or several points on the structure, or a dynamic property such as the frequency of the first mode.

In theory the hyperbolic shape of the suspension cable should fully support the dead load of the deck for the whole span. Thus the aim for a typical suspension bridge would be to get a configuration where the majority of displacements are negligible. However for the hybrid suspension bridge the configuration also has to account for the point loads caused by the additional stay cables. This provides an additional term to the parabolic bending moments, which causes the deflected configuration to form a 'W' shape, rather than the usual curve.

Due to the unusual deflected shape a root-mean-square of all nodal displacement on the deck was ruled out, as was the cube root and fourth root, since the attempts with these methods often lead to a diverging solution. An optimal solution was found to be the summation of locations where the displacements were the largest; in this case the nodes at mid-span and the quarter span (the location of the stay cable connections).

Numerous suspension cable modes were identified during dynamic analyses on the FE model. These were not monitored by the SHM systems, so they required identification and separation from the global modes. All mode shapes were normalised to unity, and any shape where a deck deflection is greater than 0.01 was classified as a global mode. Modal solutions from the FE analyses were compared to previously obtained results by their frequencies and order

(Brownjohn & Carden 2008) as another measure for the model's accuracy.

3.4.2 SHAPE FINDING ARRANGEMENTS

Two methods were available to identify the main cable tensions on the bridge:

Method 1 is to construct the bridge as it appeared in 1961; with a concrete deck, no cantilevered deck and no additional stay cables. Assuming that the stretching of the suspension cables over time causes only a slight reduction of the tensions in the suspension cables, the bridge is remodelled into its present state, and the stay cables forces are found by iteration. Ideally the evaluated stay cable tensions match the tensions monitored from the structure.

Method 2 is to take the stay cable forces measured from the bridge structure, and determine the required suspension cable forces from the current structure.

In both Method 2 and the first stage of Method 1, the main and side suspension cable forces are iterated to minimise the deflections in the main span and the towers. The second stage of Method 1 requires identifying the forces in the eight pairs of stay cables attached to the truss. For simplicity it was assumed the cable forces were symmetrical for both towers, so that only four cable forces required identification. However, when optimising stay cable forces as four variables, the results required stay cables S4 and P4 to act in compression, which is impossible. This solution diverges, resulting in ever growing forces in the S3 and S4 cable elements. Instead, the solution was modelled with cable S4 being a function of the forces in cable S2, based on the inclination and where they are attached to the truss. The number of output parameters was thus reduced to the side span deflection, tower deflection and the mean deflection of the mid and side span.

3.4.3 RESULTS

3.4.3.1 Method 1: Shape finding the Tamar Suspension Bridge's 1961 configuration

Table 3.2 shows that the shape finding process on the 1961 bridge provides a configuration where the largest deck displacement is just 2.33mm. The exaggerated displacements in Figure 3.9 shows that the largest displacements in the overall structure occur in the suspension cables, which deflect upwards under the increased strain in the suspension cables from the dead load. Note that the suspension cables would not deflect above the towers and in reality would sag below the saddles; the plots of the FE model have their displacements exaggerated to accentuate the deflected shape. The profile of the suspension cable is not ideal, since the assumption it is a parabola is only an approximation. This leads to the deck deflecting slightly

upwards at mid-span from the vertical forces in the cable, and downwards at the quarter span.

The simulated dynamic properties of the vertical modes were compared to monitored results in 1961, as shown in Table 3.3, which are taken from a paper by Williams (1984). However, for the four observed modes there is more than 10% error between the monitored and FE model results, and their cause could not be determined after several checks. Despite the difference in the modal response, it was decided that the idealised deflected shape was sufficient to advance to the next step.

Using the configuration of the bridge in 2001, the identified stay cable forces produced a wave-like deflected shape in the bridge deck, as shown in Figure 3.10. The largest deflection in the optimised shape was 86mm, which occurred at mid-span, and seemed acceptable. On examination of the dynamic results (in Table 3.3) the errors between the monitored and FE results were reduced in the 2001 model, compared from the 1961 model. Mode VS1 in particular had only 0.3% difference in its frequency, which may indicate the errors in the 1961 model were due to the uncertainties in the concrete deck. However, errors remain on mode LS1 and VS2 that are larger than 10%, which indicate that the model is still not adequately calibrated to the monitored modal properties.

Table 3.2: Initial configuration, if found by first identifying of the bridge's 1961 configuration.

	Force (kN)						Displacement (mm)			
	Suspension Cable		Stay Cable							
Year							Mid-span	Side span	Quarter span	Saltash tower
	Main span	Side span	S3	S1	S2	S4				
1961	21844	22275	N/A	N/A	N/A	N/A	2.14	-2.33	-2.14	2.72
2001	21844	22275	58	747	739	766	86.16	5.96	-38.2	5.46

Figure 3.9: Initial configuration of the Tamar Suspension Bridge in 1961.
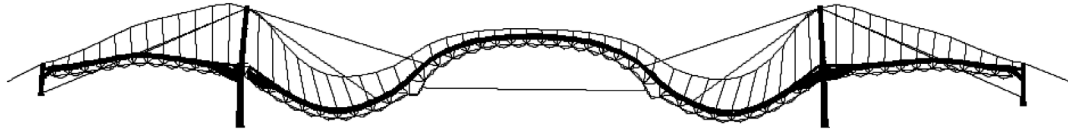
Figure 3.10: Initial configuration of the Tamar Suspension Bridge in 2001, identified via the 1961 configuration.

Table 3.3: Dynamic properties of Tamar Suspension Bridge, with a configuration found using the second shape finding method.

Year	Dynamic property	Mode				
		1	2	3	4	5
1961	Mode shape	LS1	VS1	VA1	VS2	TS1
	Frequency (Hz)	0.295	0.371	0.411	0.795	0.939
	Monitored Frequency (Hz)	-	0.32	0.37	0.67	0.83
	Error	-	15.9%	11.1%	18.7%	13.1%
2001	Mode shape	VS1	LS1	VA1	TS1	VS2
	Frequency (Hz)	0.392	0.508	0.540	0.748	0.846
	Monitored Frequency (Hz)	0.393	0.457	0.595	0.726	0.975
	Error	0.3%	11.2%	9.2%	3.0%	13.2%

where LS1 means *first symmetric lateral mode shape*, VS1 *first symmetric vertical mode shape*, VA1 *first asymmetric vertical mode shape,* VS2 *second symmetric vertical mode shape*, and TS1 *first symmetric torsional mode shape*.

3.4.3.2   *Method 2: Using measured stay cable tensions*

Method 2 is much simpler than Method 1, and uses stay cable forces obtained from the SHM system. The deflected shape in Figure 3.11 follows a similar 'W' shape profile to the Method 1 configuration (Figure 3.10), except the shape is more angular since the suspension cable tensions are reduced, as listed in Table 3.4. The cable forces are significantly different to those

identified by Method 1, especially the magnitude of the forces in the stay cables, which may indicate the suspension cable forces calculated from Method 1 are too large, despite negligible deflections to dead loads in the 1961 configuration. If the tensions calculated from Method 2 are used in the 1961 configuration, the largest deflection would be at mid-span, which is 30cm.

Table 3.5 indicates that the dynamic properties determined by Method 2 are very similar to those determined from Method 1, bearing little difference to the 2001 bridge's modal results seen previously in Table 3.3. The most significant difference between the results is on mode LS1, which has a 3.3% error to the monitored results; a much smaller error than that determined from Method 1.
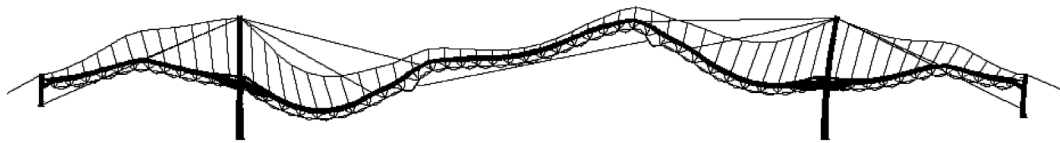
Figure 3.11: Initial configuration of Tamar Suspension Bridge; using measured stay cable forces.

Table 3.4: Initial configuration, if found by using measured stay cable forces.

	Force (kN)						Displacement (mm)			
	Suspension Cable		Stay Cable							
Year							Mid-span	Side span	Quarter span	Saltash tower
	Main span	Side span	S3	S1	S2	S4				
2001	17368	19518	1907	1984	1670	1988	40.88	43.39	-24.55	5.31

Table 3.5: Dynamic properties of Tamar Suspension Bridge, with a configuration found using the second shape finding method.

Year	Dynamic property	Mode				
		1	2	3	4	5
	Mode shape	VS1	LS1	VA1	TS1	VS2
	Frequency (Hz)	0.391	0.472	0.538	0.741	0.841
2001	Monitored Frequency (Hz)	0.393	0.457	0.595	0.726	0.975
	Error	0.5%	3.3%	9.6%	2.1%	13.7%

3.4.3.3 Choice of configuration

The frequencies for the vertical modes in the FE model using both methods were quite close. The lateral mode in Method 2 shares a closer frequency to the monitored results compared to Method 1, which suggests the cable tensions in Method 2 are closer to those found in the actual structure. The frequencies from the original version of the bridge is in Method 1 also suggests that the FE model of the bridge from 1961 is stiffer than it actually was, which has resulted in incorrect suspension cable forces. In practise, it is likely that the tensions in the suspension cables have deteriorated over time, and that the initial configuration of the Tamar Suspension Bridge in 2001 before the upgrading scheme was unlikely to be the same as its configuration 40 years previously.

For the choice of configuration, it seems more feasible to use stay cable tensions already measured from the structure, alongside modal properties that already bear a similar match. Since only the current configuration for the model is required for future work, it is also unnecessary to attempt to calibrate the 1961 FE model to provide a better match with the monitored dynamic results, then modify it further to meet the current model's dynamic properties. Thus the arrangement calculated from Method 2 was the adopted as the optimised initial configuration.

3.5 SENSITIVITY OF STATIC AND DYNAMIC RESPONSE TO THE STRUCTURAL PROPERTIES

Following the identification of the initial configuration, it is apparent from the errors between the frequencies that the FE model may be optimised further to match the measured results. This also suggests that while the initial configuration, or indeed any parameter used in the secant method, may be used to minimise the error between the predicted and monitored results, there are plenty of uncertainties remaining that may be removed by the usual model updating methods.

Several sensitivities analyses were performed to see how the first five modes are affected by varying Young's Modulus and density of the various bridge elements, as well as the stiffness of the gap and the ends of the spans. The sensitivity was determined by adjusting the parameters in Table 3.1 by 2%. Mode order may change in response to a parameter change, so mode shapes were paired together based on the Modal Assurance Criterion (MAC) values between the original and adjusted versions of the model (Allemang & Brown 1982).

Figure 3.12 shows that the sensitivity to the Young's modulus of the structural parameters in the 1961 bridge is quite similar to the sensitivity seen in 2001 bridge with additional stay cables, in Figure 3.13. While the 1961 bridge experiences higher levels of variation, one finds that in both figures the Young's modulus of the truss has a more pronounced effect on higher order modes, such as the first vertical sidespan mode (SS) which varies by 0.0059Hz in the 1961 version of the bridge. The suspension cable Young's modulus and cable forces play a larger role in determining the frequency and order of the first few modes, such as VS1, since their ratio to the deck structure's stiffness (via the Irvine-Caughey parameter) infers whether the bridge acts like a beam or a suspended cable (Irvine & Caughey 1974).
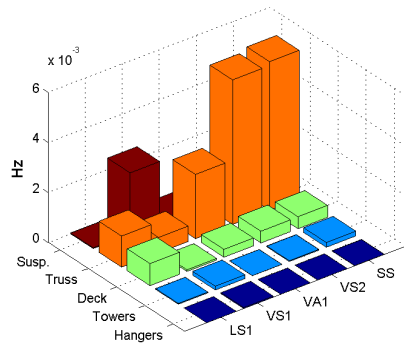
Figure 3.12: Absolute effect of Young's modulii on the first five natural frequencies for the 1961 bridge.
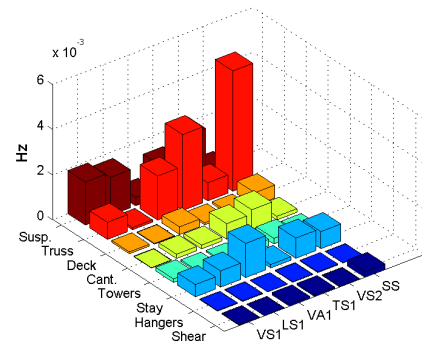
Figure 3.13: Absolute effect of Young's modulii on the first seven natural frequencies for the 2001 bridge.

Figure 3.14 and Figure 3.15 show that the density of the truss and deck elements are also a highly influential parameter to the structure's dynamic properties, for both the 1961 and 2001 versions of the bridge. The density of the suspension cable appears to have a stronger influence on LS1 and VS2 in particular, while producing a barely limited response upon the other modes. Since the modal displacements for modes LS1 and VS2 in the cable are large compared to the deck (9:1 for LS1), it is understandable that the increased mass causes the cable's natural frequency to drop.
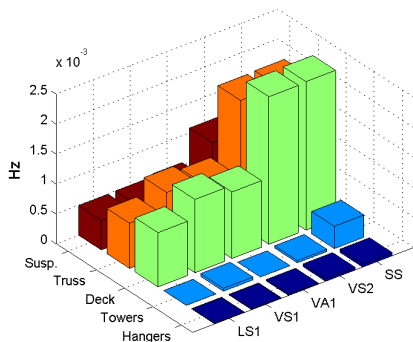
Figure 3.14: Absolute effect of density on the first five natural frequencies for the 1961 bridge.
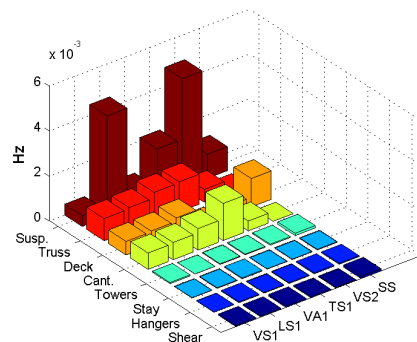
Figure 3.15: Absolute effect of density on the first seven natural frequencies for the2001 bridge.

While altering the structural parameters may give dynamics results from the FE model that are closer to those monitored, they will also modify the initial configuration of cable-supported structure and negate some of the progress made throughout the shape finding process. Thus Figure 3.16 to Figure 3.18 investigate the influence of structural properties on deflections at mid-span, S2 and P2 stay cable connections and the centre of the side spans, again by adjusting their original value by 2%. Figure 3.16 shows that it is the Young's modulus (and consequently the tension) of the suspension and stay cables that determine the vertical deflection of the bridge, while the members in the deck and truss provide next to no change.

87

One finds that 1GN/m² variation in the Young's Modulus changes the mid-span deflection by 8.7mm when applied to the suspension cable, and a 1.7mm deflection when the stay cable tensions are adjusted.

The sensitivity of the structural densities in Figure 3.17 are unsurprising, since the most susceptible element groups (the deck and the truss) also form the majority of the dead load. Likewise, since the stay cable connections are at a quarter-span, their sensitivities are simply a fraction of the mid-span sensitivities.
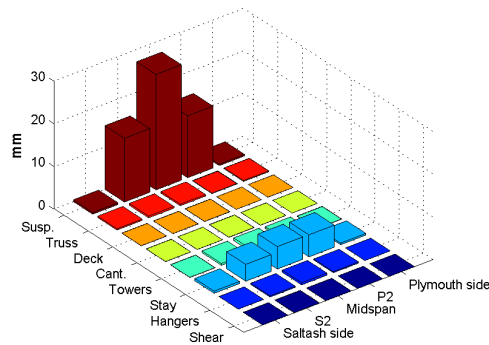
Figure 3.16: Absolute effect of Young's modulii on the deflection of the 2001 bridge's deck.
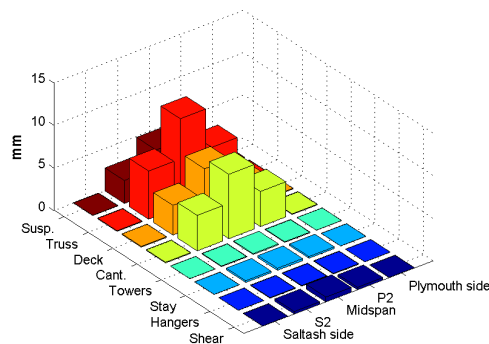
Figure 3.17: Absolute effect of density on the deflection of the 2001 bridge's deck.

The effect of spring stiffnesses representing the bearings were also investigated, however these were modified by 1MN/m rather than 2% since the stiffness of the simulated expansion gap is small (0.001N/m) in comparison to the stiffness at the side towers (1GN/m). Since the main span is connected to the Plymouth side, Figure 3.18 shows that the stiffness at Plymouth tower and the expansion gap determine its deflected shape by holding their ends in place. The stiffness at the Plymouth tower has the largest sensitivity at the quarter span deflection since it affects the lopsidedness of the deflected shape; increasing the stiffness causes the deck to sag towards the Plymouth main tower. The spring stiffnesses were also investigated to see how they affected dynamic properties, as shown in Figure 3.19, however only VA1 had a

significant sensitivity to the expansion gap stiffness since it moves in the longitudinal direction, as well as vertical.
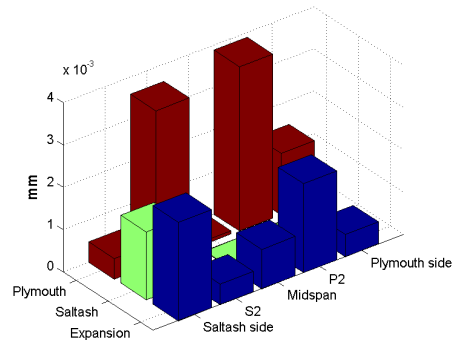
Figure 3.18: Absolute effect of gap stiffness on the 2001 bridge's deck deflections.
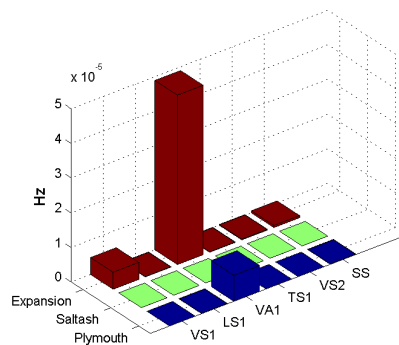
Figure 3.19: Absolute effect of gap stiffness on the 2001 bridge's first seven frequencies.

3.6 SUMMARY

This chapter presents the methodology used to create the FE model for a hybrid suspension bridge. An initial configuration for the suspension bridge was identified via the secant method, a finite difference approximation of the Newton-Raphson iteration method.

Two different methods were used; the first method optimised the shape of its original configuration in 1961, followed by identifying the additional stay cable tensions for the 2001 upgrade; the second determined the suspension cable forces using the 2001 version of the bridge and monitored stay cable forces. Although it was desirable for both to produce a similar response, the second method was selected since there were too many uncertainties when optimising two different configurations.

Despite the difficulties presented during the shape finding process, it was observed that for the Tamar Suspension Bridge, the relationship between structural parameters and response was similar for both the typical and hybrid cabled configurations. It was identified that the

suspension cable is the most influential parameter determining the static shape of the structure, as well as governing the responses of sway and other mode shapes where the cable has a large modal displacement. It is also shown that deck members have an increasing influence on higher order mode shapes.

REFERENCES

Abdel-Ghaffar, A.M., 1976. Dynamic analyses of suspension bridge structures.

Allemang, R.J. & Brown, D.L., 1982. A correlation coefficient for modal vector analysis. In *Proceedings of the 1st International Modal Analysis*. pp.110–116.

Anderson, J.K., 1965. Tamar Bridge. In *ICE Proceedings*. pp.337–365.

Brownjohn, J.M.W. & Carden, P., 2008. Real-time operation modal analysis of Tamar Bridge. In *IMAC-XXVI: Conference & Exposition on Structural Dynamics*. Orlando, Florida, USA, pp.1–8.

Buonopane, S.G. & Billington, D.P., 1993. Theory and History of Suspension Bridge design from 1823 to 1940. *Journal of Structural Engineering*, 119(3), pp.954–977.

Cobb, F., 2008. *Structural Engineer's Pocket Book* 2nd editio., Butterworth-Heinemann.

Ernst, H.J., 1965. Der e-modul von seilen unter beruecksichtigung des durchhanges. *Bauingenieur*, 40(2), pp.52–55.

Irvine, H.M. & Caughey, T.K., 1974. The linear theory of free vibrations of a suspended cable. *Proceedings of the Royal Society, London*, A341(1626), pp.299–315.

Karoumi, R., 1999. Some modeling aspects in the nonlinear finite element analysis of cable supported bridges. *Computers & Structures*, 71(4), pp.397–412.

Kim, H.-K., Lee, M.-J. & Chang, S.-P., 2002. Non-linear shape-finding analysis of a self-anchored suspension bridge. *Engineering Structures*, 24(12), pp.1547–1559.

Kim, K.-S. & Hae, S.L., 2001. Analysis of target configurations under dead loads for cable-supported bridges. *Computers & Structures*, 79(29-30), pp.2681–2692.

Moser, P. & Moaveni, B., 2011. Environmental effects on the identified natural frequencies of the Dowling Hall Footbridge. *Mechanical Systems and Signal Processing*, 25(7), pp.2336–2357.

Murakami, H., 2001. Static and dynamic analyses of tensegrity structures. Part II. Quasi-static analysis. *International Journal of Solids and Structures*, 38(20), pp.3615–3629.

Ren, W.-X., Blandford, G.E. & Harik, I.E., 2004. Roebling Suspension Bridge. I: Finite-element Model and free vibration response. *Journal of Bridge Engineering*, 9(2), p.110.

Williams, C., 1984. Vibration monitoring of large structures. *Experimental Techniques*, 8(112), pp.29–32.

CHAPTER FOUR

EFFECT OF TEMPERATURE ON SUSPENSION BRIDGE PERFORMANCE - STATIC

4.1 INTRODUCTION

The objective of Structural health monitoring (SHM) is to ascertain whether faults, such as damaged members, weakened connections and other forms of degradation, are present in the structure. These may affect the stiffness, mass or energy dissipation of the structure, which in turn may be reflected in either the static or dynamic response of the system. Initially data is collected from the structure under typical operational conditions, and features are extracted of its supposedly undamaged response. Subsequent data collected from the structure are compared to this training data, and if the features deviate significantly then it may be a sign some part of the structure may be below operational standards.

Variations in the structural response may also be a result of changing thermal conditions, such as the air temperature and solar radiation. In SHM systems these contributions need to be determined, otherwise the systems' ability to identify changes caused by structural damage will be compromised.

The focus of this chapter is to identify variations in quasi-static response of the Tamar Suspension Bridge, and see how much they relate to the temperature variation with time and space. Observations are made from time-series results of the quasi-static displacements of the bridge, which bear some similarities to the monitored temperatures of the structure. These data will be studied to see how the temperature and thermal displacements relate, with attempts to replicate these responses via the finite element (FE) model of the bridge to identify causes for this behaviour.

The FE model is also used to predict behaviour unrecorded by the monitoring system. One such application is the tension in the suspension cables and the hangers. The thermal elongation of cable elements may also cause deflections in the towers, which are also observed. The response of the stay cable tensions to the expanded shape of the structure will also be considered. The section finishes with some observations of thermal lag on the structure, which appear as nonlinearities and disguise trends in the data.

4.2 INSTRUMENTATION OF BRIDGE FOR LONG-TERM MONITORING

4.2.1 DESCRIPTION OF THE FUGRO MONITORING SYSTEM

Our research into the response of the structure to environmental conditions is a product of several years of data collected by long-term monitoring systems installed on the Tamar Suspension Bridge. During the strengthening and widening process detailed in Chapter 3, an

array of sensors was installed by Fugro Structural Monitoring to monitor the state of the bridge along with environmental conditions (such as wind speed, direction and air temperature). The sensor system, which is still operational, includes strain gauges, anemometers, humidity sensors, thermometers and level pressure sensors. The locations of the sensors are presented in Figure 4.1.
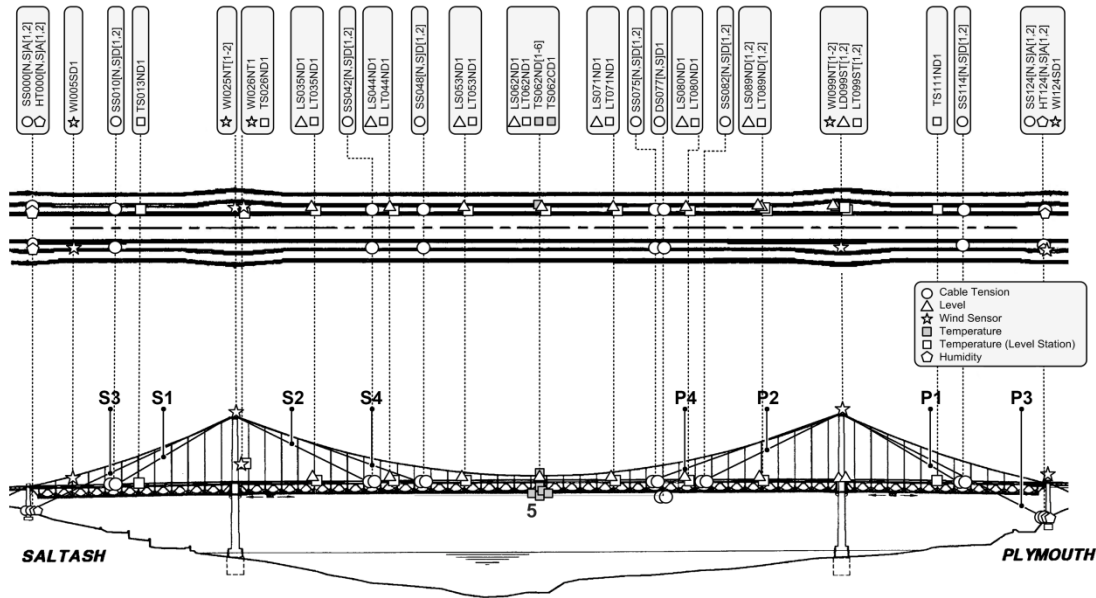
Figure 4.1: Location of sensors in the Fugro monitoring system.

The sampling frequency of the data acquisition system was originally 1Hz, until April 2009 when it was subsequently changed to 0.1Hz, since there was a data loss between January and March 2009 caused by a shortage of computer storage space. In both cases the signals were condensed into hourly summaries.

The sensors used in the Fugro monitoring system are as follows:

4.2.1.1   Strain gauges and extensometers on the stay cables

The load in stay cables attached to the towers (S3, S1, ..., P3) are measured by resistive strain gauges attached to the main tensioning bolts at the deck anchor points, as shown in Figure 4.2. Gauges are arranged in pairs 180 degrees apart around the bolt; one aligned axially to the cable, while the other measures the hoop strain. The four gauges are connected to a full Wheatstone Bridge, with the hoop gauges compensating for the temperature.

The tensions in the longitudinal cables under the truss (cables 5) are obtained from linear potentiometric (consisting of a resistor with a sliding contact) displacement transducers.

4.2.1.2   Level sensing system

The Fugro Level sensing system consists of several Level Sensing Stations (LSS) distributed at

eighth span centres. Each LSS (shown in Figure 4.3) consists of a fluid manometers with vertical displacements obtained from pressure measurements of the fluids' head. The system is based on a similar system installed by Fugro on the Lantau Fixed Crossing (Wong et al. 2001), with height measurements specified to be accurate within 5mm. Fluid temperature sensors are also installed at each LSS.

4.2.1.3 Tower displacement measurements

The relative displacement between the tower tops of the two main towers is measured by an electronic distance measuring device, which is attached to a wall on the upper portal of the Plymouth tower. A laser reflects off a vertical array of mini prisms on the upper portal of the Saltash tower, which ensures no measurements are lost due to the sway of the towers.

4.2.1.4 Wind sensors

Anemometers measure the speed of the wind at the top of the Saltash and Plymouth tower, as well as at the deck level of the Saltash tower and on the Saltash and Plymouth side spans; the sensor near the Saltash tower is shown in Figure 4.4. Additionally the direction of the wind is measured at the top of the Saltash tower. The sensors consist of a Vector Instruments A100L2 anemometer to measure speed, and W200P wind vane to measure direction.

4.2.1.5 Temperature sensors

Thermogauges monitor the temperature of the suspension cable, deck, air and truss. The majority at located at the centre of the main span, but they are also found with the level sensors. The sensors on the cable and deck structure consist of platinum resistance thermometers (PRTs) mounted upon a stainless steel shim, which is held against the structure by an adhesive; Figure 4.5 shows the thermogauge monitoring the suspension cable temperature is held against the surface of the cable. While it is preferable for the sensor to be located inside the cable, when the sensor system is a retrofit to the bridge this would involve cutting away the cable-wrap and getting access through the wires. This increases the likelihood for the wires to corrode, or compromise the tension in the cables, and as such it would be more preferable to avoid this solution altogether. The air temperature sensor is a ceramic element contained within a stainless steel sheath, protected by a radiation shield.

Figure 4.2: Strain gauges on a stay cable's tensioning bolts.

Figure 4.3: Box for a level sensor located on the bridge deck.

Figure 4.4: Anemometer located on a mast near the Saltash tower.

Figure 4.5: Thermogauge on the outside of the suspension cable.

4.2.2 DESCRIPTION OF UNIVERSITY OF SHEFFIELD'S SYSTEM

There was interest in observing how the deformation of the bridge structure may create variations in cable tensions, and possibly manifesting in the modal results as nonlinear effects.

4.2.2.1 Extensometers

Some of the first sensors the University installed on the structure were a set of three pull-wire extensometers at the across the expansion gap near the Saltash tower; one on the North side, one on the South and one in the middle. These extensometers were ASM WS12 linear potentiometers with a measurement range of 0 to 500mm, with the sensor attached to the Saltash tower structure and the pull-out cables mounted to brackets attached to the truss, as

shown in Figure 4.6. The movement of the bridge is measured by how much wire has been pulled from the extensometer (or returned, if moving the other direction), which is directly proportional to an analogue output current varying from 4 to 20mA. The measurements from the extensometers were sampled at a rate of 0.2Hz.

Figure 4.6: Extensometer mounted across the expansion joint.

4.2.2.2 Total Positioning System

Unfortunately there were problems and limitations with the level sensors; all but two of the level sensors (LS080 and LS089) produced erroneous measurements, and were unusable. Also the deformation on all axes (vertical, longitudinal and transverse) need to be recognised to understand the mechanisms acting in the bridge, but the LSS only provide vertical deflections.

Of all the methods available to monitor the deformed shape of the bridge (Brownjohn & Meng 2008), only slowly varying movements were of interest, so there was no need for a inertial based systems with fast sampling rates. A Global Positioning System (GPS) was considered, but ruled out since it required multiple high-cost sensors. Thus Total Positioning System (TPS) technology offered the best solution to fully characterise the quasi-static deformations of the bridge deck and towers.

The TPS on Tamar Suspension Bridge, which consists of a Robotic Total Station (RTS) and 15 reflectors, was installed in September 2009. The reflectors are distributed evenly along the southern cantilevered lane of the bridge (Figure 4.7), as well as located on the saddle and deck levels of the towers (Figure 4.8). These allow the RTS to calculate the relative coordinates of each target in three axes, to provide data on the bridge's static configuration. The locations of the reflectors are shown in Figure 4.9.

Figure 4.7: Reflector positioned on the outer beam of the cantilevers.

Figure 4.8: Reflector located on the side of a Saltash main tower.
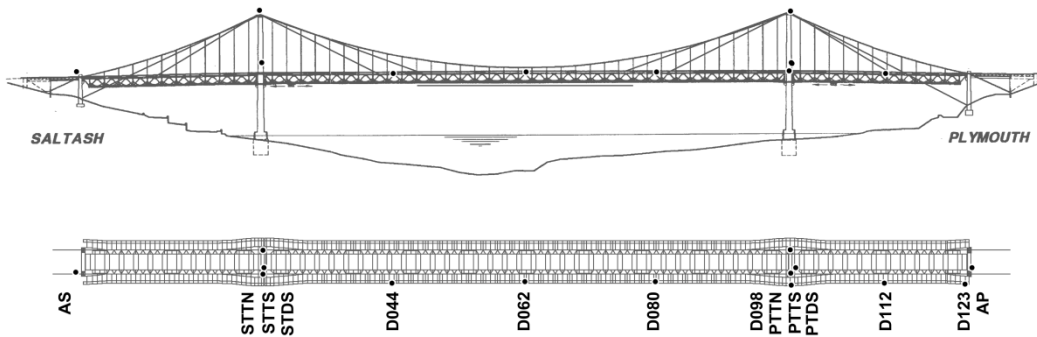
Figure 4.9: Reflector locations on the suspension bridge; for deck and towers.

The RTS unit is a Leica TCA1201 (shown in Figure 4.10), which is designed for measuring distances of more than 8km under ideal weather conditions, and has an accuracy of 2mm + 2 ppm when measuring distance. For the Tamar Suspension Bridge, the farthest reflector is 650m from the RTS, which may have up to 3.3mm error when measuring the distance, and 3.2mm error in the vertical and lateral directions. The accuracy of the theodolite component of the RTS is 1 arc-second. The RTS is capable of working reliably within the glass housing used for weather protection. However, there are occasions when poor weather conditions, such as morning mist, compromise the operation of the system due to light refraction in water droplets. Otherwise the measurements have been reliable.
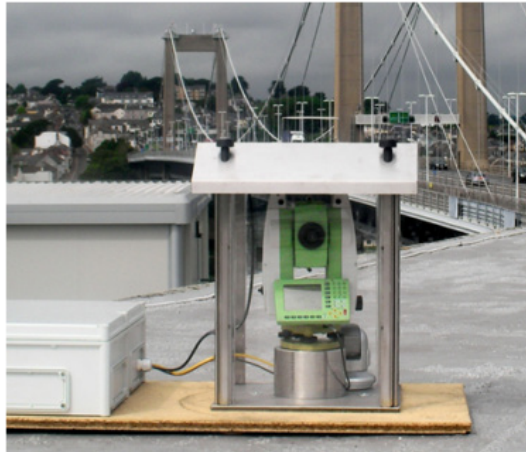
Figure 4.10: RTS located on the Tamar office roof, overlooking the Tamar Suspension Bridge.

The RTS is positioned on the roof of the Tamar Bridge office, monitoring the reflectors positioned on the south side of the main span and Plymouth side spans. The roof location was chosen for its security from public access (being hidden from view and difficult to reach), and for being near the control area of the bridge authority. Unfortunately, due to the location of the sensors and narrow angle of view, reflectors located beyond the Saltash tower expansion joint cannot be identified by the RTS target location system. In fact, the first candidate location was on top of the Plymouth tower for its clear view of the deck. However, vibrations on the top of the tower induced excessive errors on the RTS readings, especially in the vertical direction. Thus this location was dropped in favour of the control room roof. The locations of the reflectors are identified at intervals of approximately 30 minutes, each cycle of the fifteen reflectors taking about 10 minutes.

4.2.3 DATA MANAGEMENT

The data from the Fugro system are stored as a comma-delimited ASCII file for each day, and a smaller text file contains hourly values of the mean, minimum, maximum and standard deviation. The data acquisition of the extensometer data was managed by a virtual instrument (VI) programmed in LabVIEW, which is installed on the Toughbook. The data from the extensometers are stored as binary files every 24 hours.

The data files are stored on a Panasonic Toughbook (a robust laptop), which is used by the University of Sheffield (Fugro data files are also stored at the Tamar office's control room). The Toughbook is also used for configuring the university-owned sensors on the bridge, as well as processing their data. The location for the Toughbook and other data acquisition equipment is within a closed off control chamber near the Plymouth abutments, as shown in Figure 4.11. The Toughbook is connected to the internet via an ADSL router, so any changes to the

configuration of the sensors can be made through Remote Desktop.

Figure 4.11: Unit containing Toughbook laptop, located in a control chamber.

The Toughbook transfers the data files every 24 hours via FTP to a server at Sheffield, which runs a MATLAB script to upload the recent measurements to a database system. The data from the database is consequently used for post-processing by MATLAB and a real-time web viewer.

For the TPS, GeoMos Monitor software is installed on the Toughbook to adjust control settings and the periodic measurements of the TPS runs. GeoMos Monitor stores the measurements from the RTS into a Microsoft Structured Query Language (MS SQL) database. Subsequently, a MATLAB script on the university server reads the data from the Toughbook database, and writes it to the MySQL database on the server. Missing data are added using the co-integration method (Cross et al. 2011), which provides an interpolation of missing recordings using data points neighbouring gaps in the data.

Like the data from the Fugro system, the measurements from the TPS and the extensometers are copied to a database at the University of Sheffield. Since the Toughbook is connected to an ADSL router, any changes to the configuration of the sensors can be made through Remote Desktop, rather than at the laptop in Plymouth (which is more than 230 miles away from Sheffield).

As a note for the reader, despite extensometers being installed on the structure the periods where they are operational are fairly short, and do not run all year round. For this reason the monitored quasi-static data used in this thesis is mostly acquired by the TPS. Information about the extensometers was included to provide the reader a complete overview of the University of Sheffield's monitoring system to date.

4.3 TIME SERIES OF DISPLACEMENTS AND TEMPERATURE DATA

The time series of quasi-static deformations demonstrate that the response of the bridge follows diurnal cycles, with peaks around midday and troughs during the evening or vice-versa. Approaching noon the deck RTS reflectors move longitudinally towards the expansion gap at the Saltash main tower as shown in Figure 4.12, since the main span is continuous with the Plymouth side span. Similarly Figure 4.13 shows that the deck sags vertically during the morning, and rises throughout the afternoon. The largest vertical displacements occur near the mid-span of the deck, and their sizes are more than twice the longitudinal expansion of the bridge. Due to the expansion gap at the Saltash tower, the bridge deforms asymmetrically, with more sag occurring on the Saltash side of the main span than towards the Plymouth end.
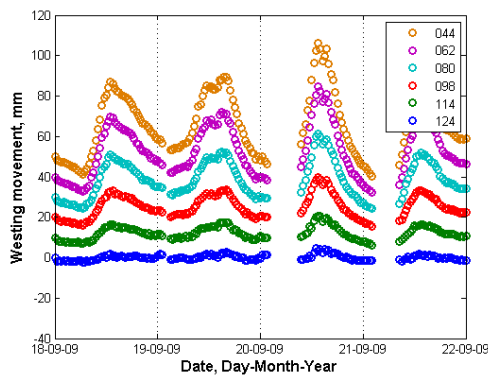
Figure 4.12: Westerly movement (longitudinal expansion) of the Tamar Suspension Bridge.
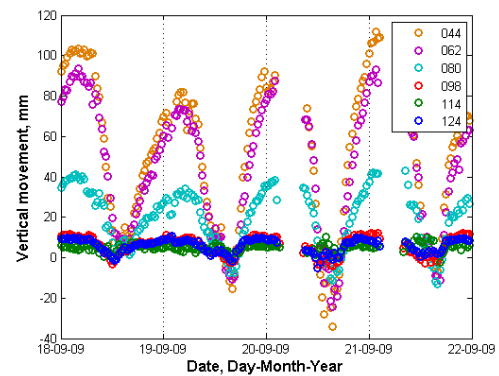
Figure 4.13: Vertical movement of the Tamar Suspension Bridge.

Figure 4.14 shows that while there are variations in the transverse displacements of the deck, particularly on reflectors around the centre of the main span, the response is unlike that exhibited by the vertical and longitudinal displacements, with an apparently random distribution across the day, with no distinct pattern.
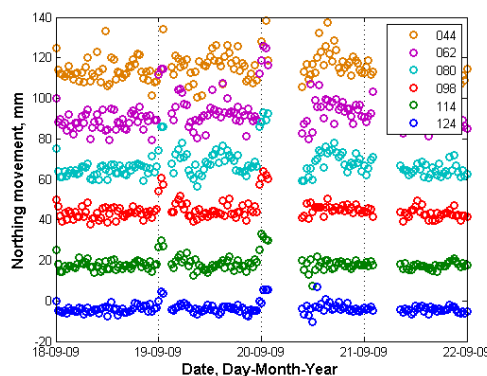
Figure 4.14: Northerly (transverse) movement of the Tamar Suspension Bridge.

The initial assumption was that these time-varying structural displacements are caused by weather conditions as well as by traffic loading on the bridge as both rise and fall though-out the day. An investigation was carried out to determine the extent to which these environmental conditions drive the structural responses, and what parts of the structure are the most critical links between the cause and the effect.

Temperature data are a standard parameter to extract from a monitoring system, and fairly straightforward to use for determining structural responses via theoretical models. What is not so straightforward is measuring and applying the correct mix of temperatures in a performance simulation. Comparing the time series results of the static responses with those for the monitored temperatures, Figure 4.15 suggests that there is a possible relationship between the cable temperature and the vertical and longitudinal displacements since all plots have similar diurnal profiles. The behaviour of the transverse motion is irregular, however, and does not correlate with any temperature data from the bridge.

As observed already, environmental conditions other than temperature also exhibit diurnal behaviour, since they are not independent of each other. For example in daylight hours the temperatures across the structure increase as it is warmed by the sun, while road traffic is heaviest during daylight hours. A comparison with another set of data with a smaller temperature variation is required to confirm that temperature is a significant variable.

Figure 4.16 shows a period where the temperature varied only slightly; webcam images of the bridge showed that the 3rd and 4th of October were overcast, while the traffic levels were similar to those exhibited in Figure 4.15. The quasi-static response of the structure is reduced as a result of limited temperature variation. This verifies that the temperature has a significant effect on Tamar Bridge's quasi-static response.
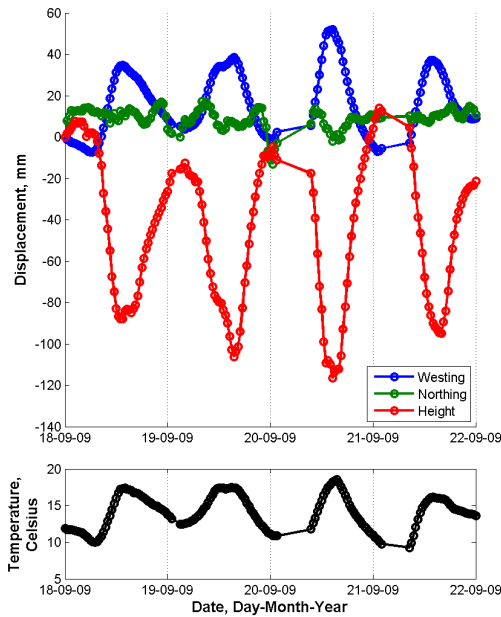
Figure 4.15: Comparison of the displacement of the reflector at cross-girder 044, with the monitored cable temperature.
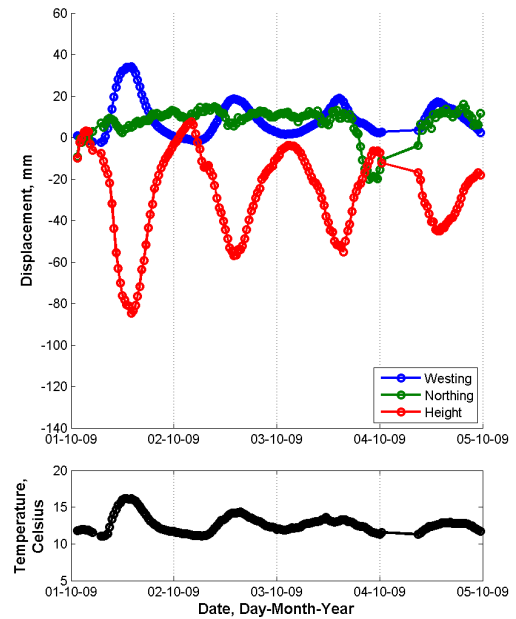
Figure 4.16: Displacement of the reflector at cross girder 044 during a 4 day period, where there is little variation in the temperature.

4.4 APPLICATION OF TEMPERATURES TO FINITE ELEMENT MODEL

It is a given that the bridge responds to a variety of stimuli that are uncontrollable, unpredictable and difficult to measure. Controlled excitation of civil infrastructure for structural identification is typically challenging, due to being in continuous operational use. Achieving adequate signal to noise ratios requires levels of controlled loading that are unachievable without great expense and inconvenience.

Reconciling the observed cause-effect relationships and providing a physical explanation required development of the Tamar Bridge FE model, described in Chapter 3. The model is used under controlled conditions to provide an acceptable prediction or mirror of the behaviour exhibited by the structure. The validated model could be used to predict responses for conditions not yet observed (e.g. extreme environmental loads) and also to identify what parts of the structure are governing this response.

4.4.1 APPLYING THERMAL CONDITIONS

The FE analysis requires a combination of two different sub-analyses in order to determine the total response of the structure: one thermal, the other structural. A multi-physics analysis was

applied to combine the two; first solving the problem via a thermal analysis, then transferring the results as an additional load to the structural analysis.

Values for temperature were imposed on all nodes of the FE model to determine the thermal strains. The temperatures range from -10°C to 40°C in increments of 1°C, since these values bracket the upper and lower extremes of the monitored temperature data. 1°C increments were adopted to identify nonlinear responses in both the static and modal performance, as well as variations in the mode shapes that may arise when the mode order changes. This fine resolution was chosen to catch any step changes in performance.

The strains determined from the first stage thermal analysis are then transferred to the second stage structural analysis to determine the resulting internal stresses and thermal expansion of the elements. A benchmark temperature is required to determine the variation in stresses caused by a change in temperature. For this study the benchmark was chosen as 17.5°C, the same temperature where there are 0 displacements in the monitored RTS results.

4.4.2 ELEMENT AND MATERIAL PROPERITES

While ANSYS 12.1 has a variety of element types that are usable for both thermal and structural analyses, most were not suitable for the FE model since they were either volumetric elements or incapable of representing certain behaviour in the model. Between the thermal and structural analyses the element types and material properties were switched to retain their capabilities. The structural analysis uses the properties described in Chapter 3. The thermal analysis uses similar elements used for conducting heat, such as LINK33 and SHELL57.

The material properties for the thermal analysis in Table 4.1 and Table 4.2 were taken from a design code by the Comité Euro-International du Béton (1993) and the relevant British Standards (British Standards Institution 2004; British Standards Institution 2005). After some initial investigations, the thermal elongation coefficient for the cables was reduced by a third to 8×10^{-6}m/m°C, to provide a better match with the monitored results. Following the transient studies (in Chapter 6) the reduced expansion coefficient is a consequence of studying the problem as a quasi-static analysis rather than a transient one; the cable's wrapping insulates the cable, creating a thermal lag between the peak temperatures of the deck and the suspension cable.

Table 4.1: Thermal material properties

Parameter	Value		Comments
	At -20°C	At 100°C	
Thermal elongation of steel	12×10^{-6}m/m°C	12×10^{-6}m/m°C	Eurocode 3
Thermal elongation of concrete	10×10^{-6}m/m°C	10×10^{-6}m/m°C	CEB-FIP Model Code 1990
Specific heat capacity of steel	416 J/kg °C	488 J/kg °C	Eurocode 3*
Specific heat capacity of concrete	900 J/kg °C	900 J/kg °C	Eurocode 2
Thermal conductivity of steel	54.7 W/m °C	50.7 W/m °C	Eurocode 3
Thermal conductivity of concrete	1.71 W/m °C	1.50 W/m °C	Eurocode 2*
Thermal elongation of cable steel.	8×10^{-6}m/m°C	8×10^{-6}m/m°C	Reduced to provide closer match to monitored data.

* Linear interpolation for 20°C performed.

Table 4.2: Structural material properties.

Parameter	Value	
	At -20°C	At 100°C
Young's modulus of steel.	205 GN/m^2	198 GN/m^2
Young's modulus of cable steel.	155 GN/m^2	150 GN/m^2
Young's modulus of concrete*.	33.6 GN/m^2	22.8 GN/m^2
Density of steel.	7850kg/m³	7850kg/m³
Density of steel cable.	7850kg/m³	7850kg/m³
Density of concrete.	2400kg/m³	2400kg/m³

* Assuming a concrete grade of C20/25.

4.4.3 SEASONAL TEMPERATURE VARIATION

While the temperature is controlled across the model, in reality the structure's temperature is not a single uniform global value. Some elements may experience higher levels of solar radiation and air convection than others, and there may be some variations in their surface's emissivity.

There is a significant difference between temperatures in the orthotropic deck, suspension cable and truss around noon every day; Figure 4.17 shows a typical example of this behaviour. The deck and suspension cables are generally the warmest elements since they are irradiated by the sun; the deck being slightly warmer since the black surfacing is unlikely to reflect the sun's rays. The truss however is mainly shaded by the cantilevered deck, and receives very little solar heating. Most of the heat transfer and temperature variation is via air circulation or by conduction across the deck and truss connections. In the evenings the bridge temperatures are at the their lowest, and like the Tsing-Ma bridge their values converge (Xu et al. 2010).
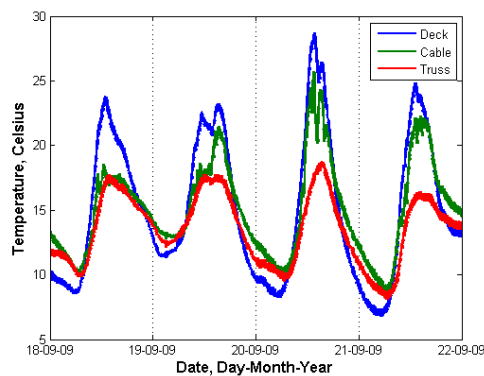
Figure 4.17: Monitored temperatures across bridge cross section.

The relationship between temperature and response is not linear, particularly for cable temperature, as shown by the lines of best fit in Figure 4.18. Above 15°C the deck temperature rises considerably compared to the cable temperature, while the truss temperatures are lower. The trends are quite dispersed, since the figure represents an accumulation of several days of data laid on top of each other.
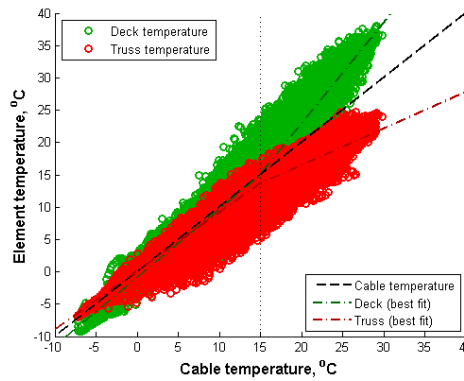
Figure 4.18: Cable temperature vs. deck and truss temperature.

The dispersed trends are formed by the hysteretic nature of the data, which is formed by thermal lag between the cable and the deck, or truss; the temperature of the elements may not peak at the same time, nor do they have the same rate of cooling. The elliptic relationships in the data are more obvious in Figure 4.19, where only 4 days are observed (18th to the 22nd of September, 2009) and the marker colour represents the time of day the sample was read. From the results one finds that, for the same cable temperature, the deck is at a higher temperature as it warms during the morning, compared to when it cools in the afternoon. This shows the deck is more able to gain heat from solar radiation than the cable, and can emit the heat just as easily. The hysteresis is less evident in the truss temperatures, which is more dependent on the surrounding air temperature.
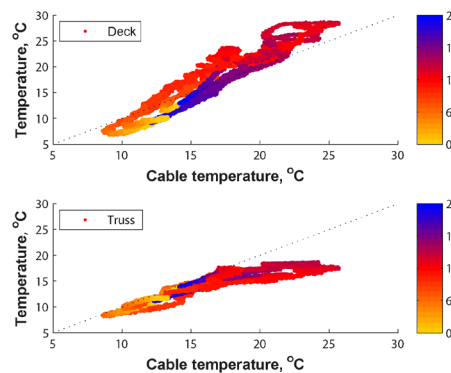
Figure 4.19: Elliptic relationship of bridge temperatures.

Figure 4.20 demonstrates that a sizable portion of this variation is seasonal. During winter periods the daylight hours are shorter and solar intensity is reduced, so there is little solar heating in the structure. In the UK the sky is more likely to be overcast and the majority of heat is produced by air warming and indirect solar radiation of the structure, when the rays are diffused by clouds and atmosphere. This makes the temperatures across the structure uniform. In summer solar radiation plays a bigger role, providing more heating in the deck and

cable leading to higher temperatures than those of the truss.
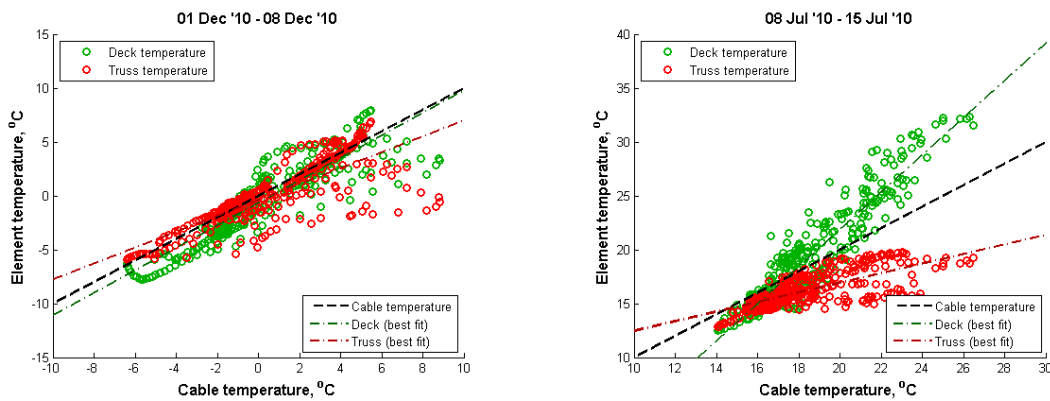
Figure 4.20: Cable temperature vs. deck and truss temperature, for a week in December (left) and July (right).

Since the analysis is not 'time dependent', an approximation was made to account for this seasonal behaviour, as the well as the various contributors to the structure's temperature, like cloud cover and wind chill. Using the data collected from the bridge, the deck and truss temperatures are approximated by functions of the cable temperature. Since larger temperature differentials occur for cable temperatures exceeding 15°C, these functions were bilinear; the coefficients of the equations dependent on whether the cable temperature was above or below 15°C:

$$\tau_d = \begin{cases} 1.07\tau_c + 0.06 & \tau_c \leq 15 \\ 1.55\tau_c - 8.02 & \tau_c > 15 \end{cases} \tag{4.1}$$

$$\tau_t = \begin{cases} 0.97\tau_c - 1.59 & \tau_c \leq 15 \\ 0.56\tau_c + 5.31 & \tau_c > 15 \end{cases} \tag{4.2}$$

where τ_d, τ_c and τ_t are the temperatures of the deck, cable and truss respectively, measured in degrees Celsius.

4.5 MONITORED AND PREDICTED DISPLACEMENTS OF THE DECK

4.5.1 LONGITUDINAL AND VERTICAL DISPLACEMENTS

The longitudinal expansion for the deck in Figure 4.21 demonstrates a linear relationship with the suspension cable temperature in both the monitored and FE model results, which in both cases are taken from location cross girder 044. A simple check to determine the validity of the results can be made by dividing the slope of the data by the distance between the reflector and the end of the Plymouth side span, as shown by Table 4.3. The returned values for the

majority of the reflectors are close to the expansion coefficient of steel (12×10^{-6}m/m°C); which should be expected. The values diminish when the reflectors are located closer to the tower, which is due to the curvature of the deck caused by the cable or (for reflector 123) short distances from the side tower (since it is a minor assumption that the expansion originates here).
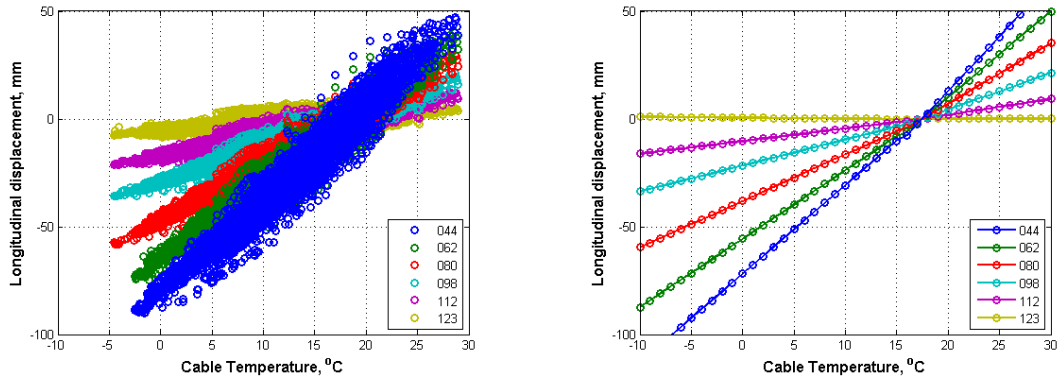
Figure 4.21: Longitudinal expansion of the deck. Left: Monitored results from RTS. Right: Predicted results from FE model.

Table 4.3: Determination of thermal expansion coefficients, using slope of FE and monitored data and distance from Plymouth side tower (GC124).

Reflector	Distance from cross girder 124 (i.e. Plymouth side tower), m	Monitored results		FE results	
		Slope, mm/°C	Slope / Distance from CG124, m/m°C	Slope, mm/°C	Slope / Distance from CG124, m/m°C
044	369	4.32	11.7×10^6	4.51	12.2
062	286	3.52	12.3×10^6	3.51	12.3
080	204	2.59	12.7×10^6	2.39	11.7
098	121	1.66	13.6×10^6	1.37	11.3
112	61	1.01	16.6×10^6	0.62	10.2
123	6	0.43	74.2×10^6	-0.045	-7.71

Figure 4.22 demonstrates the variation of vertical deflection of the bridge deck with main cable temperature, comparing the monitored results and the FE prediction. This response is caused by the elongation of the cable elements; removal of the suspension and stay cable elements and gravity effects from the FE model significantly reduces the vertical deflection of the deck, almost completely. Since the suspension cable provides vertical support to the deck,

it is credible for the deck to lower when the cable expands and sags.
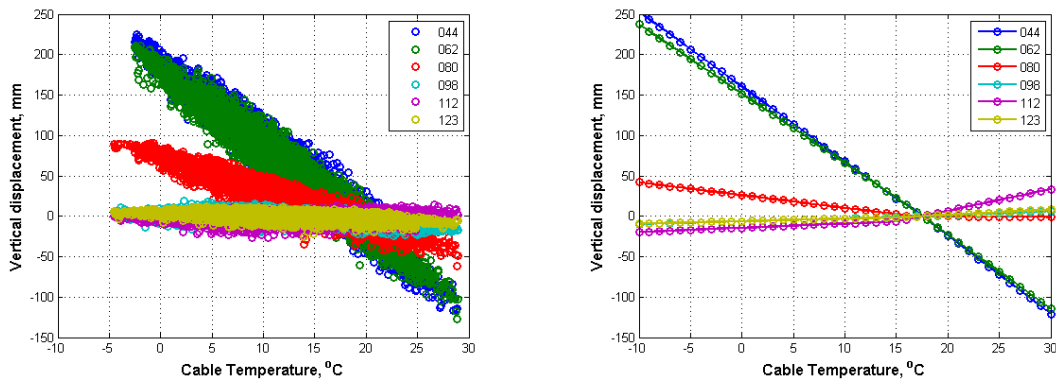
Figure 4.22: Vertical displacement of the deck. Left: Monitored results from RTS. Right: Predicted results from FE model.

4.5.2 EXPANSION DIFFERENTIALS

When the deck is heated, the bridge not only expands but hogs, creating a difference in longitudinal displacements between the top and the bottom of the deck. For the suspension bridge deck this curvature would be a combination of two effects illustrated in Figure 4.23. One of these is already demonstrated in Figure 4.22; the deck sags at higher temperatures due to the elongation of the suspension cable.

There is also a variation in temperature through the cross-section of the bridge deck, since the top is directly warmed by the sun. Thus the top surface expands further, and the deck bends upwards. While the sag of the suspension cable is governing the shape of the bridge deck, it would be worthwhile to check for any influence of temperature gradients.

Expansion differential due to :

Sagging of the cable.   **Warming of the top side.**
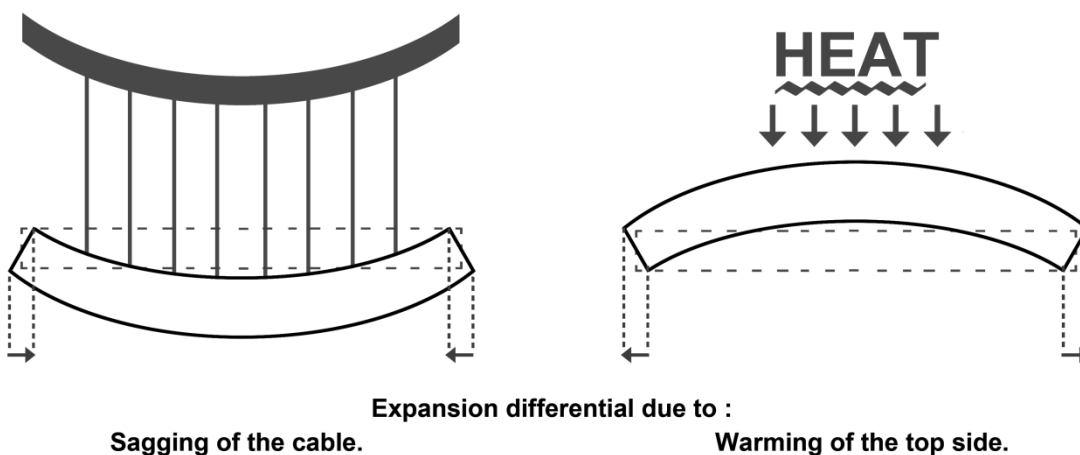
Figure 4.23: Possible ways temperature may cause differences in longitudinal expansion between the upper and lower sides of the deck.

The FE model was applied to determine the difference in longitudinal displacements between the top and bottom chords of the deck. The results for each cross girder location are shown in Figure 4.24. Overall the differential is small, and does not form a significant part of the deformed shape of the structure. There is also very little evidence that the warmer top surface causes the deck to curve upwards, apart from at cross girders 098 and 123 where an obtuse angle forms in the lines at 15°C. This response may be because these cross-girders are located near the towers and are unlikely to displace vertically, making the expansions caused by warming of the top chord more evident.
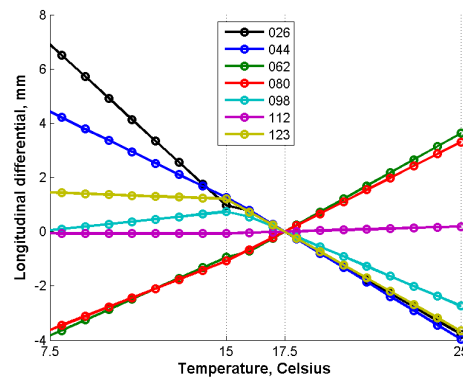
Figure 4.24: Expansion differential vs. Cable temperature.

4.6 VARIATION OF SUSPENSION CABLE TENSIONS

The temperature-induced variations of the tensions in the cable elements were predicted using the FE model and are shown in Figure 4.25. The U-shaped plot of the tensions is characteristic to a suspension bridge cable, ensuring that the resolved horizontal forces throughout the cable remain the same, despite the varying pitch of the cable. The tensions in the main cables drop as the temperature increases leading to cable slackening and increasing sag of the deck.

The tensions are offset at the towers (-7m and 328m) since the horizontal force equilibrium at the tower saddles is affected by the contributions of the stay cables. As the stay cables are affected differently by the expansion of the deck structure, either tautening or slackening, they change the forces at the tower saddle. Consequently the tensions in the suspension cables have to increase or decrease to maintain the force equilibrium in the towers, which is why there is a different variation in suspension cable tension for the three spans.
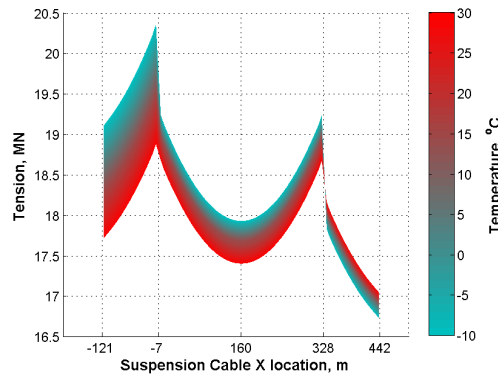
Figure 4.25: Simulated variation in main suspension cable tensions, due to temperature.

Figure 4.26 shows the variation in the suspension cable tensions caused by temperature, except the analysis was performed on the 1961 configuration of the bridge. The plot shares the same contours and U shaped plot as the 2001 configuration, and the greater tensions are due to the suspension cables carrying more bridge mass, since the stay cables are absent. The offsets in the suspension cable tensions from the previous graph are absent, and the plot is symmetrical since the stay cables have been omitted. Thus the only variation is due to the expansion of the cable and the deck.
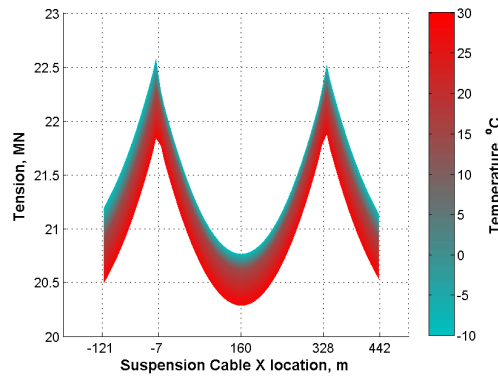
Figure 4.26: Simulated variation in main suspension cable tensions, considering bridge with no stay cables.

Figure 4.27 represents the change in hanger tensions with respect to the temperature. There are some outlying points located near the towers which are associated with the hangers at the end of the truss, which only carry about half the load of an intermediate hanger. The parabolic curve in the hanger tensions is a reaction to the forces from the suspension cable, rather than the camber of the deck.

Like the suspension cable the hanger tensions reduce as the temperature increases. Since there are similarities with the suspension cable tensions in Figure 4.25, such as the variations on the side spans and the offsets at the tower, a portion of this response is a result of the changing vertical forces in the suspension cable, rather than the elongation of the hangers.
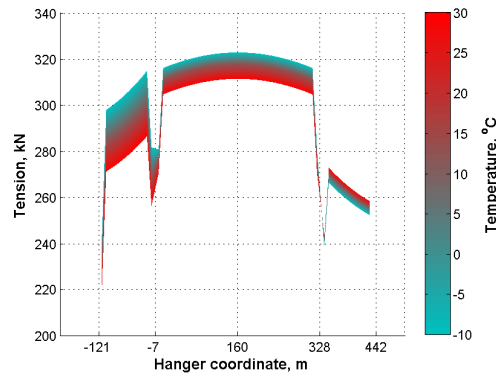
Figure 4.27: Simulated variation in hanger tensions, due to temperature.

4.7 TOWER DEFLECTION RELATIONSHIP WITH CABLE TEMPERATURE

As a consequence of the cable tensions dropping and the deck sagging, the towers move longitudinally inwards as temperature increases, as shown by Figure 4.28 and Figure 4.29. This behaviour is likely to be related to the thermal expansion of the suspension and stay cables. Xu et al. (2010) showed similar behaviour with the Tsing-Ma suspension bridge, where the towers are pulled towards the main span as the cables slacken, and vice-versa. The kink in Figure 4.29 is caused by the temperatures that were applied as a bilinear relationship. This suggests that the deflection of the towers are not directly driven by the suspension cable tensions, otherwise the relationship would be absolutely linear across 17.65 MN. It seems likely that the shape of the deck and the stay cable tensions also have some influence.
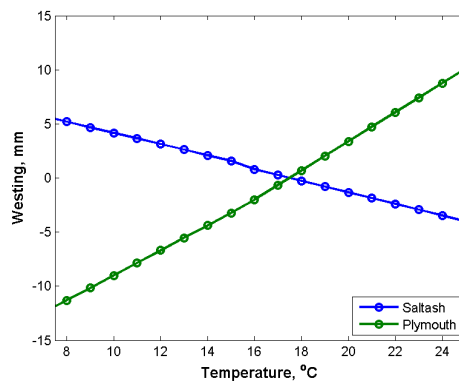
Figure 4.28: Predicted westerly deflection of towers at saddle levels vs. Suspension cable temperature.
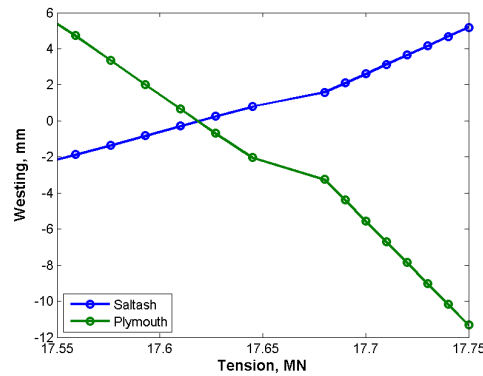
Figure 4.29: Predicted westerly deflection of towers at saddle levels, vs. Suspension cable tension at mid-span.

In Figure 4.30 the different 'noise' levels between the two seasons becomes more obvious. The winter periods have a much clearer linear relationship compared to the periods observed in summer months. This response may demonstrate some influences of solar radiation on the concrete towers that have a larger heat capacity than the steel components of the bridge. This response will be explored later in the Chapter 6.
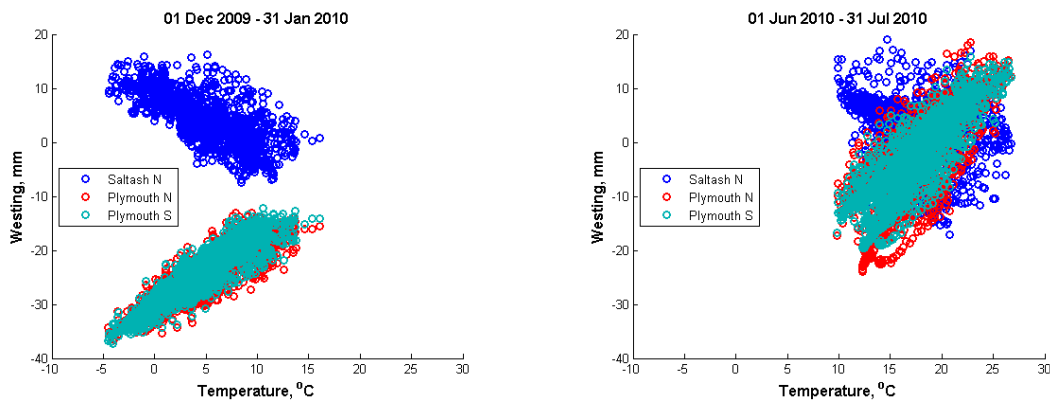
Figure 4.30: Monitored westerly deflection of towers at saddle level. Left: During winter. Right: During summer.

4.8 RESPONSE OF STAY CABLE TENSIONS TO TEMPERATURE AND THERMAL RESPONSES

4.8.1 RELATIONSHIP WITH THERMAL DISPLACEMENTS

The stay cable tensions respond according to expansion and contraction of the bridge, as shown in Figure 4.31. As the deck expands and moves towards the Saltash tower, the cables (connecting to the main span) slacken. The opposite applies to Plymouth; the deck moves away from the tower, so the cables tauten. At first appearance both the monitored and predicted response to the bridge in Figure 4.31 demonstrate linear relationships. However there is a slight bilinear response appearing in the monitored data at the Plymouth tower, where the slope becomes shallower at larger tensions.
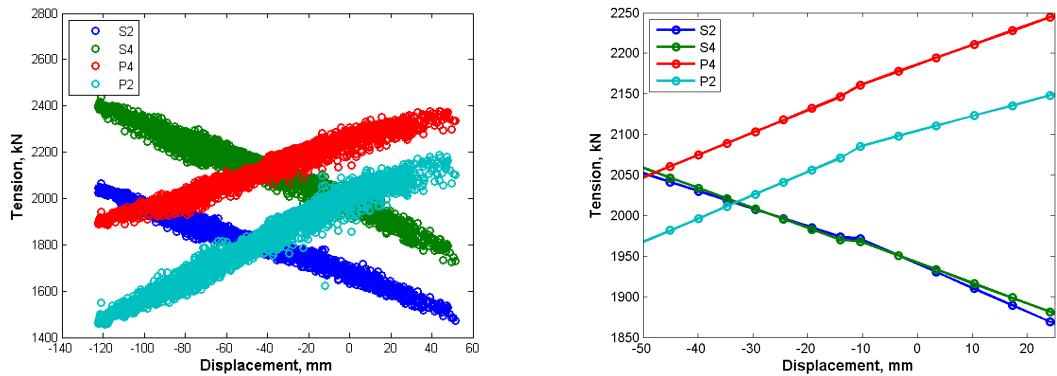
Figure 4.31: Stay cable tensions plotted against longitudinal expansion. Left: Monitored. Right: FE model prediction.

4.8.2 TIME LAG WITH STAY CABLE RESPONSE

Superficially the bi-linearity in Figure 4.31 is not understandable, since it is expected that cable tensions have a simple linear relationship with the expansion of the deck. Upon closer examination of daily time series, results such as on the 16th of April 2010 in Figure 4.32 indicate the peak times for main span stay cable tensions differ depending on whether they are attached to either the tower at Saltash or Plymouth. This behaviour differs from that shown by time series of deck displacements, where the vertical and horizontal deflections for all reflector locations peak simultaneously.

While the peak longitudinal and vertical displacements coincide, it is observed that there are time lags between the truss temperature and the deck (and suspension cable) temperatures. The minimum S2 and S4 stay cable tensions occur at the same time as the deck and cable temperatures reach their maxima. Similarly truss temperatures peak close to the times of peak P2 and P4 stay cable tensions. Watson et al. (2007) also observed some lag between the temperature of the bridge and the displacements of a bridge, where the peak displacement would occur after the peak temperature. This was accounted to rapid changes in the temperature of the structure.

The time series of the tower deflections shows a match to the stay cable tensions time series, with one difference. The peak displacement of the Plymouth towers occur at almost the same time as the deck displacements, while the peak tensions in P2 and P4 occur 1.5 hours later. It is unclear whether the stay cable tensions are reacting to the response of the towers, vice versa, or whether both are responding to the same effect.
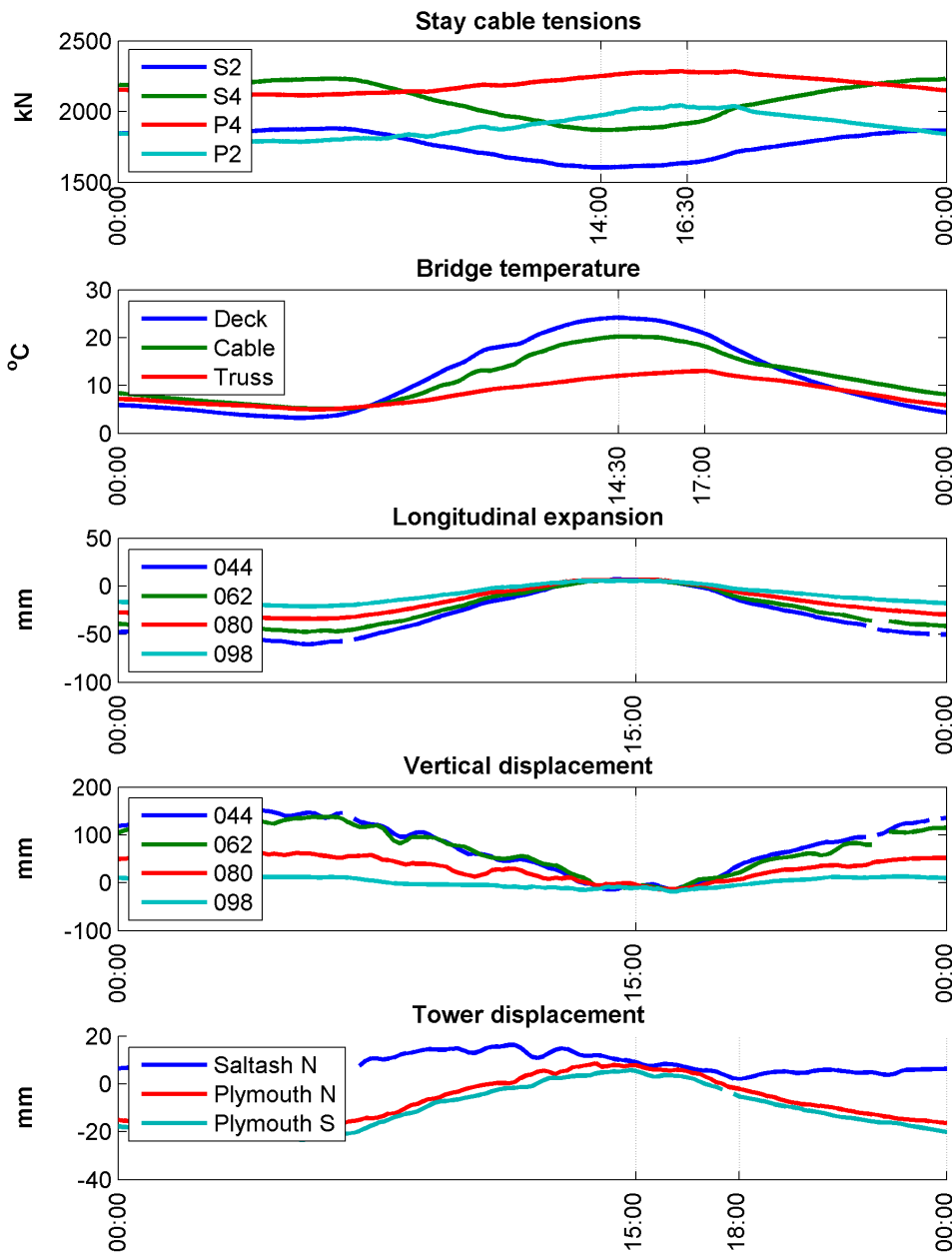
Figure 4.32: Time lag in the bridge's response, during the 16th of April 2010.

4.8.3 HISTOGRAMS OF PEAK BRIDGE RESPONSES

The current thermal analyses do not allow for time dependent effects, so it has not been possible to use it to investigate the causes of thermal lag demonstrated in the previous section. These effects will be explored later in Chapter 6.

Since the data from the Tamar Bridge was accumulated over a long period, it is possible to get an impression of the time lag using histograms of occurrence time for maximum parameter values, using bins of 30-minute intervals. The data were separated into winter and summer periods since there was a distinguishable difference between the two seasons.

116

There are occasionally peaks in the stay tension responses caused by large traffic load. These were ignored for this analysis, but will be investigated in Chapter 7.

Figure 4.33 indicates that throughout the year there are usually delays between peaks in the Saltash (S2, S4) and Plymouth (P2, P4) stay cable tensions, with Figure 4.34 identifying this interval as approximately 3 hours. One noticeable difference between the two seasons is the variation of the time for S2 and S4 peak tension. During winter almost 80% of the monitored days have respective stay cable tensions peaking within the same hourly period. However for the summer period the maximum tensions in S2 and S4 vary over a wider period.
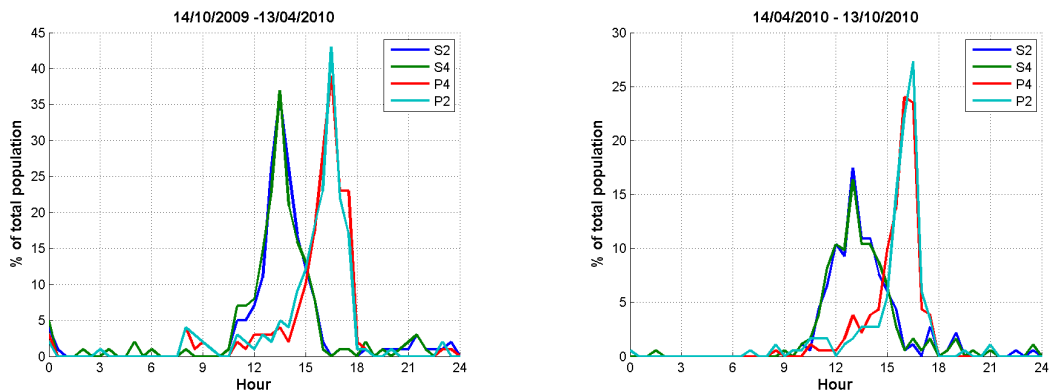
Figure 4.33: Population distribution for the time of peak stay cable tensions. Left: Winter period. Right: Summer period.
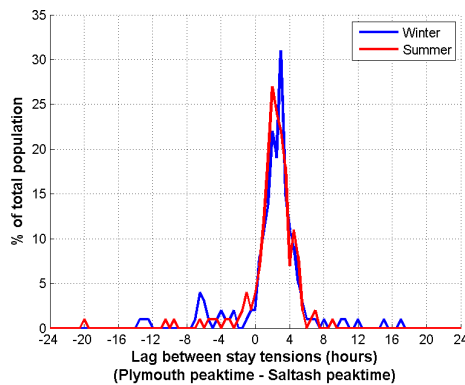
Figure 4.34: Population distributions for the length of time between peak stay cable tensions

Figure 4.35, which is similar to Figure 4.33 but for temperatures instead, suggests that peak bridge temperatures have a similar distribution to the stay cable tensions; deck and cable temperatures peak at similar times as the S2 and S4 cable tensions, while the truss temperature peaks later like the P2 and P4 cable tensions. Figure 4.36 shows that the time between interval between the deck and the truss temperatures may be between 0 and 4 hours: more variable than for the stay cable tensions.

However it is while comparing the summer and winter periods that the link between truss temperature and P2/P4 stay cable tensions breaks down, since the time of peak truss

117

temperature deviates across a wider period of times than P2/P4 tensions. In several time series, there are days where the peak truss temperature occurs before the peak deck temperature, while the maximum P2/P4 tension occurs after minimum S2/S4 tensions. The air temperature follows a similar pattern to the deck and cable temperatures, suggesting that the air below the truss may be cooler, and creating the lag.
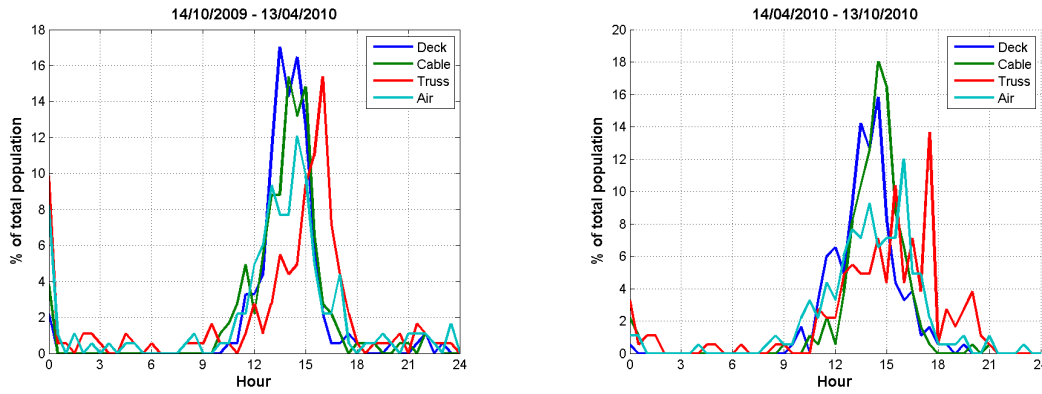
Figure 4.35: Population of the peak bridge temperatures. Left: Winter period. Right: Summer period.
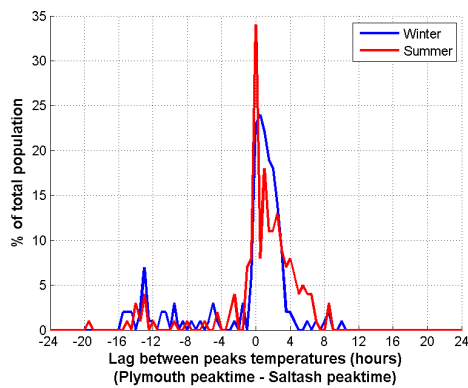
Figure 4.36: Population distributions for the length of time between peak deck and truss temperatures.

Similar histogram characteristics are observed for the tower saddle deflections in Figure 4.37, however the majority of peak Saltash tower deflections occur 2-3 hours after the peak deck displacements, while it was previously seen that the majority of Plymouth stay cables tensions peaked later. The Saltash towers appear uninfluenced by the expansion gap during both seasons; the delayed response is a consequence of the large specific heat capacity of concrete.
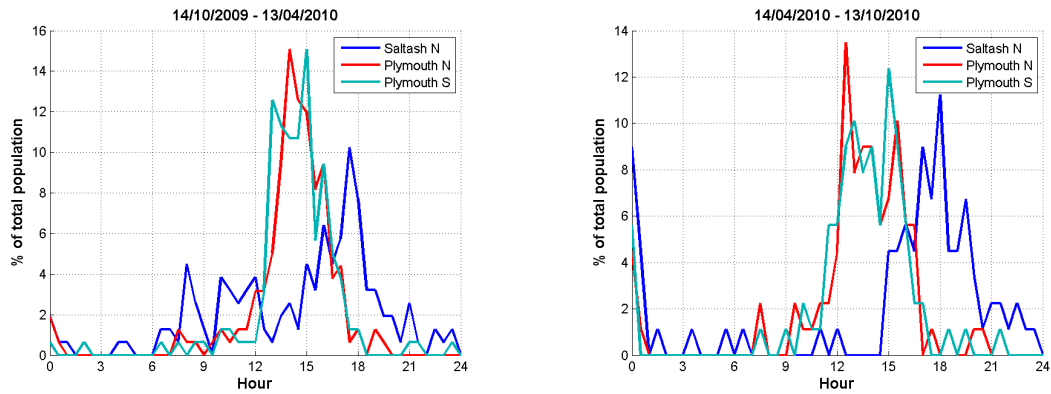
Figure 4.37: Population of the peak tower deflection. Left: Winter period. Right: Summer period.

From closer observation of the time series results, there are also the occasional days in summer where the Saltash tower moves outwards from the main span, rather than inward as suggested previously by the FE simulation. These anomalous responses cause the Saltash tower deflections to appear as a noisy lump when plotted against the expansion of the bridge in Figure 4.38. The Plymouth towers have a clearer relationship, since they are pulled inwards by the cables as the deck expands. The summer data also show the Saltash tower has a 10mm deflection in both the easterly and westerly directions, irrespective of the expansion of the deck.
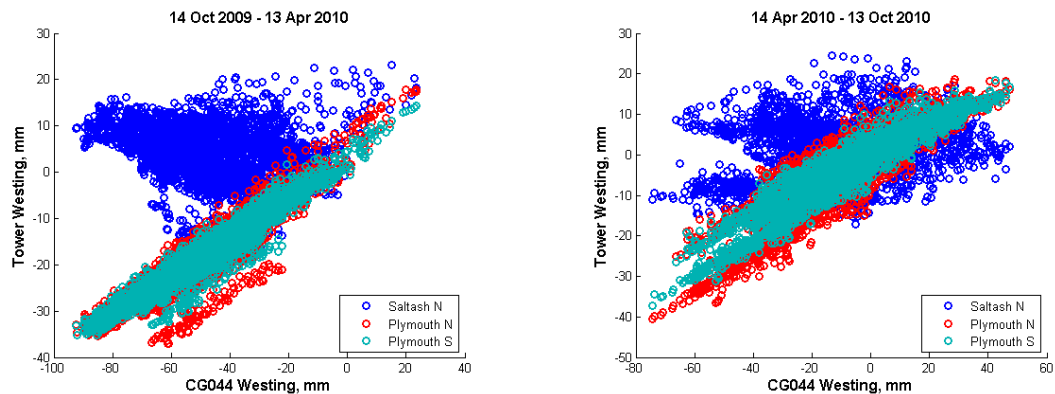
Figure 4.38: Expansion of deck vs. sway of towers. Left: Winter period. Right: Summer period.

4.8.4 RELATIONSHIPS BETWEEN TEMPERATURE AND STAY CABLE TENSIONS

Possible relationships may link the temperature of the deck and truss with the main span stay cable tensions. The strength of the relationships between deck or truss temperature and S2/S4/P2/P4 stay cable tensions were explored using the correlation coefficients between the variables.

Figure 4.39 demonstrates that the S2 and S4 tensions have a clear correlation with the deck temperature. This is likely to be a consequence of the almost perfectly linear expansion of the bridge deck with temperature. P2 and P4 tensions have a less well defined relationship with

temperature due to the previously observed time lag effects, which cause the winter data to fan out at high temperatures, and the summer data to 'arch'. There is a bi-linear trend for P2 and P4 in the FE simulation results of Figure 4.40, although it is much weaker than for the monitored results which suggests the relationship is not significantly linked to the temperature differential of the deck structure.
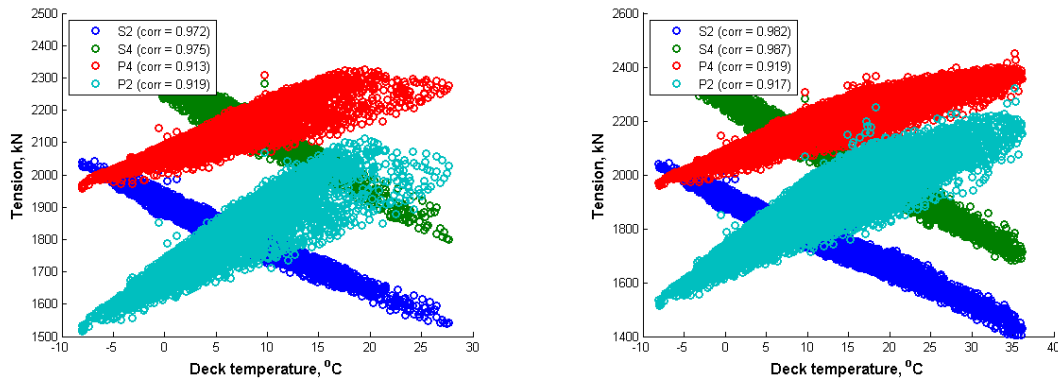
Figure 4.39: Stay cable tensions vs. deck temperature. Left: Winter period. Right: Summer period. Correlation coefficients are given in the legend
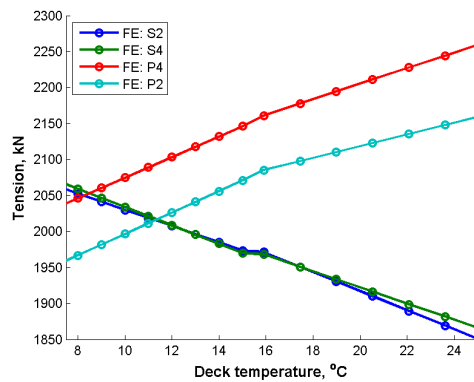
Figure 4.40: Predicted stay cable tensions vs. deck temperature.

4.8.5 REGRESSION ANALYSES INVOLVING STAY CABLE TENSIONS

4.8.5.1 *Regression analysis model formulation*

While the stay cable tensions do not seem to be directly related to the bridge temperature or structural response, they could be instead a combination of two or more variables. Regression analyses are used to quantify relationships between monitored parameters, and have been used in SHM to determine how temperature gradients and thermal inertia may affect the structural properties of the bridge (Sohn et al. 1998; Peeters & De Roeck 2000).

For example, say you had an $N \times M$ input matrix $\mathbf{X}$ which consist of M inputs over a period of N observations, and an $N \times 1$ output vector $\vec{y}$ which consists of a single output over the same N observations. The linear filter used in the regression analysis models the relationship

between the matrix of inputs $\mathbf{X}$ to the vector of outputs $\vec{y}$:

$$\vec{y} = \mathbf{X}\vec{C} + \vec{C_0} + \xi \tag{4.3}$$

where $\vec{C}$ is a vector of coefficients which weights each input, $\vec{C_0}$ is a vector containing a uniform offset, and ξ is the filter error.

The filter coefficients are determined through Least Mean Square minimisation to achieve as little error between the simulated and monitored outputs as possible. For example, suppose $\vec{C_1}$ is an initial candidate for $\vec{C}$, and all offsets are removed from $\mathbf{X}$ and $\vec{y}$ by subtracting the first observation from all rows ($\hat{\mathbf{X}} = \mathbf{X} - \begin{bmatrix} \mathbf{X}_1^T & \cdots & \mathbf{X}_1^T \end{bmatrix}^T$ and $\hat{\vec{y}} = \vec{y} - \begin{pmatrix} y_1 & \cdots & y_1 \end{pmatrix}^T$). The error between the monitored and simulated response for the i-th observation is determined by $\varepsilon_i = \hat{y}_i - \hat{\mathbf{X}}_i \vec{C_1}$. The error sum of squares $S\left(\vec{C_1}\right)$ provides a measure of the overall fit for all N observations:

$$S\left(\vec{C_1}\right) = \sum_{i=1}^{N}\left(\hat{y}_i - \hat{\mathbf{X}}_i \vec{C_1}\right)^2$$
$$= \left(\hat{\vec{y}} - \hat{\mathbf{X}}\vec{C_1}\right)^T \left(\hat{\vec{y}} - \hat{\mathbf{X}}\vec{C_1}\right) \tag{4.4}$$

The function $S\left(\vec{C_1}\right)$ is quadratic, so there must be a particular $\vec{C_1}$ which provides an overall minimum. This would be the optimum value of $\vec{C}$ to be implemented into Equation 4.3, and is provided by:

$$\vec{C} = \arg\min_{\vec{C_1}} S\left(\vec{C_1}\right)$$
$$= \left(\frac{1}{N}\sum_{i=1}^{N}\hat{\mathbf{X}}_i^T \hat{\mathbf{X}}_i\right)^{-1} \cdot \frac{1}{N}\sum_{i=1}^{N}\hat{\mathbf{X}}_i^T \hat{y}_i \tag{4.5}$$
$$= \left(\hat{\mathbf{X}}^T \hat{\mathbf{X}}\right)^{-1} \hat{\mathbf{X}}^T \hat{\vec{y}}$$

Finally, the offset of the outputs $\vec{C_0}$ is determined by:

$$\vec{C_0} = \hat{y}_1 - \hat{\mathbf{X}}_1 \vec{C} \tag{4.6}$$

4.8.5.2   Application to the structure

In this study, linear regression analysis was carried out on stay cable tensions to determine a weighted relationship with the truss, deck and suspension cable temperatures. While the stay cable temperatures were not monitored, it is expected they would behave much like the suspension cables. The model of the simulated stay cable tensions produced by the regression analysis will have the following form:

$$\vec{T} = C_d\vec{\tau_d} + C_c\vec{\tau_c} + C_{tr}\vec{\tau_{tr}} + C_0 + \varepsilon \qquad (4.7)$$

where $\vec{T}$ is a vector of the monitored tensions in the stay cable, C_d, C_c and C_{tr} are coefficients relating to the deck, cable and truss temperatures respectively, $\vec{\tau_d}$, $\vec{\tau_c}$ and $\vec{\tau_{tr}}$ are vectors of the deck, cable and truss temperatures respectively, C_0 is the offset representing the baseline tension in the stay cable, and ε is the filter error.

The coefficients determined from regression analyses performed upon the winter data are presented in Table 4.4. The largest coefficients suggest S2 and S4 tensions are determined the deck temperature, while the P2 and P4 tensions are influenced by the temperature of the truss. The remaining contribution is from the temperature of the suspension cable themselves, causing an increase in stay cable tensions due to deck sag. Figure 4.41 plots the predicted tensions based upon the formulae in Table 4.4 against the monitored stay cable tensions. For all stay cables the errors between the two are less than 5%, demonstrating a clear linear regression.

Table 4.4: Coefficients determined from the regression analysis, performed upon data collected in the winter period.

Stay Cable	Deck coefficient, C_d (kN/°C)	Cable coefficient, C_c (kN/°C)	Truss coefficient, C_{tr} (kN/°C)	Baseline stay cable tension, C_0 (kN)
S2	-17.2	4.6	0.0	1815
S4	-21.5	5.0	-0.8	2169
P4	-1.5	3.8	13.3	2201
P2	0.0	6.9	16.7	1896
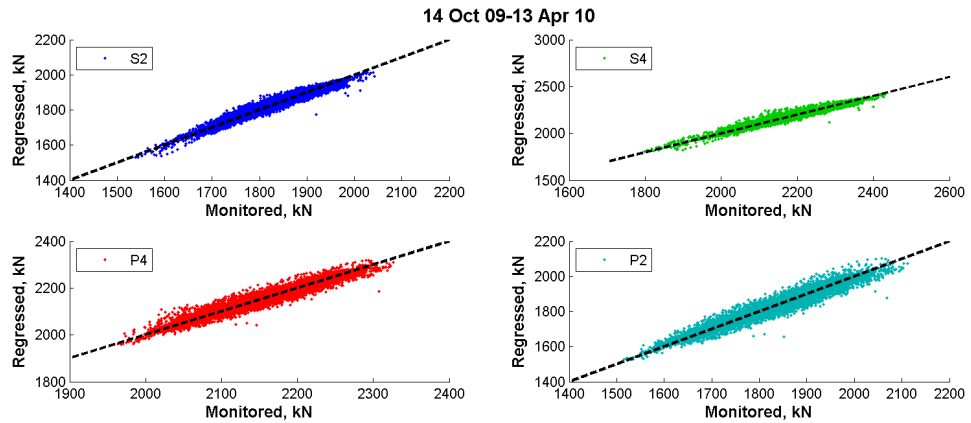
Figure 4.41: Monitored stay cable tensions plotted against regressed tensions, for the winter period.

For the summer data, the coefficients for the Saltash cable tensions in Table 4.5 are weighted towards the deck temperature, as before, however the truss temperature has a much greater influence on the overall response. The P2 and P4 tensions suggest the suspension cable temperature has more influence than truss temperature. This is reversal of contributions found in the winter data suggesting that the response of the cable plays a larger role in summer, either by the sagging shape of the bridge deck or the deflection of the towers. Regression errors in Figure 4.42 are also small, although there appears to be a skew in the relationship for P2 and P4 tensions.

Table 4.5: Coefficients determined from the regression analysis, performed upon data collected in the summer period.

Stay Cable	Deck coefficient, C_d (kN/°C)	Cable coefficient, C_c (kN/°C)	Truss coefficient, C_{tr} (kN/°C)	Baseline stay cable tension, C_0 (kN)
S2	-11.5	1.1	-4.9	1842
S4	-16.9	4.2	-4.1	2193
P4	0.2	8.7	3.5	2155
P2	-1.8	15.1	6.5	1854
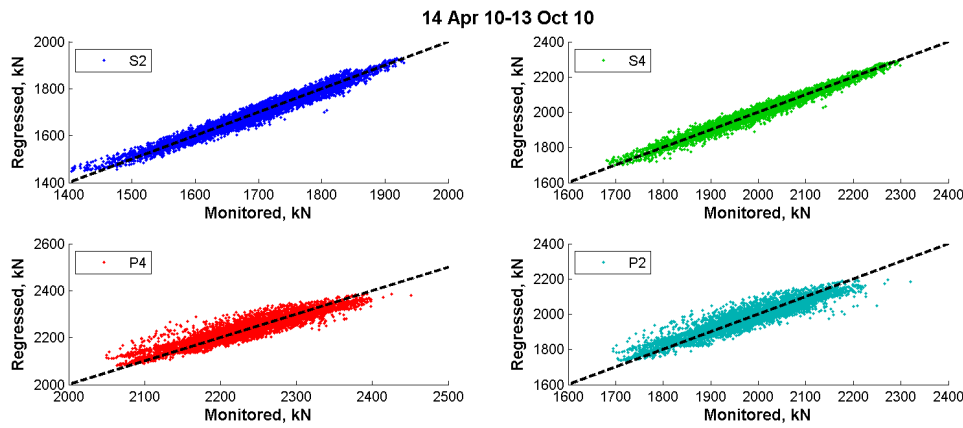
Figure 4.42: Monitored stay cable tensions plotted against regressed tensions, for the summer period.

Tensions predicted by the FE were also investigated; the coefficients are presented in Table 4.6. The FE model coefficients compare better with the monitored summer values period, where the deck and cable temperatures govern the response of the Saltash and Plymouth stay cables respectively, with the truss temperature has limited influence.

The suspension cable temperature has a larger effect on the response of the Saltash tensions in the FE simulation that it does for the monitored data, which is likely to be a consequence of using the cable temperatures as the controlled variable.

Table 4.6: Coefficients determined from the regression analysis, performed upon FE model data.

Stay Cable	Deck coefficient, C_d (kN/°C)	Cable coefficient, C_c (kN/°C)	Truss coefficient, C_{tr} (kN/°C)	Baseline stay cable tension, C_0 (kN)
S2	-23.0	18.7	-6.2	1880
S4	-16.4	11.9	-7.8	2278
P4	3.5	12.2	-0.4	1893
P2	-3.4	18.3	1.4	1700

4.9 SUMMARY

Within this chapter the response of the Tamar Suspension Bridge to temperature was considered. The recorded temperatures on the structure show diurnal variations, with the largest temperatures being on the surface of the deck. The temperature of the cable is generally lower than the deck, while the truss is the coolest overall since it is shaded from the sun. Temperature differentials were evident on the warmest days of the year, and were thus incorporated into the FE thermal analyses when simulating responses at high temperatures.

In both the monitored and predicted results the structure was observed not only to expand longitudinally, which is typical of bridge structures, but also to sag and rise vertically as a result

of elongation of the main suspension cable. For the Tamar Suspension Bridge the vertical deflections of the deck are more than twice the size of the longitudinal deflections for a similar temperature range. The tensions in the suspension cable and hangers also decrease when warmed, as a result of the elongation of the suspension cable elements.

Changes in the stay cable tensions depend on their location with respect to the direction of bridge expansion; the stay cables connecting main span to the Saltash tower slacken as the bridge expands, and vice versa for Plymouth tower. The longitudinal deflection of the towers is mainly due to the tautening of the additional stay cables, with some contribution from the thermal expansion of suspension cables. It is also observed that changes in the stay cable tensions would affect the suspension cable tensions; offsets and different variations in their tensions would develop in order to maintain horizontal force equilibrium at the tower saddles.

Some non-linearities were identified with the stay cable tensions and tower displacements, when compared against the suspension cable temperature. Dividing the data into summer and winter periods has shown that the nonlinearities occur when there are also temperature variations across the structure, caused by increased levels of solar radiation in the summer. Separating the data have also indicated that Plymouth stay cables respond differently between each season, which is seemingly due to solar radiation levels and temperature variation across the deck.

The long-term monitoring data have helped indentify intervals between the peak response of the temperatures, displacements and stay cable tensions. The time between peaking of P2/P4 tensions and S2/S4 tensions differ by 3 hours on most occasions, while the time between peak deck and truss temperatures may differ by 4 hours at most. These time gaps are more variable during the warmer half of the year, suggesting that they may be related to solar radiation, longer days or rapid warming of the structure.

The thermal analyses used for this chapter are thus unsuitable to investigate the cause of these responses, due to time dependence. Simplifying the problem as a quasi-static analysis does not account for the differing heat capacities of certain materials, or that the deck elements may more rapidly warm due to solar radiation than the shaded truss elements. These responses will be investigated in Chapter 6 by applying time varying thermal loads to the FE model.

REFERENCES

British Standards Institution, 2004. *Eurocode 2. Design of concrete structures. General rules. Structural fire design*,

British Standards Institution, 2005. *Eurocode 3. Design of steel structures. General rules. Structural fire design*,

Brownjohn, J.M.W. & Meng, X., 2008. Methods for measuring structural deflection and applications to bridge deck performance monitoring. In H.-M. Koh & F. Frangopol, eds. *The Fifth International Conference on Bridge Maintenance, Safety and Management, IABMAS2010*.

Comité Euro-International du Béton, 1993. *CEB-FIP Model Code 1990: Design Code*, Thomas Telford Limited.

Cross, E., Worden, K., Koo, K.-Y. & Brownjohn, J.M.W., 2011. Co-integration and SHM of bridges. In *8th International Workshop on Structural Health Monitoring*. Stanford, California.

Peeters, B. & De Roeck, G., 2000. One year monitoring of the Z24-bridge: Environmental influences versus damage events. In *Modal Analysis*. SEM, United States, pp.1570–1576.

Sohn, H., Dzwonczyk, M., Straser, E.G., Law, K.H., Meng, T. & Kiremidjian, A.S., 1998. Adaptive Modeling of Environmental Effects in Modal Parameters for Damage Detection in Civil Structures. In *SPIE 3325*. pp.127–138.

Watson, C., Watson, T. & Coleman, R., 2007. Structural Monitoring of Cable-Stayed Bridge: Analysis of GPS versus Modeled Deflections. *Journal of Surveying Engineering*, 133(1), pp.23–28.

Wong, K.Y., Man, K.L. & Chan, W.Y., 2001. Monitoring Hong Kong's bridges - Real-time Kinematic spans the gap. *GPS World*, 12(7), pp.10–18.

Xu, Y.L., Chen, B., Ng, C.L., Wong, K.-Y. & Chan, W.Y., 2010. Monitoring temperature effect on a long suspension bridge. *Structural Control and Health Monitoring*, 17, pp.632–652.

CHAPTER FIVE

EFFECT OF TEMPERATURE ON SUSPENSION BRIDGE PERFORMANCE - DYNAMIC

5.1 INTRODUCTION

Variations in the dynamic properties of the bridge are one of the ways engineers can identify possible damage. The environmental and operational conditions will also affect the modal response of the structure, just like the static properties.

The aim of this chapter is to show how the dynamic response of a suspension bridge is affected by temperature, and determine how this response relates to either the changes in the Young's modulus or the change in configuration of the Tamar Suspension Bridge. Fluctuations have been observed in the time series of the frequencies, which are compared with temperature data. These data are correlated, and the FE model is used to determine whether it is thermal variations of steel's Young's modulus, or the elongation of the bridge elements that drives the response. This chapter will also determine whether the suspension cable tensions have a direct relationship with the frequency of the bridge. The chapter concludes by correlating the changes in frequency of the stay cables with their changes in tension, which derive from the thermal expansion of the structure.

5.2 INSTRUMENTATION FOR LONG-TERM MONITORING OF DYNAMIC RESPONSES

This study on the response of the structure utilises the data collected by the long-term monitoring systems installed on the Tamar Suspension Bridge. Details about the robotic total station (RTS) used for tracking the static shape of the bridge, as well as the systems for recording the temperature, wind and stay cable forces, can be found in Chapter 4 of this thesis.

In addition, the University of Sheffield installed a set of uni-axial QA700 and QA750 force-balance type accelerometers in 2006 to continuously monitor the dynamic response of the structure. The location of the accelerometers are shown in Figure 5.1; three accelerometers were installed close to the centre of the main span: two monitoring the vertical acceleration on either side of the bride ("VN" and "VS"), and the third measures the lateral acceleration of the bridge ("H"). The accelerometers are affixed to the upper girder of the truss. Figure 5.2 shows the vertical and lateral accelerometers attached to the southern side of the bridge deck.

Four pairs were also clamped onto the stay cables P4N, P4S, P1N and S2S, oriented in the transverse and vertical planes of the cable (in Figure 5.3), but at the time of writing only the data collected from the P4 cables are reliable. The data are sampled at 64Hz, and like the extensometer data in Chapter 4, the accelerometer data is managed by a LabView VI and are

written into binary files on the Toughbook laptop, except the data is sampled at 64Hz and are summarized every 30 minutes rather than every 24 hours. These files are transferred via FTP to the university's server.
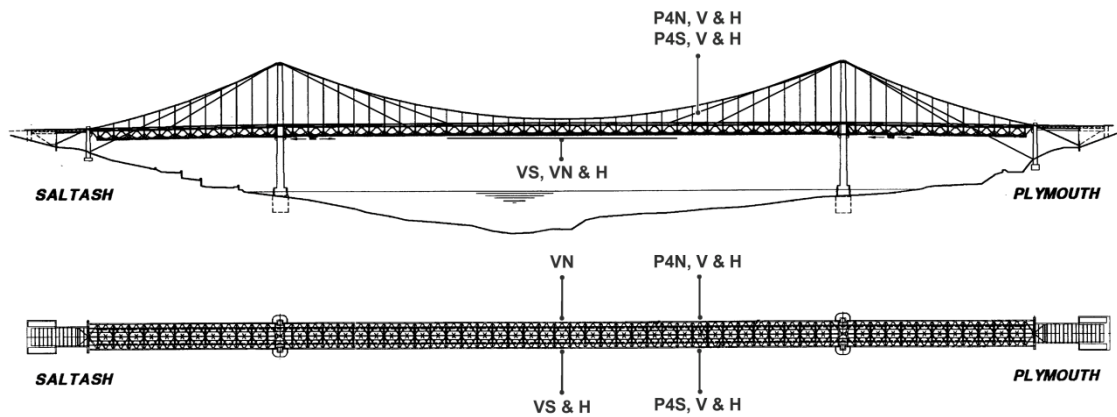
Figure 5.1: Accelerometer locations on the Tamar Suspension Bridge.

Figure 5.2: Accelerometers located on the truss.
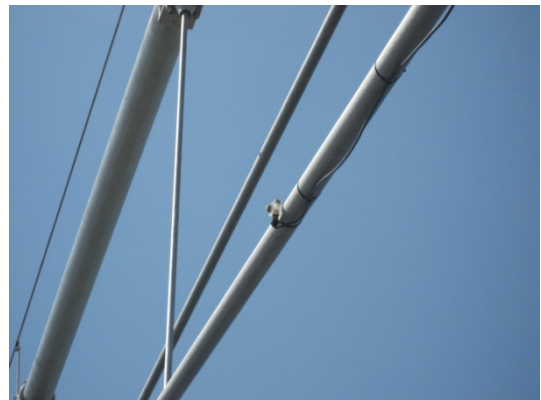
Figure 5.3: Pair of accelerometers attached to a stay cable.

The intrinsic noise of the sensors is less than 0.07mm/s² for the observed range of frequencies, and their temperature sensitivity is 0.6mm/s² per degree Celsius (Honeywell International 2005). Since the range of deck and stay cable accelerations from the Tamar Suspension Bridge are in the order of 2000mm/s², and the seasonal temperature deviation of the structure is within 50°C, the accelerometers can measure the dynamic properties of the structure with a high level of accuracy.

5.3 TIME SERIES OF FREQUENCIES AND TEMPERATURE

Modal properties are calculated from the cable and deck accelerations automatically using the data-driven stochastic subspace identification (SSI) method (Van Overschee & De Moor 1996; Peeters & De Roeck 1999), with some changes made to the acquisition and processing during the period since monitoring began. For this project the SSI procedure is called from a MATLAB

script on the university's server.

For each 30 minute file that summarises the bridge accelerations, the SSI procedure processes the data from each individual channel to determine a natural frequency and damping for each identifiable mode within that time. For example, when the channel associated with a vertical deck accelerometer is processed, a natural frequency for each identified vertical mode is produced. The frequencies and damping of the first few modes determined from each summary file are collected together in the database, so that their variation over time may be observed.

The first five mode shapes and their mean natural frequency during the monitored period are presented in Table 5.1. It is noted that the properties differ slightly from results acquired from an ambient vibration test (Brownjohn & Carden 2008), which is accounted to seasonal environmental variations on the bridge. The long-term monitoring results also show the presence of a second lateral symmetric mode, LS1b, which has a similar shape as the first lateral mode (LS1a), except the modal displacements of the deck are more pronounced in the mode shape than the suspension cable.

Table 5.1: Mode shapes and mean frequencies.

Mode	Shape	Mean $\overline{f}$, Hz
1	VS1	0.391
2	LS1a	0.472
3	VA1	0.596
4	LS1b	0.688
5	TS1	0.728

The data collected from Tamar Suspension Bridge are initially assembled into time-series to study variations in the bridge performance. Figure 5.4 shows a sample period of four days for the frequencies of the first five modes, with clear diurnal fluctuation in all five frequencies, forming troughs for most of the modes at around midday. The first lateral frequency (LS1a) in particular varies by approximately 10%.

Since the accelerometers were installed before the RTS, these changes in the time series data were the first indicator that the Tamar Suspension Bridge responded to environmental stimuli, and was the starting point for further study.
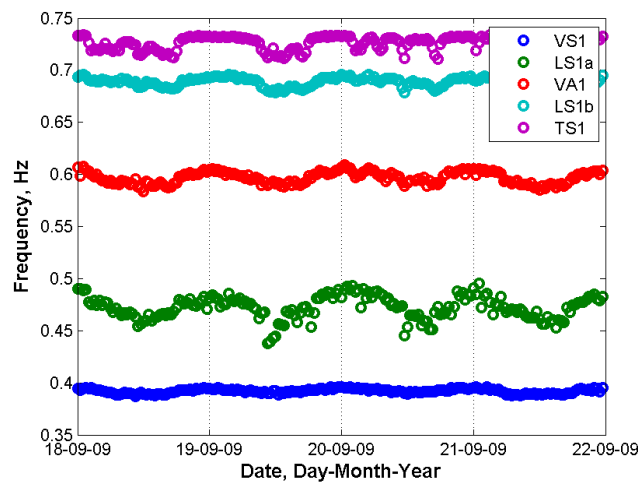
Figure 5.4: Modal frequencies over a 4 day period.

As discussed in the previous chapter the bridge is subjected to several diurnal loadings such as temperature, wind and traffic, and the first variable considered was the temperature across the structure. As shown by the typical time-series in Figure 5.5 the cable, truss and deck temperatures of the structure peak at midday, as a result of solar radiation and warmer air temperatures. It is also observed that their temperatures would be similar through the evenings, while during the day there is usually a temperature differential between the deck and the truss.
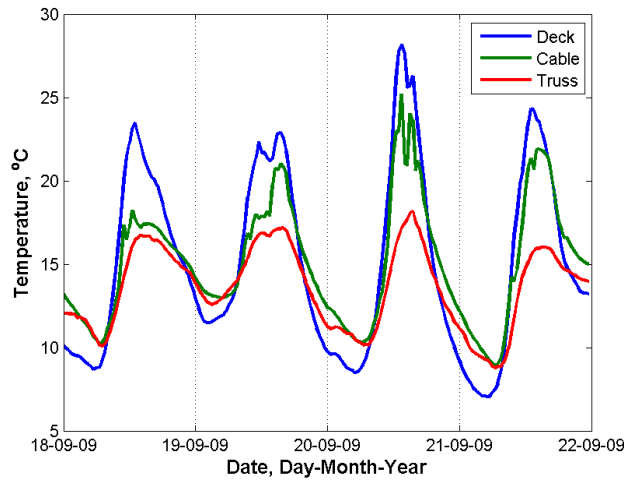
Figure 5.5: Time series of monitored deck, cable and truss temperatures over 4 days.

Figure 5.6 shows that the dynamic properties appear to have an inverse relationship with the temperature, as do the vertical static displacements. However, one of the problems when considering environmental parameters is that they are not independent. Figure 5.7 shows a different period of data, but on days when the temperature varied only slightly; webcam images show the weather to be overcast. The modal properties follow a similar pattern to the temperature, although the correlation is slightly weak on several days. On some occasions, (e.g. November 21st), there is very little variation in temperature, but still significant fluctuation in vertical mode frequencies.
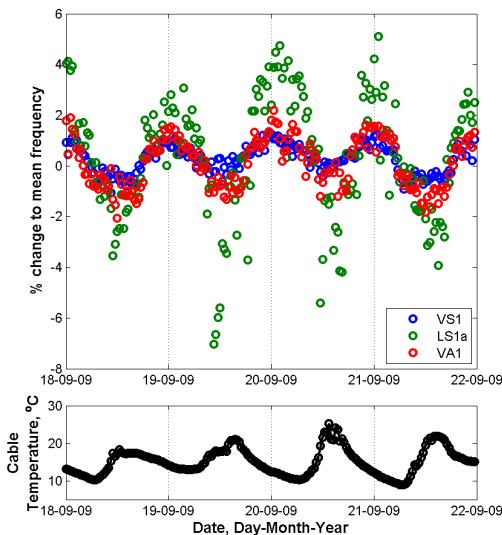
Figure 5.6: Frequency change and cable temperature time series.
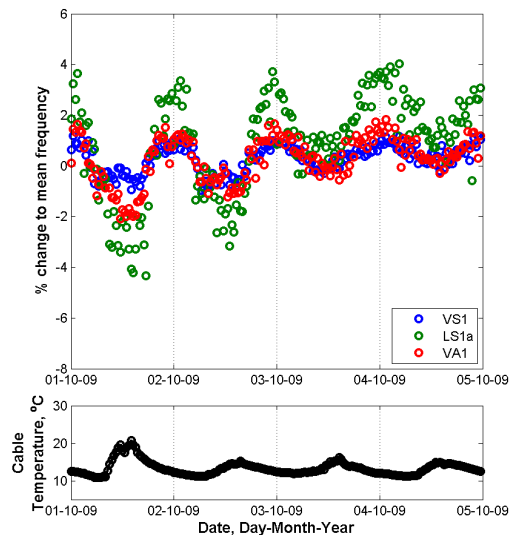
Figure 5.7: Frequency change and cable time series; with limited temperature variation.

5.4 VARIATION OF BRIDGE DYNAMIC RESPONSE WITH TEMPERATURE

5.4.1 RELATIONSHIP OF DECK FREQUENCIES TO TEMPERATURE

While the time series results suggest that some mode frequencies may be more influenced by temperature than others, for the purposes of this study only the first five modes observed by the long term monitoring will be considered for developing a comparison.

The yearly results in Figure 5.8 were categorised into two periods to identify response that may have been caused by seasonal temperature effects, such as larger temperature differentials across the deck or rapid warming. Since traffic and wind loading may also affect the dynamic properties of the structure, observed data were limited to events with wind speeds below 10 mph and a total traffic mass of 10000 kg on the bridge.

The results in Figure 5.8 demonstrate that the first five frequencies of the bridge have an inverse linear relationship with temperature. The large variation and steep slope for the first lateral symmetric mode (LS1a) suggest that it is the most affected by temperature. However, of the five observed modes it has the greatest scatter. Conversely, the first vertical symmetric mode (VS1) frequency has little scatter and a very slight slope, suggesting that the dispersal of the data in LS1a is also related to thermal effects.

While the static responses in Chapter 4 were noisier in the observed summer period compared to winter, the behaviour of the frequencies for both seasons as very similar; there is no indication of effects caused by temperature differentials, and both periods appear to have the same thermal lag effects. There are also two 'bumps' forming underneath the main group of data for the first torsional mode, TS1.
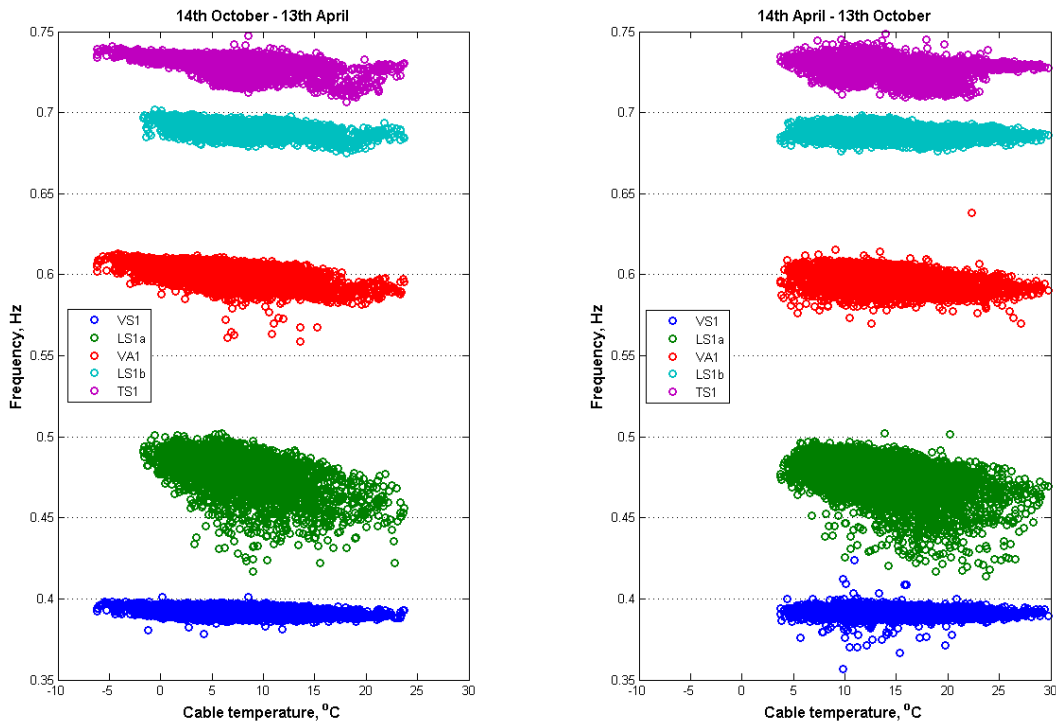
Figure 5.8: Deck frequency vs. cable temperature. Left: Summer. Right: Winter.

5.4.2 AVERAGED DAILY DECK FREQUENCIES

Averaging frequencies and temperatures to single daily values reduces the noise but leaves the trend, an approach adopted by Ding and Li (2011), and shown in Figure 5.9, which provides an idea on seasonal variations of the frequencies, since all diurnal responses have been smeared into a single value. However, the first lateral sway mode (LS1a) remains noisy compared to the other data, and the approach ignores possible effects that may be caused by thermal variations through the deck section.
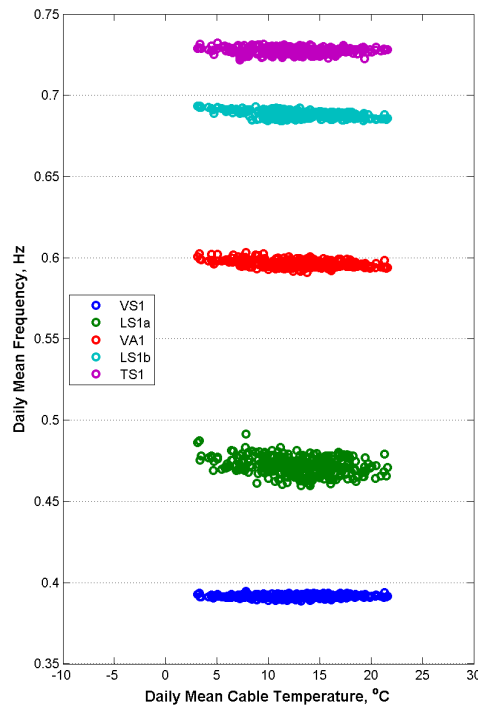
Figure 5.9: Daily averaged frequencies vs. daily averaged temperature.

5.4.3 PREDICTED FREQUENCY CHANGE BY FINITE ELEMENT MODEL

5.4.3.1 *Simulating dynamic variations caused by thermal responses on the FE model*

In cable supported steel structures there are two possible causes for a reduction in stiffness with temperature increase:

- The reduction of steel's Young's modulus when temperature increases, as listed in Table 4.2 in Chapter 4, and

- The elongation and slackening of the cables leading to lower tensions and hence reduced geometric stiffness.

Modal responses of the bridge for a range of temperature were simulated by the FE model. The procedure was similar to that described in Chapter 4 for static response, except with a subsequent modal analysis step incorporating the pre-stressing effects from the thermal and static analyses.

A similar approach to the Xia et al. investigation could be used to see how the suspension bridge response relates to diurnal variations (Xia et al. 2011). This study is mostly focusing on seasonal variations, and would be arduous if performed via several transient analyses, however it would be worthwhile seeing the transient response on the suspension bridge's

dynamic properties in the future.

5.4.3.2 *Material and thermal expansion*

Figure 5.10 and Figure 5.11 demonstrate the predicted change in frequency caused by changing material properties and elongation of the cables respectively, their responses separated to compare their influence on the overall change in dynamic response. The plots demonstrate the change in frequency with respect to values obtained at the reference temperature, which was previously stated in Chapter 4 as 17.5°C. The results are presented as a percent change since the model has not been fully updated to match the monitored results, plus it provides direct comparisons between the first seven modes observed by the FE model easier.

Figure 5.10 demonstrates a linear reduction with cable temperature. This is the expected behaviour for the material properties, since temperature causes a reduction in steel Young's modulus, and thus a reduction in the overall stiffness of the structure. For modes VS1, LS1b and TS1 in Figure 5.10 there is approximately 0.65% variation in the frequencies across the monitored 40°C range, while for modes LS1a and VA1 the variation is smaller; changing by ~0.4% over 40°C.

The frequency variation in Figure 5.11 caused by the elongation of the elements is mostly linear, although the slope for all modes increases as the cable temperature increases. The most significant change with temperature is the frequency of the lateral modes (LS1a and LS1b), which suggests that the large change in frequency observed on the prototype for the first lateral mode (Figure 5.4) may be a result of elongation and tension reduction of the main suspension cables. For the other observed modes the changes due to tension reduction are similar to those due to Young's modulus changes.

As previously stated in Chapter 4, while truss and deck temperatures are generally the same as the cable at low temperatures, above 15°C a larger temperature differential is modelled between the deck, cable and truss, since at high temperatures this was more likely than all temperatures being the same, which results from solar radiation providing more heat to the exposed area (which will be demonstrated in Chapter 6). Despite this nonlinearity the trends in both Figure 5.10 and Figure 5.11 show little variation caused by the imposed temperature differential in the deck structure. This corresponds with the monitored results in Figure 5.8, where the data is just as dispersed during summer as winter, showing little evidence that the natural frequencies are linked to the temperature gradient of the deck. The combined response is presented in Figure 5.12, with predicted frequency changes reducing by at least

0.85% over the 40°C range, and the largest response is from mode LS1b; varying by 1.93% over 40°C.
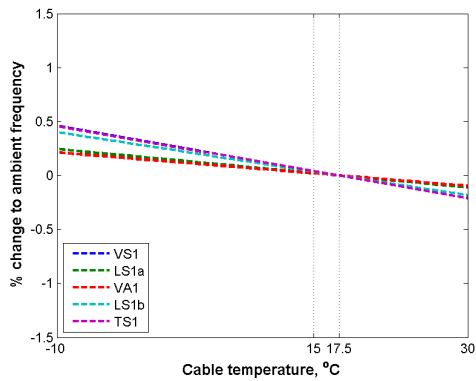
Figure 5.10: Frequency changes vs. Cable temperature, resulting only from Young's modulus variation.
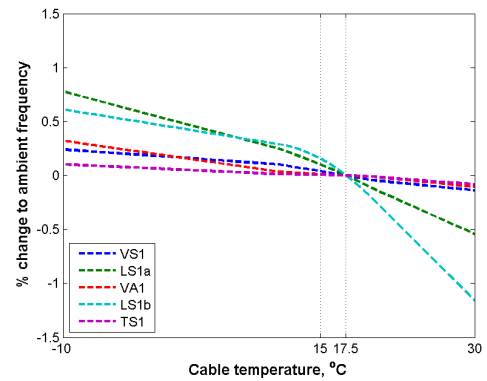
Figure 5.11: Frequency changes vs. Cable temperature, resulting only from thermal expansion.
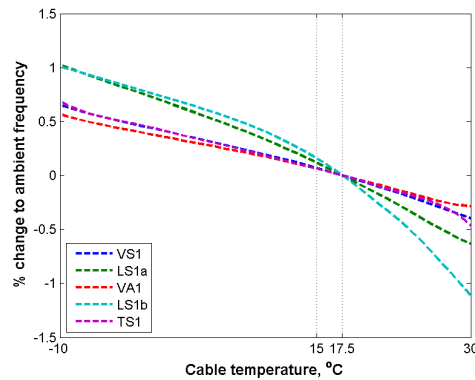
Figure 5.12: Total change in frequency with temperature, predicted from the FE model.

5.4.3.3 *Thermal effects on suspension cables only*

The variation of mode LS1a's frequency in the monitored results (Figure 5.8) and the simulated results (Figure 5.11) is considerably more significant than the other modes, which relates more to the thermal expansion of the elements than the change in material properties. If the only modified temperature in the FE model is the suspension cable, and the truss and deck remain at a constant temperature, Figure 5.13 shows that the frequency for all modes drop. This reduction is due to the slackening of the suspension cable tensions, as a consequence of the expansion of the suspension cable. Mode LS1a in particular is very sensitive to changes in the suspension cable tensions (from Chapter 3) and has the largest fall in frequency.

However, the simulated change in frequency of LS1a when all temperatures are modified (Figure 5.12) is not as large as those when only the cable temperature is adjusted; modifying all temperatures indicates a 0.041%/°C reduction to LS1a's frequency, whereas a 0.105%/°C reduction is attributed to increasing the cable temperature only. If the equivalent change in the deck and truss temperatures are considered instead (and the cable temperature remains

constant), Figure 5.14 shows that the frequency of LS1a increases, since the cable tautens with the expansion of the bridge deck. This is combined with the response caused by the slackening, thermally-expanding suspension cable to produce the behaviour seen previously in Figure 5.12. The other four modes decrease with when the temperature of the deck structure increases, since the increased thermal stresses lower the deck structure's stiffness (Equation 2.52 in Chapter 2, with negative values for T), in addition to the thermal reduction of the members' Young's modulus.
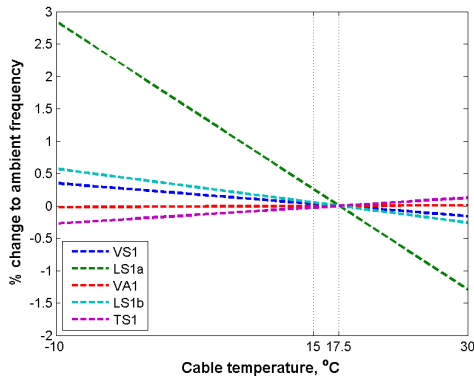
Figure 5.13: Frequency changes vs. Change to cable temperature only.
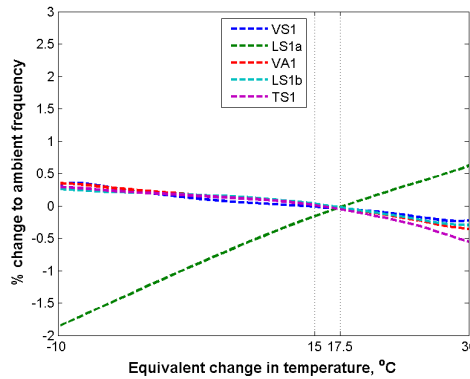
Figure 5.14: Frequency changes vs. Change to deck and truss temperature only.

5.4.3.4   Removal of the stay cables

The effect of deleting the stay cables from the FE model of the bridge is shown in Figure 5.15, where the change in modes LS1a and VA1 are as large as the changes in the other modes. The difference between the two figures suggests that the larger variation in the first two lateral modes (LS1a and LS1b) may also be due to inclusion of stay cables in the suspension bridge, since they hinder its lateral motion.
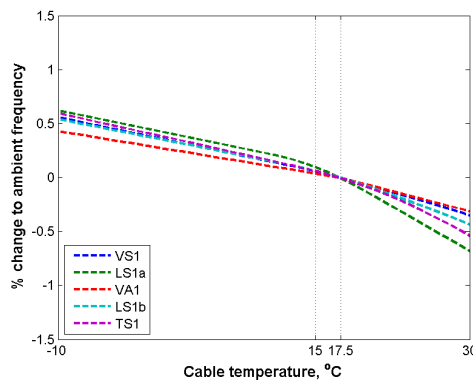
Figure 5.15: FE predicted change in frequencies with temperature, but with stay cables removed.

5.4.3.5   Comparisons between the monitored and simulated frequency changes

Even so, the variation in frequency predicted by the FE model is considerably less than the variation displayed by the monitored results. Table 5.2 shows that on modes LS1a, VA1 and

TS1 the variation reflected in the monitored data is more than twice that predicted by the finite element model, especially LS1a which differs by a factor of five.

This suggests that the model has missed some effects. The main assumption is that there are various combinations of thermal responses (in the deck, cable and towers) that are not being explored in the FE model. It may also be possible that, despite limiting the data to conditions of low traffic and wind speed, a combination of load conditions is causing this variability. The effect of traffic upon the structure is explored in Chapter 7.

Table 5.2: Approximate change in frequency vs. cable temperature for the first 5 modes.

Mode	Shape	Change in Frequency ($\times 10^{-3}$ Hz/°C)	
		Monitored	FE Model
1	VS1	0.098	0.097
2	LS1a	0.990	0.197
3	VA1	0.497	0.114
4	LS1b	0.348	0.354
5	TS1	0.307	0.191

5.5 EFFECT OF THERMAL-INDUCED STRUCTURAL RESPONSES ON THE FREQUENCIES

5.5.1 QUASI-STATIC DISPLACEMENTS

As seen in Chapter 4 there are some significant displacement variations in the bridge which result from spatial variation of temperature, particularly in the vertical plane. If the shape of the structure is altered, the dynamic properties could change as a result. The sag of the suspension cable will also change the magnitude of horizontal forces within the cable system, making the suspension cable behave more or less like a hanging cable than a taut one. These ideas were tested to see if they had any effect on the dynamic behaviour of the bridge.

Unfortunately in the same period that the RTS data were collected, the lateral accelerometer data was incorrect, so all lateral frequency estimates from that period are unreliable. Thus only half a year of data was available where both frequencies and static displacements were

monitored. This is further reduced by limiting the data to low levels of traffic and wind.

In order to provide a larger set of static displacement data, a prediction method was first trained via regression analysis on the RTS data with the temperature of the truss, deck and cable, and then used to generate the missing configuration data when the lateral frequencies were reliable. This approach is justified by the result in Chapter 4 that suggests a good correlation between the quasi-static displacements with temperature.

Figure 5.16 and Figure 5.17 demonstrate that both the predicted (based on the method above) and monitored expansion of the bridge deck at CG044 (quarter-span closest to the expansion gap) has an inverse linear relationship with the first five frequencies of the bridge. Similarly the frequencies of the bridge increases as deck rises vertically, as seen in Figure 5.18 and the FE model prediction in Figure 5.19. Since temperature is linearly related to the quasi-static displacements of the bridge and the frequencies (as seen in the previous chapter), this relationship is unsurprising.

However, the monitored results suggest that the clusters in Figure 5.8 are a result of the expansion of the bridge as follows: Troughs form in the frequency response when the bridge at CG044 expands by ~5mm, or contracts by ~40mm. At present it is not known what is causing this response, however since the frequency drops it does not seem to be caused by friction at the bearings, which would effectively stiffen the structure and cause the frequencies to rise (Moser & Moaveni 2011).
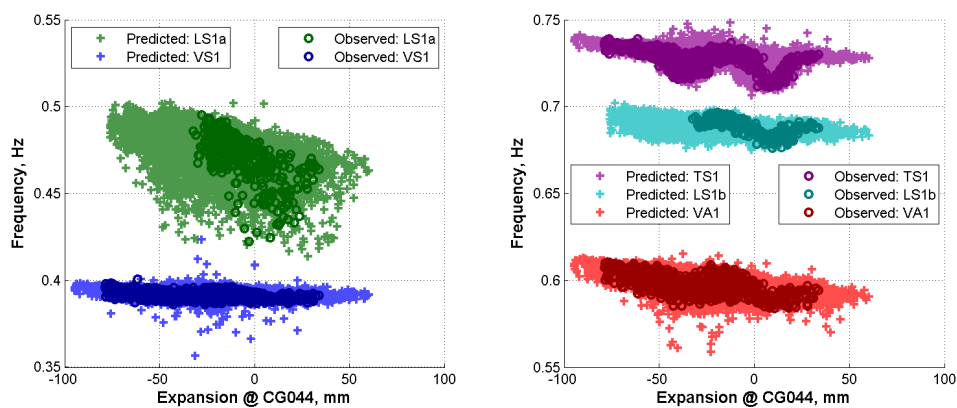
Figure 5.16: Frequency of deck vs. monitored longitudinal expansion at CG044.
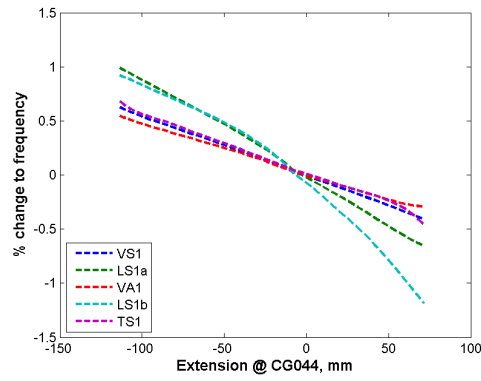
Figure 5.17: Frequency change vs. FE model expansion at CG044.
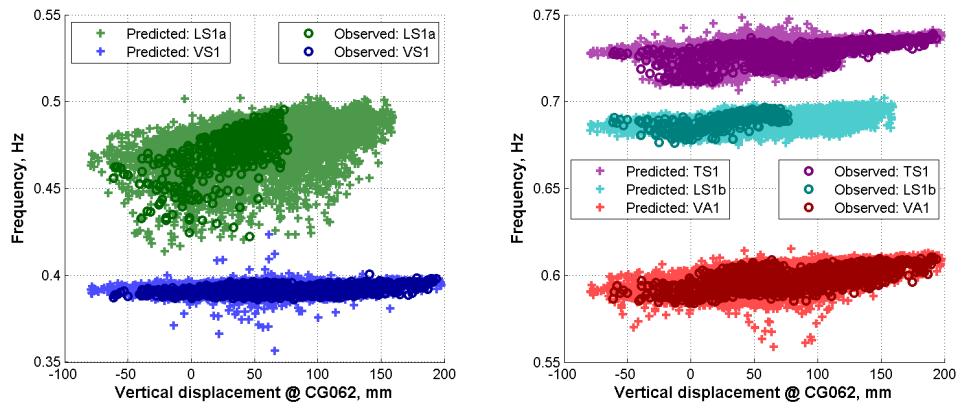
Figure 5.18: Frequency vs. monitored vertical displacement at CG062.
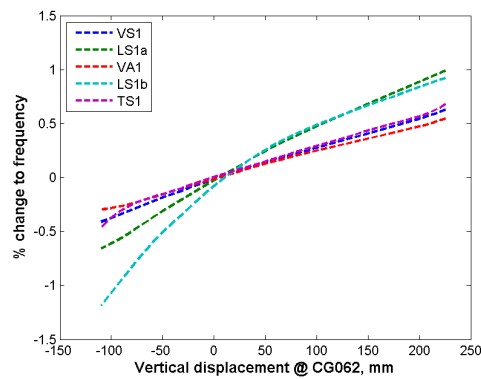
Figure 5.19: Frequency change vs. simulated vertical displacement of CG062.

5.5.2 SUSPENSION CABLE TENSIONS

While a portion of the change in frequency may be attributed to the slackening of the cable elements, the FE model predictions shown in Figure 5.20 suggest no such relationship between the tensions of the suspension cables with the bridge frequencies, and that the frequencies have more in common with quasi-static deformations of the deck structure.
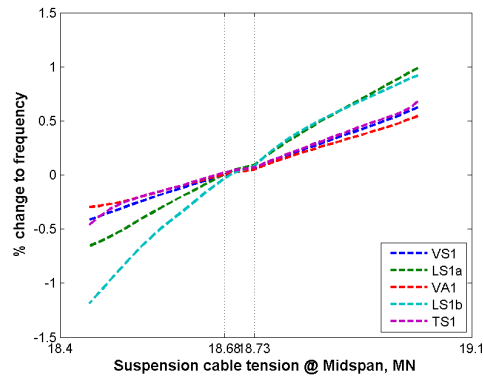
Figure 5.20: FE model suspension cable tension at midspan vs. Frequency change.

5.6 RELATIONSHIP OF STAY CABLE FREQUENCIES TO CHANGES IN TENSION

The majority of this chapter has explored changes in the frequencies of the bridge deck. Frequencies for the stay cables are also available since selected cables are instrumented with accelerometers. These frequencies are expected to be affected by changes in the stay cable tensions, which change cable transverse stiffness. For a simply supported cable, the *n*th stay cable mode's frequency is related by the equation below (Humar 1990):

$$\left(\frac{f_n}{n}\right)^2 = \frac{T}{4mL^2} + \frac{n^2\pi^2 EI}{4mL^4} \tag{5.1}$$

where T is the tension in the cable, m is cable mass per unit length, L the effective length of the cable, and E its Young's modulus.

For the Tamar Suspension Bridge stay cables, the second term in the right-hand side of Equation 5.1 is comparatively negligible. For this reason the stay cable frequencies in Figure 5.21 are practically simple multiples of the first harmonic, and were divided by the order of their respective mode to collapse them into a single plot. Vertical and lateral frequencies will also be slightly different, since vertical modes are affected by the sag of the cable (as shown by Equations 2.29 and 2.30 in Chapter 2). The frequency data for the first mode of P4S has a different gradient to the other data, since it is hindered by the attached water barrel. Otherwise all cable frequencies all have a linear relationship with the tension in the cable, suggesting they are unaffected by environmental effects other than by the changing tension in the cable.
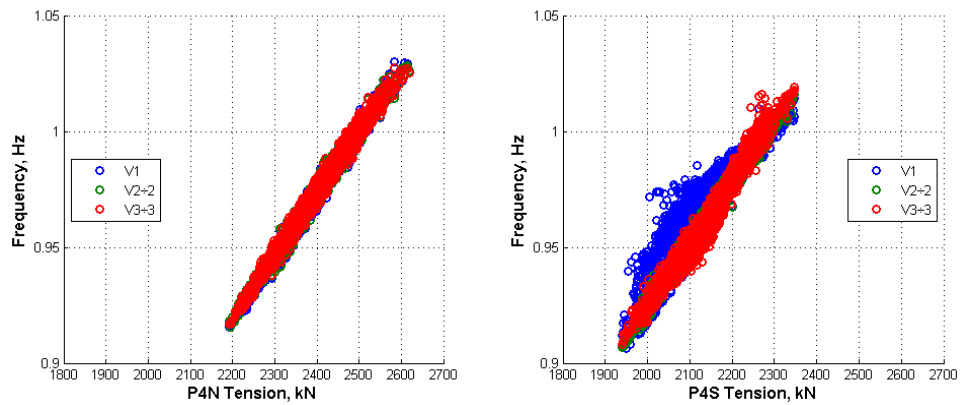
Figure 5.21: Stay cable frequencies plotted against tension (1st of March to 25th of November, 2011).

5.7 SUMMARY

Dynamic data have been collected from the Tamar Suspension Bridge for several years, and have demonstrated diurnal variations in the natural frequencies. Since the frequencies trough at midday, it was suspected that there is a significant effect of temperature on the response of the structure. After filtering out effects of wind and traffic loading, there is an inverse linear relationship between the frequencies and the temperature of the structure. For the Tamar Suspension Bridge the largest variation was on LS1a, which varied by approximately 10%. However, the correlation shows wide scatter regardless of the suspension cable's temperature, suggesting it is more susceptible to unaccounted effects than the other modes.

The relationships between frequencies and temperature were confirmed with an FE model of the bridge, although this showed the change in response to be less than observed in the monitoring. According to results from the FE model, the thermal elongation of the structure causes a similar change in frequency as the variation in steel's Young modulus caused by temperature. The frequency of the lateral sway modes were more affected by the thermal expansion as a consequence of their sensitivity to variations in the suspension cable tensions.

Since temperature affects the quasi-static configuration of the structure, the frequencies share a similar linear relationship with the thermal expansion of the structure. There are also two troughs in the monitored frequencies of three modes for specific values of deck expansion. These responses are unlike other reported non-linearities attributed to expansion gaps, as they reflect a reduction of the structure stiffness rather than an increase.

Changes in the frequency of the stay cables were also observed, but these were attributed directly to the change in tension of the stay cables, which would be caused by the movements of the deck and elongation of the stay cables.

REFERENCES

Brownjohn, J.M.W. & Carden, P., 2008. Real-time operation modal analysis of Tamar Bridge. In *IMAC-XXVI: Conference & Exposition on Structural Dynamics*. Orlando, Florida, USA, pp.1–8.

Ding, Y.-L. & Li, A., 2011. Temperature-induced variations of measured modal frequencies of steel box girder for a long-span suspension bridge. *International Journal of Steel Structures*, 11(2), pp.145–155.

Honeywell International, 2005. Q-Flex® QA-750 Accelerometer data sheet. Available at: http://www51.honeywell.com/aero/common/documents/myaerospacecatalog-documents/Missiles-Munitions-2/QA750_DataSheet.pdf [Accessed October 4, 2012].

Humar, J.L., 1990. *Dynamics of structures* 1st ed., Prentice-Hall, Inc.

Moser, P. & Moaveni, B., 2011. Environmental effects on the identified natural frequencies of the Dowling Hall Footbridge. *Mechanical Systems and Signal Processing*, 25(7), pp.2336–2357.

Van Overschee, P. & De Moor, B., 1996. *Subspace identification for linear systems*, Kluwer Academic Publishers.

Peeters, B. & De Roeck, G., 1999. Reference-based stochastic subspace identification for output-only modal analysis. *Mechanical System & Signal Processing*, 13(6), pp.855–878.

Xia, Y., Xu, Y.L., Wei, Z.-L., Zhu, H.-P. & Zhou, X.-Q., 2011. Variation of structural vibration characteristics versus non-uniform temperature distribution. *Engineering Structures*, 33, pp.146–153.

CHAPTER SIX

EFFECT OF SOLAR RADIATION ON SUSPENSION BRIDGE PERFORMANCE

6.1 INTRODUCTION

As identified from Chapter 4, arbitrarily applying temperatures to the finite element (FE) model can determine the thermal displacements of the bridge, but cannot recreate the full range of responses observed. This is because there are many combinations of temperatures across the structure, which may cause different elongations of the elements and hence affect deformed shapes of the structure. Some responses observed in Chapter 4 are a result of transient effects and cannot be replicated via a static analysis. For example, the observed nonlinearities with the stay cable tension and the poor correlations involving the monitored tower deflections suggest some time dependency.

Different regimes of thermal loading will also be experienced: solar radiation and air temperatures are lower during winter than in summer, and as a result the structure behaves differently. So far these responses have been observed from data from long term monitoring systems. Computer simulations using mathematical models have only considered single days of response, thus not demonstrating variations caused by differing seasonal effects.

Before transient thermal response mechanisms were studied closely by structural engineers, temperature effects were represented through a series of empirical equations (Churchward 1981; Hirst 1984), using thermal loads as variables. However their application is limited to bridges of a similar construction and similar climate. Ho and Liu (1989) were among the first to explore transient effects from monitored thermal loads, using 207 days of data collected from a concrete bridge in Hong Kong, with calibration of simulated response with a one dimensional finite difference model. There are a few other studies that have considered the thermal response of a concrete structure (Moorty & Roeder 1992; Minhoto et al. 2005; Xia et al. 2011), commenting on the temperature gradient through structure depth, as well as thermal lag between the top and bottom faces, which are attributed to the shading of the structure and the low thermal conductivity of concrete.

Several studies have observed the thermal response of steel structures. Tong et al. (2001; 2002) performed sensitivity studies on a numerical model to determine the material properties of a steel box section, and observed how the temperature gradient was affected by various beam profiles. Yim and Wang (2010) identified a temperature gradient through the deck of the Zhanjiang Bay (cable stay) Bridge from results collected by their monitoring system. The effect of heat flow on suspension bridge spans and abutment has been previously studied by Xia et al. (2012). Their investigation uses results collected from Tsing-Ma Bridge during a single day, both from monitored data and FE models.

As remarked in the Tsing-Ma Bridge investigation, from the thermal response viewpoint, a suspension bridge is a much more complex system than a typical bridge; the various members have different thermal responses due to their various material properties, shape and size, as well as their location in the structure. Structural responses are also coupled, making it difficult to link specific causes and effects: cable slackening could be caused by thermal expansion or relative movement between deck and tower(s). Thermal analysis of the Tamar Suspension Bridge is further complicated by the combined effect of the suspension and additional stay cables linking deck and towers, as well as the shading of the truss by the cantilevered lanes.

In this investigation, the work from Chapter 4 is continued to cover observation of time dependent thermal effects on the structure, by analysing long-term monitored responses from the bridge itself, as well as through FE transient analyses. However unlike most investigations, the transient thermal effects are analysed for 5 days in each of the 12 months of a single year, rather than for a single day. This approach should cover seasonal effects on the thermal response, resulting from differing ranges of air temperature and applied solar radiation.

6.2 HEAT TRANSFER ANALYSIS

6.2.1 HEAT TRANSFER EQUATIONS

The temperature field T of a cross section at time t may be expressed by Poisson equation models for the 3D transient heat flow process (Minhoto et al. 2005), representing the heat travelling through a homogenous solid via conduction:

$$k\left(\frac{\partial^2 T}{\partial x^2} + \frac{\partial^2 T}{\partial y^2} + \frac{\partial^2 T}{\partial z^2}\right) = \rho c \frac{\partial T}{\partial t} \tag{6.1}$$

where x, y and z are Cartesian coordinates on the bridge, k the thermal conductivity, ρ the density and c the specific heat capacity of the material. At a boundary, the heat flow in a direction normal to the surface is expressed as

$$k\frac{\partial T}{\partial n} + q = 0 \tag{6.2}$$

where n is the normal to the boundary surfaces and q is the heat flow at the boundary. For a bridge surface q consists of convection q_c, thermal radiation emitted from the surface q_r and solar irradiation q_j (Elbadry & Ghali 1983; Branco & Mendes 1993):

$$q = q_c + q_r + q_j \qquad (6.3)$$

The heat flow caused by convection leaving the surface q_c is determined by:

$$q_c = h(T_{sur} - T_{air}) \qquad (6.4)$$

where T_{sur} and T_{air} are the surface and air temperature respectively, and h the convection coefficient. The heat radiated from the surface q_r is dependent on its emissivity coefficient ε:

$$q_r = \varepsilon \sigma T^4 \qquad (6.5)$$

Where σ is the Stefan-Boltzmann constant, which is the total energy radiated from a black body per unit surface area, per unit time. Finally, The amount of solar radiation absorbed by a bridge surface (Minhoto et al. 2005; Xia et al. 2012) is

$$q_j = -\alpha J_0 \qquad (6.6)$$

where α is the solar radiation absorption coefficient of the surface material (between 0 and 1), and J_0 is the total daily irradiance on the bridge surface. An estimate for the solar radiation for any day of the year was calculated using the Johnson-Woodward model (Johnson et al. 1995; Woodward et al. 2001), which was originally intended for agricultural purposes. The model was chosen due to recommendation by Rivington et al. (2005), as well as for its simplicity. The formulae used to calculate the radiation are found in Appendix A.

6.2.2 ESTIMATION OF CLOUD COVER

In order to approximate the intensity of solar radiation on the deck, values for the cloud cover at the observed time are required. While data was available from Plymouth Airport (Roborough), the values were inadequate, as elaborated later. Thus an alternate method was required, so that FE simulated structural temperatures would be similar to the monitored values.

In order to provide an idea of the calculated cloud cover values, two dates were chosen. Days were chosen according to whether the webcam images (e.g. Figure 6.1) show either a completely cloudy day (example, January 10th, 2010), or a completely clear day (example, July 8th, 2010). There are several indicators that suggest the degree of cloud cover, the most obvious being the brightness of the images; the fog making the image from January appear duller than the image from July. It is also noticed that the shadows of the bridges have a crisp

edge when they are under direct sunlight. If image recognition software were available, these would be the features it would be trained to identify.

Figure 6.1: Webcam images taken at 11:59am on January 10th (left) and the July 8th (right) at the top of the Plymouth Tower.

Figure 6.2 shows the temperatures recorded from sensors on the surface of the cable, truss and deck for these two dates. The large difference between the deck and cable temperatures on the July 8th compared to the truss and the air temperature at midday demonstrates that heat from solar radiation contributes significantly to the temperature of the irradiated members. The truss temperature also peaks at midday, but is nowhere near the same magnitude as the deck, since it is mostly shaded by the cantilever. In comparison the bridge on the January 10th receives very little sunlight due to the overcast conditions, and as a result the monitored members are mostly the same temperature since they are warmed only by the surrounding air. This shows that the thermal gradient of the structure should be linked to the cloud cover, so an approximation of cloud cover could be determined from the difference in temperature between the top and bottom halves of the deck structure.
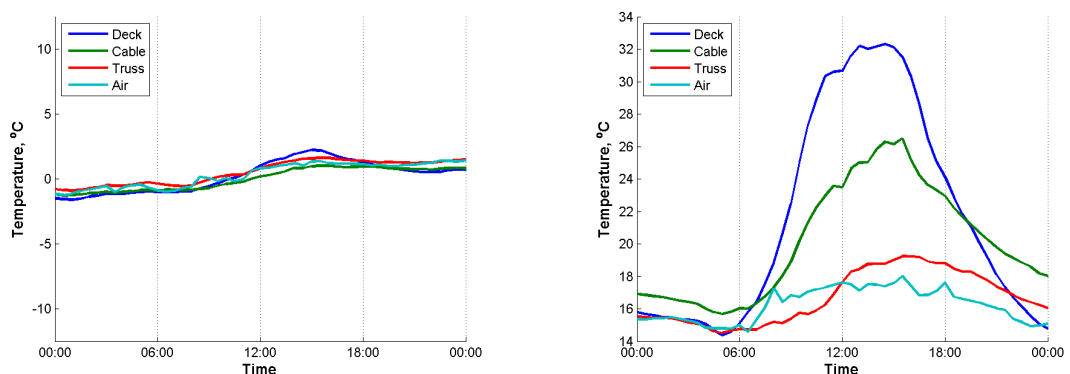
Figure 6.2: Temperature time histories. Left: 10/1/2010. Right: 8/7/2010.

The first step in developing the approximation is to normalise the temperature difference between the top of the deck and the base of the truss at a particular time $\Delta T_{b,t}$ by using the temperature of an element unaffected by solar radiation $T_{a,t}$, so that the magnitude of the

resultant variable $\overline{\Delta T_{b,t}}$ is less dependent on seasonal variations. For the Tamar Suspension Bridge, $T_{a,t}$ was taken as the truss temperature.

$$\overline{\Delta T_{b,t}} = \frac{\Delta T_{b,t}}{T_{a,t}} \tag{6.7}$$

The temperatures are converted into degrees Kelvin to avoid a zero value of $T_{a,t}$, since this would develop factors tending towards infinity during the winter.

Diurnal variations need removal from the data, since this behaviour already features in the solar radiation prediction model as a sinusoid (see Equation A.12 in Appendix A.2). Despite experimenting with high-pass Butterworth filters, it was found that using a simple moving average over a 21 hour interval ($r+1$) would remove the daily fluctuations to an acceptable degree:

$$\overline{\Delta T_{b,t}}' = \frac{\overline{\Delta T_{b,t-r/2}} + \cdots + \overline{\Delta T_{b,t}} + \cdots + \overline{\Delta T_{b,t+r/2}}}{r+1} \tag{6.8}$$

where $\overline{\Delta T_{b,t}}'$ is the modified value of $\overline{\Delta T_{b,t}}$. The resultant peaks in the smoothed data appear at similar times as clear spells in several webcam images.

The final step is to normalise these values between 0 and 1 to convert them into an equivalent cloud cover factor, f_{cc}. This was also performed over a roaming interval, with the data normalised to the maximum and minimum values within a specified range. This method assumes that within the interval there is at least one instance where the sky is completely cloudless ($f_{cc} = 0$), and one instance where the sky is totally covered in cloud ($f_{cc} = 1$).

$$f_{cc,t} = \frac{\overline{\Delta T'_{b,t}} - \mathbb{T}_{\min}}{\mathbb{T}_{\max} - \mathbb{T}_{\min}} \tag{6.9}$$

where $f_{cc,t}$ is the predicted cloud cover at time t, and $\mathbb{T}_{\min}$ and $\mathbb{T}_{\max}$ are the minimum and maximum $\overline{\Delta T'_{b,t}}$ within the observed interval:

$$\mathbb{T}_{\min=}\min\left[\overline{\Delta T'_{b,t-s/2}}; \cdots ; \overline{\Delta T'_{b,t}} \cdots ; \overline{\Delta T'_{b,t+s/2}}\right] \tag{6.10}$$

$$\mathbb{T}_{\max=}\max\left[\overline{\Delta T'_{b,t-s/2}}; \cdots ; \overline{\Delta T'_{b,t}} \cdots ; \overline{\Delta T'_{b,t+s/2}}\right] \tag{6.11}$$

It was found that an interval, s, of 60 days provides acceptable values for cloud cover. This interval also ensures cloud cover levels are determined on a month-by-month basis, since the temperature difference is larger during the summer, compared to winter.

Figure 6.3 presents the cloud cover results for the two days seen previously, as predicted by the method described, alongside results monitored from Plymouth Airport which were also available for use. The cloud cover method produces the intended results: cloud cover factors close to 1 in the January data, and low cloud cover at midday in the July data. The data collected from Plymouth Airport on the other hand does not provide an acceptable representation of the cloud cover seen in the webcam images. Apart from having just three absolute values (0.25, 0.5 and 0.9), they may also be incorrect for the Tamar Suspension Bridge location: the airport data on January 10th suggests times when there was little cloud, while the webcam images show the bridge (which is at a lower elevation) was surrounded by fog for the whole day. It is for this reason that the developed cloud cover method was used when monitored results were available. While the levels of cloud cover may not be correct during the late evening/early morning period, these periods generally occur overnight, so would have a very limited effect on the solar radiation calculations.
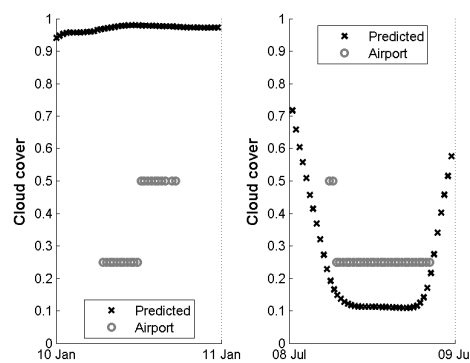
Figure 6.3: Comparison between airport-monitored and predicted cloud cover

6.2.3 APPLIED SOLAR RADIATION

Using both the temperatures monitored from the actual structure, approximate cloud cover levels and the method described in the Appendix, an estimate for the solar radiation applied to the bridge was available. Figure 6.4 presents two samples of the simulated solar radiations; one for five days in June, the other for five days in December. The applied solar radiation during the summer months is of a higher magnitude compared to winter; the largest value determined for the June samples (463W/m²) is more than 4 times the magnitude for the equivalent for December (108W/m²). In June daylight lasts 16 hours, compared to 8 hours in December, so the bridge is irradiated by the sun for a much longer period.

The orientation of the sun would also cause South faces of the tower to be warmed during one half of the day, while the North faces are in their own shade and warmed indirectly from adjacent surfaces. In the solar radiation model, the shading on one side of the tower is determined by reducing the direct beam component by a factor that depends on the pitch and orientation of the surface, as well as the position of the sun. The formulae for determining this factor are given in Section A.3 of the Appendix. The simulated results for the radiation on the East and West faces are also shown in Figure 6.4, the radiation on the East face of the towers peak at mid-morning, while on the West face they peak mid-afternoon.

All three radiation profiles contain the same contribution of diffuse radiation, as represented by the solid black line on the plots. When the sun is not directly irradiating either the East or West face (East during the afternoon, West in the morning), the overall solar radiation comes from the diffuse contribution alone.

For some days the diffuse radiation is relatively strong and contributes most of the overall radiation, such as on the 10th of June and 11th of December. This is due to high levels of cloud cover, which increases the dispersal of the light. This is elaborated in the Appendix; Equation A.10 in particular.
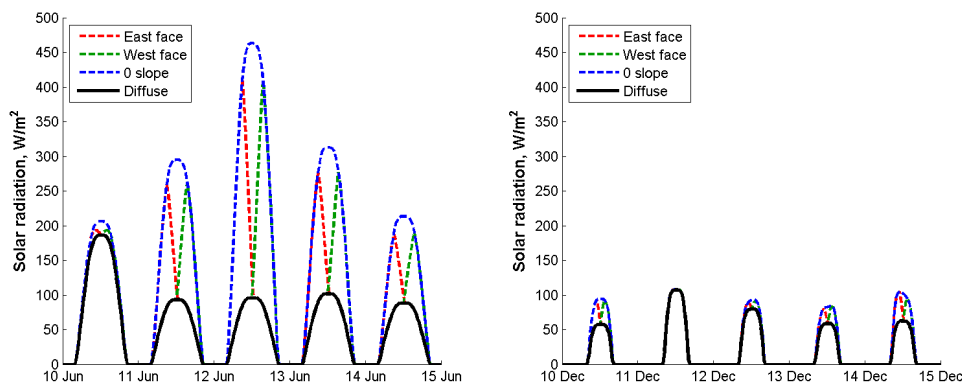
Figure 6.4: Simulated radiation on bridge. Left: 10-15 June. Right: 10-15 December.

The radiation loads will be applied to the orthotropic deck and tower faces in the FE model, which will also be subjected to air convection and surface radiation. Shading on the underside of a bridge could be approached in a similar way as the studies by Liu et al. (2012) on an 'H' shaped member. They incorporated a time dependent algorithm to identify which elements in a model were in the shade of its flanges. While this approach would be ideal for considering how the shading of the cantilevers affects the truss, it was not used in the current investigation, since radiation effects on the line elements that make up the truss would be very difficult to implement for the complex arrangement of the Tamar FE model.

152

6.3 CALIBRATION OF FE MODEL PROPERTIES

The next stage is to ensure that the response from the FE model provides a good match with results found during monitoring. The thermal response of the FE model was calibrated (trained) to daily samples of temperature data recorded from the actual structure. This allows for an adjustment for uncertainties, such as the absorption, emissivity and convection coefficients of the surfaces in the model.

To see how the bridge responds to high and low levels of solar radiation, the dates were chosen by their cloud cover: one day with a completely clear sky, one with very little sunlight. Thus the two dates used previously to determine cloud cover (January 10th and July 8th, 2010) were used to ensure the thermal response of simulated bridge has a close enough match to the monitored data.

One limitation is the inability to apply radiation to line elements such as the suspension cables, since they have no surface area. While the monitored cable temperature could be used, it was felt that a complete solar radiation analysis should include simulation of the suspension cable, since the quasi-static vertical displacements of the structure were shown in Chapter 4 to be highly dependent on the temperature of the cable.

The application of radiation to the Tamar Suspension Bridge model will be applied in two stages; the first step derives the thermal response of the suspension cable cross-section, the second is to a model of the bridge itself, to determine both its thermal and static response.

6.3.1 SUSPENSION CABLE THERMAL PROPERTIES

Each 0.72m diameter suspension cable consists of 31 steel locked-coil wire ropes. The wrapping of the cable is made from 9-gauge galvanized wire coated in zinc chromate paste. For this investigation the material properties were taken to be the same as steel.

The suspension cable cross section model presented in Figure 6.5 is made up of PLANE55 elements; 2D thermal solid elements with 3 or 4 nodes. The outside of the cable is covered by SURF151 elements, which are used to apply the monitored air temperature on all surfaces to effect surface convection and radiation, as well as to apply the solar radiation as a heat flux on the topmost side. In addition, neighbouring nodes in the models, such as within 1cm of the wrap or adjacent wires, are thermally coupled to transfer heat between the wires and the wrap.
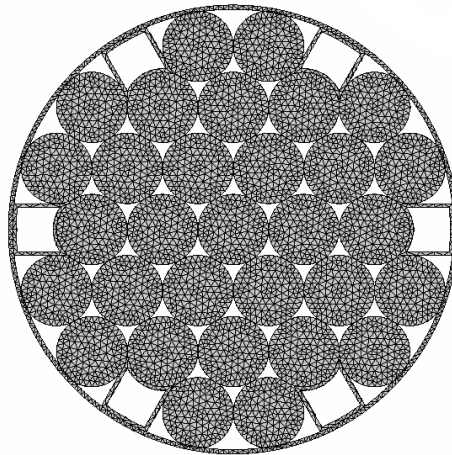
Figure 6.5: FE model of cable cross section.

The thermal material properties of the suspension cable were first trained so that the simulated temperature results coincided with monitored data collected on the clear day (July). The temperature sensor on the suspension cable is located on the southern face of the wrapping, which is directly irradiated by the sun. Due to this, the node at the midpoint of the radiated face will be used to compare the temperature of the FE model with the monitored results. However, the temperature of the cable used in the full bridge model will be an average of the temperatures at the centroid of the wires, since this better represents the temperature of the whole cable section and its thermal expansion.

Through a series of tests it was determined that the absorption and convection coefficients of the wire were the most influential parameters governing the thermal behaviour of the cable: the convection coefficient determines the time when the peak temperature occurs, and the absorption coefficient affects the amplitude of the simulated temperature. These thermal properties are presented in Table 6.1, assuming a linear relationship with temperature between -20°C and 100°C.

Table 6.1: Cable thermal properties.

Property	Wrap		Wires	
	@ -20°C	@ 100°C	@ -20°C	@ 100°C
k , thermal conductivity (W/m°C)	54.7	50.7	54.7	50.7
c , heat capacity (J/kg°C)	416	488	416	488
h , convection coefficient (W/m²°C)	18.5		-	
ε , emissivity coefficient	0.8		-	
α , absorption coefficient	0.75		-	

By adjusting each variable a solution was produced where the peaks in the simulated and monitored results coincided, as shown by Figure 6.6. However, several discrepancies exist between the two results. The first is that the temperature of the simulated results rises an hour before the monitored results, since daylight hours should begin at almost 04:30 on July 8th. The second is that monitored cable temperature drops sharply after 16:00, which is not observed in the simulation. From inspection of the webcam results, it appears the weather became slightly misty during this period, so it was reasoned the low levels of solar radiation and heat loss due to air moisture caused the drop in cable temperature, and that the results for the morning were acceptable. It is observed that the cable temperature never matches the air temperature, since it takes longer than 12 hours for the cable to completely cool down; the difference in temperature during the early hours of the morning is due to residual heat in the cable from the previous day.

The comparison for the cloudy day is shown in Figure 6.7, however since the monitored cable temperature is already similar to the surrounding air temperature, the applied solar radiation causes a minor peak in the FE results at midday. Since the error is 4°C at most, and the results from the clear weather provided reasonable results, the material properties for the suspension cable identified during the training stage were deemed acceptable.
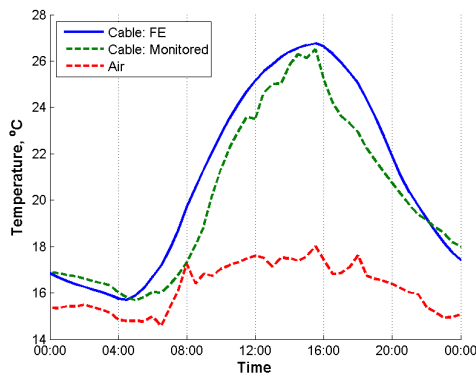
Figure 6.6: Cable and air temperature, for 8/7/2010.   Figure 6.7: Cable and air temperature, for 10/1/2010.
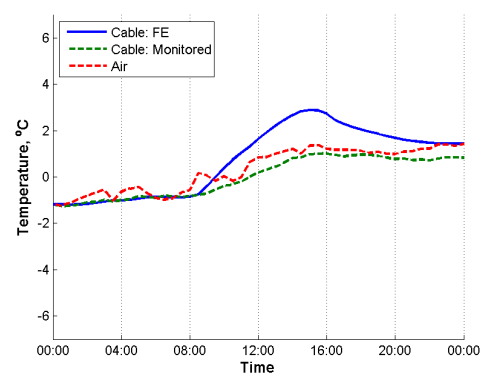
The temperature gradient of the wires through the suspension cable section is shown in Figure 6.8, using thermal boundary conditions provided by the assumed clear sky data (in July). During the early hours of the morning the wires are all the same temperature and are still cooling down from the previous day. At approximately 04:30 the wires begin to heat up, since the sun has risen above the horizon and the wrapping becomes warmed by both the solar radiation and air convection. This is also the time when a temperature differential begins to develop across the cable cross-section; the warmest wires are located on the irradiated edge of the suspension cable. Since the coolest wire is on the opposite side of the section, it appears

most of the internal wires conduct the heat from the irradiated side very rapidly across the whole section, rather than being warmed by the air temperature. At 16:00 the peak temperature in the cable is reached, with a simulated temperature difference of 2.55°C across the cable.

Beyond 16:00, the solar radiation and surrounding air temperature levels are too low to maintain the heat within the suspension cable, so the external wires cool by air convection and radiating heat through the side of the cable, At 20:00, when the wrapping is no longer irradiated by the sun, there is only 0.27°C temperature variation across the cable, since all heat in the internal wires is lost very quickly to the wrapping by conduction. This limited variation in temperature continues through the evening.
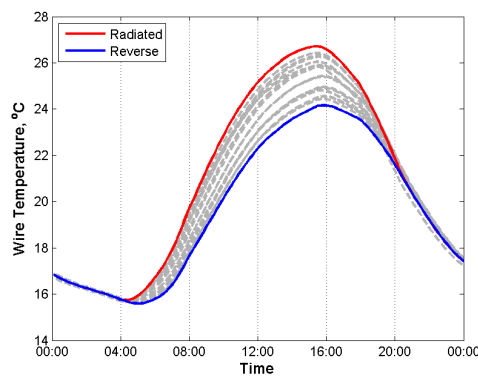
Figure 6.8: Temperature of wires across the cable cross-section, on July 8th.

6.3.2 COMPLETE BRIDGE MODEL THERMAL PROPERTIES

A similar calibration process was performed with the deck to ensure that both the thermal and quasi-static response of the FE behave as the monitored response. Heat capacities, expansion and conduction coefficients were adopted from the thermal studies in Chapter 4. Since the thermal behaviour of asphalt and steel is radically different, the properties of the deck were adjusted, since they are modelled as a single SHELL63 element, rather than separate layers. The parameters used in this procedure are given in Table 6.2; the gross density and thickness of the deck are used to calculate a smeared heat capacity for both the steel deck and asphalt on top. Temperature data for the concrete towers was unavailable, so the concrete absorption and convection coefficients were taken from equivalent values on Tsing-Ma Bridge (Xia et al. 2012) since they could not be calibrated from the Tamar Suspension Bridge towers. Thermal properties of the asphalt were also adopted from the same paper.

Table 6.2: Parameters used to determine smeared heat capacity of orthotropic deck components.

Material	Deck thickness, w (m)	Heat capacity, c (J/kg°K)	Density, ρ (kg/m³)	$w \times \rho \times c$ (J/m²K)	Gross heat capacity (J/kg°K)
Asphalt	0.038	960	2100	76.6×10^3	-
Bitumen	0.002	-	-	-	-
Deck plate	0.013	440	7800	46.6×10^3	-
Gross properties	0.053	-	3419	123.2×10^3	680

Simulation of convection effects on the truss would be complicated by its composition of beam elements of different lengths and section properties. Due to the added complexity of the analysis, the FE model does not simulate the thermal behaviour of the truss. Instead the monitored truss temperatures are applied to the nodes on the lower stringers of the truss, since they directly represent its thermal response. This temperature is usually similar to the air temperature, so it is expected that the lower half of the truss is mainly heated by the surrounding air, and intermediate elements between the deck and the lower stringers of the truss receive additional heat via conduction from the deck.

Like the cable, the deck properties were first calibrated to the monitored temperatures: the convection coefficient of the bridge deck was adjusted to ensure the simulated deck temperature peaks at the same time as the monitored results, while the absorption coefficient was modified so that the temperature peaks at the same magnitude. These properties are shown in Table 6.3. The adopted thermal conductivity of the combined asphalt and steel deck is that of the asphalt alone, since its low conductivity would determine how quickly the heat would spread in the span-wise and lateral directions, and in the vertical direction heat would be rapidly transferred through the highly conductive steel. Elbadry and Ghali (1983) and Branco and Mendes (1993) use similar values for their emissivity, absorption and convection coefficients, so by comparison the properties used in this study are a reasonable size.

Table 6.3: Typical heat transfer properties.

Property	Asphalt and Steel Deck		Concrete Tower	
	@ -20	@ 100	@-20	@100
k, thermal conductivity (W/m°C)	2.5		1.71	1.50
c, heat capacity (J/kg°C)	680		900	
h, convection coefficient (W/m²°C)	26		25	
ε, emissivity coefficient	0.9		0.7	
α, absorption coefficient	0.9		0.65	

The calibrated results for July are shown in Figure 6.9. The temperature of the deck shows a good match during the morning, midday and evening, however the monitored results have a steeper rise and fall. Since this trend suggests shorter daylight hours than calculated from the sunlight formulae (in the Appendix), the shallower slopes may be caused by a difference in cloud cover during the morning and evening, and represent an acceptable error. It is observed that the temperature of the suspension cable peaks an hour after the temperature of the deck; the wrapping of the cable apparently makes it less able to gain and lose heat by convection and radiation. The calibrated properties were confirmed by the results from the cloudy day (January 10th), shown in Figure 6.10.
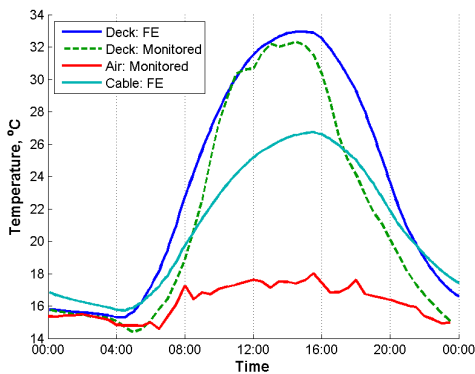
Figure 6.9: Deck, cable and air temperature, for 8/7/2010.
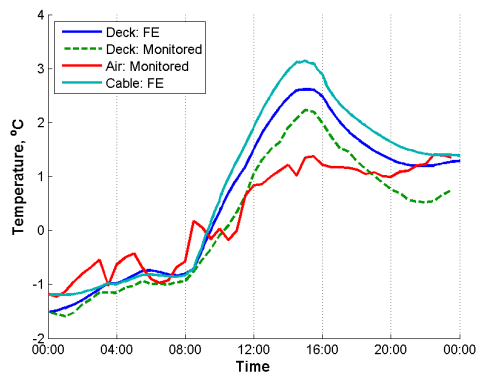
Figure 6.10: Deck, cable and air temperature, for 10/1/2010.

6.3.3 COMPLETE BRIDGE MODEL STRUCTURAL PROPERTIES

6.3.3.1 *Calibration using monitored expansion data.*

Following the calibration of the FE model's thermal properties to replicate the monitored thermal response, it was used to investigate the relationship of the deck expansion with temperature, without modification of the structural properties.

Figure 6.11 compares the simulated and monitored expansion at the gap for July 8th, using results from the modified FE model. There is a slight offset in the values at the start of the analysis and at its peak, which is due to the reference temperature for the thermal analyses being 17.5°C (as chosen in Chapter 4). Since the reference point for temperature and absolute displacement differs from the actual structure, the comparison is made with the relative variation between the monitored and simulated deflections. The thermal expansion of the bridge deck determined from the FE model was greater than the monitored results; the simulated expansion of the bridge deck is 19.6mm larger than the monitored expansion. This indicates slight differences in the structural response, which require identification.
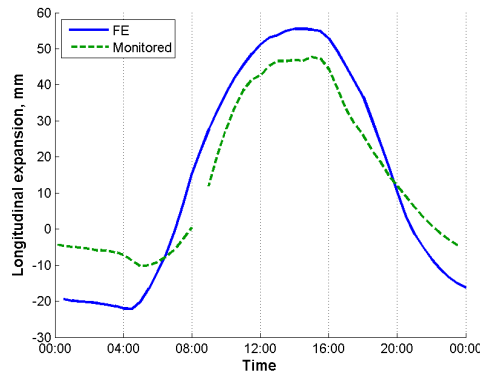
Figure 6.11: Longitudinal expansion at CG025, for 8/7/2010.

In order to compare the thermal responses of the FE model and actual bridge to differing temperatures across the structure, regression analyses were performed on the simulated and monitored data. The coefficients from the regression analyses demonstrate the sensitivity of the output to each input, and can identify which members of the simulated model influence the deck structure's overall thermal expansion too much. For these regression analyses, the temperatures across the bridge were used as the independent inputs, and the expansion of the deck as the dependent output. By using different combinations of temperatures and comparing the correlation of the predicted data to the monitored, Table 6.4 indicates a good fit can be provided by using the deck and truss temperatures as independent inputs, since using the cable temperature offered only a 0.1% improvement.

Table 6.4: Goodness of fit between measured expansion, and expansion predicted using linear regression models with different structural temperatures.

Combination of variables	Deck	Cable	Truss	Deck & Truss	Deck, Cable & Truss
Correlation coefficients of regression analysis prediction to monitored data	99.22%	97.68%	80.87%	**99.90%**	99.91%

The coefficients of the monitored properties shown in Figure 6.12 (left) indicate an almost equal influence of both deck and truss temperatures; the expansion of the deck can be (roughly) approximated from the average of the deck and truss temperatures. The coefficients from the FE simulated properties (middle) imply that the expansion is weighted towards the deck temperature, since the coefficient associated with the deck is much larger, while the negative coefficient related to the truss temperature implies an increase in temperature

causes the deck to contract. While this response to the temperature of the truss is counter-intuitive, the deck temperature on July 8th is higher than that of the truss, and the combination of the two variables would produce a similar expansion as the monitored response. This differing response may be related to errors within the FE simulated temperatures, since the simulated deck and truss temperatures have an almost symmetric rise and fall during day-light hours, while the monitored deck temperature sharply drops after 15:00 (as seen in Figure 6.9).

To see if the results were produced from variations in the thermal response between the model and the actual structure, the monitored temperatures were imposed as thermal boundary conditions on the FE model instead, and whether the regression analysis coefficients for the new simulated responses are a closer match to the coefficients determined from the monitored data. The coefficients determined from this FE analysis are shown on the right-hand side of Figure 6.12, and provide a much closer match to the coefficients determined from the monitored thermal response; both the coefficients are positive, but the expansion of the FE model is still mostly weighted towards the temperature of the deck.
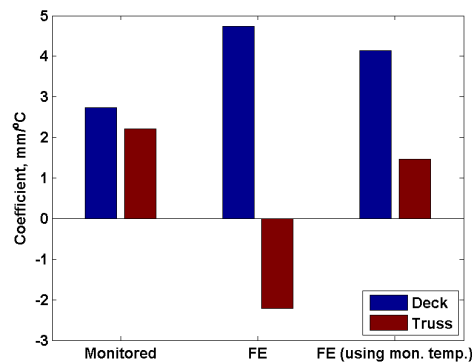
Figure 6.12: Calculated coefficients from regression analyses on the simulated bridge expansion on 8/7/2010.

To further check whether the structural properties used in the FE model were acceptable, the expansion of the deck structure was observed using the data available on January 10th, as shown in Figure 6.13. However, the extensometer on the bridge was not operating at the time, so the expansion data from the nearest RTS reflector, which is at CG044, was used in its place. The time series response is slightly offset (due to the choice of ambient temperature in the FE model), but both the monitored and simulated response demonstrate a peak near 15:00. After this peak the monitored expansion steadily reduce, while on the simulated expansion drops more sharply at 16:00, like the temperature of deck in Figure 6.10.

This sharp drop manifests in the regression analysis on the January 10th data in Figure 6.14; the monitored response (left) has a positive coefficient associated to the truss temperature, while for the simulated response (middle) the same coefficient is negative. Like the July 8th data, this

160

difference is associated with errors from the simulated thermal response, and if the FE model uses temperatures recorded from the structure on January 10th, the coefficients produced from the regression analysis on this data (right) are a good match to the coefficients produced from the monitored data. As a result, it seemed the simulated expansion of the bridge subjected to the recorded temperature seems were an acceptable match to the monitored data on both training dates.
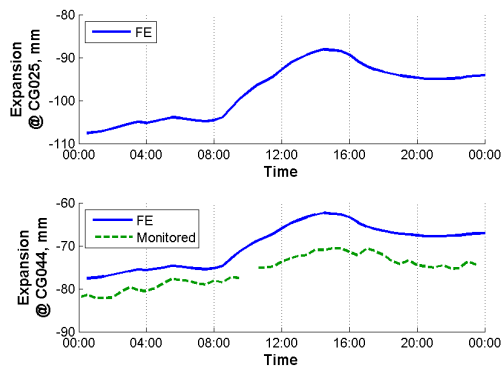
Figure 6.13: Longitudinal expansion at CG025 and CG044, for 10/1/2010.
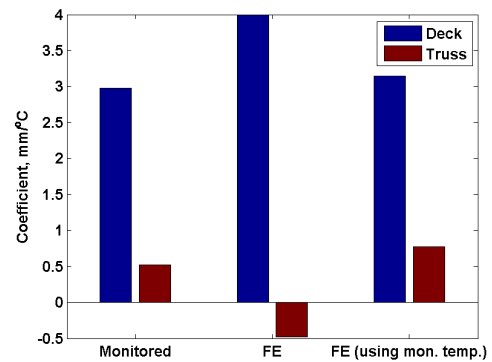
Figure 6.14: Calculated coefficients from regression analyses on the simulated bridge expansion on 10/1/2010.

From further investigations it was found that the regression analysis coefficients produced from the FE model could be improved further by increasing the deck structure's ability to hog when the deck is warmer than the truss, since the thermal displacements will move vertically rather than longitudinally. This can be achieved by decreasing the stiffness of the deck, and increasing the stiffness of the truss. The model used in the analysis was unmodified, however, since the coefficients determined from the regression analysis vary on a day-by-day basis, and the data from the two days of simulated results provided a satisfactory match to the monitored data.

6.3.3.2 Calibration using vertical deflection data

The vertical deflection of the mid-span on July 8th is shown in Figure 6.15. Like the longitudinal expansion, the FE results are offset with respect to the monitored results, but vary by a similar amount. The monitored results have a jagged profile however, which is accounted for by temporary variations in other loads such as traffic and wind. There is also a 1 hour difference between the troughs of the FE and smoothed monitored data, the results from FE model peaking after the deck. Since the cable temperature peaks after the deck temperature in the time series results (Figure 6.9), it appears the vertical deflection in the FE model is more dependent on the cable temperature than the temperature of the deck structure. However

this is not evident in the response for January 10th, shown in Figure 6.16, where the smoothed monitored results peak at almost the same time. Since this anomaly could not be easily removed without a rigorous model updating process, and the simulated results provided a reasonable reproduction of the monitored deflections, it was decided that the FE model was acceptable for reproducing the vertical response of the bridge to thermal loads.
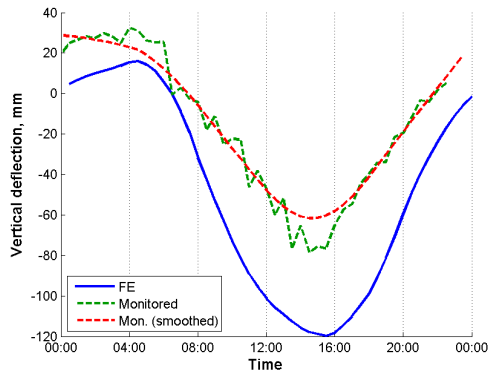
Figure 6.15: Vertical deflection at CG062, for 8/7/2010.
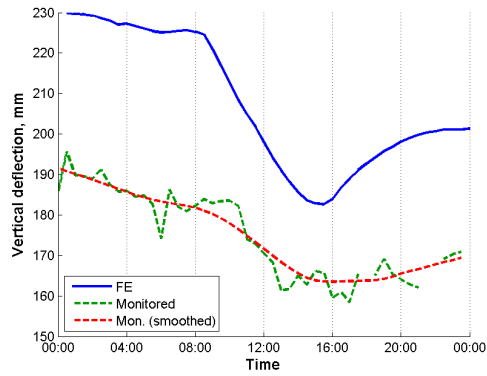
Figure 6.16: Vertical deflection at CG062, for 10/1/2010.

6.4 DIURNAL AND SEASONAL VARIATIONS OF THERMAL LOADING AND STRUCTURAL RESPONSE

So far in this investigation, an FE model of the suspension cable has been developed to reproduce the monitored temperatures, and the thermal and structural properties of the full bridge model are calibrated to replicate the monitored thermal behaviour of the suspension bridge for two days – one cloudy, one sunny.

Assuming the FE model of the suspension cable and the full bridge provide an accurate representation of the bridge through a transient heat analysis, they can be used to simulate the bridge performance for longer periods and a variety of thermal conditions. In order to determine how the bridge responds to time dependent thermal loading throughout the year, sixty days of monitored performance data were chosen for a detailed study. These data comprise a rich set of temperature, RTS, and extensometer information tracking behaviour of the bridge.

6.4.1 SUSPENSION CABLE TEMPERATURE

Five consecutive days (10th to the 14th) were chosen for each of the 12 months to represent variations that occur seasonally, rather than just diurnally. Like the calibration tests, these periods include effects of solar radiation and air convection, plus monitored truss temperatures.

The simulated cable temperatures from the FE model in Figure 6.17 demonstrate a good fit with the monitored results, with occasional anomalies; overall the data have a correlation coefficient of 0.968. Errors between the simulated and monitored results tend to occur around midday, when the monitored cable temperatures are much higher than the simulated temperatures, particularly in March and October. Observations at night, however, provide a close match, which suggests that the error lies within the applied solar radiation.

Webcam images for January 13th and November 10th, when there is temperature difference between deck and truss in excess of 5°C, suggest there may be less cloud cover than the approximate values (such as shown in Figure 6.3). This may explain the pronounced error between FE and monitored results observed during winter and occasionally in spring, since clear dates with shorter daylight hours and reduced solar intensity will be treated the same as overcast dates with a higher solar intensity. Further development of the cloud cover approximation would be required, either by normalising the values using predicted daily solar intensities, incorporating air temperature in the method or using an interval that is shorter than 60 days. However the majority of the simulated results fit well enough for further application, so the predicted cable temperatures were transferred to development of the full bridge model.
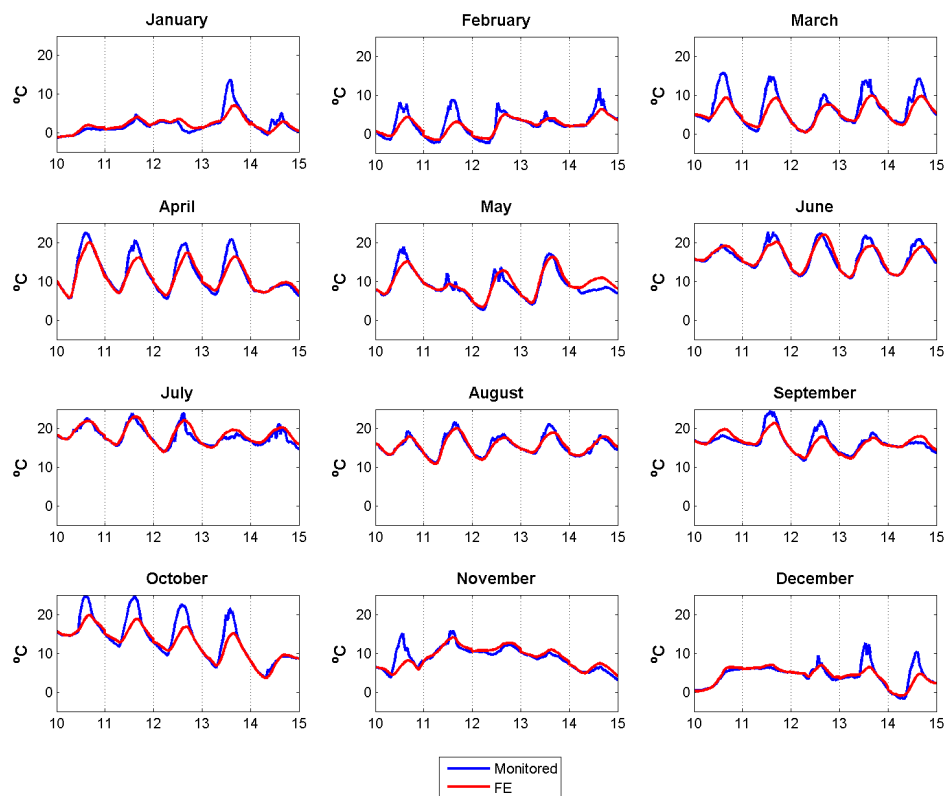
Figure 6.17: Monitored and simulated cable temperatures, for the 60 observed days.

6.4.2 DECK TEMPERATURE

Compared to the cable results, Figure 6.18 shows even better agreement between the results monitored from the bridge and the simulated temperatures from the FE model, providing an overall correlation coefficient of 0.969. Errors generally occur when the peak daily temperatures do not match the monitored results at noon, which appears to be the same error as seen in the cable temperatures. It is also possible that monitored results may be lower than predicted due to wet conditions where surface water absorbs heat. Sadly, for the days where this may be a possibility, such as May 14th and July 13th when the temperature time series are capped at the peak, there are no webcam images available.
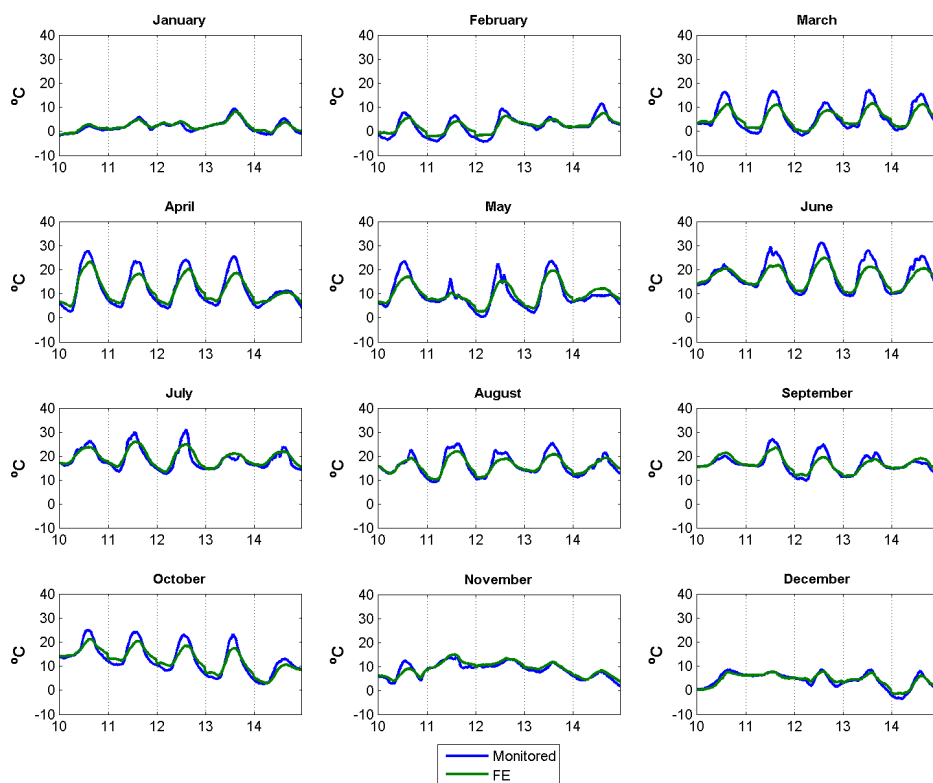
Figure 6.18: Monitored and simulated deck temperatures, for the 60 observed days.

Figure 6.19 shows temperature contours of the deck at midday on July 8th, alongside a plan view of the deck and beam layout to help explain their shape. In the orthotropic steel deck and the cantilevers, the temperature is warmer at their centre than at the edges, where the deck is supported by either span-wise or transverse beams. These beams act as heat sinks to the deck, conducting heat through the top of the truss rapidly due to the high thermal conductivity of steel. For similar reasons, the shear boxes are typically the hottest features on the bridge, since they are a sheet of metal. The coolest temperature in the simulated deck is in the cantilevers at the point where the cross bracing meets the stringers; the cross bracing acts as a

164

heat sink for the cantilevered deck.
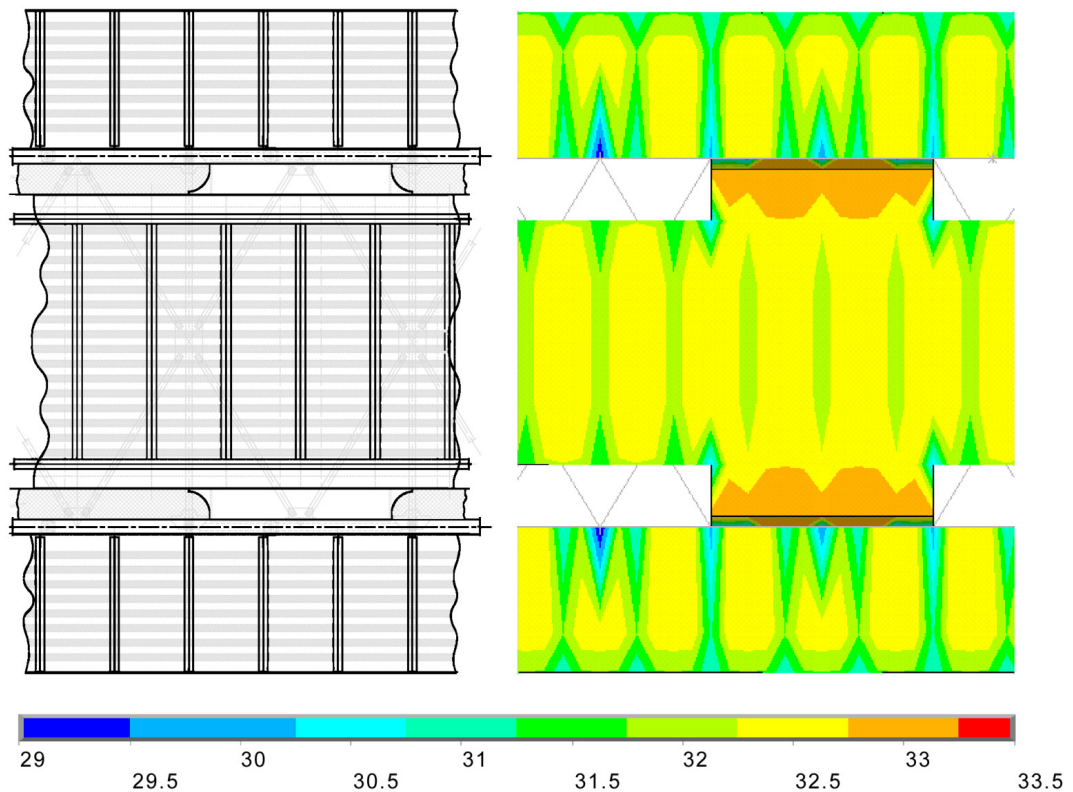
Figure 6.19: Temperature profile across deck. Units in degrees Celsius.

6.4.3 QUASI-STATIC DISPLACEMENT OF DECK STRUCTURE

6.4.3.1 *Time series*

Figure 6.20 presents the longitudinal expansion time series for the 60 days of observed data, comparing the results predicted from the FE analysis at CG044 to the monitored results. Results at the expansion joint would have been preferred, but there is not enough data collected from the extensometers to provide a suitable comparison. Both sets of data show larger longitudinal movements of the deck during summer months compared to winter, due to larger variations in deck temperature. For the most part the simulated time series overlap the monitored results, indicating a decent match, however the FE results tend to underestimate the peak deflections at midday and midnight, because of the same errors in the temperature results.
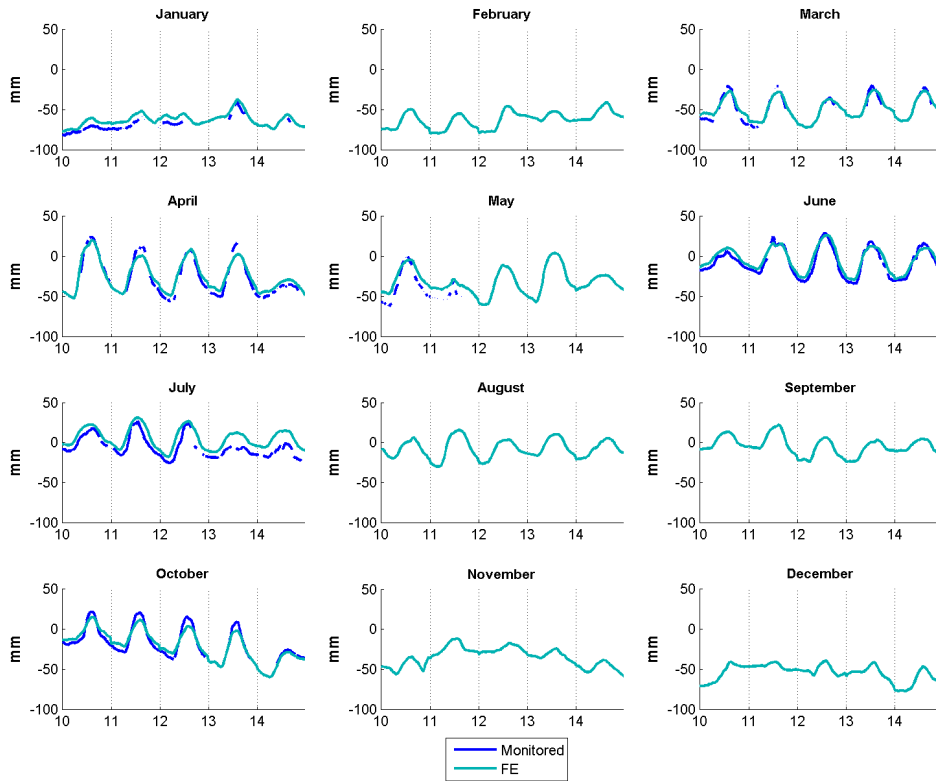
Figure 6.20: Monitored and simulated longitudinal expansion at CG044, for the 60 observed days.

The simulated and monitored vertical deflections of the deck at mid-span (CG062) in Figure 6.21 demonstrate that the deck of the suspension bridge lowers towards midday, due to the expansion and slackening of the suspension cable. Like the expansion of the bridge deck, the results from the FE model provide a reasonable match to the monitored (RTS) results. While the simulated results does not have jagged peaks like those seen in the monitored results, the peaks at midday are of a similar magnitude, indicating a better fit than for longitudinal expansion.
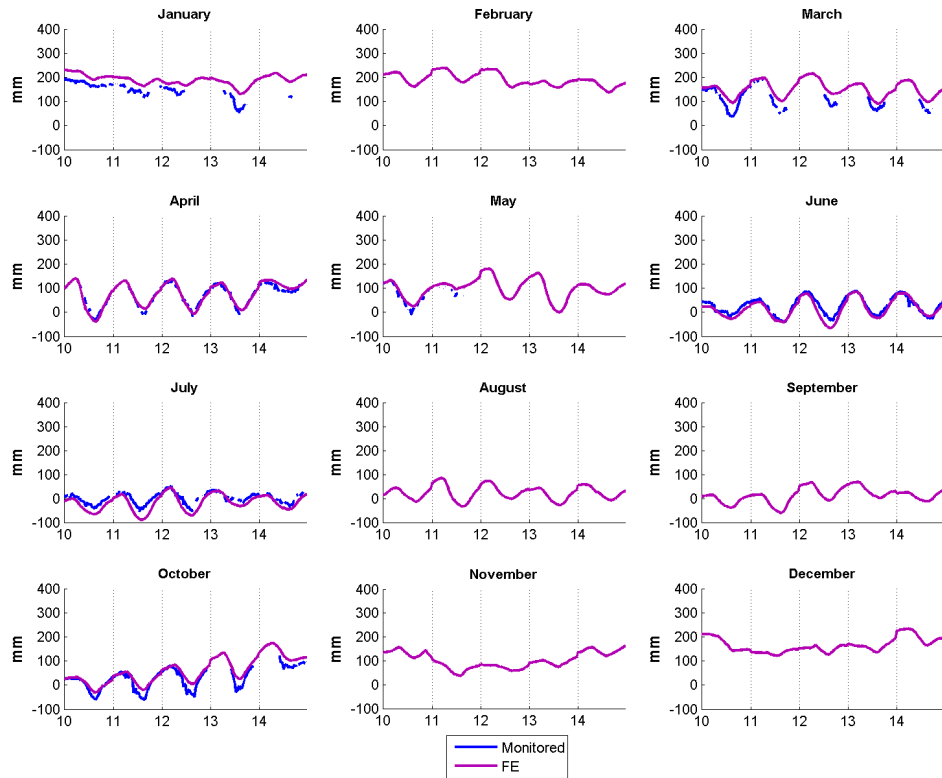
Figure 6.21: Monitored and simulated vertical deflection at CG062, for the 60 observed days.

6.4.3.2 Relationship of expansion to temperature

For periods when the solar intensity is less than 50W/m², which mostly occur at night or in winter, Figure 6.22 demonstrates that the expansion of the bridge deck at CG044 has a linear relationship with temperature, since the temperature differential across the bridge section is small. For data where the applied solar radiation exceeds 50W/m² the temperature differences between the deck and the truss are more significant, and develop a nonlinear relationship. Similar behaviour is observed in the vertical deflections at the mid-span (Figure 6.23). These results show why the nonlinear behaviour observed in Chapter 4 occurs at high temperatures, due to moderately high levels of solar radiation upon the deck surface.
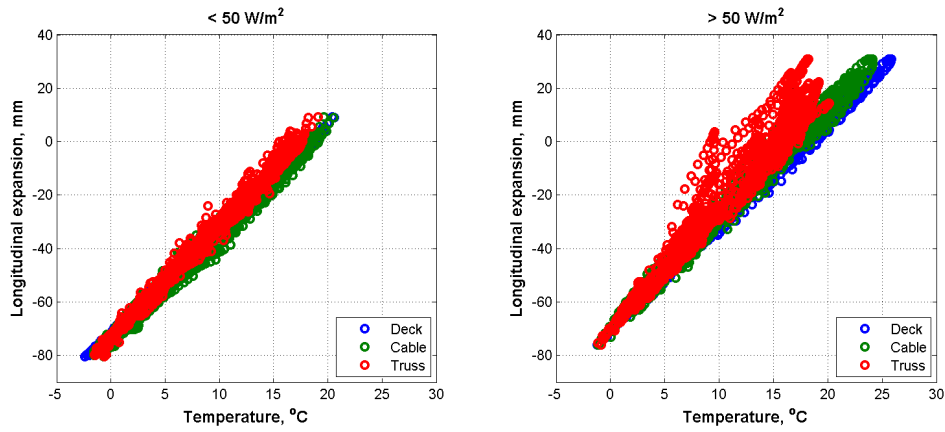
Figure 6.22: Simulated expansion at CG044 vs. Temperatures from FE model.
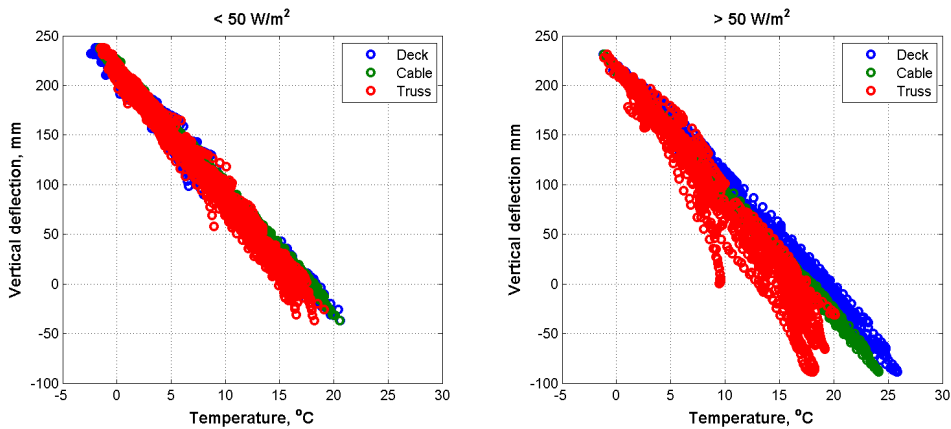
Figure 6.23: Simulated vertical displacement at mid-span (CG062) vs. Temperatures from FE model.

When the regression analysis is performed for the whole 60 days of longitudinal displacements, Figure 6.24 shows that the predicted response from the regression analysis has a close fit to the actual response. This shows that the longitudinal response in the FE model is strongly related to the temperature of the deck and the truss, rather than to other inputs such as the suspension cable temperature. For the monitored results (Figure 6.25) the coefficient associated with the deck temperature is larger than the truss temperature coefficient; another implication that the thermal response of the FE model is not influenced by the truss temperature enough to match the monitored response. The scatter in Figure 6.25 indicates either other factors or thermal lag are involved. It is more likely to be the latter, since the correlation can only be marginally improved by adding contributions from other temperatures. Nevertheless the monitored expansion data and its regression analysis prediction have a correlation coefficient of 0.990, indicating a very close fit and that the deck and truss temperatures mostly determine the longitudinal thermal expansion of the deck structure.
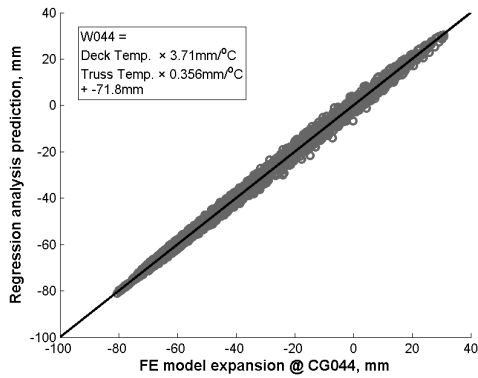
Figure 6.24: Regression analysis on the simulated displacements at CG044.
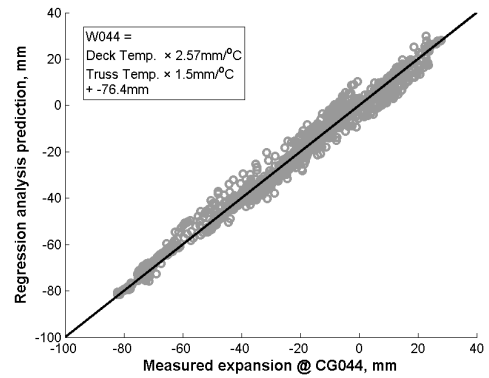
Figure 6.25: Regression analysis on the monitored displacements at CG044.

For the vertical deflection observed in the FE model, the high correlation shown in Figure 6.26 indicates a high dependency upon the structural temperatures; the cable temperature in particular, since the value of its associated coefficient, 10.2mm/°C, is considerably higher than those related to the deck and the truss. Considering the regression analysis results for the monitored vertical deflections (Figure 6.27), the largest coefficient is also for the suspension cable temperatures, although it is half the size of the coefficient determined for the FE results. Similar to the expansion of the bridge, the points are more dispersed, although this is due to the jagged peaks observed in the time series. Since the monitored samples and their regression analysis predictions have a correlation coefficient of 0.982 it would seem the most significant parameters are these three structural temperatures.
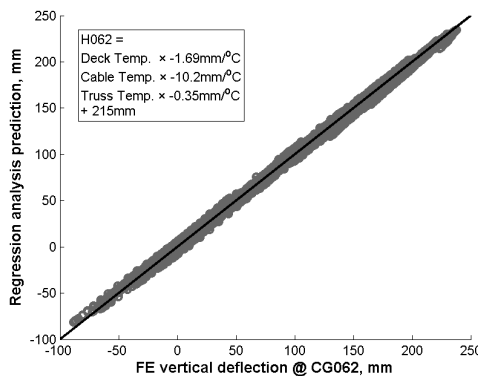
Figure 6.26: Regression analysis on the simulated vertical displacements at the centre of the main span.
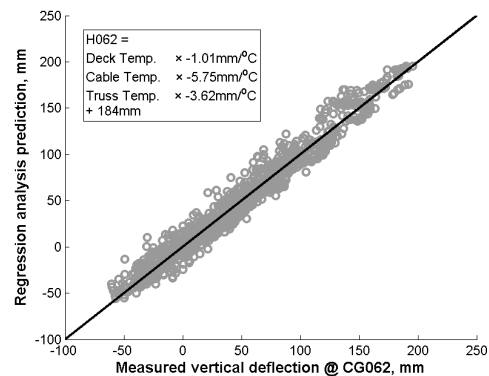
Figure 6.27: Regression analysis on the monitored vertical displacements at the centre of the main span.

6.4.3.3 *Expansion differential between top and bottom of deck structure*

The variation of longitudinal expansion at CG025 with height was investigated with regard to the temperature-dependent hogging of the deck. When the differential is positive, the top of the deck moves closer to the expansion gap than the bottom of the truss. Figure 6.28 and Figure 6.29 aims to show how this expansion differential observed in the FE model results is a function of both the cable temperature and the thermal gradient across the deck structure, for

the cross girders at Saltash tower (CG025) and Plymouth tower (CG096) respectively. The plots are 3D surfaces viewed down the expansion differential axis. The surfaces are developed by a Delaunay triangulation of the available data (Barber et al. 1996), hence the expansion differential is indicated by the colour. Blue areas show that the deck has moved West more than the base of the truss, and vice-versa for the red areas. The dashed white lines indicate almost equal movement of deck and truss (0mm difference), as well as the slope of the surfaces.

In both results there are straight, diagonal bands of equal colour forming in the surface plots, indicating a linear relationship with both of the observed variables. As stated in Chapter 4, an increase in cable temperature causes the cables to lengthen and the bridge profile to sag. On the other hand, if the temperature differential increases (the deck temperature becoming warmer than the truss) the deck expands further than the truss, causing the bridge to hog.

The mostly horizontal variation of the colour gradient in Figure 6.28 establish that the cable temperature is more influential over the curvature of the bridge deck at CG025 than the thermal gradient, since the longitudinal displacements of the structure are mostly unrestrained at the expansion gap. At the Plymouth tower, where the deck structure is continuous, the diagonal colour gradient of Figure 6.29 show that both the cable and thermal gradient have an almost equal bearing on the expansion differential.
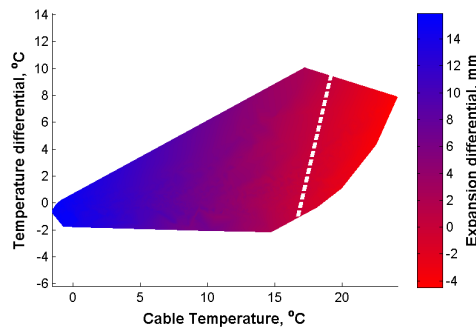
Figure 6.28: Expansion differential through depth of deck structure at Saltash tower (near CG025), vs. Cable temperature and temperature differential through depth of deck structure.
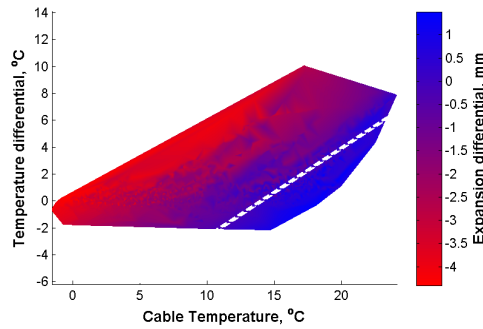
Figure 6.29: Expansion differential through depth of deck structure at Plymouth tower (near CG096), vs. Cable temperature and temperature differential through depth of deck structure.

6.4.4 CONCRETE TOWER TEMPERATURE AND DEFLECTION

6.4.4.1 Temperature and longitudinal time series

So far the temperature of the deck and the consequent deck displacements have been replicated in the data, showing the temperature difference between the deck and the truss is linked to the solar radiation absorbed by the deck, and that the deck structure not only sags due to thermal expansion of the suspension cable, but curves upwards due to its own thermal gradient. The next step studies the transient thermal effects on the concrete towers affect the bridge's structural response.

Since there were no temperature sensors on the towers during the period of analysis, there was no way of calibrating the tower temperatures predicted from the FE model. The initial temperature for each five day set (at midnight of the 10th day for each month) the temperature of the tower sides was simply the monitored air temperature. For the following consecutive four days (midnight for the 11th to the 14th day of each month) the initial temperature uses the final temperature calculated from the FE analysis for the previous day.

Simulated temperature time series for the Plymouth tower in Figure 6.30 show the temperatures of the towers' faces during the morning are warmer than the deck (in Figure 6.18). This is because the concrete of the towers retains heat gained from solar radiation from the previous day, while the steel members lose heat very rapidly. This simulated behaviour is similar to the monitored thermal response of the Zhang-Jiang Bay Bridge's concrete bridge, for the same reason (Yim & Wang 2010). The temperature of the southern face is the largest of the four, since it is subjected to higher levels of solar radiation. The next largest temperature profile is the eastern face, which retains the heat gained from being radiated in the morning over the remainder of the day.
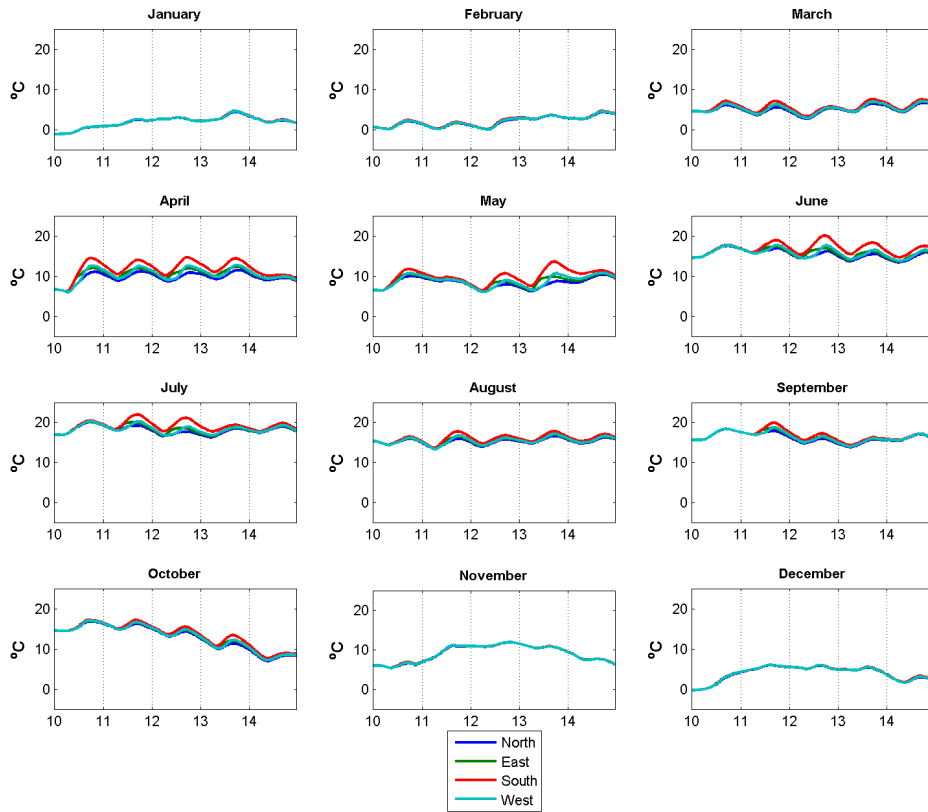
Figure 6.30: Simulated temperature of tower faces, for the 60 observed days.

The temperature of the concrete towers peak much later than the temperature of the deck and the cable, at around 17:30 during the summer. This is a consequence of smaller emissivity and convection coefficients used for the material properties of the concrete, compared to steel, as well as the high heat capacity of the concrete (in Table 6.3). Comparisons between the time series for the tower temperatures and the deck temperature indicate the time difference between their peak times during winter is mostly 1.5 hours, which rises to a 3 hour gap during summer, as shown by Figure 6.31 (the blue bars). The suspension cables also peak after the deck, but the delay between the two is typically within an hour.
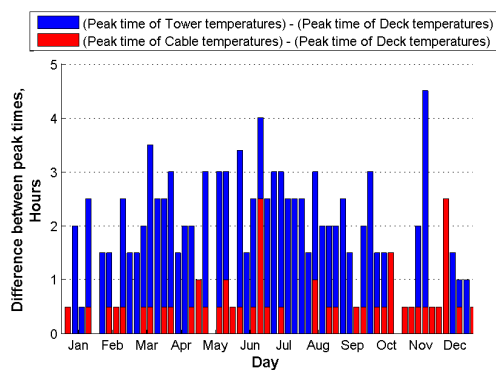
Figure 6.31: Difference in peak temperature times.

In Figure 6.32 the simulated sway of the Plymouth tower peaks at around midday, like the deck displacements. Since the behaviour of the monitored results and the FE results mostly peaks at midday, rather than at a later time as the tower temperature time series, one can conclude that most of the tower motion is due to the thermal response of the deck structure, pulling the towers towards the mid-span by the suspension and stay cables. While the correlation coefficient between the monitored and simulated results is 0.868, indicating a good but not perfect fit, the peaks at midday bear little similarity to the time series of the tower temperature. The truncated peaks in the April and October plots suggest a closer match with the suspension cable temperature, which has a similar error.
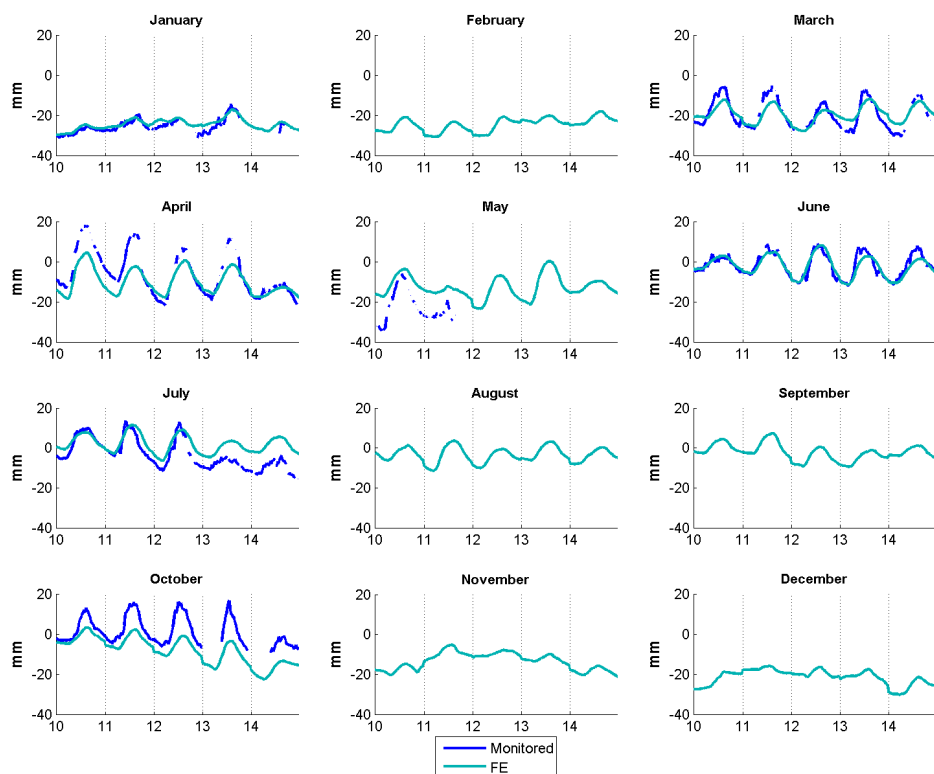
Figure 6.32: Monitored and simulated westerly movement of Plymouth tower top, for the 60 observed days.

While the time series of longitudinal deflection of the Plymouth tower forms peaks at midday, the time series of the simulated Saltash tower deflections in Figure 6.33 create troughs at the same time; the tower tops moving towards the mid-span as the suspension cables slacken. However the behaviour of the monitored results is mainly irregular, suggesting the actual Saltash tower is less affected by the expansion and sag of the deck than the FE model predicts.

Despite the monitored response being mostly erratic, the June, July and October periods indicate a common feature in the results where the tower sways Westwards during the

morning, and Eastwards in the afternoon before returning to an almost neutral position. These differentials may be caused by temperature differentials across the tower, where the irradiated face is warmer than the opposite side, and would cause the tower to curve in the opposite direction. This response would be present on the Plymouth tower, but the cables pulling the tower in the opposite direction hide it. It may be possible to work backwards from the structural displacements to estimate the temperature on either side of the tower, but this will not be investigated in this thesis.
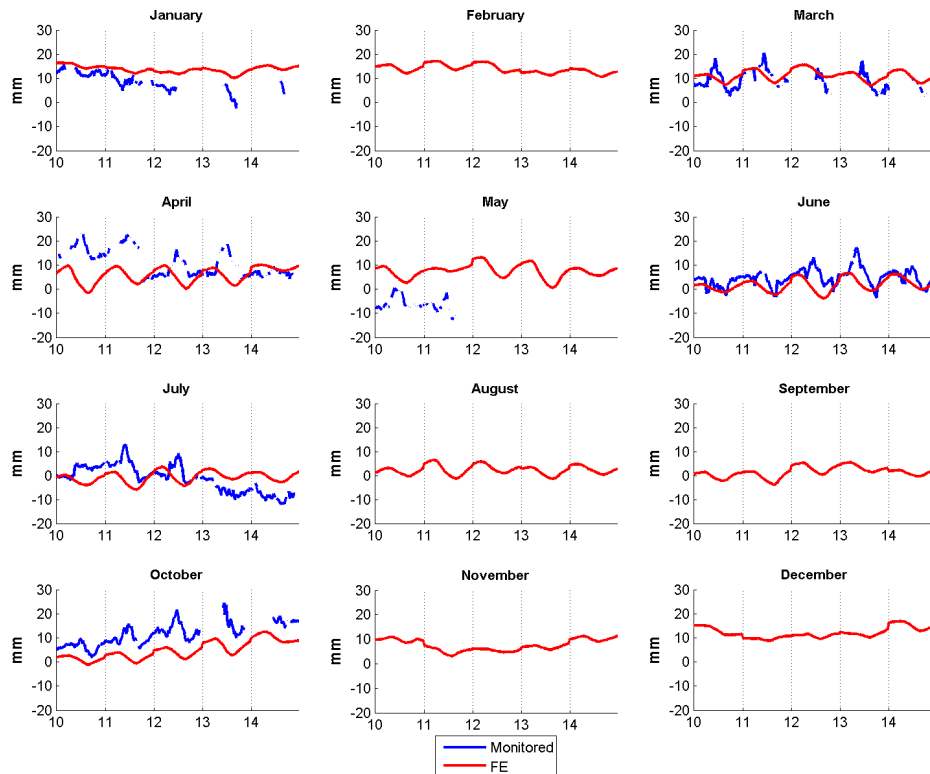
Figure 6.33: Monitored and simulated westerly movement of Saltash tower top, for the 60 observed days.

6.4.4.2   *Effect of cable temperature on Plymouth and Saltash towers*

Figure 6.34 and Figure 6.36 plot the Plymouth and Saltash tower displacements respectively against the cable temperature to check whether their different behaviour is linked to the thermal response of the structure. For the Plymouth towers there is a definite positive relationship, an increase in cable temperature increases the deflection towards the mid-span. There is some phase difference in the relationship, causing otherwise linear trends to open slightly to form elliptic loops. The linearity indicates it is mostly the thermal response of the structure which governs the Plymouth tower sway, rather than the delayed thermal response of the tower.

However, the points in the monitored results do not fall perfectly on a single line, unlike the FE results in Figure 6.35. If the points are colour coded to the time of day they occur, it is clear that the plot is made up of several offset 'bands', rather than overlaid on a single line as the FE results. In the time series results, these occur when there are differences between the monitored and simulated results, such as April 10th to 11th, May 10th and July 13th to 14th. For these days in particular the errors are also manifested in the time series of the longitudinal expansion (Figure 6.20), yet the error is minimal in the temperature time series of both the deck and the cable (Figure 6.17 and Figure 6.18). Traffic jams have been identified, but they cause deflections no more than 4mm, i.e. much less than the thermal effects. The other possible cause for the multiple bands is that the heat stored in either the concrete towers or the suspension cable from previous days causes a temporary inflexion of the tower.
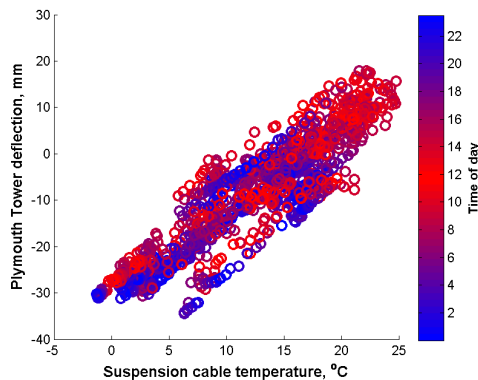
Figure 6.34: Time dependence of monitored Plymouth tower deflection vs. Suspension cable temperature.
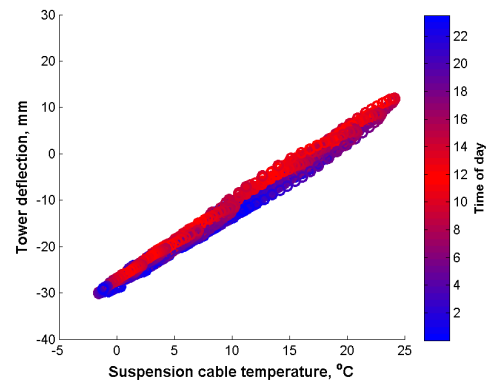
Figure 6.35: Time dependence of simulated Plymouth tower deflection vs. Suspension cable temperature.

The monitored deflections of the Saltash tower (Figure 6.36) do not have a linear relationship with the cable temperature. Instead, the plots consist of several superposed elliptic loops, the deflection being greater during the morning than in the afternoon for the same temperature. This suggests the daily sway of the tower is independent of the thermal response of the structure. However, the colour coded results uncover a trend of blue dots within the scattered mass, which follow a similar trend as the FE model results in Figure 6.37. Therefore the response from the FE model is not a total misrepresentation of the actual tower deflections, since the tower moves slightly, eastwards, when the cable tensions decrease. However this response is only observed near midnight, and during the day other factors determine its sway. This may be due to the temperature differences between the faces of the towers, as observed from temperature time series, although this requires further study.
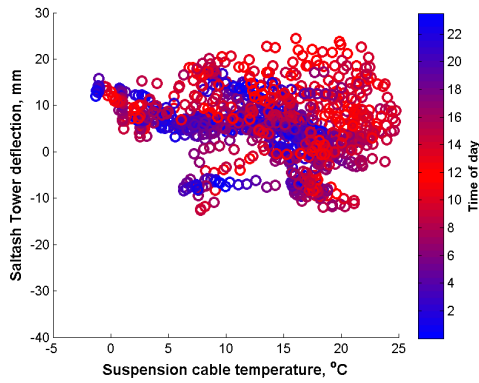
Figure 6.36: Time dependence of monitored Saltash tower deflection vs. Suspension cable temperature.
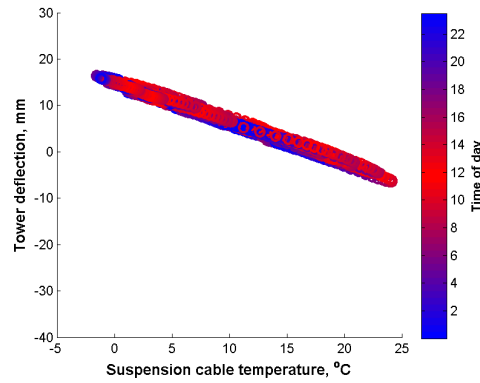
Figure 6.37: Time dependence of simulated Saltash tower deflection vs. Suspension cable temperature.

6.4.5 TRANSIENT THERMAL EFFECTS ON CABLE TENSIONS

We have observed an almost instantaneous thermal response in the deck, while the towers take 1.5 to 3 hours longer to warm up due to their concrete bulk. Also the sway of the Plymouth towers appears to be linked with the expansion of the bridge deck, while the thermal response of the Saltash towers is mostly independent of the whole structure.

The next step to consider is the response of the cables, to see whether their behaviour mostly relates to the temperature of the cable (which takes an hour longer to warm up than the deck) or the dissimilar response of the deck and the towers.

6.4.5.1 Stay cable tensions

As seen in Chapter 4, some nonlinear relationships were observed involving the monitored main span stay cable tensions. Figure 6.38 demonstrates the relationship of the main span stay cable tensions to the expansion at CG044. The Saltash stay cable tensions have an almost linear relationship with expansion since the cable tensions slacken when the bridge deck expands. In contrast, the Plymouth stay cable tensions form a nonlinear, slightly curved relationship, with a clump of samples forming below the main set of data points. This suggests a changing response, caused by the elongation of the stay cables, the sway of the towers or both.
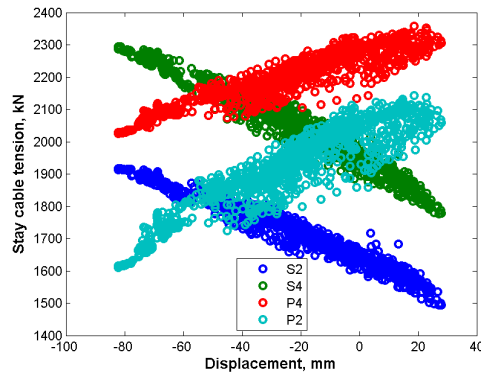
Figure 6.38: Monitored main span stay cable tensions vs. CG044 expansion.

The behaviour observed in these results is much clearer if only one day is studied, and the time of day which each sample occurs is clearly identified. Figure 6.39 shows the samples collected on the 15th of April, which was chosen since it clearly demonstrates the elliptical relationship of the stay cable tensions with expansion. Each point is colour coded: dark blue if the sample was collected at midnight, green if sampled at mid-morning, red if mid-afternoon, and neighbouring points are various hues in-between.

The colour coding demonstrates that these elliptical relationships are formed by the stay cables being slacker during the morning than the afternoon, for the same amount of deck expansion. For the Plymouth stay cable tensions (the plot on the right) the elliptical relationship is more pronounced, the tension in the stay cables being lower in the morning than in the afternoon. An interesting feature for this day in particular is that it has captured an increase in all stay cable tensions between 10:00 and 12:00 (between -10 and 0mm displacement), which is caused by a traffic jam on the bridge. The effect of traffic on the stay cable tensions are explored in Chapter 7.
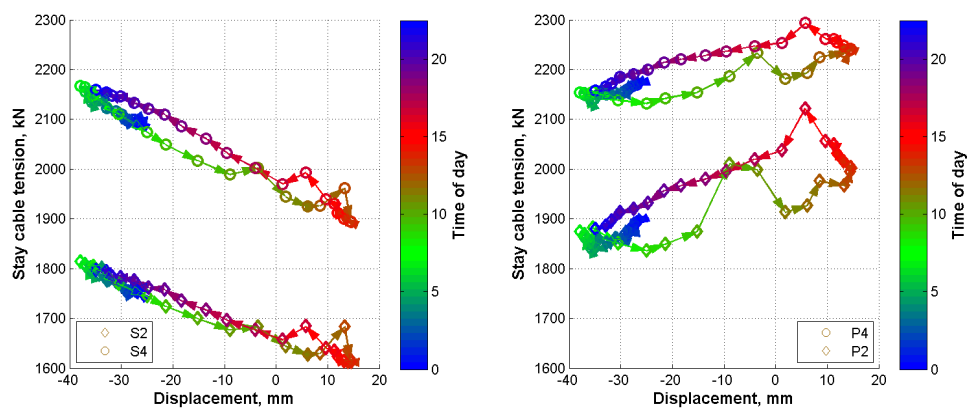
Figure 6.39: Time dependence of main span stay cable tension vs. Expansion at CG044, for the 12th of October, 2010.

The results from the FE simulations in Figure 6.40 show linear trends between the stay cable tensions and the expansion of the bridge deck, for both the Saltash and Plymouth stay cables. This shows that whatever effect is causing the elliptic response in the monitored results, the FE model is unable to replicate it, either due to incorrect loading, or due to some feature missing from the model.
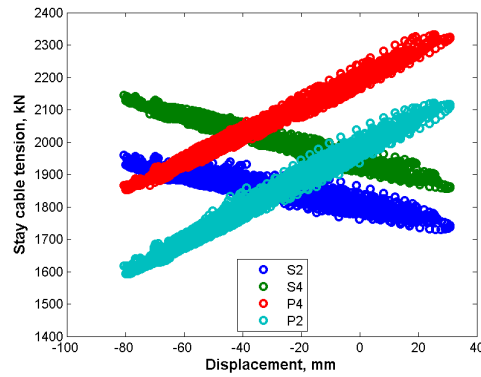
Figure 6.40: FE model stay cable tensions vs. expansion at CG044.

Some days in time series of the P4 stay cable tensions in Figure 6.41 demonstrate a good match between the simulated and monitored response. On the occasions when there are errors the variations in the simulated tensions are larger than those monitored. The elliptic behaviour in Figure 6.39 is accounted for by the lag in the stay cable tensions; the peak tensions occur 2.5 hours later than the peak longitudinal expansion. The stay cables in the FE model peak at almost the same time as the deck expansion, which is why the elliptic behaviour is less obvious.

Since it is harder for the cable elements to gain and lose heat than the deck, as seen in Figure 6.9 for the suspension cable temperature, this could be a cause of thermal lag in the structure, and that the absence of the elliptical behaviour is due to the over-simplification of the stay cables in the FE models. However, a later peak would mean the cable would be slacker in the morning than the afternoon, since the cable is still expanding. This was not observed in the FE model.
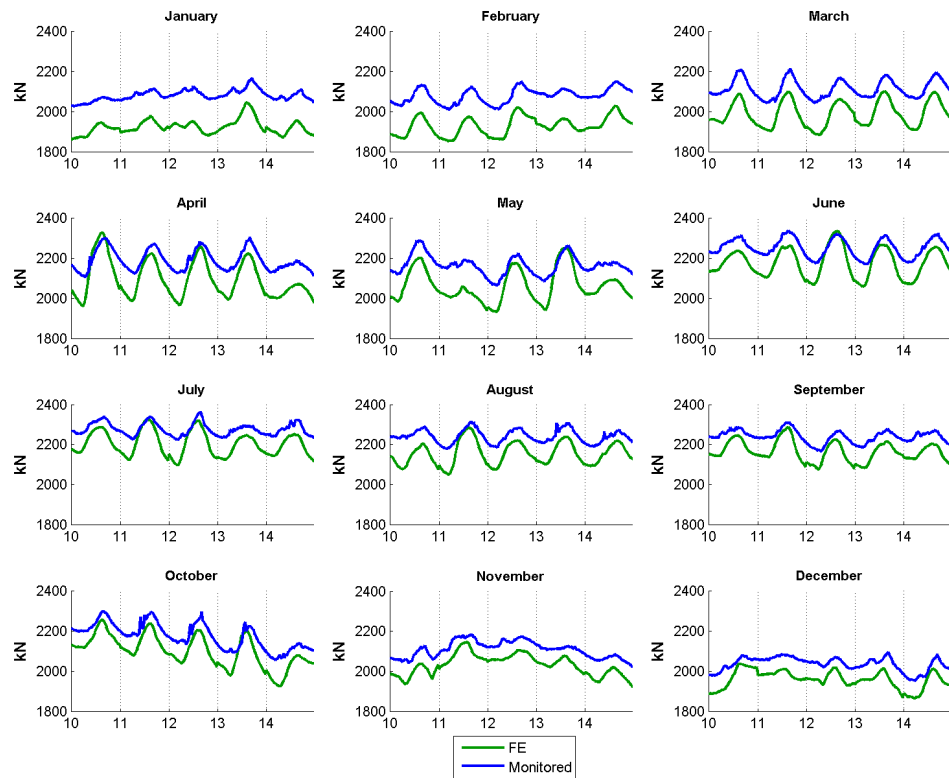
Figure 6.41: Monitored and simulated P4 tensions, for the 60 observed days.

While the simulated Saltash stay cable tensions in Figure 6.42 may differ in magnitude to the monitored tensions, they are capable of approximating the behaviour of the structure. The results for the Saltash stay cable tensions are highly dissimilar to the Plymouth stay cable tensions, as represented by the differing responses. As with the time series for the Saltash tower deflections, this implies that simulated responses for the Saltash tower are poor representations of the actual structure.

Both sets of results suggest that tensions drop and rise through the day with the deck expansion, although the monitored results drop considerably more, even during winter when solar radiation levels are low. It appears the varying thermal stresses in the FE stay cables are transferred to the tower deflections instead, rather than manifesting in the stay cable tensions. Furthermore, the jagged peaks in the monitored cable tensions have similarities to the peaks in the Saltash tower deflections. A good example is within the October period, which shows an upwards trend over the 5 observed days in both data sets. This suggests deflections in the Saltash towers are affecting the stay cable tension, as well as the expansion of the bridge deck.
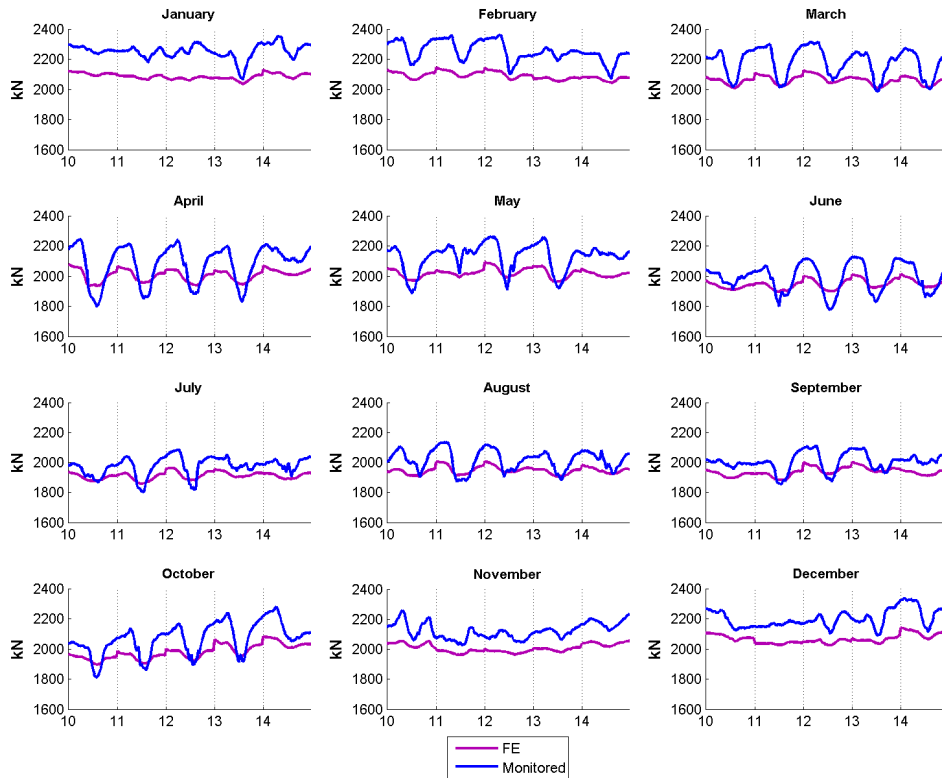
Figure 6.42: Monitored and simulated S4 tensions, for the 60 observed days.

The tower deflections seem to manifest in the stay cable tensions, either in the elliptic behaviour of the Plymouth stay cable tensions versus the deck expansion (Figure 6.39), or similar spikes in the time series of the Saltash tower deflections and cable tensions (Figure 6.33 and Figure 6.42). Because of this, it may be possible to consider the monitored tensions as a function of the movements of both the deck and the tower. Figure 6.43 and Figure 6.44 consider the monitored tensions in stay cables S4 and P4 respectively, as a surface plot against the RTS monitored longitudinal deflections of the tower to which they are attached, and the monitored longitudinal displacement of the closest RTS reflector on the deck.

The colour gradient representing the S4 tensions (Figure 6.43) varies only along the expansion axis, which suggests little participation of the tower deflections. For the P4 tensions (Figure 6.44) the gradient is angled diagonally, indicating a combined effect of tower and deck movement. The slope of the colour gradient shows that the P4 tension increases when either the deck expands westwards, or the Plymouth tower top moves eastwards. This demonstrates that the thermal lag exhibited in the Plymouth stay cable tensions is due to the variations between the thermal deflections of the deck and the tower, rather than the thermal response of the stay cable.
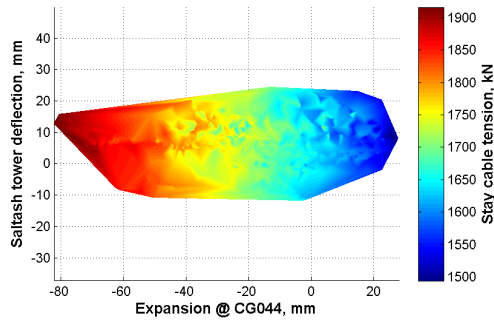
Figure 6.43: Effect of deck expansion and tower deflection on the Saltash stay cable tensions (tensions mostly influenced by deck movements).
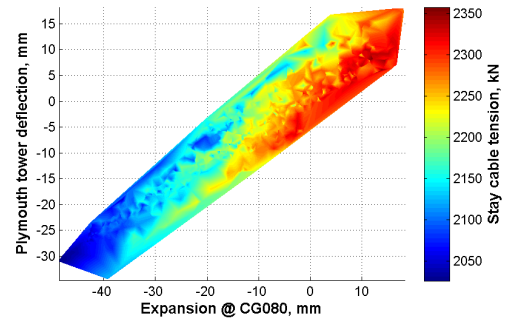
Figure 6.44: Effect of deck expansion and tower deflection on the Plymouth stay cable tensions (both tower and deck movements affect cable tension).

The next question is what causes the lag between the deck and tower displacements. One possible explanation is that the material properties of the concrete tower reduce heat loss, so the towers continue to curve west after midday since they are irradiated on their East face during the morning. Another cause may be the thermal lag exhibited in the suspension cable, which may slacken after midday and cause variations in the horizontal force equilibrium at the tower tops. Unfortunately, since the tower temperature and suspension cable tensions were not monitored, these responses need to be studied at another time.

6.4.6   SIMULATED SUSPENSION CABLE TENSIONS

The time series of the suspension cable tensions predicted by the FE model are shown in Figure 6.45, which decrease at midday as expected from the similar drops observed in the vertical deflection time series.
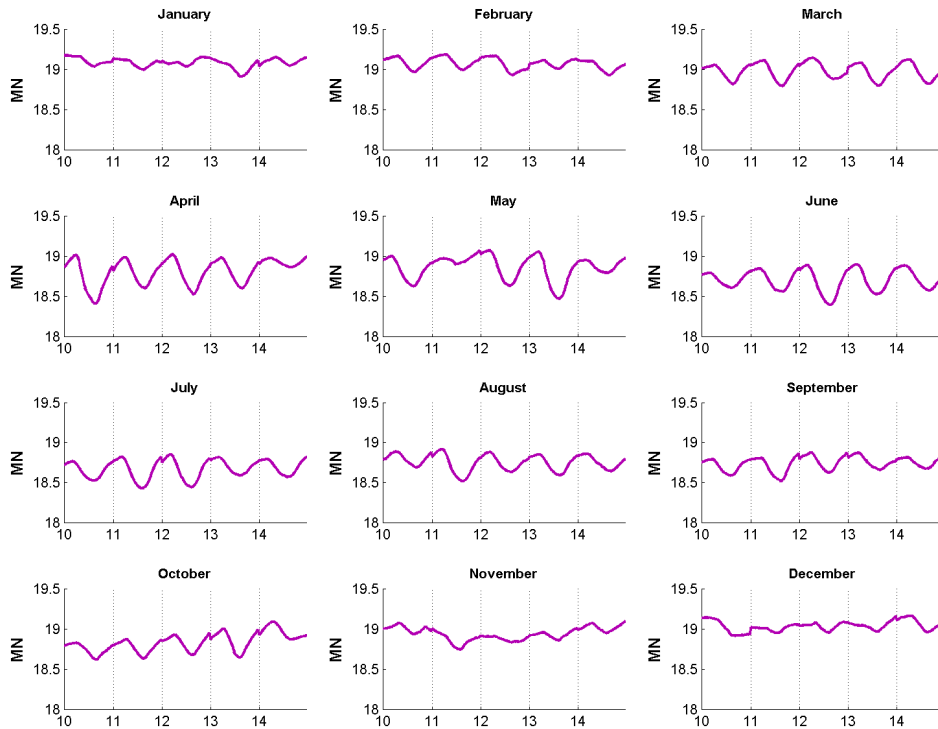
Figure 6.45: Simulated mid-span suspension cable tension, for the 60 observed days.

The initial assumption for the suspension cable tension was that it would have an inverse relationship with the cable temperature; the thermal elongation of the cables would cause a slackening of the cables. However, the results in Figure 6.46 suggest this relationship is not linear, and instead forms a triangular shape (ΔABC). The top edge of the triangular region (line AB) is formed by samples during midnight hours, which is when the cable, deck and truss should be at the same temperature. During the day, (line AC and line BC) the suspension cable tensions follow a trend with a steeper gradient. Line AC and BC form the other two edges of the triangular region, since the slope of the–diurnal relationship between the suspension cables' temperature and their tension gets steeper during summer months (when the cable is warmer), compared to the winter.

The cause for the formation of this triangular region becomes slightly clearer when the suspension cable tensions are plotted against the deck temperature instead, as shown in Figure 6.47. The diurnal relationships between the deck's temperature and the suspension cable tension has the same gradient throughout the year (~-31.3kN/°C), which indicates a direct daily response of the suspension cable tensions to the behaviour of the deck.
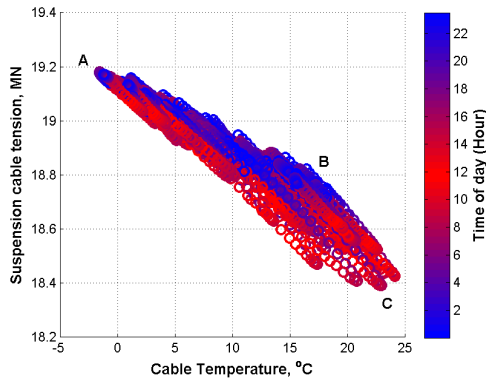
Figure 6.46: Time dependence of simulated suspension cable tension vs. Suspension cable temperature.
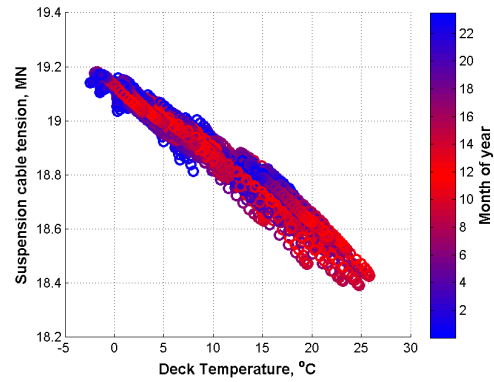
Figure 6.47: Time dependence of simulated suspension cable tension vs. Deck temperature.

Despite the suspension cable tensions bearing more of a relationship to the deck temperature than the temperature of the suspension cable itself, there remains a few nonlinearities in Figure 6.47 that have yet to be taken into account. A regression analysis was performed on the simulated suspension cable tensions to identify these other variables. Table 6.5 shows that a good linear fit utilises the temperature ("temp.") of the deck, suspension cable and truss, as well as the sway of the Plymouth and Saltash towers (PX and SX, respectively). The expansion and vertical deflection of the deck structure could be incorporated as variables, but their quasi-static response is mostly dependent on the temperature of the deck, truss and cables. Using the temperature of the deck structure rather than its shape also provides a closer correlation to the simulated suspension cable tension.

Table 6.5: Correlation of FE simulated suspension cable tensions to regression analysis predictions.

Variables	Correlation coefficient
Cable temp.	0.9614
Deck temp.	0.9774
Truss temp.	0.9077
Deck temp. + Truss temp.	0.9886
Deck temp. + Cable temp. + Truss temp.	0.9895
PX + SX	0.9643
Cable temp. + PX + SX	0.9761
Deck temp. + Cable temp. + Truss temp. + PX + SX	**0.9966**
Expansion @ CG062 (mid-span) + Vertical deflection @ CG062 + Cable temp. + PX + SX	0.9806

The prediction from the regressions analysis provided a decent match to the results from the FE model, as shown by the mostly linear relationship in Figure 6.48. The calculated coefficients imply that suspension cable tensions decrease not only when the temperature of the suspension cables increase, but when the towers move inwards towards the main span and

when the thermal gradient of the deck structure increases (since the coefficient associated with the truss temperature is positive, and vice versa). The latter in particular is significant, since it suggests some relaxation of the suspension cable tensions may be associated with a thermal gradient across the deck structure, causing a vertical rise in the deck structure.
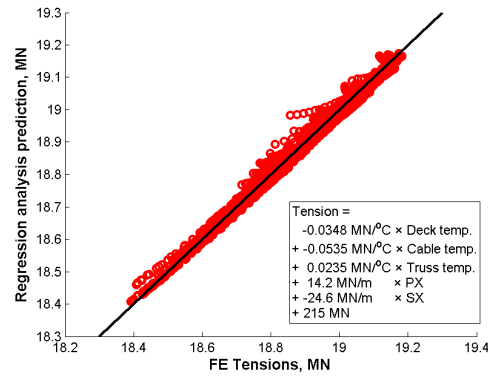
Figure 6.48: Regression analysis on the suspension cable tension.

6.5 SUMMARY

In order to predict the solar radiation applied to the bridge, a method for approximating the levels of cloud cover at any time was developed based upon the monitored temperature gradient of the bridge. The method provides a good match between the simulated bridge temperatures from the FE model and temperatures monitored from the structure, both for the day of data used to calibrate the model and the 60 days for the whole year used to check the performance of the model. The largest errors are generally found in winter, when the cloud cover predictions are affected by days with spring-like weather.

Via the monitored and simulated time series of the bridge, the investigation showed evidence of thermal lag between the deck, suspension cable and towers. The time difference between the peak temperatures of the deck and the suspension cable elements is approximately 1 hour, since the cable is insulated by its wrapping. As the concrete towers require more heat to warm up than the steel deck, and are less able to lose heat from their surface by radiation and convection (since their convection and emissivity coefficients are smaller), their peak temperature occurs approximately 1.5 hours after the peak temperature of the deck during the winter, and 3 hours later during the summer.

The structural response determined from the FE model shows that the expansion of the bridge is mostly determined by the deck and the truss temperature in an almost equal contribution. Regression analyses indicate that a rise in cable temperature also causes the mid-span of the

bridge to lower, although a thermal gradient in the deck structure creates a slight upwards deflection, typically providing a 3% contribution to the overall vertical displacement of the bridge deck. Any nonlinear behaviour observed between the bridge temperatures and the structural displacements is related to moderately high levels of solar radiation, which creates thermal gradients across the deck structure.

The simulated tower temperatures suggests that heat from the previous day is retained overnight and carried through to the next day, due to the thermal properties of concrete. Slightly jagged profiles in the monitored Saltash tower and stay cable deflections may also indicate a coupling in their thermal responses, since its proximity to the expansion gaps allows the tower to move independently from the overall structural, unlike the Plymouth Tower. It would be interesting to observe the monitored temperature data from the East and West faces of both towers to confirm this behaviour.

The monitored stay cable tensions show an elliptical relationship with suspension cable temperature, cables connected to the Plymouth tower showing this effect more than those connected to the Saltash tower. This response correlates with the monitored deflections from the towers, indicating that the delayed thermal response of the concrete tower and its curvature due to thermal gradients, affects the stay cable tensions. The simulated suspension cable tensions show a relationship not only with the temperature of the cable itself, but also with the deflection of the towers and the upwards curvature of the deck caused temperature gradients.

REFERENCES

Barber, C.B., Dobkin, D.P. & Huhdanpaa, H., 1996. The Quickhull Algorithm for Convex Hulls. *ACM Transactions on Mathematical Software,*, 22(4), pp.469–483.

Branco, F.A. & Mendes, P.A., 1993. Thermal actions for concrete bridge design. *Journal of Structural Engineering*, 119(8), pp.2313–2331.

Churchward, A., 1981. Prediction of Temperatures in Concrete Bridges. *Journal of the Structural Division*, 107(11), pp.2163–2176.

Elbadry, M.M. & Ghali, A., 1983. Temperature variations in concrete Bridges. *Journal of Structural Engineering*, 109(10), pp.2355–2374.

Hirst, M.J.S., 1984. Thermal loading of concrete bridges. *Canadian Journal of Civil Engineering*, 11(3), pp.423–429.

Ho, D. & Liu, C.-H., 1989. Extreme Thermal Loadings in Highway Bridges. *Journal of Structural Engineering*, 115(7), p.1681.

Johnson, I.R., Riha, S.J. & Wilks, D.S., 1995. Modelling daily net canopy photosynthesis and its adaptation to irradiance and atmospheric CO2 concentration. *Agricultural Systems*, 50(1), pp.1–35.

Liu, H., Chen, Z. & Zhou, T., 2012. Theoretical and experimental study on the temperature distribution of H-shaped steel members under solar radiation. *Applied Thermal Engineering*, 37, pp.329–335.

Minhoto, M.J.C., Pais, J.C., Pereira, P.A.A. & Picado-Santos, L.G., 2005. Predicting asphalt pavement temperature with a three-dimensional Finite Element method. *Transportation Research Record: Journal of the Transportation Research Board*, 1919, pp.96–110.

Moorty, S. & Roeder, C.W., 1992. Temperature-Dependent Bridge Movements. *Journal of Structural Engineering*, 118(4), p.1090.

Rivington, M., Bellocchi, G., Matthews, K.B. & Buchan, K., 2005. Evaluation of three model estimations of solar radiation at 24 UK stations. *Agricultural and forest meteorology*, 132(3-4), pp.228–243.

Tong, M., Tham, L.G. & Au, F.T.K., 2002. Extreme thermal loading on steel bridges in tropical region. *Journal of Bridge Engineering*, 7(6), p.357.

Tong, M., Tham, L.G., Au, F.T.K. & Lee, P.K.K., 2001. Numerical modelling for temperature distribution in steel bridges. *Computers and Structures*, 79(6), p.11.

Woodward, S.J.R., Barker, D.J. & Zyskowski, R.F., 2001. A practical model for predicting soil water deficit in New Zealand pastures. *New Zealand Journal of Agricultural Research*, 44(1), pp.91–109.

Xia, Y., Chen, B., Zhou, X. & Xu, Y.L., 2012. Field monitoring and numerical analysis of Tsing Ma Suspension Bridge temperature behavior. *Structural Control and Health Monitoring*.

Xia, Y., Xu, Y.L., Wei, Z.-L., Zhu, H.-P. & Zhou, X.-Q., 2011. Variation of structural vibration characteristics versus non-uniform temperature distribution. *Engineering Structures*, 33, pp.146–153.

Yim, J. & Wang, M.L., 2010. Temperature effects on cable stayed bridge using health monitoring system: a case study. *Structural Health Monitoring*, 10(5), pp.523–537.

CHAPTER SEVEN

EFFECT OF VEHICULAR LOADING ON SUSPENSION BRIDGE PERFORMANCE

7.1 INTRODUCTION

The previous chapters have shown that thermal loads affect the quasi-static and dynamic response of the Tamar Suspension Bridge. However, there are other environmental and operational conditions acting on the structure, which may have a similar diurnal loading pattern as the thermal loads.

One of these loading conditions is the total mass of traffic on the bridge. Not only would the imposed load cause additional deflections in the deck and saddles of the tower, but the tensions in the suspension and stay cables would increase. The additional mass upon the deck and extra tension in the structure may also manifest as variations in the dynamic properties. We have already seen evidence of the thermal loads in Figure 6.39, where the stay cable tensions in both the Saltash and Plymouth tower increase simultaneously at rush hour – despite the Saltash and Plymouth stay cable tensions having a differing relationship with the bridge's temperature (one inverse, the other direct).

This chapter aims to demonstrate that the presence of various levels of traffic has an influence on the structural response of the Tamar Suspension Bridge. In the first section, sample time-series of modal frequencies are presented, offering a good indication that traffic levels affect the dynamic properties of the structure significantly. The second section presents traffic counts from toll records and approximations for the mass of traffic on the structure to show how the flow of traffic across the bridges changes over the course of a year, as well as during a day.

The remainder of the chapter considers the relationship of the total mass of the vehicles with the performance of the bridge through a combination of the long-term monitoring data and theoretical results produced from the validated Finite Element (FE) model. This study is used to determine the magnitude of deflection of the deck and towers under increasing levels of traffic, as well as changes in the tensions of the suspension and stay cables. The investigation concludes with some observations on how the dynamic properties simulated from the FE model change, which comprises of the bridge's natural frequencies, modal masses and structural damping.

7.2 TIME SERIES AND VARIATION OF FREQUENCIES

7.2.1 DIURNAL FLUCTUATIONS OF THE FREQUENCIES

From several years of monitored, one of the most notable features were the diurnal variations viewed the time series of the bridge's natural frequencies, a 4 day sample of which is shown in Figure 7.1. In all five of the observed modes the frequency drops during the day, becoming its lowest at midday before rising again throughout the evening. The most variation is seen in the results collected for the first lateral mode, LS1a, which may change by as much as 5% of its base value.
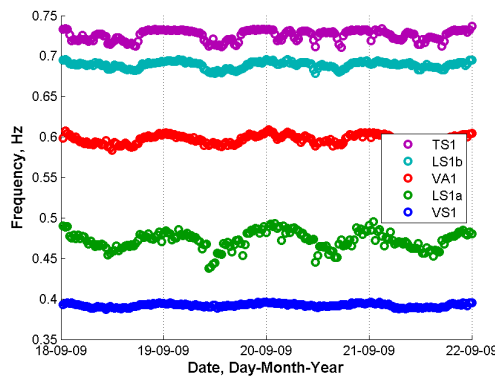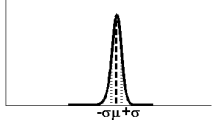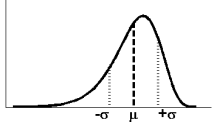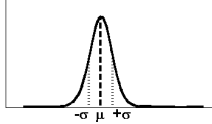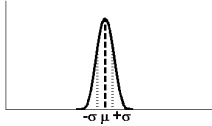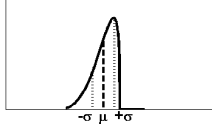
Figure 7.1: Frequency time series.

Inspection of the distribution of the modal frequencies in Table 7.1 shows that all but one of the observed frequencies has a standard error less than 1%, while that for LS1a is more than twice this range. The skew of the frequencies for most of the modes is negative, which implies that there are longer tails in the frequency distributions below the mean, rather than above it, which biases the mean.

While the standard error is low, the challenge for Structural Health Monitoring (SHM) research is that damage and deterioration may cause similarly small changes in the global response of the structure which need to be discriminated from those occurring naturally.

Table 7.1: Statistical properties of the modal frequencies.

Mode	Shape	Mean μ, Hz	Standard Deviation σ, Hz	Standard error, $\frac{\mu}{\sigma}$	Skew, $\frac{\mu_3}{\sigma^3}$	Distribution Profiles
1	VS1	0.391	0.00252	0.64%	-0.313	
2	LS1a	0.472	0.01176	2.49%	-0.802	
3	VA1	0.596	0.00573	0.96%	-0.080	
4	LS1b	0.688	0.00368	0.54%	+0.019	
5	TS1	0.728	0.00530	0.73%	-0.795	

where μ_3 is the third moment about the mean.

On close inspection the frequency time series formed trapezoidal profiles with plateaus between 08:00 and 17:00, which suggests that dynamic characteristics of the bridge relate to the levels of traffic. Examples of this behaviour are shown in the first three modes in Figure 7.2 to Figure 7.4, where the 31 days of time series results collected from June 2009 are rearranged by the hour they occurred. Additionally the behaviour of frequency data collected during the weekend is markedly different from data from midweek; the time series profiles appearing more rounded, and less deviation in the frequencies.
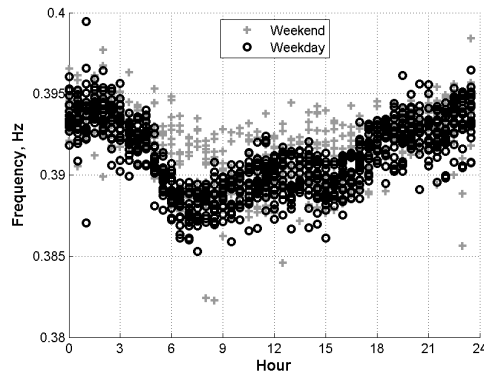
Figure 7.2: Diurnal variation frequencies for VS1.
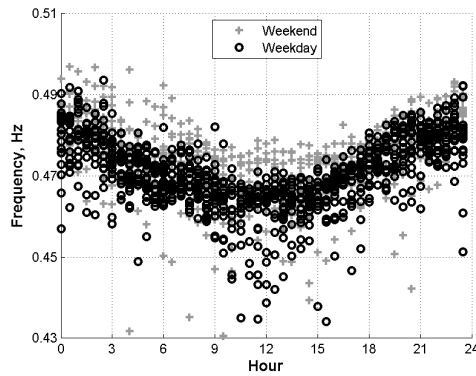
Figure 7.3: Diurnal variation frequencies for LS1a.
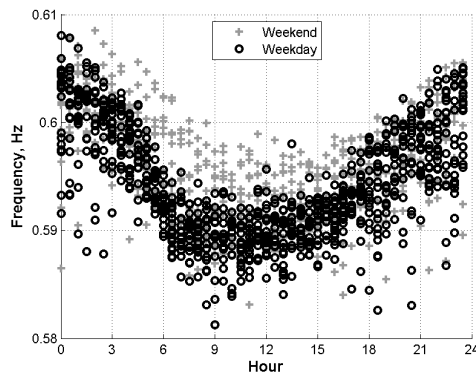
Figure 7.4: Diurnal variation frequencies for VA1.

7.2.2   DETERMINATION OF PERIODICITIES IN THE FREQUENCY DATA"

Since the data have been separated into groups for weekday and weekend performance the time intervals are uneven and discrete Fourier transform cannot be used. Hence Lomb-Scargle periodograms were obtained, which is designed for unevenly spaced signals (Press & Rybicki 1989).

The procedure for identifying the spectral power for each sampling frequency of interest f_s is

as follows: Given a set of data values $\vec{x} = \begin{bmatrix} x_1 & \cdots & x_N \end{bmatrix}^T$ and the times which they occur $\vec{t} = \begin{bmatrix} t_1 & \cdots & t_N \end{bmatrix}^T$, the mean ($\mu$) and variance ($\sigma^2$) of the data in $\vec{x}$ is first identified, and a circular frequency is determined for each sampling frequency of interest ($\omega_s = 2\pi f_s$). Consequently, a constant time offset for each sampled frequency $\hat{t}_s$ is computed by

$$\tan(2\omega_s \hat{t}_s) = \frac{\sum_{i=1}^{N} \sin(2\omega_s t_i)}{\sum_{i=1}^{N} \cos(2\omega_s t_i)} \tag{7.1}$$

The spectral power p for each value of ω_s is defined by Equation 7.2.

$$p(\omega_s) \equiv \frac{1}{2\sigma^2} \left\{ \frac{\left(\sum_{i=1}^{N} (x_i - \mu) \cos(\omega_s t_i - \omega_s \hat{t}_s) \right)^2}{\sum_{i=1}^{N} \cos^2(\omega_s t_i - \omega_s \hat{t}_s)} + \frac{\left(\sum_{i=1}^{N} (x_i - \mu) \sin(\omega_s t_i - \omega_s \hat{t}_s) \right)^2}{\sum_{i=1}^{N} \sin^2(\omega_s t_i - \omega_s \hat{t}_s)} \right\} \tag{7.2}$$

Finally, periodicities in the observed data can be distinguished by arranging the spectral powers and the sampling frequencies as Lomb-Scargle periodograms.

The application of the constant $\hat{t}_s$ makes $p(\omega_s)$ independent for all the times in $\vec{t}$. This choice of offset makes Equation 7.2 identical to the equation one would obtain if estimating the harmonic content of a data set at a given circular frequency ω_s via linear least-squares fitting to the model $x(t) = A\cos(\omega_s t) + B\sin(\omega_s t)$. The method is computationally heavy; it takes $M \times N$ operations to determine M frequencies from a data set of size N. However, since the method weights data on a point-by-point basis (rather than time-by-time, like Fourier transforms), it is considerably advantageous for applications where the data is uneven. The spectral power is reweighted by the variance of the observed data, so it does not represent the deviation of the observed mode's natural frequency, but shows the most significant periodicities in the data.

The periodograms presented in Figure 7.5 to Figure 7.7 show the periodic behaviour of the first three frequencies, suggesting the presence of harmonics in the data. The largest peak in the periodograms indicates a diurnal response of the natural frequencies, occurring exactly once per day. The smaller peaks that occur at 0.85 and 1.15 show that the response is not perfectly

periodic. Additionally the VS1 data contain second and third order harmonics which represent the departure from a perfectly sinusoidal character. The periodic responses shown in these periodograms may be attributable to the troughs forming between 06:00 and 09:00 in the time series of the natural frequencies, which may relate to high levels of traffic during rush hour. These observations point to the need to explore in detail the effects of traffic on modal properties. These harmonics are barely visible for LS1a and VA1, indicating the natural frequencies may not be as highly influenced by the traffic on the bridge as VS1.
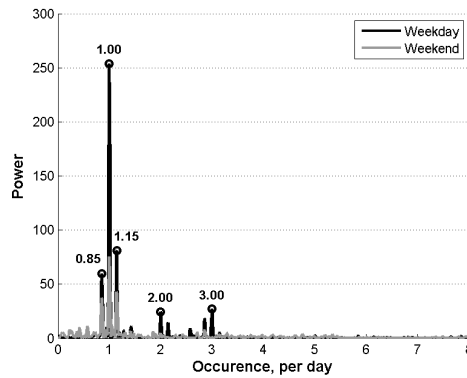
Figure 7.5: Lomb-Scargle periodogram for VS1 frequencies.
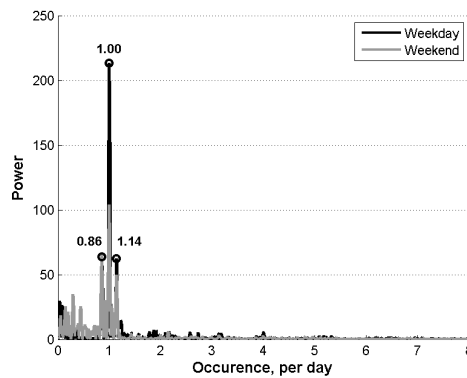
Figure 7.6: Lomb-Scargle periodogram for LS1a frequencies.
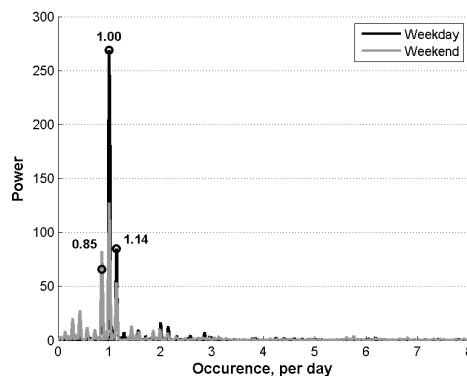
Figure 7.7: Lomb-Scargle periodogram for VA1 frequencies.

7.2.3 TYPICAL TRAFFIC JAM CAPTURED BY THE MONITORING SYSTEMS

The bridge monitoring has also enabled real-time viewing of the structure's behaviour, providing the ability to spot anomalous behaviour, either by visual inspection of web viewer chart or by automated detection process. Once such an event is identified, a wider set of sensor data can be investigated to determine whether the behaviour is consistent with other responses, and hence a true anomaly, or is a sensor error.

One such event occurred on the 11th of April 2011, when stay cable tensions peaked at 08:00, as shown in Figure 7.8. Usually variations in P2 and S2 tensions mirror each other over a daily cycle due to the thermal expansion of the deck (as seen in Chapter 4) and it is unusual for P2 and S2 tensions to *both* increase at the same time, especially during a short period. This is a clear performance anomaly.
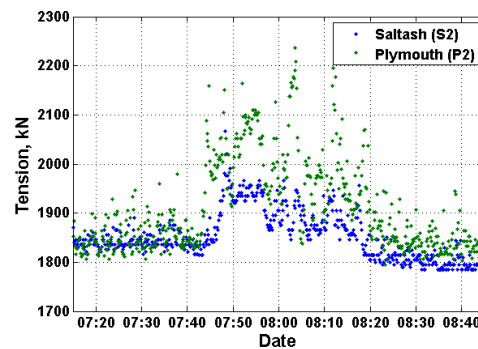
Figure 7.8: Stay cable tensions on the morning of the 11th of April, 2011.

Webcams on the Plymouth tower capture images of the traffic on the bridge every 30 seconds. Figure 7.9 shows that the bridge was experiencing a 20 minute long traffic jam at the time; three Plymouth-bound traffic lanes were filled by closely spaced, slow moving traffic as shown by the right-hand image. Such jams are uncommon, with more evenly distributed and faster moving traffic, as in the left-hand image. It seems that the additional mass of the bridge-long traffic jam increased the stay cable tensions by 200kN. This event provides an opportunity to study the effect of traffic alone, without any wind or thermal effects.

Figure 7.9: Webcam images of the deck. Left: At 8:30am. Right: At 8:50am.

Further investigation of the collated responses also showed that the vertical deck acceleration levels attenuate at the time of the loading, shown in Figure 7.10. This reduction in the dynamic response is consistent with the slower traffic speeds.
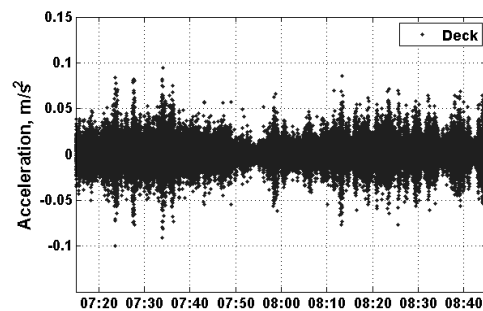
Figure 7.10: Vertical deck acceleration near the time of traffic jam.

To detect successfully any damage in the bridge, both the diurnal and abnormal, yet undamaged, variations of the structural response require identification, so that damage detection thresholds are adjusted accordingly. Since the time series suggests a degree of variation is due to the presence of traffic, the next step is to quantify the changes relating to the vehicle loading.

7.3 DETERMINATION OF GROSS TRAFFIC MASS

7.3.1 VEHICLE CLASSIFICATION AND POPULATIONS

As well as the instrumentation on the bridge, toll records provide hourly-sampled data that categorize and count the vehicles travelling from Saltash to Plymouth. From the total records of eastbound traffic there are ten possible vehicle categories, 4 of which include trailers. Since they represent a small percentage of the bridge traffic, they are included in a higher tier. These categories are presented in Table 7.2, of which almost 93% of the vehicles using the bridge are classed as a car or a van. The average gross weight of the vehicles was determined from a

study by the British Department for Transport (2008). While cars and vans are in the same classification, vans have nearly double the average gross weight of a car. In order to determine a reasonable weight for CLASS02 vehicles it was assumed that British cars make up 404.1 billion kilometres of road usage, whilst vans use 68.2 billion kilometres (Department for Transport 2008). This would mean that nearly 86% of the vehicles in this category are cars, which is used to factor the vehicle weight accordingly.

Table 7.2: Vehicle classification and bridge traffic.

Class	Vehicle	Average gross vehicle weight, kg.	% of monitored population
CLASS00	Unknown	N/A	0.01
CLASS01	Motorcycles, etc.	0*	1.75
CLASS02	Cars	$(0.856 \times)$ 1500	92.92
	Vans	$(0.144 \times)$ 2600	
CLASS03, CLASS06	Two axle HGV**	6800	3.33
CLASS04, CLASS07	Three axle HGV**	17400	0.61
CLASS05, CLASS08, CLASS09	Four (or more) axle HGV**	22800	1.39

Note: For CLASS02 the average gross vehicle weight is 1660.

* Unknown average mass; treated as negligible to the overall mass of traffic.

** HGV: Heavy Goods Vehicles

Figure 7.11 shows a seasonal variation of car and van crossing each month, in the Saltash-Plymouth direction only. Considering the largest numbers are during summer, the increased traffic levels can be attributed to holiday traffic returning from Cornwall. The number of HGVs travelling across the bridge on the other hand remains constant throughout the whole year.
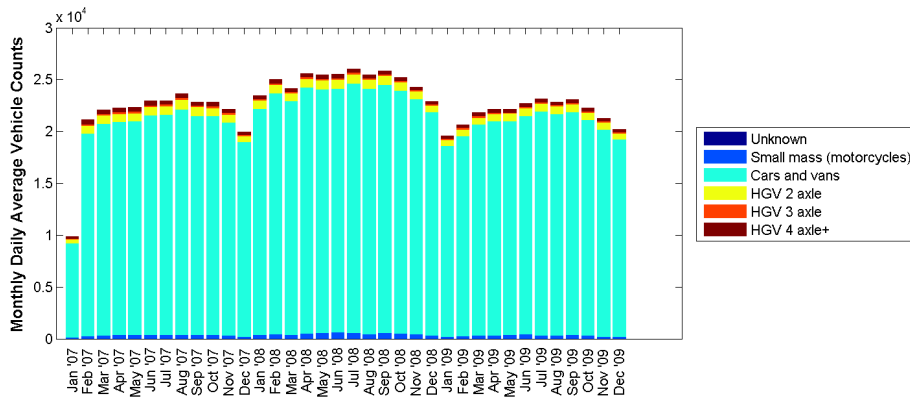
Figure 7.11: Daily average number of vehicles, per month.

The only data available on the Bridge traffic flow is from the toll records and the web-cam images. There is no information on whether or not the HGVs are laden, the actual vehicle weights or the axle spacing. An approximate value for mass of each vehicle was determined by multiplying the traffic counts by the average weight of a vehicle as given in Table 7.2. Cars provide the majority of the traffic mass on the bridge, as shown by Figure 7.12, with four axle HGVs also providing a significant portion of the remaining total mass due to their large weight.
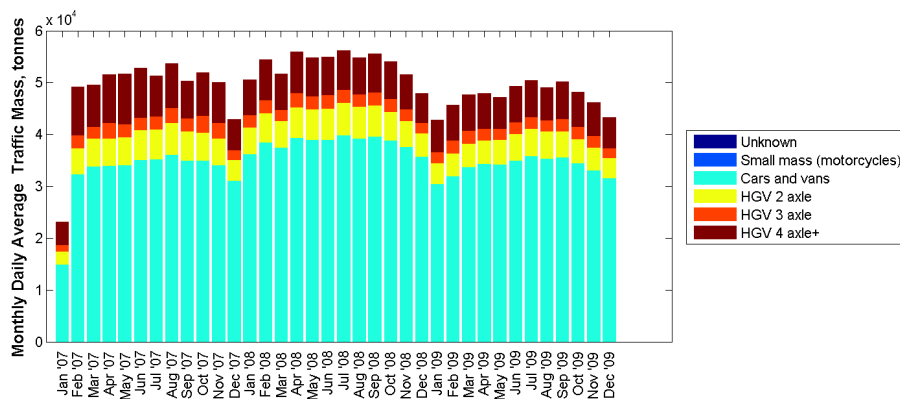
Figure 7.12: Total mass of vehicle classes, per month.

While seasonal variation of the traffic could be significant, this investigation only concerns daily variations, and the effects of varying mass and load on the structure. Figure 7.13 presents averages for the Plymouth-bound hourly traffic mass arranged in 24 one-hour bins, for samples collected mid-week and at the weekend respectively. The trapezoidal profile is a mirror of the profile previously seen in the frequency results (Figure 7.2 to Figure 7.4); both graphs have a plateau between 07:00 and 17:00 and a distinct peak at 08:00 caused by rush-hour traffic. The similarities in the results suggest that the ideal time to identify the modal properties of the bridge would be between midnight and 04:00, when the levels and mass of traffic on the bridge are very low. It is also the time when temperatures are most stable.

The traffic mass for records collected at the weekend have a different hourly profile compared to records collected midweek. The weekend traffic does not have a pronounced peak at 08:00, but instead a shallower rise and fall, that peaks at 11:00. The number of HGVs travelling at the weekend is reduced, so the majority of the additional mass on the bridge consists of cars and vans. Due to the change in commuter behaviour over the weekend, the mass of traffic on the bridge reduces by about a third.
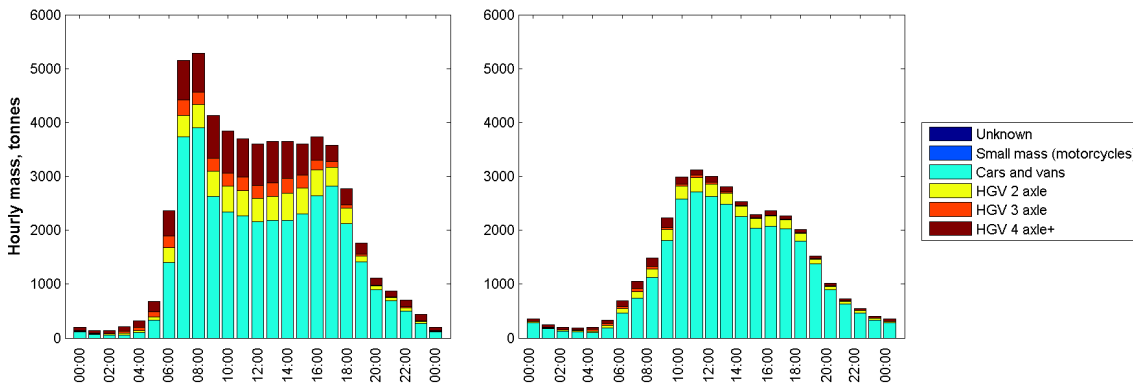
Figure 7.13: Mean mass of traffic per hour. Left: Mid-week traffic. Right: Weekend traffic.

7.3.2 DERIVATION OF VEHICLE LOADING

To consider how the additional vehicle mass may affect the static and dynamic properties of the bridge, the hourly traffic counts are reduced into half-hour samples to match the sampling rate of bridge response data. Assuming that each hourly count consists of the number of vehicles within the subsequent hour, a linear interpolation can be applied to determine the traffic at 15 and 45 minutes past the hour, as demonstrated in Figure 7.14. This value would then be halved so that the half-hourly counts should sum towards the hourly counts. The timestamps for the records were then reduced by 15 minutes so that they were located at 00 and 30 minutes past the hour.

Since vehicle counts were unavailable for the Plymouth to Saltash direction, the interpolated value needed to be increased to approximate traffic moving in both directions. One method is to double the half-hourly counts, which assumes that at any moment the traffic moving in one direction is the same travelling in the other. The alternative was to flip the vehicle counts about 13:00 (so morning traffic became afternoon, and vice versa), which assumes that the traffic travelling in the morning makes a return journey during the afternoon. There is a similarity in the average hourly traffic mass (Figure 7.13) to the frequency time series (mode VS1, Figure 7.2, in particular), which indicates a sharply rising peak at 08:00 and a smaller, shallower peak at 17:00. Since the traffic appears to act differently during the afternoon

compared to the morning, it was opted to approximate total vehicle counts by simply doubling the interpolated values.
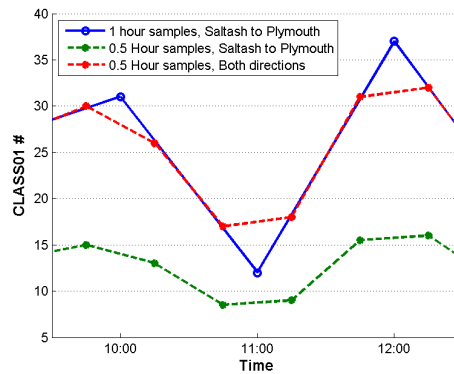
Figure 7.14: Example of the half-hourly interpolation of hourly toll counts.

Since this investigation is concerned with the direct and indirect effects of traffic on the bridge at any one time, these half hourly results need to be reduced to estimate the average number of vehicles on the bridge in that half-hour period. Assuming a vehicle travels at the 30mph speed limit across the 563m length of the bridge, the crossing takes 42 seconds. Therefore the average number of vehicles on the bridge would be approximately 1/43rd of the half-hourly count.

This was checked by comparing the vehicle mass determined this way from a single day of toll records, shown in Figure 7.15, to traffic masses determined from 144 webcam images on the same day in Figure 7.16. This was confirmed with another day's worth of webcam images, shown in Figure 7.17 and Figure 7.18. It is noted from the webcam images (Figure 7.16 and Figure 7.18) that there is almost no traffic bridge during the early hours of the day, yet there are several vehicles crossing late in the evening. The presence of traffic after the 17:00 rush hour further supports the previous decision to double the interpolated vehicle counts (in Figure 7.14). Fitting a 24th order polynomial to the results produced a similar profile as the toll records, with a peak either forming at rush hour (for weekday traffic) or at noon (for weekend traffic). The ratio of the peaks between half-hourly gross traffic masses from vehicle counts to vehicle mass determined from webcam images is almost 42:1; reasonably close to the ratio approximated using the average vehicle speed.
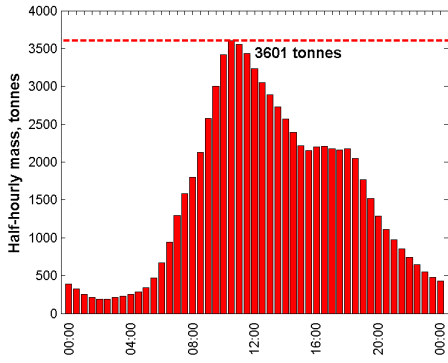
Figure 7.15: Half hourly traffic mass for Saturday 20/6/2009.
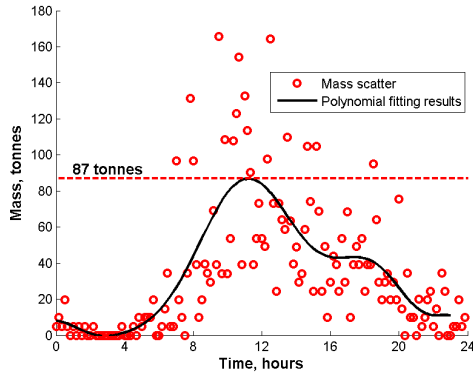
Figure 7.16: Traffic mass determined from webcam images, for Saturday 20/6/2009.
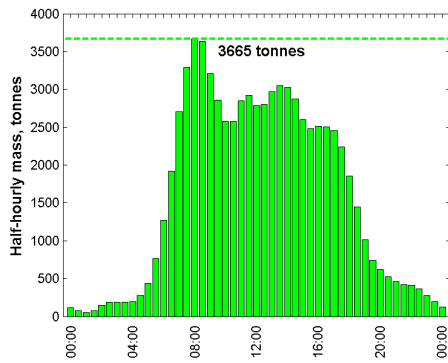
Figure 7.17: Half hourly traffic mass for Thursday 7/1/2010.
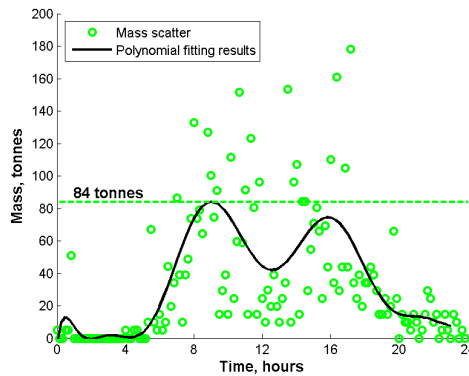
Figure 7.18: Traffic mass determined from webcam images, for Thursday 7/1/2010.

Consequently, the half-hourly sampled data shown in Figure 7.19 are reduced by a factor of 42.51, which was determined from the webcam images, to approximate the traffic mass on the bridge in Figure 7.20. Admittedly, this approach does not consider changes in traffic flow when the bridge is fully laden or empty, but since both the traffic and quasi-static modal properties of the bridge are being handled in 30 minute averages, as opposed to instantaneous values, this is a reasonable approximation.
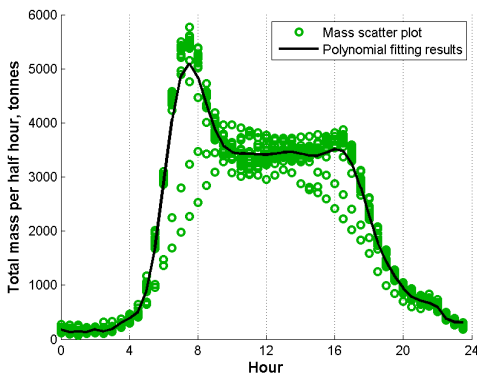
Figure 7.19: Total mass on bridge during a daily period, for 15 daily samples.
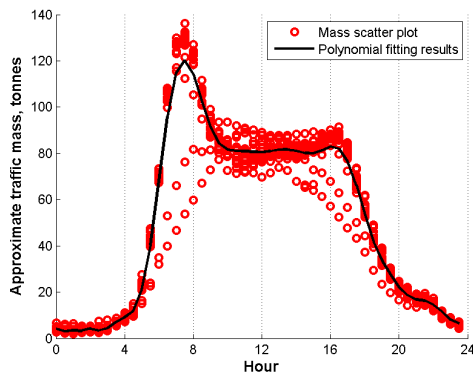
Figure 7.20: Assumed mass of traffic on bridge during a daily period.

7.4 APPLICATION OF VEHICLE LOADS TO FE MODEL

While several years of toll records are available that can be used to establish the effect of traffic mass on the structural response, there are several unknowns in the process. Apart from not knowing the exact vehicle masses and the traffic Plymouth-Saltash traffic flow, the spacing of axles in vehicles and of the vehicles on the bridge would affect the behaviour of the structure. Scatter due to other environmental conditions could be further reduced, at the expense of reducing number of usable samples. This is where the finite element (FE) model can be usefully applied, to determine the response of the bridge with other conditions remaining perfectly constant.

In smaller-span bridges it is understood that there will also be some variation caused by dynamic loading, such as vehicle-structure interaction or when the transit time of the vehicle comes close to the period of a particular mode. For this study only the first five modes are being considered, where the frequencies are below 1Hz. Since the frequencies of the vehicle would be high by comparison, and it takes almost 40 seconds for the vehicle to travel across the span, it was not expected that dynamic excitation would cause considerable variation in the modal properties of the bridge.

Since the observed frequencies are low, the modes are more likely to respond as quasi-static deflections rather than as a vibration. So for this investigation the bridge behaviour was studied by adding frozen vehicle masses to the deck. The masses are applied as a row of three 1660kg rigid vehicles on the structure, each vehicle made up of two masses at either axle, assuming an even distribution, and incrementing their number in successive runs of the FE model as shown in Figure 7.21. To consider the effects of asymmetrical applied masses, the same analyses were performed with the vehicles located on the northern lanes (Figure 7.22), one line of traffic situated on the cantilevered deck.
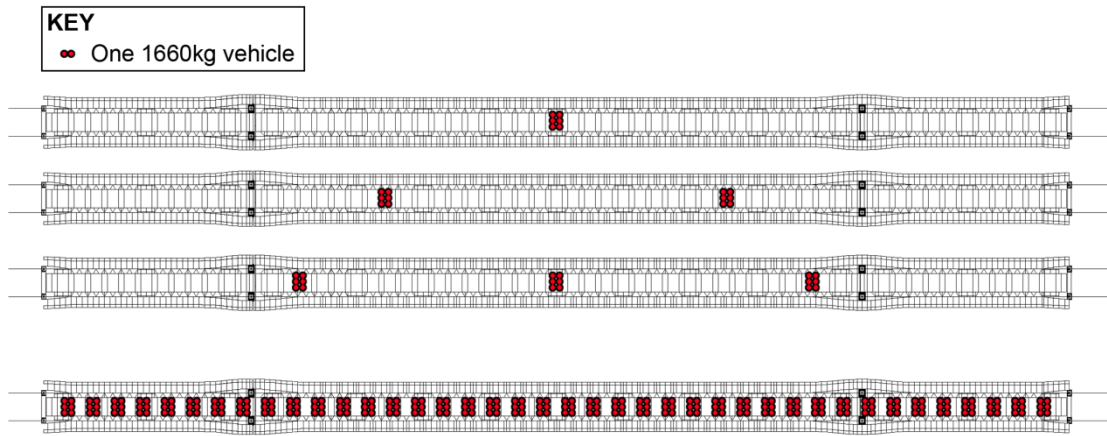
Figure 7.21: Distribution of 3, 6, 9 and 120 vehicles, along the central lanes.
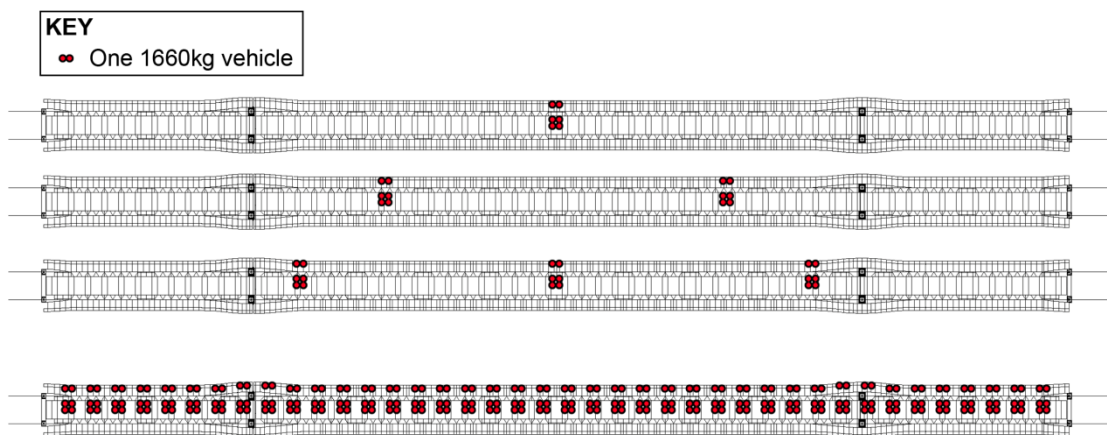
Figure 7.22: Distribution of 3, 6, 9 and 120 vehicles, along the northern lanes.

7.5 CHANGES IN STATIC CONFIGURATION CAUSED BY MASS OF TRAFFIC

7.5.1 VERTICAL DEFLECTION OF BRIDGE AT MID-SPAN

In this section the relationship of vehicle mass and bridge vertical deflection is studied using monitored data and FE simulations. For the monitored data, only samples were used with less than 5 mph wind speeds and cable temperatures between 5 and 10°C to minimise impact of wind and temperature variations.

Due to even mass distribution in the FE simulation, the deflection of the bridge increases linearly with the load, as shown in Figure 7.23. The initial unevenness in the plot is due to the position of the masses; a vehicle at mid-span causes a similar deflection to that of two vehicles located at quarter span. For the monitored results in Figure 7.24 the scatter is considerable and may derive from several causes (e.g. the non-zero temperature variation), as well as the uncertain vehicle masses. The line of 'best-fit' suggests a downward trend, the deck deflecting

202

downwards with the increased traffic mass like the FE model results, although the regression is ill-conditioned.
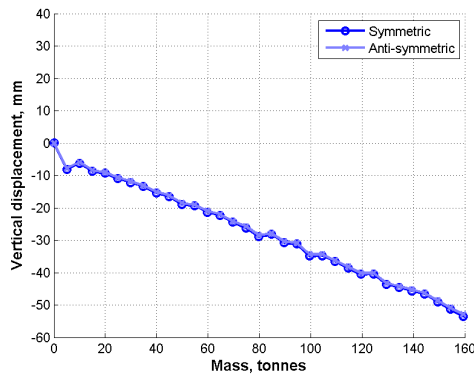
Figure 7.23: Simulated maximum deck deflection vs. Traffic mass
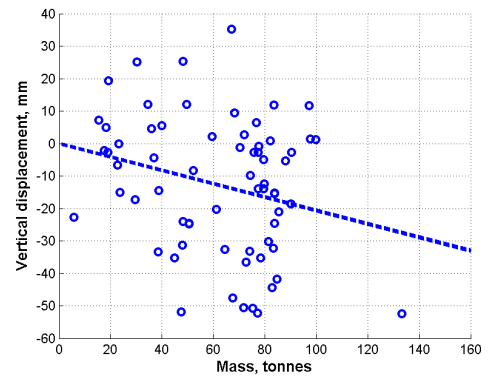
Figure 7.24: Monitored maximum deck deflection vs. Traffic mass

7.5.2 CHANGE IN SUSPENSION CABLE TENSION

Figure 7.25 shows the simulated, almost linear, relationship of suspension cable tensions with traffic load. Suspension cable tensions rise in the side spans as well as in the main span in order to maintain horizontal force resolution at the saddle. The variations in the suspension cable tension are also visible in the hanger tensions in Figure 7.26, which increase from the larger imposed load, as well as the increased vertical component in the suspension cables.
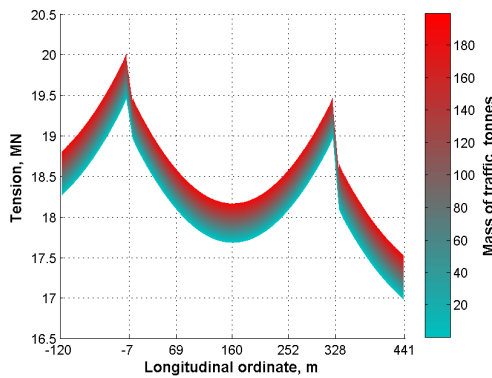
Figure 7.25: Variation of suspension cable tension against traffic mass.
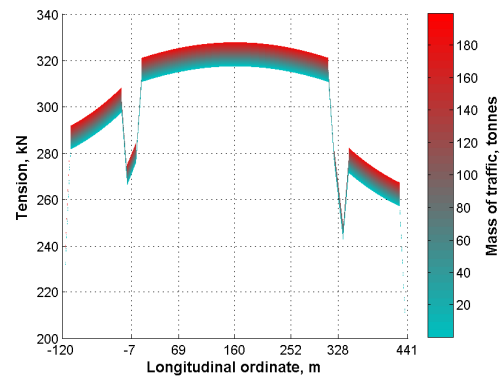
Figure 7.26: Variation of hanger tension against traffic mass.

7.5.3 LONGITUDINAL SWAY OF TOWERS

Since the suspension and stay cable tensions change with vehicle load, towers may be expected to deflect as well with respect to the magnitude of the load on the deck. Although the suspension cable tensions vary to avoid the towers from deflecting, force imbalances may still occur caused by differing cable lengths and angles. The FE results in Figure 7.27 show that the towers move towards the mid-span as the traffic mass increases, although the deflections are negligible; their ratio to the tower height is about $1:1.3 \times 10^4$ when the bridge is fully loaded. The monitored deflections were highly susceptible to the wind speed, so the samples

in Figure 7.28 were limited to less than 1mph winds. The trends from the monitored results suggest similar behaviour to the FE model, although the data are dispersed, likely due to remaining thermal effects.
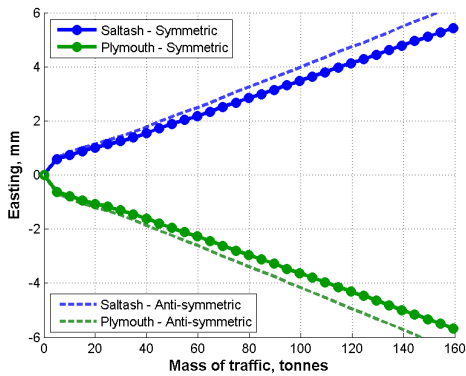
Figure 7.27: Simulated span-wise tower deflection vs. Traffic mass.
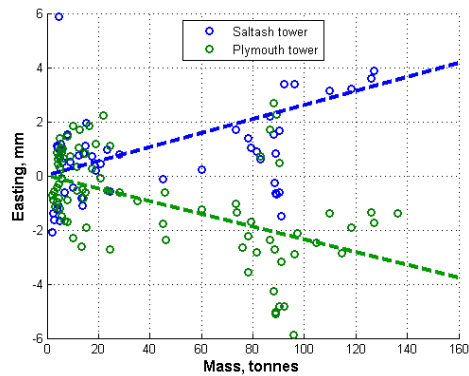
Figure 7.28: Monitored span-wise tower deflection vs. Traffic mass.

7.5.4 CHANGE IN STAY CABLE TENSIONS

The FE model results in Figure 7.29 and Figure 7.30 show the expected linear increase of stay cable tensions with vehicle load. This appears to be consistent with the loading from the traffic jam shown in Figure 7.8, although on observation alone it appears the FE model has underestimated the simulated tension variation by 200kN. A slight offset is present in the S2 and P2 when there are only two vehicles on the span, when the vehicles are located close to the stay cable terminations. Stay cable tensions on the side spans also rise to resolve horizontal forces at the towers, although the variation in cable tensions is not as significant as the simulated variation of the suspension cable tensions. This may suggest that in the existing structure a larger portion of the traffic mass is accommodated by the suspension cable tension rather than the additional stay cables.
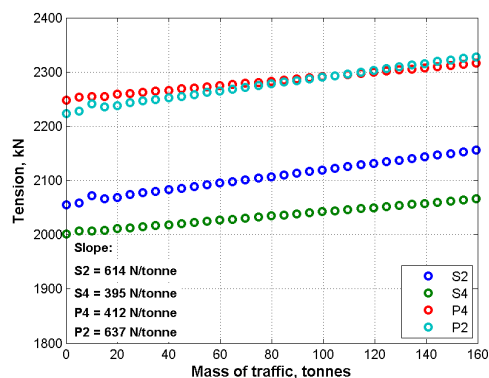
Figure 7.29: Simulated main span stay cable tensions vs. Traffic mass.
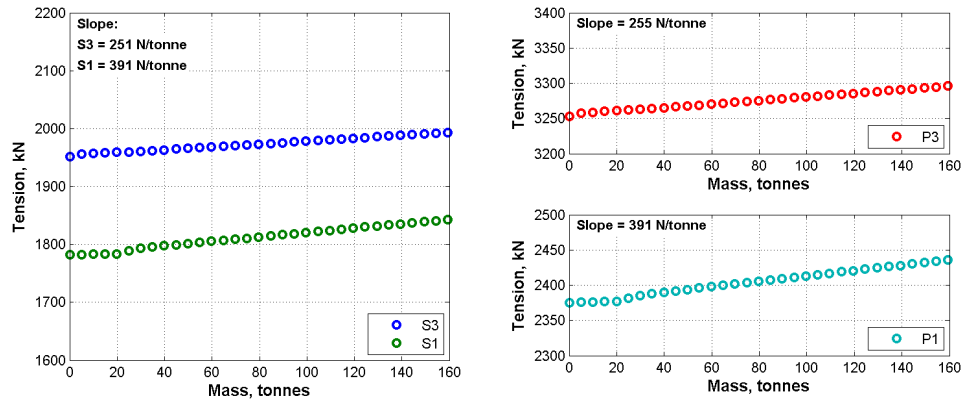
Figure 7.30: Simulated side span stay cable tensions vs. Traffic mass

As with deck deflections, the monitored stay cable tensions in Figure 7.31 and Figure 7.32 are too dispersed to discern a clear relationship with traffic load, and there is little improvement on the clarity of the trends if observed cable temperature range is reduced to samples between 5 and 7°C. This suggests that it is difficult to appreciate how stay cable tensions change when observing long periods of data, since the various thermal responses of the structure obscure subtle trends. The change in stay cable tensions would be better appreciated under a shorter time frame under controlled conditions (which may be investigated with the trailer in Chapter 7). It is noted that the dual trends in the Plymouth stay cable data in Figure 7.31 are due to thermal lag in the cables; there are different tensions in the cable when it warms up compared to when it cools.
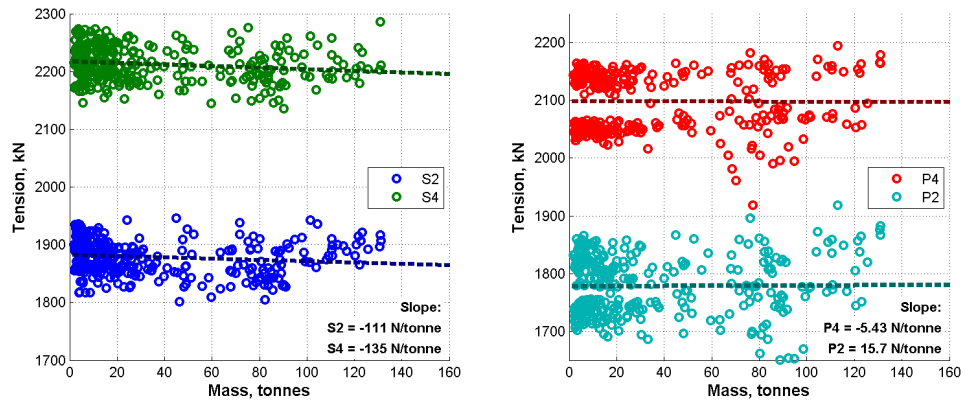
Figure 7.31: Main-span stay cable tensions, from monitoring results.
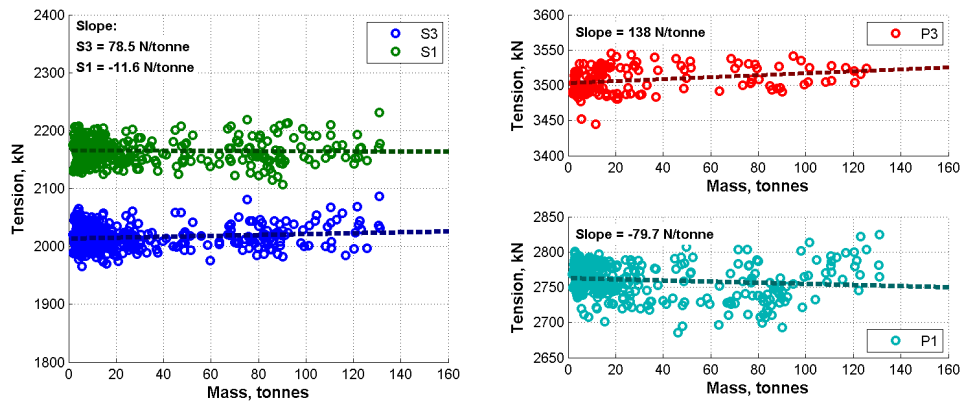
Figure 7.32: Monitored side-span stay cable tensions vs. Traffic mass.

7.6 CHANGE IN MODAL PROPERTIES CAUSED BY TRAFFIC MASS

7.6.1 VARIATION OF DECK STRUCTURE'S NATURAL FREQUENCIES

Following the analysis of the quasi-static properties, variations in the dynamic properties of the bridge were also investigated. Compared to the mass of the bridge deck, which is 3190 tonnes, the gross mass of traffic should be relatively insignificant; the largest observed traffic mass in this study is 160 tonnes. However, considering the modal frequency variations observed in the time series and the FE predicted variation in the suspension and stay cable tensions, this section uses the finite element model to check that if traffic should have a discernible effect on modal properties.

Out of the first five monitored frequencies shown in Figure 7.33, the first three modes show a clearly correlated inverse linear relationship with the traffic mass. Hence the trapezoidal plots seen in the frequency time series are also linked with the total mass of traffic on the structure. As expected by inspection of Figure 7.1, the mode with the largest change due to the traffic mass is LS1a, whose frequency varies by 0.0320% per tonne.

Mode VS1 and VA1 frequencies both vary by 0.0137% and 0.0163% per tonne respectively, although the frequency of mode VA1 is almost twice that of VS1, so its variation is much more obvious within the time series. Additionally, previous investigations (in Chapter 5) have shown that the frequency of mode VS1 is insensitive to thermal effects, so the observed variation must be caused by the traffic loading on the bridge. This result could be useful for indirect approximation of the traffic mass on the bridge.

37% of the sampled frequencies for TS1 lie within 0.5% of the baseline frequency, 0.73Hz, which is why there is no obvious trend in the results unless a line of "best fit" overlays the

data. However, 80% of the samples lie below the baseline, which is due to the frequency data for this mode being highly skewed (as seen previously in Table 7.1); the mean frequency for TS1 (0.728Hz) is smaller than its median frequency (0.730Hz). Wind speeds could not have been a factor as observed samples were limited to 5mph speeds at most. Since the reduction in the response seems to be unrelated to the extent of the vehicle load, it is suspected that the eccentricity of the loading might be the cause for this behaviour.
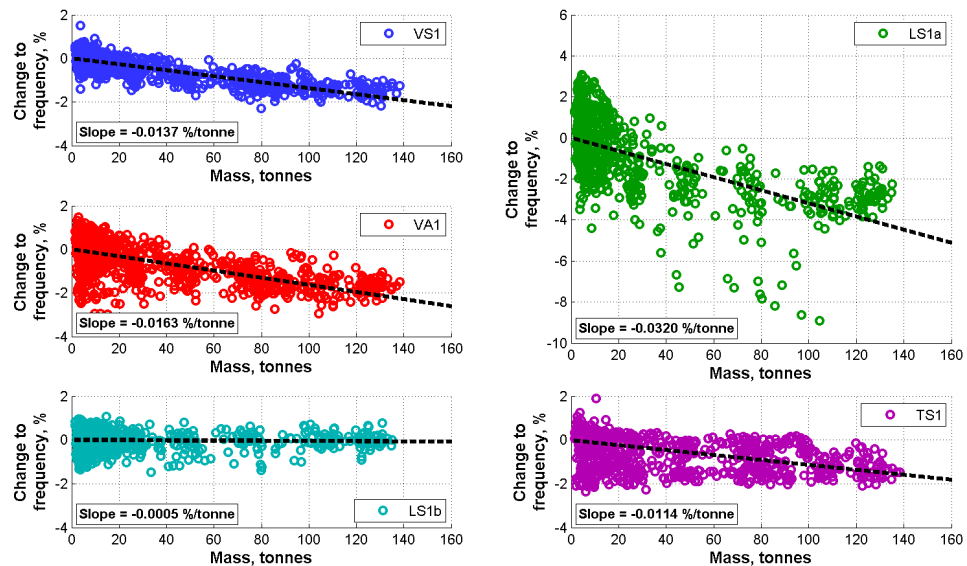
Figure 7.33: Monitored frequency change vs. Traffic mass.

The FE model results in Figure 7.34 show an inverse linear relationship between traffic mass and modal frequency for modes VS1 and VA1, like the monitored frequencies, decreasing by 0.00725% and 0.00690% per tonne respectively. The biggest difference between Figure 7.33 (measurement) and Figure 7.34 (analysis) is the behaviour of the first lateral symmetric mode LS1a, for which the FE model predicts an increase in frequency as the traffic mass increases, rather than a decrease. The effect of increased tension stiffening is greater than that of the additional mass on the bridge; the latter effect dominates for the vertical modes. Since the monitored results for this mode have clearly shown a consistent drop during the day, there is a mystery in the behaviour of this mode.

For the simulations with vehicles aligned down the centre lanes (Figure 7.21), the increase in frequency for TS1 is very slight compared to the other modes. This increase in frequency is consistent with the increased tension stiffening in the cables as for LS1a. However, when vehicles are instead located in the three northern lanes (Figure 7.22), Figure 7.35 shows that the frequency of TS1 decreases by -0.0027% per tonne; the eccentricity of the masses

increasing the rotational inertia of the deck section. This reduction is consistent with observations from the monitoring, the eccentric loads arising due to only one cantilevered lane being used for vehicles.

For simulations with bridge eccentrically loaded, the frequency of LS1b drops linearly with the level of additional mass, as for the vertical mode frequencies. However, for simulations with vehicles positioned down the central lanes of the bridge, the frequency-mass relationship forms a slight arc with negative curvature reaching a minimum of 0.2% less than its base value near 110 tonnes of applied mass. On closer inspection of the FE results, shown by the graphics in Table 7.3, increasing the imposed mass causes LS1b to adopt a similar mode shape as a neighbouring 'cable mode' (that is dominated by the movement of the suspension cables) at 0.727Hz. Beyond 110 tonnes, when most of the modal displacements in LS1b are in the cables rather than the deck, the mode consequentially responds more to the tension stiffening in the cable than to changes in the mass of the deck, like LS1a, and increases as a result.
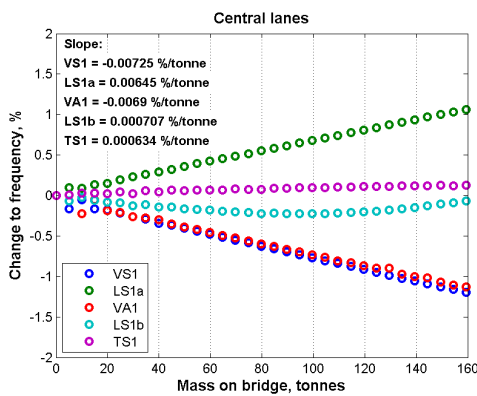
Figure 7.34: Traffic mass vs. frequency change, vehicles in centre lanes.
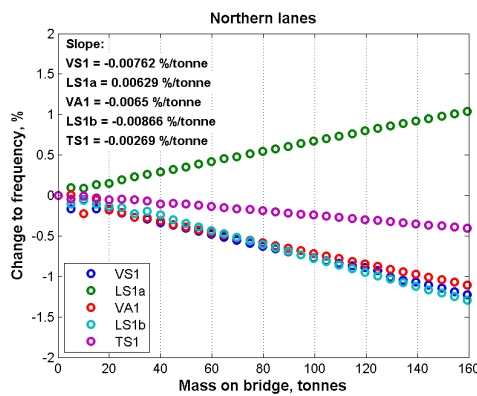
Figure 7.35: Traffic mass vs. frequency change, vehicles in northern lanes.

Table 7.3: Variation in modal properties for mode LS1b.

Mass	Central Lanes	Northern Lanes
0	Frequency: 0.7376Hz Modal mass: 1455 tonnes	Frequency: 0.7376Hz Modal mass: 1455 tonnes
79.7 tonnes (48 vehicles)	Frequency: 0.7360Hz Modal mass: 320 tonnes	Frequency: 0.7347Hz Modal mass: 104 tonnes
159.4 tonnes (96 vehicles)	Frequency: 0.7372Hz Modal mass: 115 tonnes	Frequency: 0.7296Hz Modal mass: 572 tonnes

Since some traffic travelling from Saltash to Plymouth travel uses the northern cantilever of the bridge, it would be worthwhile seeing whether the torsional mode shows a different response between morning and evening rush hours. At first appearances of the hourly arranged time series for mode TS1 in Figure 7.36 the data are more dispersed than the first three modes (Figure 7.2 to Figure 7.4), and the diurnal trough is only 0.05Hz deep, 7% of its base value. However, given that the frequency of the mode drops more when vehicles are on the northern lanes, there is a large collection of samples between 06:00 and 09:00, where the frequencies reach the lowest values in the day. This supports that the traffic travelling at this time of day have a larger effect on TS1 than the vehicles travelling during the afternoon, and demonstrates the different responses observed in the FE results. The Lomb-Scargle periodogram of TS1 in Figure 7.37 also suggests a considerable influence from a second harmonic, similar to those exhibited in VS1 (in Figure 7.5) which are also attributed to rush hour traffic.
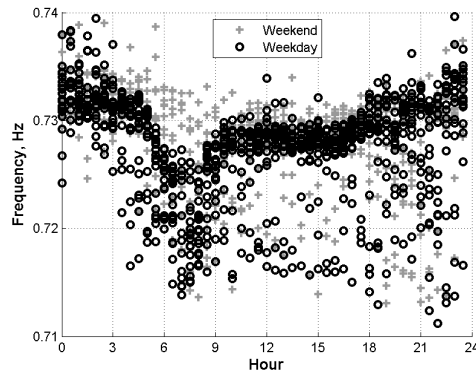
Figure 7.36: Diurnal variation frequencies for TS1.
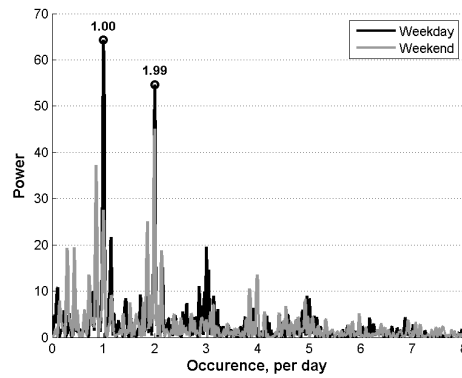
Figure 7.37: Lomb-Scargle periodogram for TS1 frequencies.

While linear relationships between the traffic mass and frequencies appear in both monitored and FE model results, the gradient of the trends from the monitored results listed in Table 7.4 are generally three times the slope of the FE model results. The table also highlights the different behaviour of mode LS1a between the monitored and FE model results, the slope of the monitored results being almost 5 times that from the FE model. This shows that while the procedure in the FE model is capable of demonstrating the change in dynamic response, it is unable to provide results that match the monitored data satisfactorily. Apart from variations caused by other ambient conditions, it is suspected that the stochastic distribution of the vehicles in space and time, as well as the location of heavy vehicles, create the deviations in the monitored results.

Table 7.4: Relationship of reported frequencies to applied traffic mass.

Mode	Monitored		FE model	
	Hz	Hz/tonne	Hz	Hz/tonne
VS1	0.394 +	-5.409×10^{-5}	0.403 +	-2.967×10^{-5}
LS1a	0.482 +	-15.405×10^{-5}	0.472 +	$+3.077\times10^{-5}$
VA1	0.602 +	-9.802×10^{-5}	0.537 +	-3.787×10^{-5}
LS1b	0.690 +	-0.350×10^{-5}	0.751 +	-2.663×10^{-5}
TS1	0.731 +	-8.313×10^{-5}	0.772 +	$+0.530\times10^{-5}$

7.6.2 CHANGES IN MODAL MASS

For the purposes of this investigation, the term "modal mass" defines a scalar parameter that relates to the level of response of a mode (Brownjohn & Pavic 2007). The scaling of the mode shapes presented here is that the point where the maximum response of a particular mode takes a unit value, and the modal mass is used as a physical interpretation of the modal displacements when the mode is excited. For example, for the same force and dynamical amplification factor, modes of vibration with large modal masses are more difficult to drive than those with small modal masses. Modal masses can be calculated as

$$m_n = [\varphi_n]^T \mathbf{M} [\varphi_n] \qquad (7.3)$$

where m_n is the nth modal mass in kg, $[\varphi_n]$ the $N \times 1$ nth unity scaled mode shape vector which has no units, and $\mathbf{M}$ an $N \times N$ mass matrix of a system with N degrees of freedom.

From the FE results in ANSYS, the modal masses are determined from the provided mass-normalised deck displacements as follow:

$$m_n = \frac{1}{\left(\max(\bar{\varphi}_n)\right)^2} \qquad (7.4)$$

where $\bar{\varphi}_n$ is the mass-normalised mode shape for the nth mode.

Table 7.5 presents the modal masses of the first five modes determined from the FE model, which shows that the largest modal masses when the bridge is unloaded are in VS1, VA1 and LS1b, all three being larger than 1400 tonnes. When the simulated vehicle masses are aligned

down the centre of the bridge, the largest variations of the modal masses from their unloaded

state are in modes LS1b and TS1, which differ by 92.0% and 42.8% respectively. The behaviour

for their variation is shown in Figure 7.38. For TS1, the increase in the modal mass is directly

related to the gross traffic mass on the bridge, its modal mass increasing by 0.252% per tonne.

The modal masses for the first three modes also increase linearly, but their base values only

changes by 0.0165% per tonne at most. In other words, for these four modes the FE model

suggests that the increase in traffic mass slightly reduces the response to a given dynamic load.

Table 7.5: Variation of simulated modal mass with increasing traffic mass.

	Central lanes				Northern lanes		
Mode	Modal mass, tonnes			Max. variation of modal mass, %	Modal mass, tonnes		Max. variation of modal mass
	Unloaded bridge	*Traffic: 80 tonnes*	*Traffic: 160 tonnes*		*Traffic: 80 tonnes*	*Traffic: 160 tonnes*	
1 (VS1)	1482	1503	1522	+2.7%	1490	1496	+1.0%
2 (LS1a)	348	349	351	+0.6%	323	304	-12.8%
3 (VA1)	1936	1963	1976	+2.9%	1954	1779	+4.3%
4 (LS1b)	1455	320	115	-92.0%	104	572	-95.9%
5 (TS1)	742	895	1059	+42.8%	817	908	+22.5%

However, the behaviour of the modal mass for LS1b is dissimilar to the other four observed

modes, its value decreases when higher levels of traffic are applied to the FE model.

Additionally the trend shallows as more mass is added; the modal mass of the unloaded

structure decreases from 1455 tonnes to 320 tonnes when loaded with 80 tonnes of traffic. As

mentioned previously for its natural frequency (Table 7.3), the drop in LS1b's modal mass is

due to the mode-shape taking on the characteristics of a neighbouring cable mode having a

reduced modal mass, and normalising to its reduced modal displacements.

Figure 7.39 shows that when the FE model is loaded on the northern lanes instead, the

relationship of modal mass to additional mass for several modes changes, in the same way as

demonstrated for the natural frequencies. While there is no significant change in mode VS1

and VA1, the modal mass of mode LS1a reduces further by 0.0778% per tonne. The

eccentricity of the vehicle masses also limits the increase in TS1's modal mass, rising by 0.127%

per tonne, as opposed to 0.252% per tonne when applied axially.

While the possible deviation in the modal mass of mode LS1b remains pretty high when the traffic is in the northern lanes, when the simulated traffic mass is larger than 95 tonnes the modal mass increases. On inspection of the mode shape (in Table 7.3), once LS1b takes on the properties of the neighbouring cable mode (at 95 tonnes), it reverts back to its original shape, with larger modal displacements taking place in the deck. However, this effect has not been observed in modal tests upon the bridge to date, so will require further investigation.
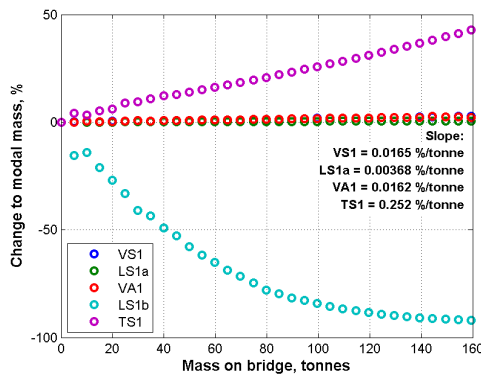
Figure 7.38: Change in modal mass vs. Traffic mass on bridge; traffic mass in central lanes.
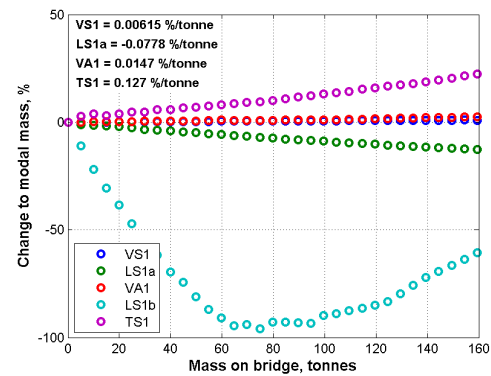
Figure 7.39: Change in modal mass vs. Traffic mass on bridge; traffic mass in northern lanes.

7.6.3 VARIATION IN MONITORED DAMPING WITH TRAFFIC MASS AND VERTICAL DECK ACCELERATION

As well as the variation in the frequencies, changes in the monitored modal damping were also investigated to check any relationship with vehicle traffic, and are presented in Figure 7.40. The damping for modes LS1b and TS1, which is relatively low among the damping values for all modes, shows very little change when the traffic mass is increased. On the other hand, there is a slight positive trend in the slopes for the first three modes, the largest change exhibited on LS1a which increases by 0.0082% per tonne. While it is not clear from the experimental results what causes the increase in damping with the additional vehicle mass, the damping shares a linear relationship with the vertical deck acceleration, shown in Figure 7.41. This may suggest in increase in friction at the joints in the deck and the truss as dynamic response levels increase.
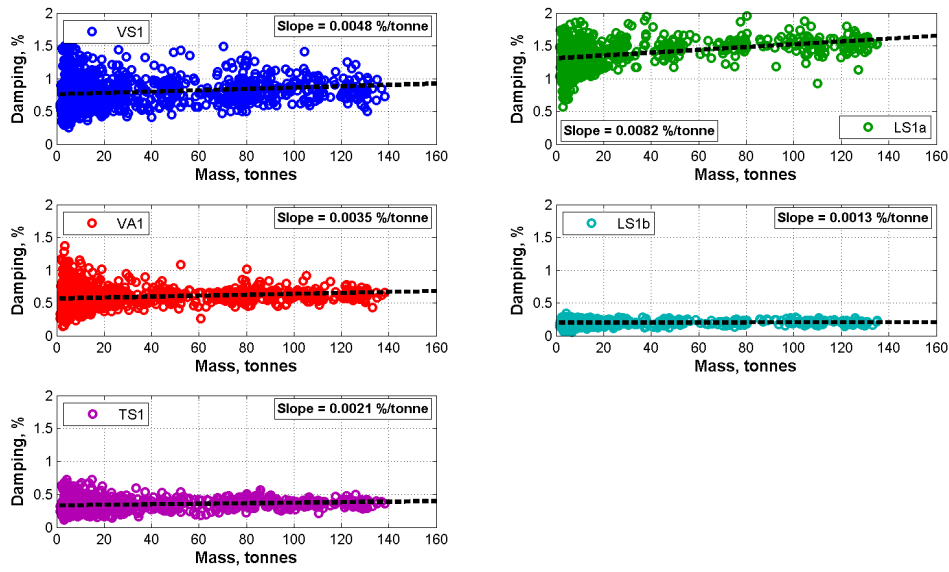
Figure 7.40: Monitored modal damping vs. Approximate traffic mass
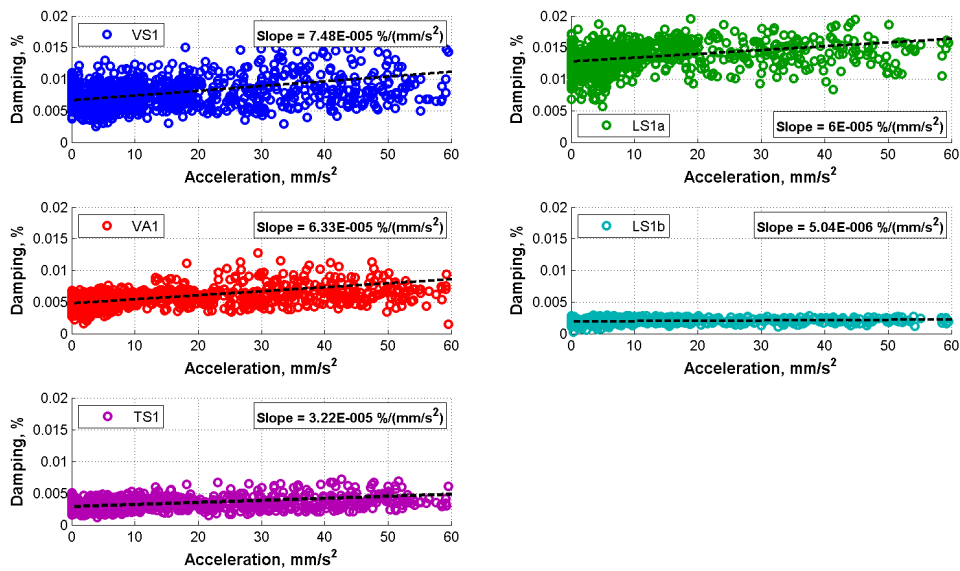
Figure 7.41: Monitored modal damping vs. Vertical deck acceleration

7.7 SUMMARY

FE analyses on the Tamar Suspension Bridge model suggested linear relationships between the mass of traffic on the bridge and the structural deflections. The data collected from the long-term monitoring system indicate that this behaviour is occurring on the actual structure, although clarity of trends is reduced due to non-stationarities in other forms of loading such as temperature. Assumptions about stochastic spacing of the vehicles in the actual structure, and the location of large point loads such as HGVs (which will be explored in Chapter 7) may also affect reliability of the observations.

The modal property data collected by the long-term monitoring system suggest that the natural frequencies decrease linearly with traffic levels. Changes in frequencies were replicated for most of the modes in the FE model, although there remain slight discrepancies between observed and simulated trends, which are likely due to the non-stationarities in other loadings. The results from the FE model also suggest that the eccentricity of the traffic loading pattern across the deck also has a significant influence, especially on the torsional mode.

There is some variation in the FE model simulated modal masses for mode LS1a and VA1 as the total traffic mass change. As with the natural frequencies, allocating the vehicle masses to one side of the bridge also modifies TS1 modal mass variation as traffic loads increase. A similar but lesser effect is observed in some other modes. The monitored results also suggest that there is an increase in damping for the first three modes as a result of the additional traffic on the structure.

Even with long periods of monitoring, performance data for a narrow range of loads is sparse. Identifying the response from monitored data also requires knowing details of axle load on each vehicle, lane occupied and span-wise location. This is possible to ascertain from monitored results, requiring time the vehicle enters bridge, its weight, speed and what lane it travels.

REFERENCES

Brownjohn, J.M.W. & Pavic, A., 2007. Experimental methods for estimating modal mass in footbridges using human-induced dynamic excitation. *Engineering Structures*, 29(11), pp.2833–2843.

Department for Transport, 2008. *Road Statistics 2007: Traffic, Speeds and Congestion*, London.

Press, W.H. & Rybicki, G.B., 1989. Fast algorithm for spectral analysis of unevenly sampled data. *The Astrophysical Journal*, 338, pp.277–280.

CHAPTER EIGHT

SUSPENSION BRIDGE RESPONSE DUE TO EXTREME VEHICLE LOADS

8.1 INTRODUCTION

It is a rare opportunity to monitor the response of a bridge when it is loaded by a trailer that is significantly heavier than the standard design heavy vehicle, the passage of a vehicle of an extremely heavy vehicle provides an excellent chance to excite a large civil structure and estimate its structural characteristics. Whilst ambient vibration tests do not require large excitation devices like a heavy vehicle, conditions such as traffic are not controlled, and weather conditions may vary during the testing period so that system identification procedures have to manage significant non-stationarities.

There are numerous papers that have described development of numerical models of a vehicle travelling across a bridge. The majority treat the vehicle as a series of spring-mass-dampers that are excited by the irregularities of the road (Mulcahy 1983; Green & Cebon 1997; Xia et al. 2000; Guo & Xu 2001; Haji-Hosseinloo & Bakhtiari-Nejad 2010). The resulting vehicle-structure interaction can lead to changes in the observed dynamic properties of the bridge (Yang et al. 1995; Yang 2004; Li et al. 2003; Kwon et al. 2005). There are also several documented site investigations monitoring the bridge deck vibration with excitation provided by a heavy vehicle (Mazurek & DeWolf 1990; Paultre et al. 1995; Calcada et al. 2005; Lin & Yang 2005; Yin & Tang 2011; Kim et al. 2011) .

The quasi-statically varying shape of cable supported bridges change during the passage of a heavy vehicle, due to the flexible deck structure and redistribution of forces in the cables. During a controlled vehicle loading the deflections at certain points in the structure might be tracked via positioning systems installed upon the structure, such as the investigations performed on the Forth Suspension Bridge in the UK (Roberts et al. 2006) and Batman cable-stayed bridge in New Zealand (Watson et al. 2007).

Chapter 7 discussed how the natural frequencies of the bridge structure changed as a result of the large added mass of vehicles. It is expected that similar behaviour may also be exhibited when there is a large concentrated mass on the structure. C.-Y. Kim et al. (2001) observed a change in the monitored natural frequencies of three bridges whilst under various traffic and heavy-vehicle loadings, However the variations experienced by the Namhae suspension bridge were very low, changing by only 0.01% at most. De Roeck et al. (2002) performed a numerical simulations of a vehicle traversing a box girder bridge, and showed how the change in the natural frequency of the modelled structure depended on the ratio of the vehicle's mass to the bridge. Law (2004) observed the first natural frequency of a simulated bridge decreasing as the vehicle moved towards its centre, the location of the vehicle affecting the dynamic

characteristics of the structure.

The focus of this chapter is a site investigation on the performance of Tamar Suspension Bridge during passage of a heavily laden vehicle, which provided an opportunity to observe changes in response to a travelling concentrated mass, with an unusual ratio of vehicle and bridge weights. The objective of this investigation was to record the deflection of the bridge deck and towers, as well as to check for any variation in modal properties.

The FE model of the bridge was used to provide a prediction of these responses via a series of static analyses and a transient analysis, which was compared against the results determined from the monitoring system. This investigation also uses the FE model to simulate the variation of the suspension and stay cable tensions as the bridge reconfigured to adapt to the moving loads. Finally, the frequencies of the structure are predicted via the FE model, and compared with limited analysis of the structure dynamic response component.

8.2 SITE INVESTIGATION ON THE TAMAR BRIDGE

8.2.1 TEST DETAILS

Full Scale Dynamics Ltd (FSDL), a University of Sheffield spin-off company founded by Vibration Engineering Section (VES) were contracted by the Tamar Bridge and Torpoint Ferry Joint Committee to record the deformation of the bridge while a 151 tonne electrical transformer for a power station was transferred from Plymouth to Saltash.

The trailer carrying the transformer crossed the bridge during the early hours of October 31st 2010, shown by Figure 8.1, and FSDL were on site to monitor and study bridge behaviour using their Structural Health Monitoring (SHM) system. The bridge was closed to avoid additional traffic loads, due to the abnormal bulk of the trailer; the bridge is designed to support 40 tonne vehicles, while the gross weight of the trailer and its tractors is approximately 269 tonnes: more than the gross weight of a traffic jam across the 335m main span.
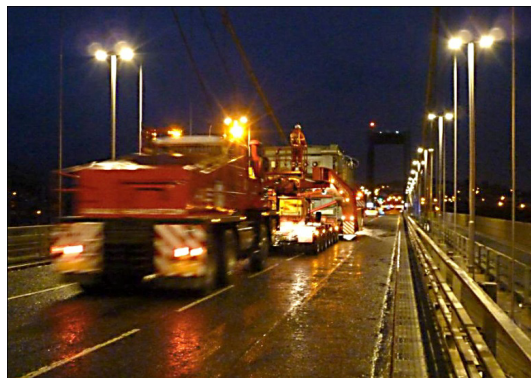
Figure 8.1: Trailer crossing the Tamar suspension bridge.

Two robotic total stations (RTS) located at the Tamar Bridge office tracked the position of two reflectors on the bridge: one monitored the reflector at the top of the northern Saltash tower; the other tracked the reflector at the centre of the main span. Accelerations were collected from accelerometers attached to one of the stay cables, aligned perpendicularly to capture its transverse and vertical movements. Signals from the deck accelerations at mid-span were also available, but were unfortunately too corrupted to be viable to include in this investigation. Another monitoring system on the bridge that was installed by Fugro also provided data on the stay cable tensions, as well as the weather conditions which were constant for the duration of the vehicle loading.

Since there was an interest in capturing as much of the bridge's behaviour as possible, the sampling rates were increased for the sensors on the VES system: the accelerometers read measurements at 32Hz, and the RTS measurements at 3.0Hz. Sensors on the Fugro system, such as those measuring the stay cable tensions, remained at their previous sampling rate of once every 10 seconds.

Figure 8.2 shows the longitudinal dimensions for the transport arrangement of the trailer, which is pulled by two FAUN trucks with an 8x8 wheelbase at either end. Wheelbase and axle weights were approximated from provided technical drawings and datasheets from similar tractor models (Inter-Commerz 2008). It is assumed the trailer supports 16.9 tonnes per axle with a 1.5m wheelbase along the length of the trailer, and 2.5m axle track. The container for the transformer is elevated clear from the road, providing a 15.2m unloaded gap along the deck.
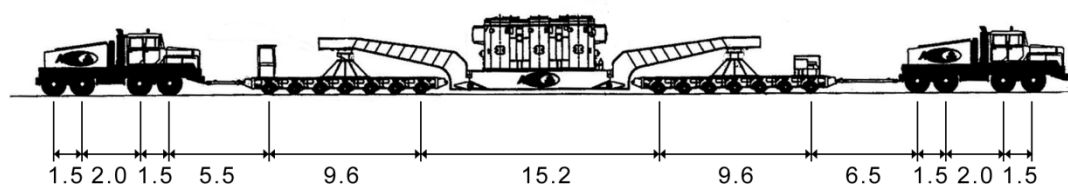
Figure 8.2: Trailer layout. Units are in metres.

The designed loading capacity of the Tamar Suspension Bridge is 1865 tonnes, if the load was distributed along the whole span of the bridge, or with a single 180 tonne vehicle if two of the lanes are closed off to other traffic. Prior to the site investigation AECOM, the consultant engineers, checked to see if the bridge could support a 295 tonne trailer with two 46 tonne trucks, and concluded the test could be run safely.

8.2.2 FINITE ELEMENT MODEL

Prior to the measurements, the Tamar Suspension Bridge FE model was used to determine which of the reflectors on the bridge best demonstrated the response of the bridge, as well as to establish an approximation for the expected magnitude of the deflections. Following the site investigation the FE model was later used as a comparison to the monitored results, as well as predicting additional related responses that were unrecorded.

To predict the effects of the vehicle on the observed dynamic properties of the bridge, the model was treated as a series of travelling masses. The vehicle model consists of 22 bodies: 4 for each tractor and 7 for each trailer as shown by Figure 8.3. The parameters used in the model are listed in Table 8.1.
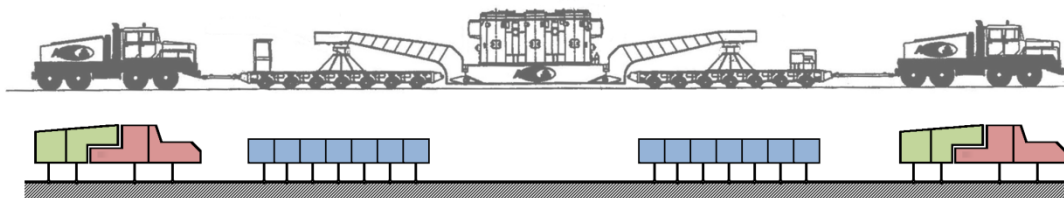
Figure 8.3: Distribution of tractor and trailer masses.

Table 8.1: Parameters for modelling the tractor-trailer model.

Parameter	Colour of mass in Figure 8.3	Value
Mass of tractor on front axles		3232.5kg
Mass of tractor on rear axles		1667.5kg
Mass of trailer upon each axles		16860.0kg

Due to the slow speed of the trailer the study was performed as a series of static analyses for each location of the vehicle. This would determine how the natural frequency of the bridge changed as the trailer crossed the structure. To illustrate the passage of the vehicle as smoothly as possible, the deck was meshed to a higher resolution than previous analyses, with divisions every 0.5m. The dimensions of the vehicle model were rounded to comply with this mesh size.

The timescale in the FE model was calibrated with the site investigation via the peak

deflections between the results, the Saltash tower's deflections in particular provided a suitable match. These recorded times were also used to approximate the speed of the vehicle, assuming to be constant, which was 5 miles per hour (~2.24m/s). The time between moving the vehicle masses from one mesh division to the next was 0.22 seconds. The approximate times when the centroid of the trailer passed particular locations was determined by the calibrated FE model results, and are presented in Figure 8.4.
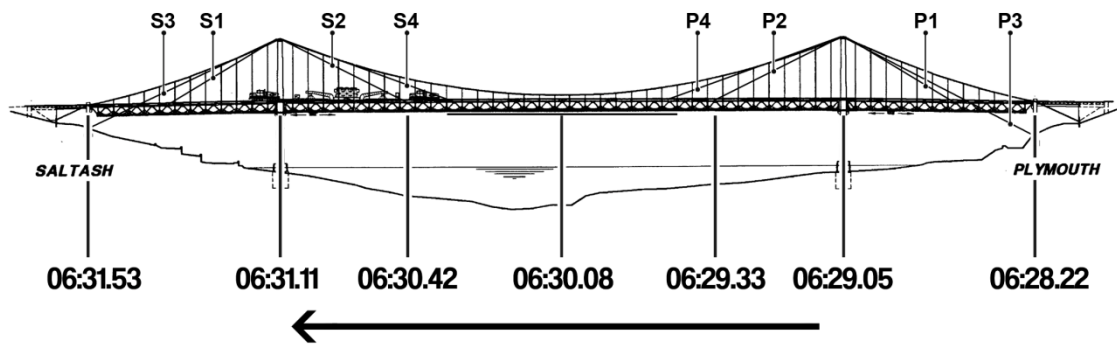
Figure 8.4: Passage of vehicle centroid across bridge, with approximate times.

8.3 QUASI-STATIC RESPONSE OF THE DECK TO THE TRAILER

8.3.1 MONITORED AND PREDICTED DEFLECTION OF THE MID-SPAN

Once the data for the site investigation and quasi-static analyses on the FE model were collected, the two were compared to validate the response of the modelled structure.

The shape of the line in Figure 8.5 demonstrates the significant negative vertical deflection when the trailer is on main span, reaching its peak at mid-span before returning to its previous state. The mid-span deflects vertically upwards when the trailer is on the side spans. As the truss girder is not continuous through the towers, the continuity has to be provided via the deflection of the towers and the suspension cables, which pull spans upwards when the neighbouring spans deflect downwards. An interesting feature is the pair of acute troughs in the FE model time series results; the gap created when the 15.2m of unsupported space between the trailers passes across the mid-span of the bridge. The slight spike in the monitored results might suggest this response was also observed on the actual structure.
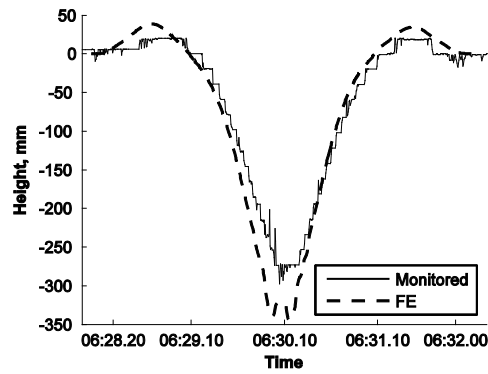
Figure 8.5: Vertical deflection of the mid-span.

The longitudinal response of the mid-span in Figure 8.6 shows that as the trailer enters the bridge, the mid-span moves east towards the bridge. This reaches a peak at approximately 06:29.45, when the trailer is close to the quarter span of the structure. This mid-span moves back west and passes back through its original displacement when the trailer arrives at mid-span, then continues in the westerly direction as the vehicle travels on the Plymouth side of the bridge. This 'S' shaped response is a result of the changing curvature of the bridge: when the trailer is at quarter span the bridge deck sags asymmetrically, and as a consequence the mid-span moves towards the depression created by the trailer.

 The mid-span also moves a little when the vehicle is on a side-span, as shown by a minor peak in the monitored results at 06:29. This appears to be due to the longitudinal continuity of the bridge deck at the Plymouth tower, since this response effects appears only very weakly when the vehicle is on the Saltash side span, beyond the expansion gap.
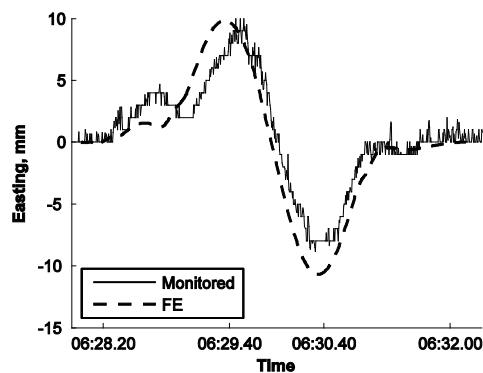
Figure 8.6: Longitudinal deflection of the mid-span.

8.3.2 PEAK DISPLACEMENTS OF THE DECK

Figure 8.7 and Figure 8.8 show the maximum positive and negative displacements of the bridge under the trailer load. 'Upper bounds' represent the maximum positive deflections for each longitudinal ordinate of the deck, determined as a 'peak hold'. Likewise 'Lower bounds'

represents 'peak hold' values on the largest negative deflections. 'Max disp.' is the bridge deflected shape for the vehicle location producing the largest absolute value of deflection.

In the case of the longitudinal deflection in Figure 8.7, 'Max disp.' corresponds to the trailer located at the quarter span near Saltash tower, causing the main span to move westwards. The Saltash side span moves eastwards, despite being detached from the main span, as a consequence of the continuity provided by the suspension and stay cables pulling the deck as the tower deflects. Taking the origin for the longitudinal ordinate as the expansion gap at the Saltash tower, the upwards curve between -7m and +120m is a result of the bridge's typical static configuration, where the stay cable tensions create slight crests in the bridge shape.
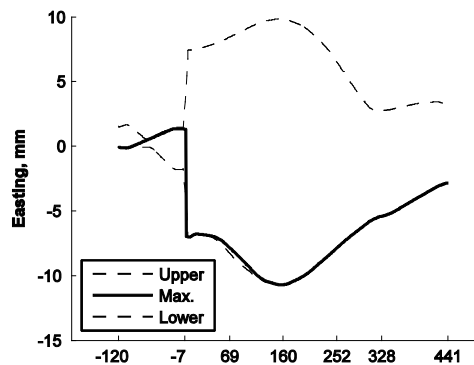
Figure 8.7: Spanwise values of maximum and minimum longitudinal deflections as vehicle crosses the bridge, along with deflected shape when vehicle is at quarter span.

'Max. disp.' in Figure 8.8 corresponds to when the trailer is located at mid-span, which causes the bridge deck to deform into a 'V' shape. It is noticed that the continuity of the bridge deck via the main cable and hangers also cause the side spans to displace vertically when the trailer is elsewhere on the bridge, as the time-series results for the main span suggest in Figure 8.5.

If the bridge was loaded by a traffic jam with the same gross mass as the trailer (270 tonnes), the mid-span would deflect by 87mm, compared to the 381mm mid-span deflection caused by the trailer. This significant increase in deflection caused by the trailer is because the mass of the traffic jam is distributed along the whole span of the bridge, which is the ideal loading condition for a suspension bridge, while the mass of the trailer is concentrated on a particular point of the bridge.
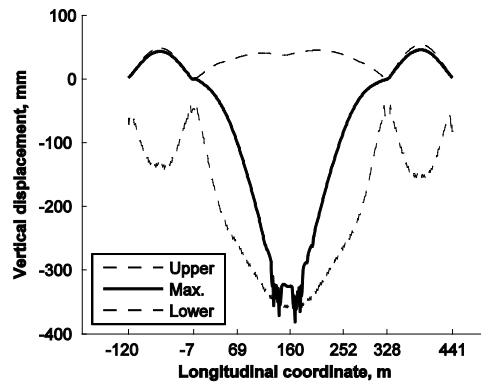
Figure 8.8: Span-wise values of maximum and minimum vertical deflections as vehicle crosses the bridge, along with deflected shape when vehicle is at mid-span.

8.4 QUASI-STATIC TOWER RESPONSE TO THE TRAILER LOAD

The vertical deflections of the deck discussed in the previous section suggest that some continuity on the adjacent spans is provided by the suspension cables as the loads in the cables adjust to the moving load. Therefore the towers would sway in response to the movements of the deck.

The easterly deflection of the Saltash towers shown in Figure 8.9 resemble the longitudinal displacements at mid-span; once the trailer moves onto the main span, the deflection of the deck causes both tower tops to move inwards. The towers revert to their original state once the trailer moves beyond the main span. The towers also deflect in the opposite direction once the trailers moves onto the Saltash side span, for the same reason. A similar but reversed response is exhibited on the Plymouth towers, which were not monitored.
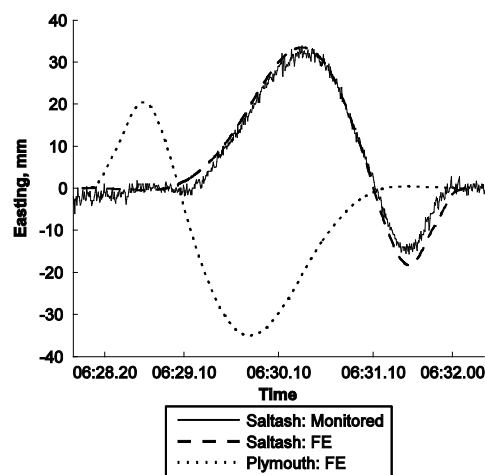
Figure 8.9: Longitudinal deflection of towers.

8.5 CHANGING CABLE TENSIONS

Since the deck deflects vertically and the towers sway as the trailer crosses the bridge, changes in the suspension and stay cables tensions, which links the tower and the deck, was expected.

Figure 8.10 shows that the tensions of the stay cables connected to the main span also peak when the trailer is near the mid-span. This is unsurprising, since in Chapter 7 we also observed the stay cable tensions peaking during heavy rush hour traffic. The peaks in the stay cable tensions occur at the same time as the trailer passes their connection to the deck (in Figure 8.4), indicating a direct relationship to the location of the trailer on the bridge. The tension of the stay cables closest to the towers, S2 and P2, provide the largest change in tension. Likewise these cables also relax significantly when the trailer is at the opposite main span location.
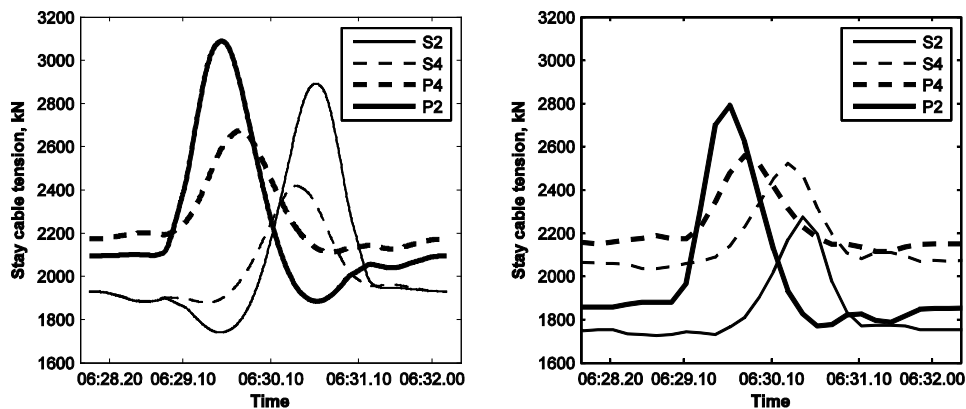
Figure 8.10: Main span stay cable tensions. Left: FE mode results. Right: Monitored results.

For tensions of the stay cables connected to the side spans, shown in Figure 8.11, the P1 and S1 stay cable tensions also peak when the trailer is situated at their deck connection. In addition, a smaller peak forms when the trailer is on the main span, which may be attributed to the main towers being pulled towards the main span.

Stay cables S3 and P3 slacken when the trailer is on their connecting side span since, unlike the other six pairs of stay cables, they anchor their connected tower saddle to the base of a side tower and are only affected by tower deflection. Similarly their tensions increases when the trailer is loading the main span since the towers are deflected towards the main span. There is also a slight crest in the tensions of stay cable P1 when the trailer is on the main span, which does not have an analogue for S1.
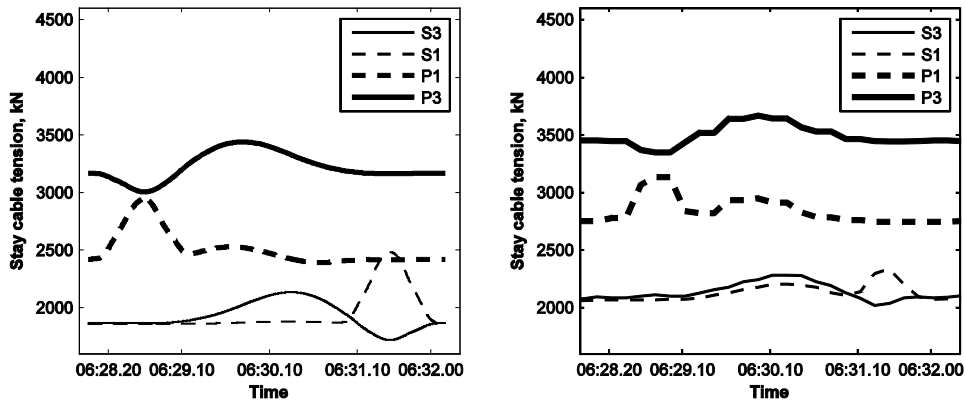
Figure 8.11: Side span stay cable tensions. Left: FE mode results. Right: Monitored results.

It was assumed that the stay cable tensions may alter the response of the suspension cable tensions, since the two are affected by the horizontal force equilibrium at the saddles. Figure 8.12 indicates that when the side spans are loaded, the predicted tensions in the loaded side-span's suspension cable reduces, as a result of the tower deflection caused by the stay cables. This differs from the response predicted by FE model of the bridge without the stay cables (Figure 8.13), where the side-span suspension cable tensions tauten when the same side-span is loaded.

Similarly the inclusion of stay cables to the structure causes the side-span suspension cables tensions to peak when the vehicle is at the quarter points of the main span, rather than halfway. This is caused by the suspension cables responding to the increasing main span stay cable tensions seen previously in Figure 8.10. The difference in magnitude of the tensions on Plymouth side span compared to Saltash side span is due to the different stay cable tensions on either tower, which were present in the unloaded structure. It should be highlighted that the differences in magnitude between the predicted and monitored S2 and S1 stay cable tensions seen previously in Figure 8.10 and Figure 8.11 may indicate that the Saltash side span suspension cable tensions are responding differently than predicted, both to support the trailer and balance the horizontal forces at the saddle.

The tension variations for the suspension cable at the two main span quarter-points are identical, despite the longitudinal asymmetry provided by the expansion gap. Thus the change in suspension cable tension is only dependent on the distance of the vehicle from the mid-span. Similarly the quarter span tensions are the same shape as the tensions at mid-span, since the majority of the total vertical load on the suspension cable is supported by its horizontal tension; the ¼ span tensions being larger due to being inclined to the horizontal.
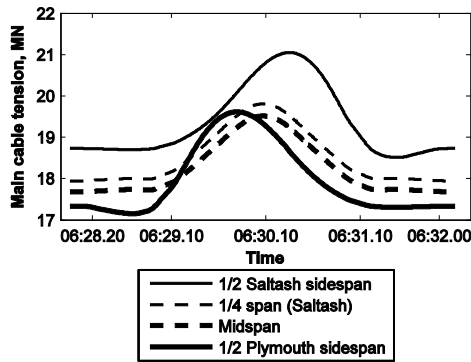
Figure 8.12: Suspension cable tensions, determined from FE model.
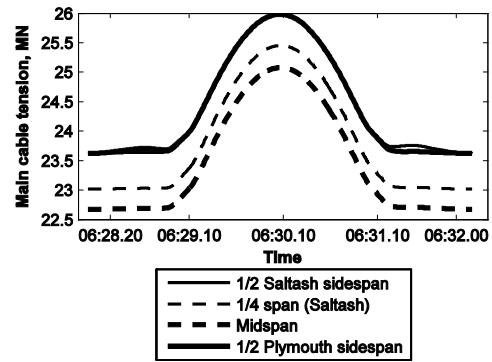
Figure 8.13: Suspension cable tensions, stay cables removed from FE model.

8.6 VARIATION IN DYNAMIC PROPERTIES OF THE BRIDGE

So far the static deflections of the structure have been observed, along with variations in cable tensions depending on the location of the vehicle. The trailer mass itself is large compared to the bridge: the 335m main span of the structure weighs approximately 3190 tonnes, making the vehicle/bridge mass ratio greater than 8%. It seems credible that both the changing tension stiffness and the travelling immense mass would have a significant effect on the dynamic properties of the bridge.

Table 8.2 and Table 8.3 show that the changes of the natural frequency and modal masses for the first six modes may be substantial. Predicted changes in the natural frequencies are 50 times larger than those documented on the Namhae Suspension Bridge (Kim et al. 2001), despite having similar span lengths, suggesting that the large mass of the trailer has a considerable effect on the dynamic response. The natural frequencies may rise as well as fall, depending on the relative effects of the extra mass and the extra tension.

Table 8.2: Change in FE simulated frequency.

Mode	Shape	Original Frequency, Hz	Change to Frequency, Hz	Variation, %
1	VS1	0.389	-0.0282	-7.2
2	LS1a	0.480	+0.0230	+4.8
3	VA1	0.533	-0.0273	-5.1
4	LS1b	0.751	+0.0095	+1.3
5	TS1	0.772	+0.0075	+1.0
6	VS2	0.841	-0.0576	-6.9

Table 8.3: Change in modal mass.

Mode	Shape	Direction for Largest Modal Mass	Original Modal Mass, Tonnes	Change to Modal Mass, Tonnes	Variation, %
1	VS1	Vertical	1795	+269	+15.0
2	LS1a	Lateral	1077	+124	+11.5
3	VA1	Longitudinal	8.5	+4.3	+50.5
4	LS1b	Lateral	903	-756	-83.7
5	TS1	Lateral	126	+631	+500.0
6	VS2	Vertical	14.2	+676	+4770

8.6.1 CHANGES IN THE NATURAL FREQUENCIES

Figure 8.14 demonstrates that troughs and peaks in the frequencies of the first three modes occur when the trailer is over the anti-node of the mode shape. For example, since the first two global mode shapes are symmetric and resemble a half-sine wave, their frequencies peak when the trailer is at mid-span. Likewise the third mode is the first vertical anti-symmetric mode and resembles a full sine wave, and the greatest effect is when the trailer is at a quarter span of the bridge. It is observed that the frequency of vertical mode shapes falls as the additional mass of the trailer moves towards the most responsive part of the structure. The frequency of lateral modes relates more to the changes in cable tensions, and will increase as a result of tension stiffening more than they decrease due to added mass.
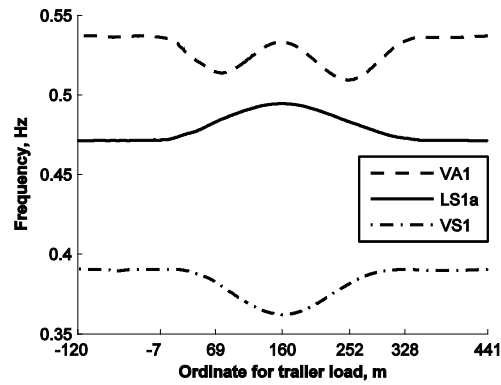
Figure 8.14: Change of frequency for Modes 1-3 as vehicle crosses bridge.

The behaviour for the next three modes in Figure 8.15 shows that the first torsional mode has a similar response to the second lateral mode, which also has a slight axial rotation. The curve of the lines for these two modes is shallower, suggesting little reaction to the location of the vehicle. This response seems credible, since the trailer model is positioned along the centre lane of the bridge, and is not likely to cause axial rotations.

The most striking effect is the frequency variation for the second vertical symmetric mode (VS2). The three central troughs are formed when the tractor is at the quarter spans and mid-span, much like the mode shape. Frequency changes when the vehicle is on the side span seem disproportionately large compared to the mode shapes although mode shape ordinates on the Plymouth side span are larger than those on the Saltash side span, as are the frequency changes.
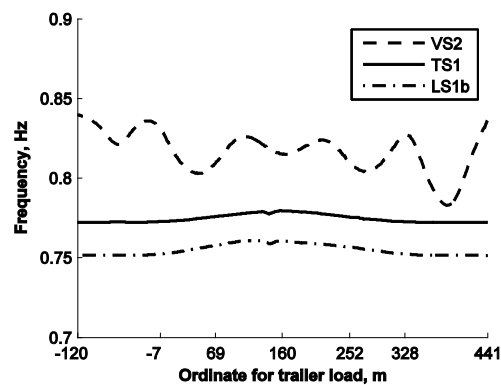
Figure 8.15: Change of frequency for Modes 4-7 as vehicle crosses bridge.

8.6.2 VARIATION OF THE MODAL MASSES

The variations of the modal masses in the trailer FE model are shown by Figure 8.16. For the first two modes (VS1 and LS1a) the modal mass changes when the trailer is upon the main span, which is also where most of their modal activity occurs. Similarly the troughs in the VA1 occur when the trailer is at the quarter span locations, where the largest modal displacement

230

in this mode occurs. This implies that the large mass of the trailer causes variations in the modal activity of the bridge, depending on the relative position of the vehicle to each mode's anti-nodes, like the natural frequencies.

The response to the trailer position varies for each mode; either increasing or decreasing. On a typical simply support beam (with no cables), the modal mass of the first mode drops as the vehicle moves towards the centre. Therefore any decrease in modal mass seems to be dependent on the modal activity of the cable relative to the deck, since a lot of the activity in modes LS1a and VA1 is in the suspension cable itself. This suggests that the increase in cable tension (both suspension and stay) due to the position of the trailer also makes these particular modes easier to excite. These relationships become less clear in latter modes, such as VS2, which is account to the number of waves in the mode shape, as well as the various slackening and tautening of the stay cables.
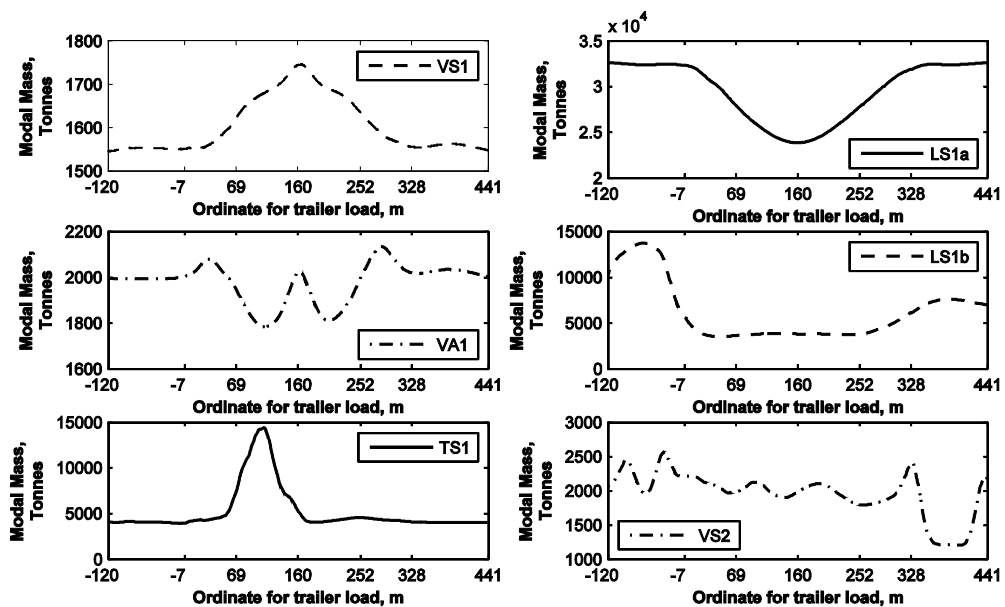
Figure 8.16: Modal mass for modes 1-5.

8.6.3 CHANGES IN THE MODAL DISPLACEMENTS OF MODES VS1 AND VS2

Since the modal masses are dependent on the mass of the structure and vehicle (which stays constant) and the modal displacements, this suggests that the modal displacements may provide more evidence in the change of activity. Figure 8.17 shows the change of the absolute modal displacements for the first vertical symmetric mode of the bridge, as the vehicle travels from one longitudinal ordinate to another. The results show that the mode shape barely

changes until the trailer is on the main span, between the -7m and 328m ordinate. On the main span from Plymouth the modal displacement decreases until the trailer reaches the mid-span, the anti-node of the mode shape, before rising again as it travels to Saltash. The 'S' shaped curve that is appearing on the main span in the plan view suggests that the mode shape is asymmetrically curving towards the half of the main span supporting the vehicle. This response shares some similarities to the behaviour of the static deformations, seen previously in Figure 8.6, where the mid-span deflects in the direction of the trailer.
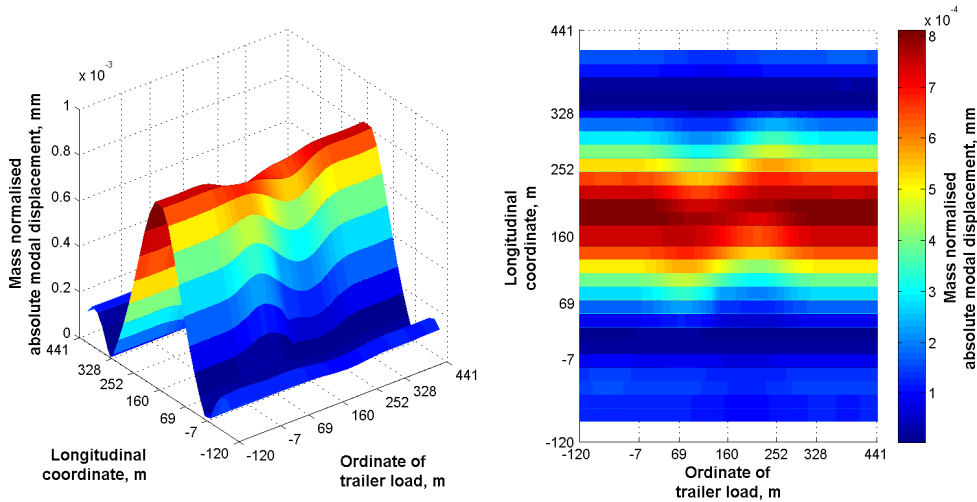
Figure 8.17: Variation of the VS1 mode shape with vehicle location. Left: Isometric view. Right: Plan view.

Figure 8.18 also shows the change in absolute modal displacements, but for the second vertical symmetric mode. This mode was selected due to the high variation in frequency and modal mass when the Plymouth side span was loaded by the trailer, which may also relate to changes in the mode shapes. When the trailer is travelling across the mid-span the isometric plot indicates the modal displacements are fluctuating with crests forming at the anti-nodes, much like the results seen previous for the first vertical mode (Figure 8.17).

Whilst the trailer is on the main span, the mode shape is mostly similar to its shape when the bridge is unloaded; the only variation is a reduced modal deflection at mid-span when the trailer is at the centre of the bridge. However, an interesting change to the mode shapes occurs when the trailer is located at the centre of a side span, which is visible in the plan view of the plot. Two vertical bands form when the trailer is near the -60m and 385m ordinates of the bridge, the modal displacements differing significantly compared to other locations of the structure. This indicates that the mode shape of the bridge is altered, with the largest modal deflections occurring on the side-span instead of the main span. The largest displacement on the Plymouth side span also corresponds to the large change in natural frequency and modal mass for this mode whilst the vehicle mass is located upon it.
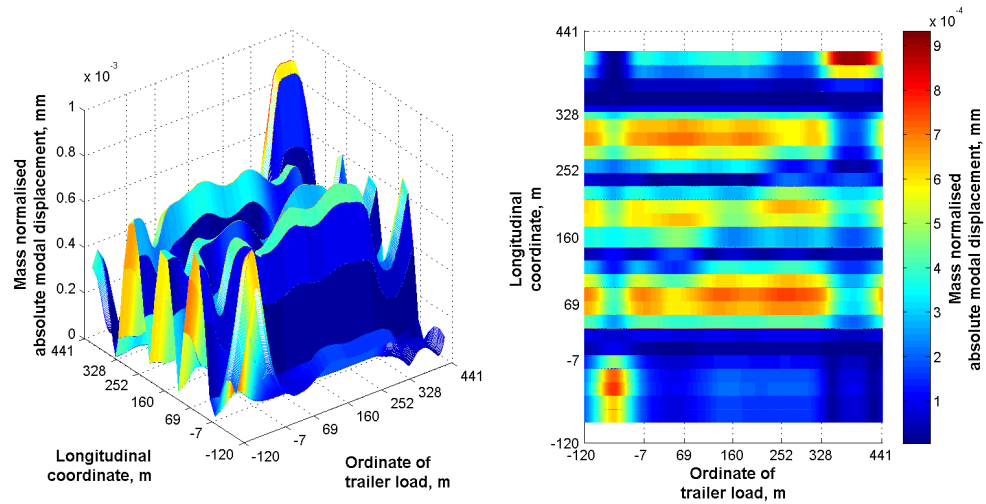
Figure 8.18: Variation of the VS2 mode shape. Left: isometric view. Right: Plan view.

8.6.4 RELATING THE FREQUENCY CHANGES TO THE MODAL DISPLACEMENTS

The following pairs of figures showing two views of a three-dimensional plot aim to link the change in frequency Δf to the vehicle location x and mode shape ordinate φ, for modes VS1 and VS2. The left-hand plots, Figure 8.19 and Figure 8.21, show the absolute value of the mass-normalised vertical mode shape ordinate φ for the mode versus span-wise location x. In Figure 8.20 and Figure 8.22 for each vehicle location x the change in natural frequency Δf previously calculated (Figure 8.14) is plotted against the modal ordinate for location x.

A colour bar indicating the ordinate x for the trailer load is also provided to help understand the changes as the vehicle moves from one half span to the other.

A linear relationship between frequency change and absolute modal displacement might be expected, for VS1 it comes close to that. While the side spans also show a linear relationship (the short lines in Figure 8.20), they have steeper slopes i.e. the first natural frequency barely changes when the trailer is on the side span.
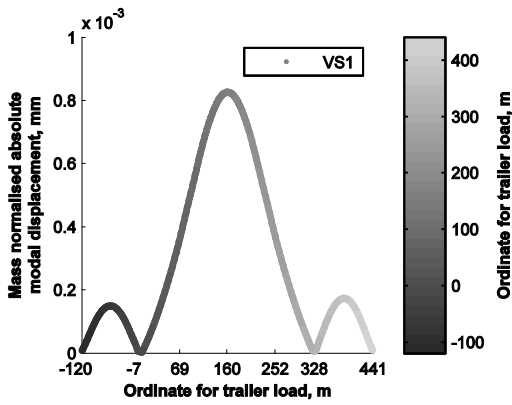
Figure 8.19: Absolute modal displacements for mode shape "VS1".
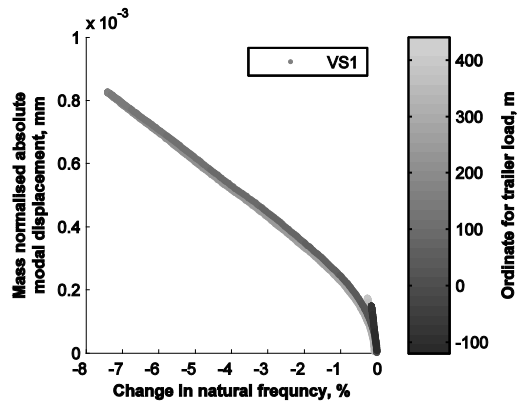
Figure 8.20: Change in frequency for VS1 vs. modal displacements.

The results for the second vertical symmetric mode is also presented here to test whether similar linear relationships occur when the mode shape for the main span consist of more than one sinusoid. Figure 8.22 shows that the relationships when the vehicle is at the quarter span of the main span follow similar gradients, although the open loops indicate the relationships are not as tight as the previous VS1 results. Likewise the change in frequency when the side-spans are loaded does not adhere to the same relationship to the mode shape like the main spans. In particular when the Plymouth side span is loaded the natural frequency change for this mode is large, despite the modal displacements on the Plymouth side-span being slightly smaller than those on the main span.
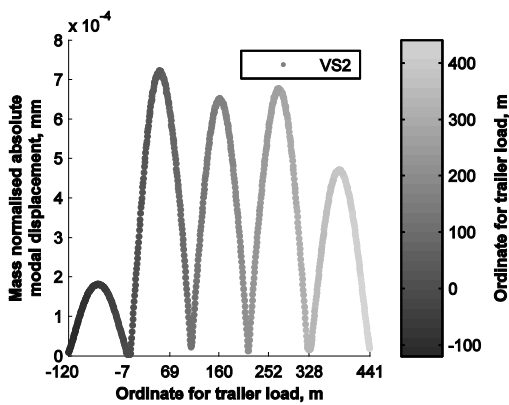
Figure 8.21: Absolute modal displacements for mode shape "VS2".
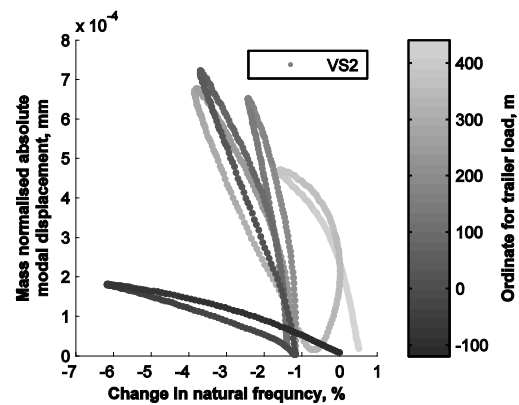
Figure 8.22: Change in frequency for VS2 vs. modal displacements.

8.7 STAY CABLE ACCELERATIONS

As well as quasi-static effect described in previous sections, the time series for the vertical and transverse accelerations of the north and south P4 stay cables were also available, as shown in Figure 8.23. The cable accelerations begin to grow once the trailer begins travelling on the main span, at 06:29.10, and reaches maximum amplitude of 0.4m/s² when the vehicle is at mid-span. Beyond that point the accelerations decrease, although the cable accelerations are larger when the vehicle is on the Saltash side span compared to when it is on the Plymouth side span.
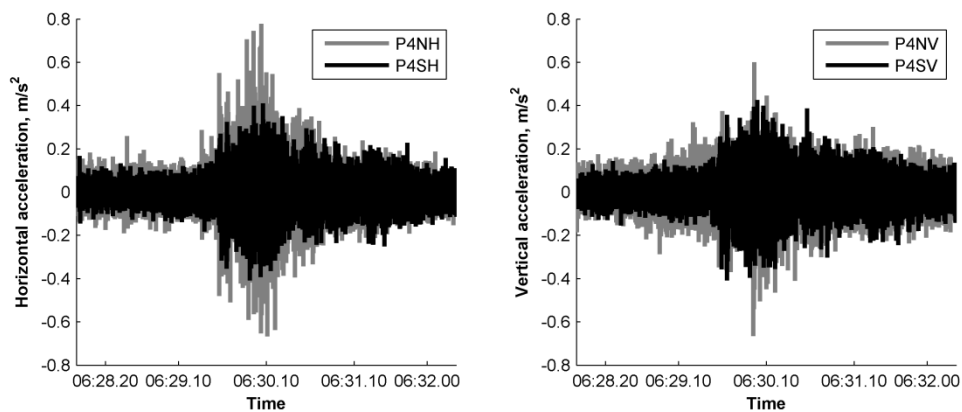
Figure 8.23: Acceleration of stay cable P4. Left: Horizontal. Right: Vertical.

The stay cable accelerations were further processed to see how the cables natural frequencies change as the vehicle travels across the bridge, as presented in the spectrogram of Figure 8.24. The average tension in the two stays cable before the bridge was loaded was 2269kN, and according to the monitoring data (see Chapter 5) would have a natural frequency of approximately 0.98Hz. Consequently the 1Hz intervals in the spectrogram comply with the second to sixth harmonics of the cable.

The frequency of the cable increases at 28 minutes, which corresponds to the time when the P4 tensions increase, and the vehicle is near its deck connection. Assuming that the change in frequency is a result of the 402kN tension rise of the P4 stay cable, and taking the cable length as 110m and its mass as 58.4kg per metre, the theoretical rise of the stay cable's natural frequency for the first harmonic is approximately 0.144Hz (Humar 1990), assuming the elastic stretch of the cable is negligible. Doubling this result appears to correspond with the rise near 2Hz for the second harmonic. The changes in the fifth and sixth harmonics are the most visible in the P4SV spectrogram, demonstrating that the increase in frequency also multiplies for the higher order harmonics.
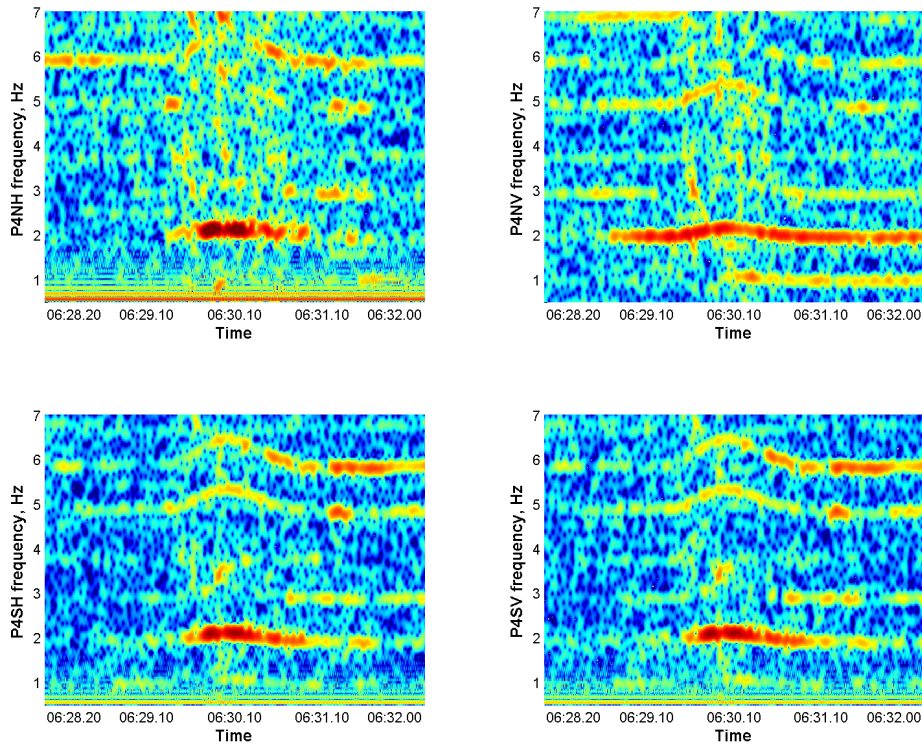
Figure 8.24: Spectrograms of the P4 stay cable frequencies.

8.8 DETERMINATION OF POSSIBLE DAMAGE TO THE STRUCTURE

Due to the abnormal loading caused by the trailer, it is possible that the Tamar Suspension Bridge has suffered some damage to its structure while attempting to bear its mass. The basis of SHM is that signs of damage to the structure can be indicated from the monitored data. Regression analyses performed on the observed data can be used to distinguish outliers, while also normalising their response to account for the environmental variability of the responses (Sohn 2007). The errors between the predicted and monitored response (ξ from Equation 4.3 in Chapter 4) are used to identify outliers; if the suspension bridge has been damaged, there should be substantially more outliers in the week after the trailer loading (October 31st 2010 onwards) than the previous week.

Since there was no RTS or deck accelerometer data available in the following week of the on-site testing, the stay cable tensions were the best available option to identify possible signs of damage to the bridge; there would be a noticeable difference in the tensions if the suspension or stay cables stretched to accommodate the load, or if some connections in the deck structure loosened during the vehicle's transit, causing the bridge to sag. The tensions from

stay cable "P4" on the southern side of the bridge were used, since it is attached near the centre of the main span where the largest deflections occurred, and was less likely to be affected by transient thermal responses from the towers than the stay cables attached to the Saltash towers (as seen previously in Chapter 6, Figure 6.34). The temperature data collected from the deck, truss and suspension cable were used to normalise the tension data. Ideally the vehicle weight would also be used, but it has been omitted to clearly show the change in response caused by the weight of the trailer. Also it is unlikely the traffic behaviour would be drastically different from one week to the next, unlike the bridge temperature.

The coefficients used for the regression analysis are calculated from data within a training period between the 21st and 24th of October 2010, which is also used to determine the acceptable error between the two monitored and simulated response. The coefficients are subsequently applied to the monitored temperatures between October 24th 2010 and November 7th 2010 to predict the stay cable tensions.

Figure 8.25 presents the error between the monitored stay cable's tensions to the response predicted from the regression analysis. The largest errors produced for the regression analysis are at the time of the site investigation (31st of October), which would be when the cable tensions increased due to the large vehicle loading. Otherwise there does not appear to be any change in the behaviour of the errors in the weeks before and after the test; excluding the outliers during the test, there are 14 outliers in the week before the test, compared to just 4 outliers in the following week. This is a strong indication that the Tamar Suspension Bridge did not suffer any damage during the trailer's transit.
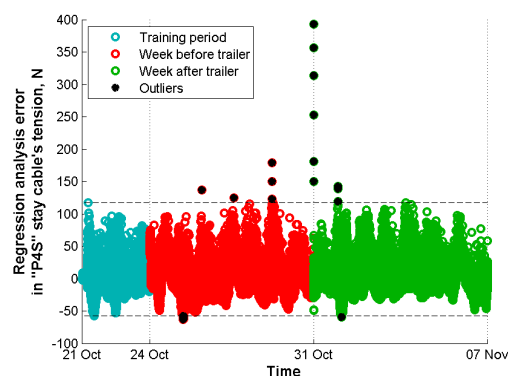
Figure 8.25: Damage diagnosis using errors from a nonlinear regression analysis, which simulates the tension of stay cable P4 using the monitored bridge temperatures.

8.9 SUMMARY

In this chapter, variations were observed in the static deflections and dynamic response of the Tamar Suspension Bridge during crossing of a 269 tonne vehicle. The study uses data collected from the site investigation, as well as the simulations using an FE model of the bridge. The static analyses using the FE model have provided a satisfactory mirror of the observed behaviour, with an acceptable match to displacements recorded by the two total stations.

The deck vertical displacements increased as the trailer moved towards the mid-span; this also caused the towers to deflect inwards and thus to lift the side spans. The stay cable tensions peaked when the trailer was near their connection to the deck, the largest response being observed in the stay cables with the steeper inclination. Variations in the suspension cable tension were observed as the vehicle travelled across the entire span of the bridge.

The frequencies simulated in the FE model fluctuated according to trailer locations, with the largest variations appearing on the first two vertical symmetric modes. Similar changes were also exhibited in the modal masses and mode shapes of the structure. In particular the dynamic properties of the second vertical symmetric mode change considerably when the trailer is on the Plymouth side span.

The largest changes to a mode natural frequency correspond to the vehicle being located on the anti-nodes of its mode shape. Comparing the mode shape to the changes in natural frequency suggests there may be a relationship, although due to the elliptic nature of some of the trends it suggests the relationship may be weak for certain modes. For each mode the gradient of the relationships tends to differ for each sinusoid of the mode shape.

The accelerations from a pair of stay cables were also observed during the monitoring, which also demonstrated an increase in natural frequency for several harmonics when the trailer travelled close to its deck connection. This variation was attributed to the increase in stay cable tension recorded for the structure.

REFERENCES

Calcada, R., Cunha, A. & Delgado, R., 2005. Analysis of Traffic-Induced Vibrations in a Cable-Stayed Bridge. Part I: Experimental Assessment. *Journal of Bridge Engineering*, 10(4), pp.370–385.

Green, M.F. & Cebon, D., 1997. Dynamic interaction between heavy vehicles and highway bridges. *Computers & Structures*, 62(2), pp.253–264.

Guo, W.H. & Xu, Y.L., 2001. Fully computerized approach to study cable-stayed bridge-vehicle interaction. *Journal of Sound and Vibration*, 248(4), pp.745–761.

Haji-Hosseinloo, A. & Bakhtiari-Nejad, F., 2010. Vibration analysis and control of a bridge under a heavy truck load. In *2010 International Conference on Mechanical and Electrical Technology*. IEEE, pp.195–200.

Humar, J.L., 1990. *Dynamics of structures* 1st ed., Prentice-Hall, Inc.

Inter-Commerz, 2008. Faun "Elelphant SLT 50 8x8 + 8x0 datasheet. Available at: http://www.inter-commerz.com/uploads/tx_ttproducts/datasheet/Faun_Elephant_SLT_50_8x8_8x0_ENG.pdf [Accessed September 15, 2011].

Kim, C.-Y., Jung, D.-S., Kim, N.-S. & Yoon, J.-G., 2001. Effect of vehicle mass on the measured dynamic characteristics of bridges from traffic-induced vibration test. In *Proceedings of SPIE, the International Society for Optical Engineering*. Society of Photo-Optical Instrumentation Engineers, pp.1106–1111.

Kim, J., Lynch, J.P., Lee, J.-J. & Lee, C.-G., 2011. Truck-based mobile wireless sensor networks for the experimental observation of vehicle–bridge interaction. *Smart Materials and Structures*, 20(065009).

Kwon, S.-D., Kim, C.-Y. & Chang, S.-P., 2005. Change of Modal Parameters of Bridge Due to Vehicle Pass. In *IMAC-XXIII: Conference & Exposition on Structural Dynamics - Structural Health Monitoring*. pp.283–290.

Law, S.S., 2004. Dynamic behavior of damaged concrete bridge structures under moving vehicular loads. *Engineering Structures*, 26(9), pp.1279–1293.

Li, J., Su, M. & Fan, L.C., 2003. Natural Frequency of Railway Girder Bridges under Vehicle Loads. *Journal of Bridge Engineering*, 8(4), pp.199–203.

Lin, C. & Yang, Y.-B., 2005. Use of a passing vehicle to scan the fundamental bridge frequencies: An experimental verification. *Engineering Structures*, 27(13), pp.1865–1878.

Mazurek, D.F. & DeWolf, J.T., 1990. Experimental Study of Bridge Monitoring Technique. *Journal of Structural Engineering*, 116(9), pp.2532–2549.

Mulcahy, N.L., 1983. Bridge response with tractor-trailer vehicle loading. *Earthquake Engineering & Structural Dynamics*, 11(5), pp.649–665.

Paultre, P., Proulx, J. & Talbot, M., 1995. Dynamic Testing Procedures for Highway Bridges Using Traffic Loads. *Journal of Structural Engineering*, 121(2), pp.362–376.

Roberts, G.W., Meng, X., Brown, C.J. & Andrew, A., 2006. Measuring the movements of the Forth Road Bridge by GPS; lorry trials. In A. Kumar, C. J. Brown, & L. C. Wrobel, eds. *The First International Conference on Advances in Bridge Engineering. Bridges - Past, Present and Future*. pp.28–36.

De Roeck, G., Maeck, J., Michielsen, T. & Seynaeve, E., 2002. Traffic-induced shifts in modal properties of bridges. In *IMAC-XX: Conference & Exposition on Structural Dynamics*. pp.630–636.

Sohn, H., 2007. Effects of environmental and operational variability on structural health monitoring. *Philosophical transactions. Series A, Mathematical, physical, and engineering sciences*, 365(1851), pp.539–60.

Watson, C., Watson, T. & Coleman, R., 2007. Structural Monitoring of Cable-Stayed Bridge: Analysis of GPS versus Modeled Deflections. *Journal of Surveying Engineering*, 133(1), pp.23–28.

Xia, H., Xu, Y.L. & Chan, T.H.T., 2000. Dynamic interaction of long suspension bridges with running trains. *Journal of Sound and Vibration*, 237(2), pp.263–280.

Yang, Y.-B., 2004. Extracting bridge frequencies from the dynamic response of a passing vehicle. *Journal of Sound and Vibration*, 272(3-5), pp.471–493.

Yang, Y.-B., Liao, S.-S. & Lin, B.-H., 1995. Impact Formulas for Vehicles Moving over Simple and Continuous Beams. *Journal of Structural Engineering*, 121(11), pp.1644–1650.

Yin, S.-H. & Tang, C.-Y., 2011. Identifying Cable Tension Loss and Deck Damage in a Cable-Stayed Bridge Using a Moving Vehicle. *Journal of Vibration and Acoustics*, 133(021007).

CHAPTER NINE

CONCLUSIONS AND FUTURE WORK

9.1 CONCLUSIONS

This thesis investigates thermal and traffic responses of Tamar Suspension Bridge studied from monitored data and simulated responses using a three-dimensional finite element (FE) model. These studies are used to identify the mechanisms for the structural responses, and to account for their variations while observing infrequent phenomena caused by abnormal loading, or deterioration of the structure.

The following conclusions result from this study.

9.1.1 QUASI-STATIC THERMAL RESPONSE OF THE BRIDGE

It is found that the suspension bridge not only expands longitudinally when the deck structure is warmed up, but also sags from the thermal expansions and slackening of the cable tensions. Due to the almost parabolic profile of the main cables, the thermal expansion of the cable results in significantly increased sag compared to the deck expansion.

Out of all the instrumented parts of the bridge, the upper surface of the deck reaches the highest temperature; its flat asphalt surface gathers large quantities of heat via solar radiation. The temperature of the suspension cable is slightly cooler, since the wrapping provides some insulation to the steel wires beneath. The underside of the deck structure is usually the coolest part of the deck structure as it is shaded by the deck and thus not directly irradiated by the sun.

The tensions in the additional stay cables are mainly affected by the thermal response expansion of the bridge deck and the deflection of the connected tower, rather than the thermal elongation of the cables themselves. The relationship of the stay cable tensions to the deck and tower deflections vary depending on their location with respect to the expansion gaps in the deck.

If the gap is located underneath the tower, the stay cable tensions slacken as the bridge deck expands towards the tower. Since the expansion of the bridge deck is more substantial than the sway of the tower caused by temperature differentials, the relationship between the tensions and the expansion of the bridge appears linear. Since the bridge movements at the expansion gap are largest, the change in tensions for stay cables located near the gap are larger.

On the other hand, if the gap is located away from the tower, the deck movements will be smaller as the bridge expands outwards. While the tensions mostly relate to the expansion of the bridge, the trend appears nonlinear due to the delayed thermal response of the tower to

the deck.

Due to the variations in the stay cable tensions caused by the deck expansion, horizontal force equilibrium at the tower tops becomes unbalanced. As a consequence, the horizontal tension within the suspension cable varies from span to span to balance the span-wise forces acting on the tower saddles. The variation in the suspension cable tensions is larger on spans near the expansion gap than elsewhere, since the change in the stay cable tensions for towers at the gap are also larger.

9.1.2 THERMAL DYNAMIC RESPONSE

The natural frequencies for the modes of vibration for the bridge have an almost inverse relationship to the structural temperature, in particular the frequency of the first lateral mode, LS1a, being the most sensitive. The FE model results indicate that this is caused by both the temperature dependence of steel's Young's modulus in the structure, as well as the thermal stresses caused by the expansion of the elements and the relaxation of the cable tensions. The presence of stay cables in the bridge increases the variation of certain frequencies. For the Tamar Suspension Bridge, this is on the first symmetric sway mode (LS1a; the stay cables providing some sway rigidity to the deck structure) and the second vertical symmetric mode (VS2; since the additional stay cables are attached at the quarter spans).

9.1.3 TRANSIENT THERMAL RESPONSES IN THE BRIDGE

The thermal gradient through the deck structure is at its largest during summer and clear days, when the solar intensity is highest. This property may be used to predict cloud cover levels from monitored data of the bridge, which is used to determine the levels of simulated solar radiation to apply during a transient thermal analysis

Several thermally influenced responses in the bridge, such as the tension in the cables and deflection of the towers, are subject to delays between the times of peak temperature within the bridge. This means they do not directly relate to temperature, and require variables relating to other thermal responses (such as the deck and tower deflections). For the Tamar Suspension Bridge, there is an occasional 0.5 to 1 hour delay between the temperatures of the suspension cable and those of the deck, also caused by the insulation properties of the wrapping. However the most significant cause of thermal lag is due to differences in the tower displacements to the deck expansion, which has between 2 and 4.5 hours difference between the peak responses. This is partly due to different construction material; the concrete of the towers retains heat for longer periods, while the steel deck gains and loses heat rapidly. The orientation of the surfaces also means the bridge deck is constantly irradiated throughout the

day, while the East and West surfaces of the towers are only directly warmed by the sun during the morning or afternoon.

9.1.4 EFFECT OF TRAFFIC MASS ON THE FREQUENCIES

There is a linear decrease in the natural frequencies for four of the five monitored modes when plotted against the approximate mass of the traffic on the bridge, although the response differs from mode to mode due to their sensitivity to the additional mass on the deck and the increased tensions in the cables. This effect may be evident in the time series of the natural frequencies, with troughs forming at the rush hour periods.

The eccentricity of the vehicular loading to the longitudinal axis of the bridge has a considerable effect on the dynamic properties, especially on the torsional modes. This property is identifiable when the traffic flows asymmetrically across the bridge, either at certain periods of the day when more traffic travels in one direction than the other, or (like the Tamar Suspension Bridge) a single outer lane is subjected to smaller loads than the opposite side.

9.1.5 CHANGE IN BRIDGE PERFORMANCE DUE TO THE LOCATION OF A VEHICLE

The passage of the heavy trailer showed that that mid-span deflects downwards and the towers bend towards the main-span with the vehicle near mid-span. In addition, the mid-span curves upwards when the trailers are on the side spans, due to the continuity provided by the suspension cables.

The horizontal forces in the main-span's suspension cables increase as the vehicles travels towards mid-span, due to the deflection of the bridge deck, while the tensions in the stay cables increase when the vehicle nears their deck connection. In order to maintain horizontal equilibrium at the towers, the suspension cable tensions in the side-spans increase as the vehicle moves towards the centre of the bridge. Since the horizontal force contribution from the additional stay cables are dependent on what side of the bridge is loaded by the vehicle, the peaks of the side-span suspension cable tensions are also off-centre.

The simulated dynamic results indicate that variations in the bridge's natural frequencies are linked to the location of the vehicle. It is at the anti-nodes of the mode's shape in particular where the variations occur, despite the same mass being applied to the bridge.

9.2 COMPARISON OF FREQUENCY CHANGES DUE TO TRAFFIC WITH CHANGES DUE TO TEMPERATURE

9.2.1 RELATING FREQUENCY VARIATION TO TEMPERATURE AND TRAFFIC MASS VARIATIONS

In this thesis the relationship of the frequencies with the cable temperature (in Chapter 5) and the mass of traffic on the bridge (in Chapter 7) has been determined. However, it is unclear which factor has the greater influence. In order to compare temperature and traffic effects on the Tamar Suspension Bridge's natural frequencies, a frequency change based on the variation of the loading conditions has to be determined.

Table 9.1 shows the mean and standard deviation of monitored suspension cable temperatures and traffic mass from the bridge. The standard deviations of the data in particular determine the typical variation of the environmental conditions on the structure, which are used to find a relative frequency change.

Table 9.1: Mean and standard deviation of cable temperature and traffic mass data.

Bridge Property	Mean, μ	Standard Deviation, σ
Cable Temperature	11.3°C	6.04°C
Gross traffic mass	47.0 tonnes	37.1 tonnes

Table 9.2 multiplies the standard deviation of the environmental conditions by the linear relationships identified from the monitored data (for traffic, gradient $C_{v,m}$ comes from Table 7.4, and for temperature the gradient $C_{t,m}$ comes from Table 5.2). The variation in frequency is similar for modes LS1a and VA1, indicating an equal contribution from both the temperature of the bridge and the traffic on the bridge. For LS1b, the frequency changes for the mode relate more to the temperature of the bridge than the traffic on the structure.

The relative changes in frequency in modes VS1 and TS1 have are more strongly related to traffic than to temperature, which explains why the diurnal variations of the two modes (Figure 7.2 and Figure 7.36) have a very close match to the daily traffic profiles (Figure 7.20). This property may be used to identify both the levels of traffic and which lanes are loaded on the structure.

Table 9.2: Monitored variation of frequencies related to temperature and traffic.

		Mode (Shape)				
		1 (VS1)	2 (LS1a)	3 (VA1)	4 (LS1b)	5 (TS1)
Monitored cable temperature	Gradient, $C_{t,m}$ ($\times10^{-3}$ Hz/°C)	-0.098	-0.990	-0.497	-0.348	-0.307
	Standard deviation, σ_t (°C)	6.04	6.04	6.04	6.04	6.04
	Frequency change, $\sigma_t \cdot C_{t,m}$ ($\times10^{-3}$ Hz)	**-0.59**	**-5.98**	**-3.00**	**-2.10**	**-1.85**
Monitored traffic mass	Gradient, $C_{v,m}$ ($\times10^{-5}$ Hz/tonne)	-5.409	-15.405	-9.802	-0.350	-8.313
	Standard deviation, σ_v (tonnes)	37.1	37.1	37.1	37.1	37.1
	Frequency change, $\sigma_v \cdot C_{v,m}$ ($\times10^{-3}$ Hz)	**-2.01**	**-5.72**	**-3.64**	**-0.13**	**-3.08**

9.2.2 REGRESSION ANALYSES ON THE MONITORED FREQUENCIES, USING BRIDGE TEMPERATURES AND APPROXIMATE TRAFFIC MASS

While observing the effect the bridge temperature on the dynamic properties of the bridge, regression analysis results gathered from the complete collection of monitored samples appeared inconclusive: the noise in the data from other sources disguised any behaviour that was associated with the thermal response of the structure.

As identified in the previous section, this is because the behaviour of most of the first five modes are more dependent on the mass of the traffic on the bridge than its thermal

responses, even when traffic levels were limited to 10 tonnes. A series of regression analyses were conducted on the monitored data, using the monitored bridge temperatures and approximate traffic mass, to determine the sensitivity of the modal properties to each variable. Since certain dynamic responses appeared to be lower at particular bridge expansion lengths (subsection 5.5.1 in Chapter 5), the observed monitored data excluded occasions when the recorded bridge expansion at cross girder "044" was between -50 to -20mm, and -10mm to 20mm.

The correlation coefficients between the monitored data and predicted data are shown in Table 9.3. The correlation coefficients of the vertically-acting modes (VS1, VA1 and TS1) are above 0.80 when considering traffic on its own; much higher than variations caused by thermal responses (deck, cable and truss temperature). This indicates that these modes are mainly affected by the traffic mass upon the structure, rather than the bridge's thermal response.

The lateral modes (LS1a and LS1b) have an almost similar dependency to traffic and temperature, although the response remains fairly dispersed. Either this mildly disordered response is because the frequency data for the lateral frequencies was reduced due to faulty readings from the lateral accelerometer, or that the dynamic response of these modes are also affected by low wind speeds (which were limited for these regression analyses).

Table 9.3: Correlation coefficients comparing regressed natural frequencies of the bridge to the monitored frequencies, using bridge temperatures and approximate traffic mass as observed variables.

Variables				VS1	LS1a	VA1	LS1b	TS1
Temperature			Traffic mass					
Deck	Cable	Truss						
			✓	0.877	0.701	0.816	0.495	0.848
✓	✓	✓		0.561	0.659	0.612	0.628	0.567
✓			✓	0.881	0.780	0.843	0.651	0.856
✓		✓	✓	0.880	0.779	0.831	0.658	0.861
	✓		✓	0.880	0.773	0.837	0.651	0.855
✓	✓	✓	✓	0.880	0.776	0.830	0.662	0.861

Apart from showing the dependency of each mode's performance to the bridge temperatures and traffic mass, the correlation coefficients barely differ when considering the deck and cable temperatures separately (with the traffic mass), or both together. Since there was little to suggest a certain combination contained any unnecessary variables, the optimal regression analyses use all possible variables to determine the results. Figure 9.1 compares the monitored natural frequencies to the results predicted by the regression analysis, and shows a mainly linear relationship for modes VS1, VA1 and TS1. "Plateaus" form in the results at higher frequencies, which occur at the start of each day. This may suggest differing time dependent effects from previous days, such as variations in the sway of the concrete towers caused by slow heat gain and loss, compared to the steel deck.
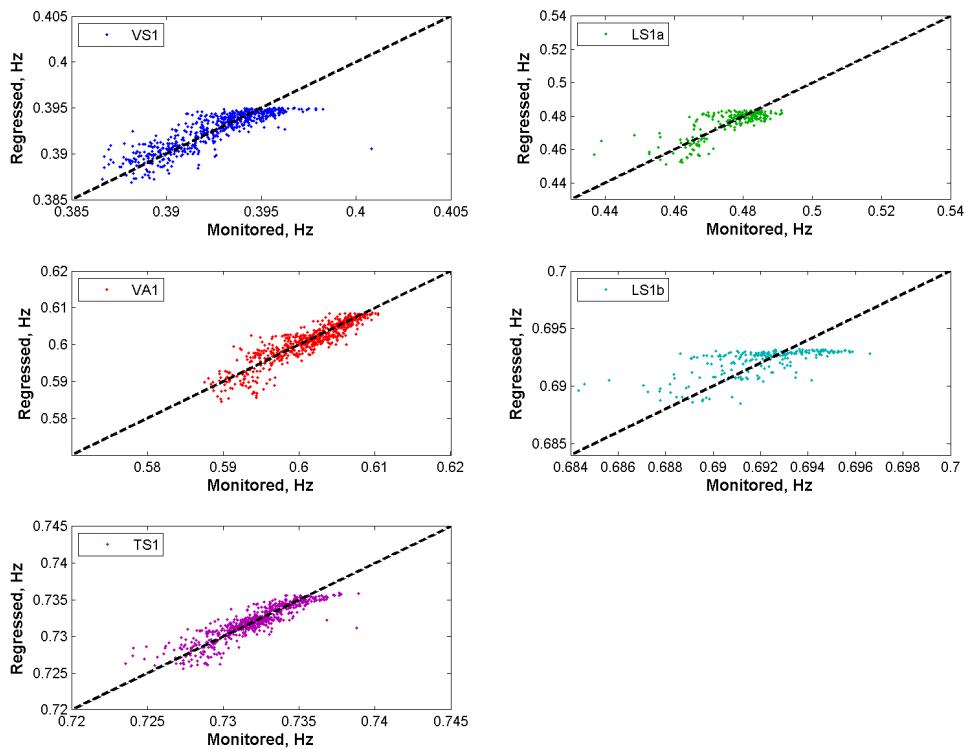
Figure 9.1: Comparison of regressed results to monitored frequencies.

The coefficients from the regression analysis provide a good indicator of the dependency of each mode's natural frequency to each independent variable. The coefficients of the regression analysis for the first five monitored modes are shown in Figure 9.2, which shows that for four of the modes (excluding LS1b) the mass of the traffic on the Tamar Suspension Bridge has a significant influence on each mode's natural frequency. On modes VS1 and TS1 in particular the response caused by traffic is considerably larger than the thermally-induced responses.

For mode LS1a the coefficients relating to the suspension cable temperature and the traffic mass are much larger than the deck and truss temperature coefficients. This would imply that the large variation of LS1a's frequency from monitored results in Chapter 5 is associated more with the tension changes in the suspension cable (caused by thermal expansion and imposed masses) rather than the temperature of the deck. Due to the limited amount of samples collected for lateral modal responses, it is unclear whether the cable temperature and traffic mass also cause the particularly noisy monitored response in LS1a, or whether wind effects also contribute, so this is open for further consideration.

Figure 9.2 also shows that increasing the deck temperature causes each mode's natural frequency to drop, which was also observed in Chapter 5 where temperature increases caused the Young's modulus and thermal stresses in the bridge to reduce the stiffness of the structure. However, the regression coefficient for the truss temperature is positive for the first four modes; an increase in truss temperature relates to a rise in each mode's natural frequency, which is an unexpected result. Since the temperature of the truss is typically lower than the deck (due to solar radiation upon the asphalt), the positive coefficient for the truss temperature may imply a dynamic variation is caused by the temperature differential through the deck structure (a larger difference between the deck and the truss causes a greater drop in frequency), which would consequently relate to the quasi-static configuration of the suspension bridge. The results from Chapter 5 implies the temperature differential through the deck structure only causes slight variations, compared to the change in dynamic response caused by the overall temperature of the deck structure. Thus it would be worthwhile to explore dynamic variations caused by thermal gradients further, possibly by observing differing thermal stresses in the deck and various initial configurations for the bridge.
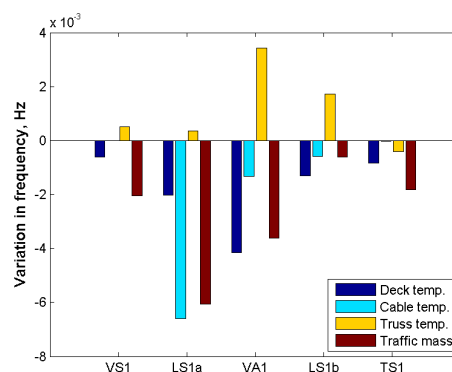

Figure 9.2: Calculated coefficients from regression analyses on the monitored bridge frequencies, using bridge temperatures and gross traffic mass.

9.3 SUGGESTIONS FOR FUTURE WORK

While this investigation has uncovered several mechanisms for the thermal response of both a suspension bridge and a cable-stayed structure, the dispersed monitored data for the natural frequencies show that there is still more to be understood about the bridge's behaviour. Since the change in the natural frequencies is slightly irregular in the time series, it would suggest that the dispersed data is caused by the rapidly changing loads from traffic or wind on the bridge, rather than the slow, quasi-static changes in structural temperature. However there is still more to discover about the effect of temperature differential and thermal lag on the dynamic behaviour of the bridge.

The following suggestions are possible routes to explore in future investigations:

- The thermal transient analysis study could be pushed further to show the variations in the dynamic properties as well. This would be achieved by taking the static displacements and stresses from the transient analysis, and subjecting them to a modal analysis, similar to the transient analysis on a concrete slab performed by Yong et al. (2011). With these results any links to the thermal lag in the bridge should conclusively demonstrated. Errors between the monitored and simulated dynamics can be used to identify nonlinear boundary conditions in the model, such as freezing of the expansion joints or temporary rigidity resulting from the structure's configuration.

- The thermal gradient through the deck structure could be explored further by using detailed FE models of a short length of the deck (around a cross-girder in a truss, or a diaphragm in a box girder, for example), which would be constructed from 3D solid elements, rather than 2D elements which provide a simplified response.

- The modal properties that are mostly affected by the mass and flow of the traffic (e.g. for Tamar Suspension Bridge the observed modes would be the first vertical symmetric, VS1, and the first torsional, TS1) could be used as a method for approximating the mass of traffic. Assuming the monitored responses are produced by an undamaged structure, these properties could be fed back into other modal data to filter out noisy responses caused by traffic (which has irregular behaviour). This could be used to identify responses relating to other environmental conditions.

- More advanced vehicles models could be applied to the structure to consider how vehicle-bridge interaction contributes to changes in the bridge's dynamic properties.

- In order to verify the reduced modal masses in the simulated data, it would be

worthwhile to observe the monitored modal displacements from bridge. This would be especially useful for identifying the extraordinary LS1b behaviour in traffic, whose simulated response is very different compared to the other modes.

- Some monitored evidence in required to identify whether vehicle location to the anti-nodes of a bridge's mode shape affects the mode's natural frequency. This could be studied by the lone passage of a heavy vehicle, like the investigation in Chapter 7 (so long as the data does not get corrupted), although this does not necessarily need to be a repeat test on the same structure. It could be observed from the passage of a single HGV during an early morning, when there is little traffic on the bridge.

Additionally, there are opportunities for identifying wind-induced responses on instrumented suspension bridges. Using long-term monitoring data, the speed of the wind and its directionality may be correlated against the dynamic properties of either a single bridge, or several with a similar deck structure (since the shape of deck's cross section will affect how the wind travels around it).

These properties may be compared to a simulated response on the structure. Different wind-induced phenomena experienced by suspension bridges (flutter, buffeting, vortex shedding, galloping) may be observed to see what wind speed is required to produce a significant response, and how these aero-elastic effects temporarily alter the configuration of the structure by twisting and uplifting the cross-section, and relieving the tensions in the suspension cables and hangers.

These changes in configuration may affect the modal properties of the structure, which could be simulated within an FE or some other mathematical model. The modelled behaviour would be checked against the long-term monitored data for similar responses, as well as determining how frequently the bridge experiences these responses.

REFERENCES

Xia, Y., Xu, Y.L., Wei, Z.-L., Zhu, H.-P. & Zhou, X.-Q., 2011. Variation of structural vibration characteristics versus non-uniform temperature distribution. *Engineering Structures*, 33, pp.146–153.

APPENDIX A

A.1 DAILY VALUES

The majority of the steps shown here have been duplicated from a paper by Rivington et al. (Rivington et al. 2005).

Total daily irradiance, J_0 is given by

$$DJ_0 = SJ_{0,s} + DJ_{0,d} \tag{A.1}$$

where D is the day length, S the sunshine duration, $J_{0,s}$ the direct beam component and $J_{0,d}$ the diffuse component. The day length in hours is calculated by

$$D = \frac{24}{\pi} \cos^{-1}(-\tan \lambda \tan \delta) \tag{A.2}$$

where λ is the latitude of the location and δ the solar declination, both measured in radians. The solar declination for a day in a year may be found by

$$\delta = -0.4084 \cos\left(2\pi \frac{d+10}{365}\right) \tag{A.3}$$

where d is the day of the Year (eg. $d = 1$ for January 1st).

The direct beam component is given by

$$J_{0,s} = 1367 \frac{2p}{\pi}\left(\tau^{1/\sin \varnothing_0}\right) \sin \varnothing_0 \tag{A.4}$$

where p is the fraction of radiation in full spectrum sunlight (1 has been used, for simplicity), 1367 is the solar constant (in W/m^2), τ is the atmospheric transmissivity and $\varnothing_0$ is the solar elevation at noon, in radians: $\sin \varnothing_0$ may be found via

$$\sin \varnothing_0 = \sin \lambda \sin \delta + \cos \lambda \cos \delta \tag{A.5}$$

Atmospheric transmissivity, τ, was calculated as a function of the elevation (ν) and range of

diurnal air temperature values on site (ΔT), as provided by Coops et al. (Coops et al. 2000), following a similar model developed by Thornton & Running (1999).

$$\tau = (0.65 + 0.008v) \cdot [1 - \exp(-B \cdot \Delta T^{1.5})]$$

(A.6)

where v is 43.2m for Tamar Suspension Bridge, and

$$B = 0.031 + 0.201 \exp(-0.185 \cdot \Delta T)$$

(A.7)

This is an alternative to the formula used by Woodward et al. (Woodward et al. 2001), where atmospheric transmissivity was a function of the day of the year. This was not adopted since the range of monitored air temperatures at Plymouth was similar for the whole observed year, probably due to atypical seasonal cloud cover, and as a result atmospheric transmissivity is affected. Baigorria et al. (Baigorria et al. 2004) has shown that transmissivity models relating to the air temperature demonstrate more reliable results for the Andes compared to models that are dependent on time.

The diffuse portion of total irradiance, $J_{0,d}$, can be calculated by

$$J_{0,d} = J_{0,p} \left(f_{blue} \cdot (1 - f_{cc}) + f_{cloud} \cdot f_{cc} \right)$$

(A.8)

where f_c is the mean daily cloud cover, which is assumed $f_c = 1 - (S/h)$, being a dimensionless value between 0 (no cloud cover) and 1 (complete cloud cover).

$J_{0,p}$ is the potential total clear sky mean daily irradiance, which is calculated by

$$J_{0,p} = 1367 \frac{p}{\pi} \left(1 + \tau^{1/\sin\varnothing_0} \right) \sin\varnothing_0$$

(A.9)

The values of f_{blue} and f_{cloud} are the relative radiation intensities under blue sky and cloudy conditions, respectively.

$$f_{blue} = \frac{1 - \tau^{1/\sin\varnothing_0}}{1 + \tau^{1/\sin\varnothing_0}}$$

(A.10)

$$f_{cloud} = F \cdot f_{blue}$$

(A.11)

The parameter f_{blue} increases the intensity of the diffuse radiation when atmospheric transmissivity is low, which is why the diffuse radiation seen previously in Figure 6.4 on cloudy days, such as the 10th of June, is larger than others. The parameter F varies depending on the

site. For the UK the mean yearly value of F varies between 0.69 and 0.87. For the purposes of this study a value of 0.884 was taken, which is the value found at Aberporth; the closest available site being 195km away from Plymouth (Miller et al. 2008).

A.2   HALF-HOURLY VALUES

Following the identification of total daily irradiance, the next step is to identify the amount of radiation upon the bridge in half-hourly steps. The daily course of the sun takes a cosine pattern; providing 0 radiation between dusk and the dawn of the following day, and reaches its peak at solar noon. Thus the hourly dependent formula for solar radiation, J_t, taken from Chen et al. (J. M. Chen et al. 1999), is

$$J_t = J_0 \cos\left(\frac{\theta - \theta_0}{\pi/2 - \theta_0} \cdot \frac{\pi}{2} \right) \tag{A.12}$$

where θ is the solar zenith angle, and θ_0 is the solar zenith angle at solar noon (solar noon not necessarily at 12:00pm). This formula is only applicable when $\theta < \pi/2$, otherwise the sun will be beyond the horizon; hence no sunlight! The solar zenith angle can be calculated by subtracting the solar elevation angle from $\pi/2$:

$$\theta = \pi/2 - \sin^{-1}\left(\cos\varphi \cos\delta \cos\lambda + \sin\delta \sin\lambda \right) \tag{A.13}$$

where φ is the hour angle. The hour angle is measured in radians (running from $-\pi/2$ to 0 during the morning, then returning to $\pi/2$ at midnight), and is calculated from a slightly modified version of the local time t, measured in hours:

$$\varphi = \frac{\pi}{12}\left(t + \frac{\zeta}{60} - 12 \right) - \frac{\pi}{2} \tag{A.14}$$

where ζ is the net time correction factor, measured in minutes. This factor accounts for the time variations within a timezone due to longitudinal variations, as well as incorporating the equation of time ξ which corrects for the eccentricity of the Earth's orbit and its tilt. The time correction factor ζ is thus

$$\zeta = 4\left(\mu - 15° \cdot \Delta t_{GMT} \right) + \xi \tag{A.15}$$

where μ is the longitude of the location in degrees, and Δt_{GMT} is the difference between the

local time t and the Greenwich mean time, in hours.

The equation of time, measured in minutes, is calculated from the equations

$$\xi = 9.87\sin(2A) - 7.53\cos(A) - 1.5\sin(A) \tag{A.16}$$

$$A = \frac{2\pi}{365}(d - 81) \tag{A.17}$$

A.3   FACTOR FOR INCLINED SURFACES

If the surface is inclined, such as on the towers, it is likely that it will be within its own shade when the sun is on its opposite side. Thus the direct beam component in Equation (A.4) has to be adjusted (Sellers et al. 1997; Wang et al. 2002):

$$J_{0,s,i} = f_i \cdot J_{0,s} \tag{A.18}$$

where f_i is the direct beam correction factor, which is limited to values between 0 and 1. This value is dependent on the angle of the slope and the solar zenith angle θ:

$$f_i = \frac{\cos\theta_i}{\cos\theta} \tag{A.19}$$

where θ_i is the angle between the solar zenith angle to the slope normal, which is determined from the inclination from the horizontal for the slope β, the aspect of the face γ (North = zero, East = 90°), the solar zenith angle and the solar azimuth ψ (North = zero, East = 90°).

$$\cos\theta_i = \cos\beta\cos\theta + \sin\beta\sin\theta\cos(\psi - \gamma) \tag{A.20}$$

The solar azimuth is provided by

$$\psi = \cos^{-1}\left(\frac{\sin\delta\cos\lambda - \cos\varphi\cos\delta\sin\lambda}{\cos\varnothing}\right) \tag{A.21}$$

where $\varnothing$ is the solar elevation at that time of day, calculated by

$$\sin\varnothing = \sin\lambda\sin\delta + \cos\varphi\cos\lambda\cos\delta \tag{A.22}$$

REFERENCES

Baigorria, G.A. et al., 2004. Atmospheric transmissivity: distribution and empirical estimation around the central Andes. *International Journal of Climatology*, 24(9), pp.1121–1136.

Chen, J.M. et al., 1999. Daily canopy photosynthesis model through temporal and spatial scaling for remote sensing applications. *Ecological modelling*, 124(2-3), pp.99–119.

Coops, N.C., Waring, R.H. & Moncrieff, J.B., 2000. Estimating mean monthly incident solar radiation on horizontal and inclined slopes from mean monthly temperatures extremes. *International Journal of Biometeorology*, 44(4), pp.204–211.

Miller, D.G. et al., 2008. Testing the spatial applicability of the Johnson-Woodward method for estimating solar radiation from sunshine duration data. *Agricultural and forest meteorology*, 148(3), pp.466–480.

Rivington, M. et al., 2005. Evaluation of three model estimations of solar radiation at 24 UK stations. *Agricultural and forest meteorology*, 132(3-4), pp.228–243.

Sellers, P.J. et al., 1997. The impact of using area-averaged land surface properties—topography, vegetation condition, soil wetness—in calculations of intermediate scale (approximately 10 km2) surface-atmosphere heat and moisture fluxes. *Journal of Hydrology*, 190(3-4), pp.269–301.

Thornton, P.E. & Running, S.W., 1999. An improved algorithm for estimating incident daily solar radiation from measurements of temperature, humidity, and precipitation. *Agricultural and Forest Meteorology*, 93(4), pp.211–228.

Wang, S., Chen, W. & Cihlar, Josef, 2002. New calculation methods of diurnal distribution of solar radiation and its interception by canopy over complex terrain. *Ecological Modelling*, 155(2-3), pp.191–204.

Woodward, S.J.R., Barker, D.J. & Zyskowski, R.F., 2001. A practical model for predicting soil water deficit in New Zealand pastures. *New Zealand Journal of Agricultural Research*, 44(1), pp.91–109.